Structural Study of Interaction between the FMN Binding Domain of Cytochrome P450 Reductase and Its Redox Partners – Cytochrome P450/Cytochrome c by NMR

and

NMR Characterization of Monomeric and Oligomeric Conformations of Human Calcitonin and Its Interaction with EGCG

by

Rui Huang

A dissertation submitted in partial fulfillment
of the requirements for the degree of
Doctor of Philosophy
(Chemistry)
in the University of Michigan
2014

Doctoral Committee:

Professor Ayyalusamy Ramamoorthy, Chair
Professor Zhan Chen
Assistant Professor Kenichi Kuroda
Associate Professor Michal R. Zochowski

Acknowledgements

I would like to first thank my supervisor, Dr. A. Ramamoorthy, for his constant support along the past five years. His advice and guidance has been very valuable not only for the progress of my project but also for my scientific career in general. In particular, his encouragement for innovation and his willingness to try the impossible has inspired me and going to continue to affect me for my future career.

I would also like to thank my committee members, Dr. Chen, Dr. Kuroda and Dr. Zochowski. Your support and suggestions on my project have been very helpful to me.

A great many thanks should go to the members of the Rams lab including the ones that have gone and the new ones that I have just fortunately met. To Shivani, Nataliya and Vivek, you have taught me most of the things that I need to know for my project. To Sam, Meng, Manoj, Neil, and Kamal, I really cherish our friendship, and thank you for being there along the way. And to Patrick, I wish I could have known you much earlier and I feel very lucky to meet you in my final year. And for the rest of the lab, thank you for always being so helpful and encouraging. You are the ones who make the lab not only a working environment for me, but a place that I belong to.

Special thanks go to my great parents, who have always encouraged me to peruse my dreams. Thank you for always standing behind me even being thousands of miles away. Thank you for making me the person who I am.

Thank you, my C222 family in Ann Abor. To Laoge, Chengzi, Angelica and Suchandan, I cannot imagine my life without you in these five years. I feel very grateful that we came together at this time of my life, and those memories we had will be accompany me lifelong.

Finally, I’m most grateful to my love, Juan Felipe, for standing beside me in good and bad times. I could not have done this without you. Thank you.

Table of Contents

List of Tables

List of Figures

List of Appendices

List of Abbreviations

CPR – NADPH-cytochrome P450 reductase

FBD – the FMN binding domain of CPR

FMN – Flavin mononucleotide

FAD – Flavin adenine dinucleotide

NADPH – Nicotinamide adenine dinucleotide phosphate

Cyt – Cytochrome

Cyt 450 – Cytochrome P450

ELDOR – Electron-electron double resonance

FRET – Fluorescence resonance energy transfer

AFM – Atomic force microscopy

DMPC – 1,2-dimyristoyl-sn-glycero-3-phosphocholine

DHPC – 1,2-dihexanoyl-sn-glycero-3-phosphor-choline

DLPC – 1,2-dilauryl-sn-glycero-3-phosphor-choline

CP – Cross polarization

SLF – Separated local field

NMR – Nuclear magnetic resonance

PISA wheel – Polarity index slant angle wheel

HIMSLEF – Heteronuclear isotropic mixing by separated local field spectroscopy

hCT – Human calcitonin

EGCG – Epigallocatechin 3-gallate

Aβ – Alzheimer beta peptid e

IAPP – Islet amyloid polypeptide

MSP – Merozoite surface protein

TOCSY – Total correlation spectroscopy

NOESY – Nuclear overhauser effect spectroscopy

STE – Stimulated echo

PFG – Pulse field gradient

SOFAST – Selective optimized flip-angle short transient

HMQC – heteronuclear multi-quantum correlation

NOE – nuclear overhauser effect

MTSL – S-(2,2,5,5-tetramethyl-2,5-dihydro-1H-pyrrol-3-yl)methyl methanesulfonothioate)

Abstract

Cytochrome P450 reductase (CPR) is a diflavin protein which donates electrons to a variety of microsomal cytochrome P450s, heme oxygenase, cytochrome b_5, cytochrome c as well as therapeutic prodrugs. It plays an indispensable role in the cytochrome P450 monooxygenase system, which is responsible for the metabolism of myriads of endogenous compounds including vitamins, steroids and hormones, as well as exogenous compounds including environmental toxins and drugs. In order to understand the electron transfer mechanism between CPR and its redox partners and get an better insight into its physiological function, it is essential to obtain detailed structural information on the electron transfer complexes. The nature of weak interactions between electron transfer proteins poses great difficulty to crystallization, while NMR spectroscopy has developed into a powerful tool in acquiring high-resolution structural information on the protein complexes. This thesis aims to unveil the structures of electron transfer complexes formed between the FMN binding domain (FBD) of CPR and its redox partners – cytochrome P450 and cytochrome c, map the binding interfaces of the complexes and propose potential electron transfer pathways. A combination of solution and solid-state NMR techniques, in conjunction with kinetics studies and molecular docking, were utilized for the investigation. Kinetics of electron transfer from FBD to cytochrome P450/cytochrome c was characterized and compared with wild-type CPR. The results support that conformational gating of CPR plays a key role in the kinetics of interprotein electron transfer. Solution NMR experiments were carried out to map the binding interfaces in the complexes, from which structural models of the complexes were generated.

In addition, high-resolution structures of human calcitonin have been investigated using NMR spectroscopy. Calcitonin is a 32-residue peptide hormone known for its hypocalcemic effect and its inhibition of bone resorption. While calcitonin has been used in therapy for osteoporosis and Paget's disease for decades, human calcitonin (hCT) forms fibrils in aqueous solution that limit its therapeutic application. The molecular mechanism of fiber formation by calcitonin is not well understood. In this thesis, by solving the high-resolution structures of hCT under two different conditions, we discovered that the peptide undergoes a conformational transition in the process of molecular association. The effect of the polyphenol epigallocatechin 3-gallate (EGCG) on hCT fibrillation was also investigated by NMR and electron microscopy, which show that EGCG efficiently inhibits fibril formation of hCT by preventing the initial association of hCT before fiber formation.

CHAPTER 1

Introduction

1.1 NADPH-Cytochrome P450 Reductase

1.1.1 Background and significance

NADPH-cytochrome P450 reductase (CPR) is a 78 kDa diflavin microsomal enzyme that plays a key role in the "cytochrome P450 monoxygenase system" – an enzyme system responsible for the catalysis of a wide variety of oxidative transformations that are essential for the livings, including the metabolism of ~75% known pharmaceuticals in humans (*1*). CPR was first isolated from yeast as "FMN-containing cytochrome c reductase" (*2*); later mammal CPR was purified from pig liver (*3*). CPR was shown to be localized to the cytoplasmic surface of the endoplasmic reticulum (*4*, *5*) and responsible for transferring electrons from NADPH to cytochrome P450s (cyt P450s), which is an essential step in the catalytic cycle of cyt P450s. Microsomal CPR is a multi-domain protein composed of an N-terminal transmembrane domain, an FMN binding domain, an FAD/NADPH binding domain and a connecting domain which covalently connects the aforementioned two domains (Figure 1.1) (*6*).

CPR is a prototype of diflavin reductases – a small family of enzymes which also include nitric oxide synthases (*7*, *8*), methionine synthase reductase (*9*), bacterial cytochrome P450 BM3 (*10*), and the reductase subunit of bacterial sulfite reductase (*11*). It is believed that CPR is the result of gene fusion between ancestral FMN- and FAD-containing flavin proteins due to evolution (*12*) for the following reasons: 1. The FMN and FAD/NADPH binding domains of CPR have shown structural similarity with bacteria flavodoxin and ferredoxin reductase; 2. The genes of the FMN and FAD/NADPH binding domains can be dissected and expressed

independently as discrete functional units, and exhibit biological activity as a functional complex after reconstitution (*13*).

CPR has been discovered in various eukaryotes including yeast, chicken, rat, cow, rabbit and human. High sequence homology was found in CPR from different species, suggesting the importance of this enzyme throughout revolution. It has been shown that deficiency and mutation of the CPR gene can lead to varies abnormalities and health problems. Knock-out of the gene in mice leads to embryonic lethality (*14, 15*), implying that CPR plays an essential role in the normal development of high-level organisms. A post-natal deletion of CPR was carried out in the liver of the mice. The hepatic CPR-null mice exhibit a series of metabolic disorders associated with the malfunction of the cytochrome P450 (cyt P450) monoxygenase system caused by CPR deletion (*16*). In addition to the major role in the cytochrome P450 enzyme system, CPR is also known to reduce cytochrome c (*4*), cytochrome b_5 (*17*) and heme oxygenase (*18*). It is also shown to be involved in bioactivation of therapeutic prodrugs such as doxorubicin (*19*) and mitomycin c (*20*).

1.1.2 Structural characteristics of CPR

The first high-resolution X-ray crystal structure of CPR soluble domain was solved by Wang *et al.* on rat CPR with the N-terminal transmembrane domain removed (*6*). It shows that the soluble domain of CPR is composed of three domain: an FMN binding domain, the overall fold of which highly resembles bacterial flavodoxin, an FAD/NADPH binding domain homologous to ferredoxin reductase, and a connecting domain between the aforementioned two domains, the functional of which has not yet been fully elucidated.

The FMN binding domain consists of a typical wound α-β-α fold – five strands of parallel β-sheets flanked by five α-helices. The FMN cofactor is located at the C-terminal end of the β-sheets with its isoalloxazine ring flanked between Tyr-140 and Tyr-178 and forms hydrogen-bonds with a number of residues at the loop regions (*6, 21, 22*). The FMN cofactor binds tightly to the domain with a dissociation constant of 2.0×10^8 M^{-1} (*22*). Removal of Tyr-140 or/and Typ-178 has been shown to cause a drastic decrease in the binding affinity between the FMN cofactor and the protein (*23*). This domain has 19 positively and 34 negatively surface charged

residues under neutral pH condition, and exhibits a large electrical dipole of 677 Debye pointing towards the FMN binding site (*22*) (Figure 1.2). The significant separation of charges is expected to play an important role in orienting the domain in a proper way to interact with its redox partners and aid in electron transfer process.

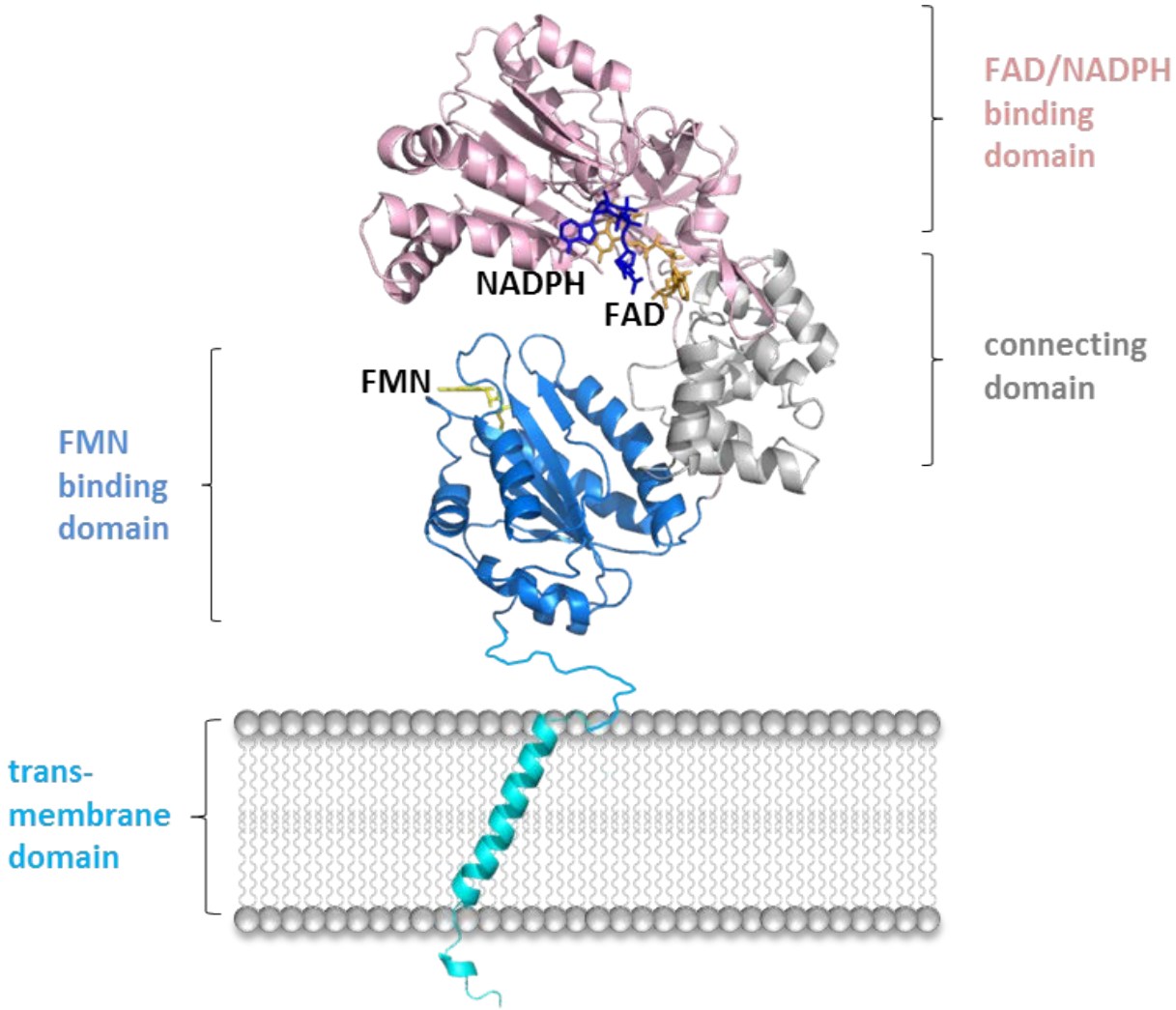

Figure 1.1 Domains of microsomal CPR. The structure of the soluble domain is an X-ray crystal structure of a rat CPR mutant ΔTGEE (PDB code 3ES9) (*24*). The transmembrane domain is proposed to adopt an α-helical conformation.

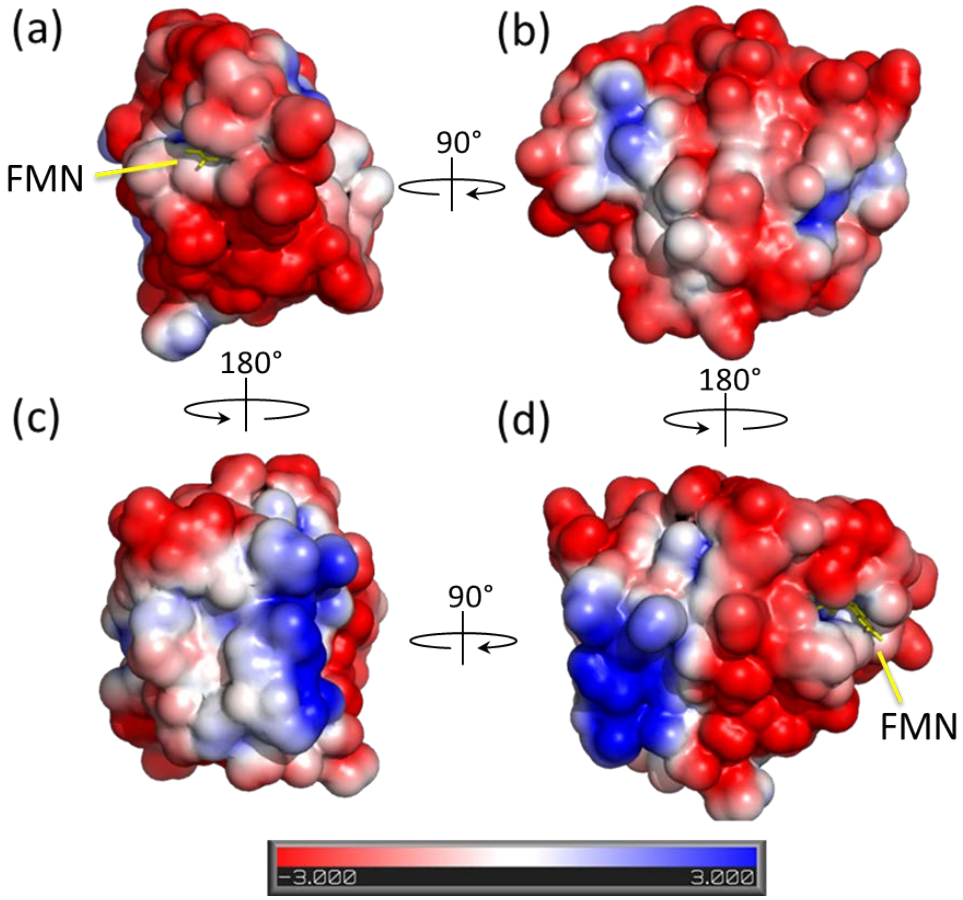

Figure 1.2 Electrostatic potential surface of the FMN binding domain of rat CPR (PDB code 1AMO) calculated using PyMOL (Version 1.1, Schrödinger, LLC) with APBS plugin (*25*). Panel (a) shows the side of FBD where the cofactor FMN is solvent exposed. FMN is indicated in yellow sticks. Panel (b) to (d) are the successive 90° clockwise rotations from panel (a) along the axis parallel to the paper plane.

The FAD/NADPH binding domain can be sequentially divided into two parts—the N-terminal portion composed primarily of antiparallel β-sheets and the C-terminal part which is, like FBD, composed of an α-β-α fold. In rat CPR, the isoalloxazine ring of the FAD cofactor binds to the intersection of the aforementioned two parts and is stacked between Trp-677 (parallel to the plane of isoalloxazine ring) and Tyr-456 (~70° tilted with respect to the isoalloxazine ring) (Figure 1.3). Deletion/Mutation of these two residues leads to significant reduction in the binding affinity of FAD. The FAD cofactor also forms hydrogen bonds with the surrounding residues, such as Arg-454, Gly-488, Ala-490, Thr-491, some of which are crucial in stabilizing the FAD cofactor by binding to its pyrophosphate group (*e.g.* Arg-454) (*26*). The

conformation and location of NADP(H) is less defined than the other two cofactors due to the spatial disorder of the nicotinamide ring in the crystal structure (*6*), similar phenomenon of which was also observed in the crystal structures of enzymes in the ferredoxin-NADP(+) reductase. The lack of electron density of the nicotinamide ring suggests a certain extent of mobility in this region of the cofactor. As observed in the crystal structure (*6*), neither of the suggested positions of the nicotinamide ring is spatially close enough to FAD for hydride transfer, and the isoalloxazine ring of FAD is "protected" by the aromatic side chain of Trp-677 from contacting NADP(H) (Figure 1.3). Therefore, it has been proposed that hydride transfer from NADPH to FAD would involve Trp-677 flipping away from FAD to make space for contacting with NADPH. Mutation of the corresponding Trp in human CPR (Trp-676) leads to a slow release of NADP(+) from the active site, implying that Trp-676 serves as a trigger for NADP(+) dissociation following hydride transfer (*27*). The adenosine-ribose and the pyrophosphate moieties of NADPH are well defined in the crystal structure, forming hydrogen bonds with residue Arg-298, Ile-535, Arg-567, Ser-596, Arg-597, Lys-602, Tyr-604, Gln-606 and Asp-639. Mutations of residues Arg-597 and Lys-602 in combination with Trp-677 lead to reduced inhibition effect by $NADP^+$ on catalysis, which suggests lower binding affinity for NADP(H) (*28*).

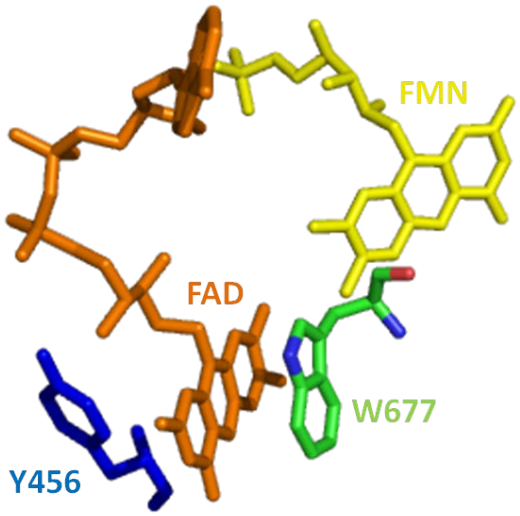

Figure 1.3 Arrangement of the FMN and FAD cofactors in CPR (PDB code 1AMO).

The connecting domain sequentially serves as a "bridge" between the FMN binding domain and the FAD/NADPH binding domain, and spatially forms direct contact with the two

catalytic domains. The interface between the connecting domain and the FMN binding domain is mainly hydrophilic, while the interface between the connecting domain and the FAD/NADPH binding domain are relatively more hydrophobic. The function of this domain has not been fully investigated, although it is suggested that it may be partly responsible for aligning and orienting the two catalytic domains to achieve optimal interdomain electron transfer (*24, 29, 30*). One of the interesting discoveries is the important role that a "hinge" (residue 232-242 in rat CPR) plays in controlling the domain movement and the efficiency of interflavin electron transfer (*24*): deletion of four residues from the "hinge" resulted in an extended conformation of CPR, which impairs electron transfer from FAD to FMN but exposes the FMN cofactor to the solvent allowing it to interact with cyt P450. The crystal structure of a chimeric yeast-human CPR revealed a fully open conformation in which the interface between the FMN binding domain and the connecting domain is completely disrupted and the FMN binding domain is fully solvent exposed (*29, 30*).

It has been postulated that the transmembrane domain of CPR adopts an α-helical conformation (*31-34*). However, high resolution structure of the transmembrane domain has not been revealed experimentally. The major difficulty lies in the hydrophobicity and dynamics of the transmembrane domain, preventing it from crystallization with the soluble domain. The transmembrane domain of CPR plays a vital role in aiding in electron transfer between CPR and cyt P450 (*31, 35, 36*). Lacking the transmembrane anchor, CPR is still able to reduce cytochrome c and other artificial acceptors, but has impaired electron transfer to cyt P450 (*6*).

1.1.3 Mechanism of internal electron transfer in CPR

As an essential component of the "cytochrome P450 monoxygenase system", CPR plays the role of transferring electrons from NADPH to cyt P450 following the pathway NADPH → FAD → FMN → cyt P450. NADPH is as an obligate two-electron donor while cyt P450 is an obligate one-electron acceptor. During the catalytic cycle of cyt P450, the two electrons from NADPH need to be shuttled by CPR sequentially to cyt P450 at different steps of the cycle, which is a remarkable feature of CPR. This characteristic of CPR is attributed to the fact that one electron-reduced semiquinone form of flavin cofactors (FADH• or FMNH•) can be stabilized in the protein structure thermodynamically, which serves as a bridge in the electron flow (*37-39*).

It is proposed that the enzyme undergoes the cycle between one electron and three electron-reduced forms under physiological conditions (Figure 1.4) due to the midpoint redox potentials for each flavin couple (Figure 1.5) (*40-42*). The blue semiquinone form of FMN (FMNH•) is both thermodynamically and kinetically stabilized. However, it is incapable of transferring electrons to cyt P450 due to its relative high redox potential comparing to that of cyt P450 (Figure 1.5), while the hydroquinone form of FMN ($FMNH_2$) is more likely to be the electron donor of cyt P450 as shown in the cycle (Figure 1.4).

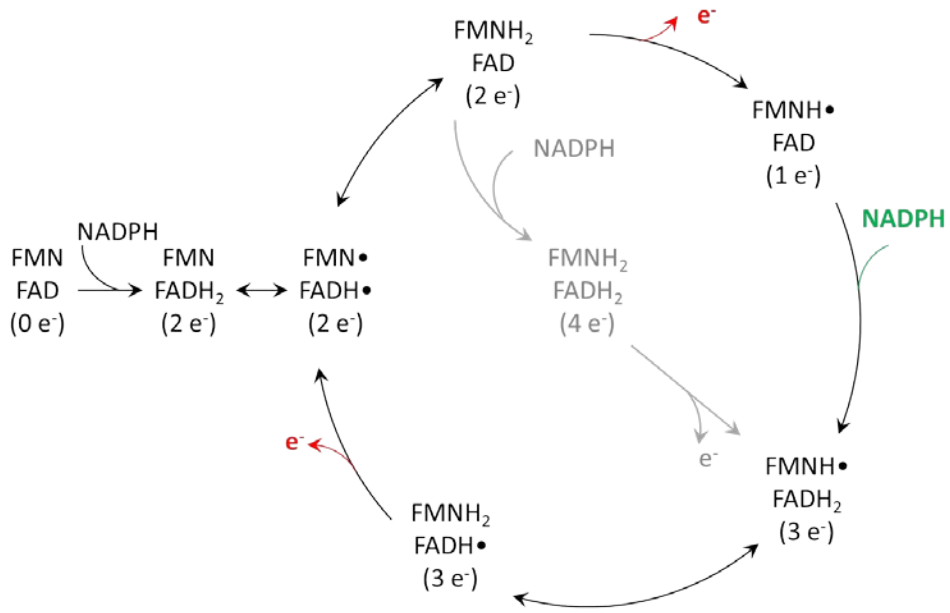

Figure 1.4 Electron transfer cycle of CPR. It undergoes the cycle between one and three electron-reduced forms as indicated by the black lines. Two electron- or three electron-reduced CPR is able to donate electrons to cyt P450, indicated in red.

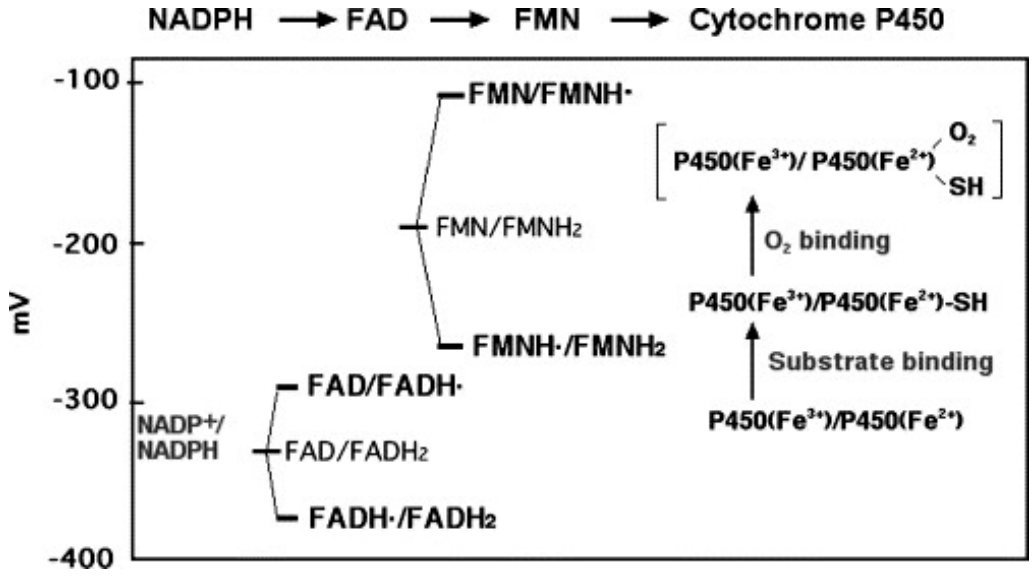

Figure 1.5 The reduction potentials of flavins in CPR. The reduction potentials of the individual redox couples of the FAD and FMN cofactors of rabbit CPR and of cyt P450 (*43*). Reprinted with permission from Iyanagi. Copyright 2005 Elsevier Inc.

Kinetics of internal electron transfer from NADPH via FAD to FMN has been investigated using a variety of methods. It has been shown that hydride transfer from NADPH to isolated FAD domain is reversible – electron transfer from $FADH_2$ to NADP+ occurs more rapidly (8 s^{-1}) than that from NADPH to FAD (3 s^{-1}) (*44*), which agrees with the redox potentials of the NADPH/NADP+ and FAD/$FADH_2$ groups (Figure 1.5). Interflavin electron transfer between FAD and FMN is relatively faster, judging from the kinetic studies which showed that the accumulation of blue disemiquinone species of CPR (FMNH•/FADH•) takes place at the same rate as hydride transfer from NADPH to FAD (*44*). The rate of interflavin electron transfer has been measured by laser flash photolysis for rabbit CPR (*45*) and temperature-jump relaxation kinetic methods for human CPR (*46, 47*), which appears to be 15 s^{-1} and 55 s^{-1} respectively. On the other hand, according to the crystal structure of CPR (*6*), the closest distance between the two flavins is 4 Å which would predict an intrinsic electron transfer rate of 10^{10} s^{-1} (*6, 48*). This conflict implies that the interflavin electron transfer is gated. Possible gating mechanism includes deprotonation of FAD blue semiquinone, interdomain movement between the FMN and FAD/NADPH binding domains. The possibility of deprotonation gating was disproved by the observation that solvent isotope effect does not affect the reaction rate (*47*). It was also shown

that viscous solvent (75% w/v glycerol) compromises the rate of interflavin electron transfer, which implies domain movement could be responsible for gating the reaction (*47*).

1.1.4 Domain movement of CPR

CPR is a multi-domain enzyme, the catalytic function of which requires orchestrated intraprotein and interprotein electron transfer. Exquisite control of the association and dissociation between the domains or proteins is essential for rapid turnover of the enzyme (*49*). In the "close" conformation of CPR observed in the crystal structure (Figure 1.6A) (*6*), FMN is not solvent exposed and thus cannot transfer electrons to cyt P450. Furthermore, the crucial residues suggested by mutagenesis studies for binding cyt P450 were not fully exposed to make contact with cyt P450 (*50*). Therefore, it is proposed that movement of the FMN binding domain relative to the rest of the CPR molecule is required during interprotein electron transfer. Similar dynamic characteristics of the FMN binding domain were also proposed in other flavin proteins (*49, 51*). For example, in the crystal structure of the reductase subunit of *E. Coli* sulfite reductase, the electron density of the FMN binding module is absent suggesting great flexibility of this domain (*52*).

Recent observations of domain movement in CPR have been the major breakthroughs in understanding the conformational change of the enzyme. A crystal structure of a yeast-human chimeric CPR (Figure 1.6B) revealed an open conformation in which there is a large separation between the FMN and the FAD/NADPH binding domains compared to the close form of the wild-type enzyme (Figure 1.6A) (*29*). Deletion of four amino acids from a "hinge" that connects the FMN binding domain with the rest of the molecule also led to extended formations in the crystal structure (Figure 1.6C) (*24*). The mutation turned out to impair interflavin electron transfer, but did not seem to affect electron transfer from FBD to cyt P450. These results suggest that the extended conformations observed in the crystal structure may resemble the conformation of CPR during interprotein electron transfer. Necessity of domain movement was also demonstrated by a mutant with an engineered disulfite bond covalently linking the FAD/NADPH and FMN binding domain, which strictly constrained interdomain movement. The mutant exhibited drastically decreased rates in both interflavin and interprotein electron transfer, unless the disulfite bond was reduced (*53*).

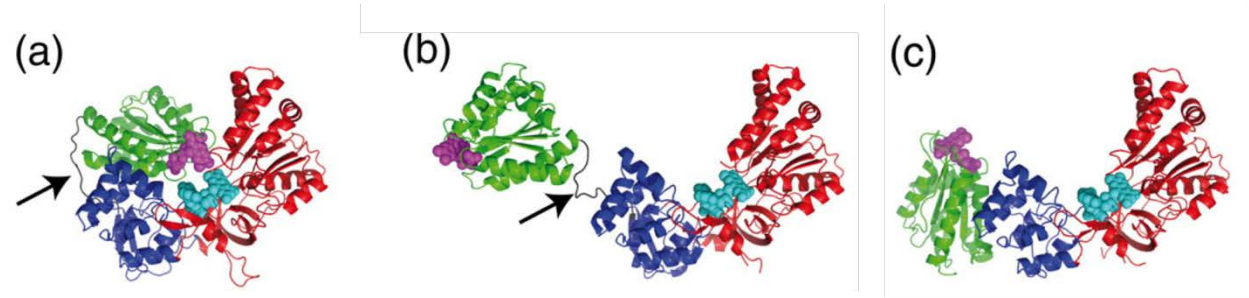

Figure 1.6 Structures of CPR. Different conformations of CPR were observed in crystal structures: (a) a closed conformation of wild-type CPR (PDB code 1AMO) (*6*), (b) an open conformation of yeast-human chimeric CPR (PDB code 3FJO) (*29*), (c) an extended conformation of a CPR mutant with four residues deleted from the "hinge" (PBD code 3ES9) (*24*). Reprinted with permission from Vincent *el al*. Copyright 2012 Elsevier Ltd.

Open conformations of CPR have also been identified by other means of investigation. A combined NMR and SAXS study concluded that the oxidized CPR exists in equilibrium between approximately equal amount of two conformations – a closed conformation and a more extended one suitable for interprotein electron transfer. The equilibrium can be shifted by reduction of the flavins and coenzyme binding (*54*). In contrast, a recent NMR study revealed that CPR exists in a predominant "close" conformation in the oxidized state by measuring the ^{15}N relaxation and ^{1}H-^{15}N residual dipolar couplings (RDC) of the CPR residues (*55*). The cause of the controversy is still to be determined. An electron-electron double resonance (ELDOR) spectroscopy study identified several conformations in two electron-reduced CPR and demonstrated the significant effect of nucleotide binding, solvent condition and pressure on the interflavin distance in the disemiquinone form of the enzyme (*56*). According to this study, nucleotide binding induces more closed conformation which favors interflavin electron transfer, while open conformation makes it easier for electron transfer to occur from CPR to its redox partners. In addition, evidence was provided showing that reduction of the flavin cofactors in CPR induces opening of the enzyme whereas coenzymn binding induces closed structure using FRET accompanied by stopped-flow kinetics measurement (*57*).

1.2 Cytochrome P450

1.2.1 Background and significance

Cytochrome P450 (cyt P450) is a super family of enzymes that are found in all kingdoms of living including bacteria, fungi, insects, plants and animals. In human beings, 57 membrane-bound cyt P450s are found to distribute in most of the tissues (*1, 58, 59*). A great proportion of the enzymes are found in the liver where they are located in the smooth endoplasmic reticulum (ER) membrane of hepatocytes (*60*). Cyt P450 metabolizes a large number and a wide variety of endogenous (*e.g.* steroids, fatty acids, lipids, etc.) (*61*) and exogenous substrates (*e.g.* environmental toxins, drugs, etc.). In particular, cyt P450 is responsible for the phase I metabolism of approximately 75% of the pharmaceuticals in use today (*1*). By catalyzing the hydroxylation reaction, cyt P450 is able to convert the hydrophobic drugs into more hydrophilic products so that they can be eliminated from the body via urine, which reduces the toxicity of the drugs. On the other hand, cyt P450 may also activate certain inert compounds or drugs to toxic products (*1*). Therefore, the bioavailability and side effects of drugs are highly dependent on cyt P450 metabolism. Understanding the structure and mechanism of various cyt P450s has a profound meaning in predicting the metabolism and toxicity of drugs and other chemicals and providing basic information for drug designing.

In addition to its important role in drug metabolism, cyt P450 is involved in many pathways of endogenous metabolism, including steroid hormone biosynthesis, prostaglandin and fatty acid metabolism, lipid oxidation and vitamin D_3 hydrolysis (*61*). Taken steroid-oxidizing P450s as an example, most of these cyt P450 isoforms are critical for human being and the level of these enzymes are relatively invariable among individuals, unlike the xenobiotic-metabolizing P450s which may vary considerably (*62*). Deficiency in these cyt P450s usually leads to serious diseases, including sex hormone deficiencies and increased risk of prostate cancer (*63*).

The most common reaction that cyt P450 catalyzes is the insertion of an atom of “activated” oxygen into the C-H bond of a substrate as described in Reaction 1, in which RH is the hydrophobic substrate and ROH is the product. Hydroxylation of an inactivated C-H bond is a challenge task to achieve synthetically due to the high activation energy. The mechanism of this reaction catalyzed by cyt P450 has intrigued chemists for decades both for the desire of

understanding the biological oxygen activation and for the development of new and economic catalysts. The general accepted catalytic cycle of cyt P450 is shown in Figure 1.7, in which two electrons were donated to cyt P450 at different steps by its redox partners – CPR and/or cyt b_5. While CPR can donate both the first and second electrons, cyt b_5 is only involved in delivering of the second electron due to its relative high redox potential (≅ 25 mV). Notably, the cycle describes a simplified version of the reaction, and in reality the steps do not always follow the linear order along the cycle. Dissociation of the substrate can occur in other steps in the cycle as well (*64*, *65*).

$$RH + O_2 + NADPH + H^+ \rightarrow ROH + H_2O + NADP^+ \quad (1)$$

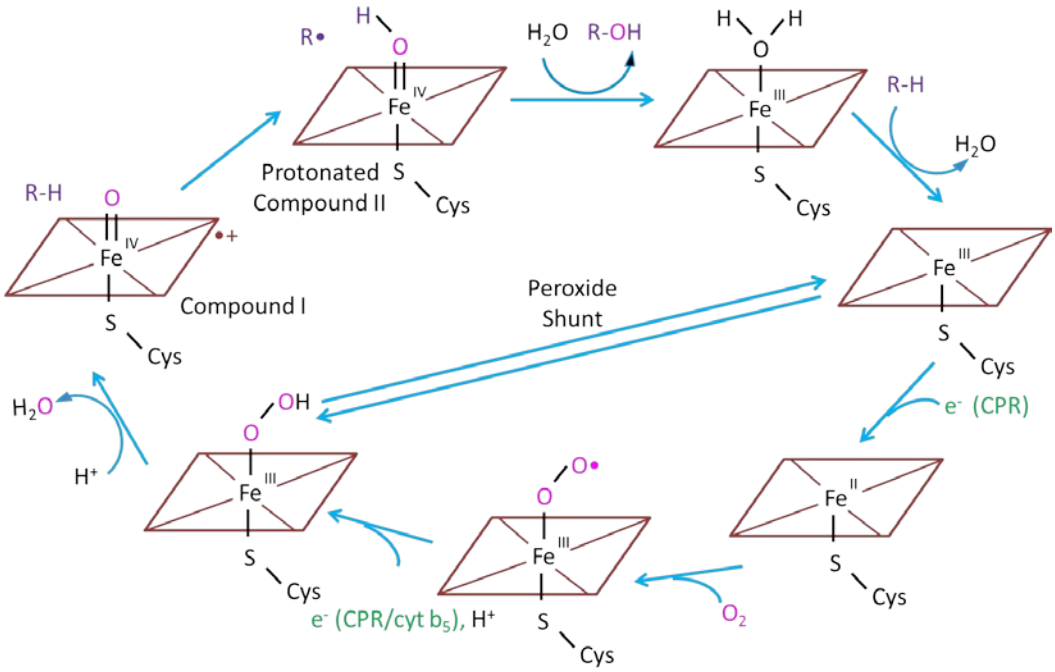

Figure 1.7 Catalytic cycle of cytochrome P450. Two electrons were delivered to cyt P450 sequentially by CPR and/or cytochrome b_5 indicated in green.

1.2.2 Structure of cytochrome P450

Up till now, hundreds of structures on 20 unique cyt P450s have been deposited in the Protein Data Bank. These structures revealed that the overall folding of cyt P450s is quite conservative across the P450 family and unique among all other proteins. A distinct difference

between prokaryotic and eukaryotic cyt P450s lies in their affinities to membrane. Unlike prokaryotic cyt P450s, eukaryotic cyt P450s are usually membrane-bound, among which the majority are incorporated in the endoplasmic reticulum and a few in mitochondria.

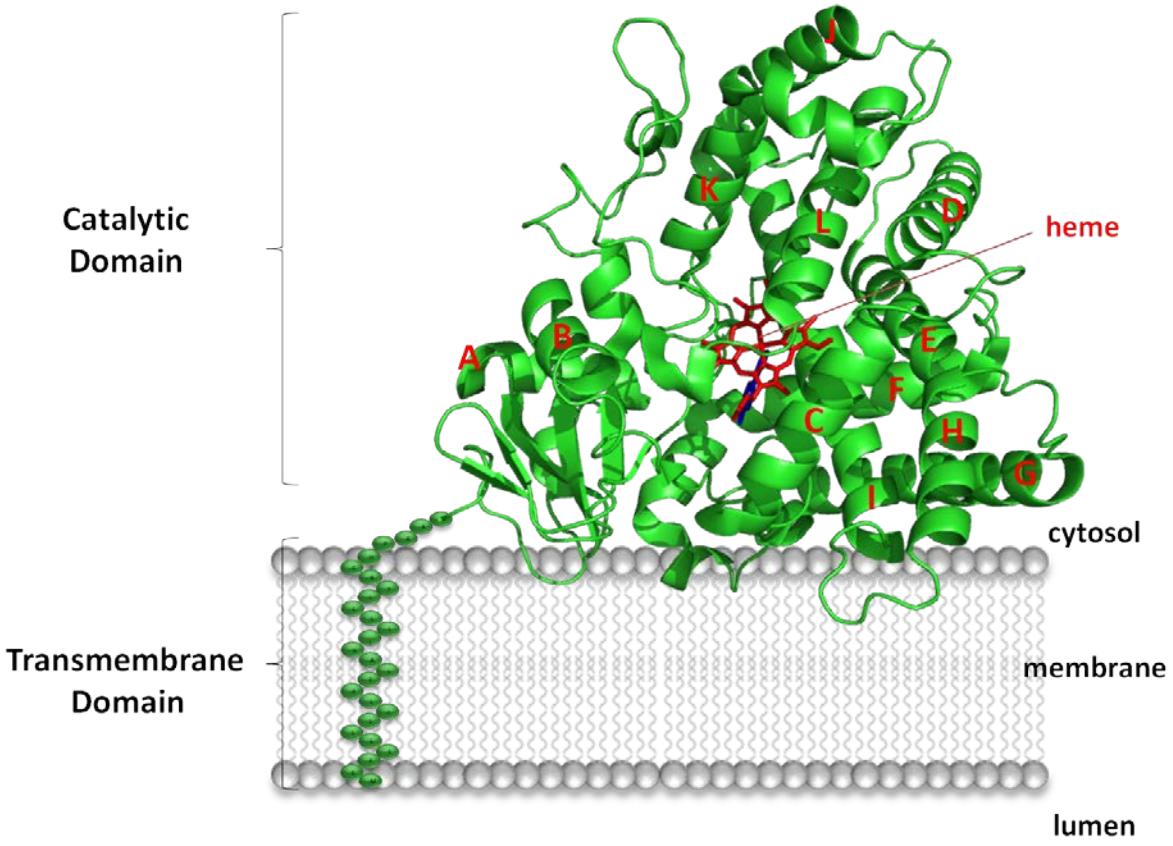

Figure 1.8 Structure of cyt P450 2B4. Cyt P450 2B4 consists of a catalytic domain (PDB code 1SUO) and a transmembrane domain. The major helices are alphabetically labeled in red.

Figure 1.8 is a structure of cyt p450 2B4 (PDB code 1SUO) – a microsomal cyt P450 from rabbit hepatocyte (*66*). It consists of a ~53 kDa catalytic domain and a transmembrane anchor. The structure of the catalytic domain has been solved in the presence of different substrates/inhibitors (*66-74*), while the transmembrane domain is proposed to adopt an α-helical conformation (*75-77*). In the catalytic domain of cyt P450 2B4, the heme was axially coordinated to Cys-436. The side on which the heme comes closest to the protein surface is called the proximal side. It is rich in positive charges (Figure 1.9) and is predicted to bind to the redox

partners of cyt P450 – CPR or cyt b_5 – driven by electrostatic interaction. Substrates enter the catalytic pocket of cyt P450 and lie on the other side of the heme. Although the overall folding of cyt P450 is conserved between different isoforms, relative positions of the secondary structural elements in the catalytic domain can differ substantially. The most conserved regions are generally close to the heme, *e.g.* helices I and L which form direct contact with the heme, while in regions that control substrate specificity, *e.g*. tbe B' helix, the structures differ most between isoforms (*62*). Even for the same cyt P450, due to the conformational plasticity of the structure, the structural features surrounding the active site are prone to large displacement to accommodate different substrates (*78*). In the case of cyt P450 2B4, there are four regions that could undergo considerable structural displacement in response to ligands – a loop preceding helix A and the N-terminal half of helix A (residue 39-57), helix B' through the C/D loop (residue 101-140), the C-terminal half of the helix E (residue 177-188), the C-terminal half of helix F through the N-terminal half of helix I (residue 203-298 (*73*).

Besides the N-terminus of the protein as a transmembrane anchor, eukaryotic cyt P450s have been shown to interact with membrane through additional binding sites. A number of microsomal cyt P450s, including cyt P450 1A1, 2B4, 2E1 and c17, were found to be membrane-bound even with the N-terminal transmembrane anchor (the first ~ 30 residues) removed (*79-84*). Antibody binding studies also revealed that the N-terminal transmembrane domain and the F-G and B-C loops of the family 2 P450s are inaccessible to antibodies due to either direct binding or in close proximity to the membrane (*85*). The insertion area of cyt P450 2B4 to the Langmuir-Blodgett monolayers was determined to be ~ 680 ± 95 $Å^2$ (*86*), which is greater than what is expected for a single transmembrane helix (170-250 $Å^2$). These evidences lead to a proposition that a hydrophobic tip of cyt P450 catalytic domain is immersed in the membrane, which could facilitate substrate access channel or orient the enzyme for productive interaction with its redox partners and aid in electron transfer.

1.3 Interaction and electron transfer between CPR and cyt P450

Cyt P450 receives two electrons sequentially from its redox partners at different stages of its catalytic cycle (Figure 1.7), the first of which is delivered by CPR and the second can be donated either by CPR or cyt b_5. Optimal interaction between CPR and cyt P450 is essential for efficient electron transfer from the reduced FMN cofactor to the heme of cyt P450. It has long

been postulated that the association between CPR and cyt P450 is driven by electrostatic interactions between a cluster/clusters of positively charged residues on the proximal surface of cyt P450 and negatively charged residues located on the FMN binding domain of CPR (Figure 1.9). For instance, chemical modification has been used to study the role of lysine and arginine residues of cyt P450 in the interaction between the two proteins. Acetylation of lysine residues in cyt P450 2B1 and 17α led to significantly reduced activity of the reconstituted cyt P450/CPR complex, implying the importance of the positively charged lysine residues in the electrostatic coupling with CPR (*87, 88*). Site-directed mutagenesis studies have indicated specific lysine and arginine residues on rat cyt P450 1A1 and 1A2 which may be involved in charge interaction with CPR (*89, 90*). A series of residues on the proximal side of cyt P450 2B4 were identified to be crucial for complex formation, the majority of which are positively charged residues including Arg-122, Arg-126, Arg-133, Lys-139, Arg-422, Arg-433, Arg-443 (*91*). Mutation of these residues into alanine dramatically decreased the interaction with CPR. On the other hand, chemical modification of negatively charged carboxyl groups on CPR was also shown to significantly impair the binding between cyt P450 and CPR (*92*). Mutations on clusters of acidic residues on the FMN binding domain of CPR revealed that Asp-208 is essential in interaction and electron transfer between the two proteins (*21, 50*). Asp-113 and Glu-115/Glu-116 also plays a critical role in mediating charge-charge interaction (*93*). Other than electrostatic interaction, it has been suggested that that certain hydrophobic residues on the binding interface, *e.g.* Val-267 and Leu-270 of cyt P450 2B4, also contributes in stablizing complex formation (13). Interaction between these two proteins was also investigated by chemical cross-linking in conjunction with mass spectroscopy, the results of which showed the C-helix of cyt P450 2B6 forms contacts with residues in the linker region between the FMN and NADPN/FAD binding domains (*94*). Antipeptide binding studies suggested that helices C and L contribute to CPR-binding in multiple cyt P450s (*95*). The results of these studies are summarized in Table 1.1.

In summary, it is generally accepted that the interaction between cyt p450 and CPR occurs between the positively charged proximal surface of cyt P450 and the negatively charged FMN binding domain of CPR. However, our knowledge regarding the specific residues involved in the interaction merely stems from a limited number of mutagenesis studies. Most of these studies measure the changes in the substrate turnover by the reconstituted cyt P450-CPR complex as a standard to evaluable whether the mutated residue is involved in complex formation or not. The

judgment is based upon the assumption that the mutation does not alter electron transfer pathway or the integrity of environment around the redox centers, the effects of which are usually hard to distinguish from that of complex formation. A high-resolution structure of the cyt P450-CPR complex is lacking due to the difficulty in co-crystallizing the two proteins as a complex, which could be attributed to either the transient nature of the complex or a lack of conformational rearrangement in CPR required for interacting with cyt P450 under crystallography conditions.

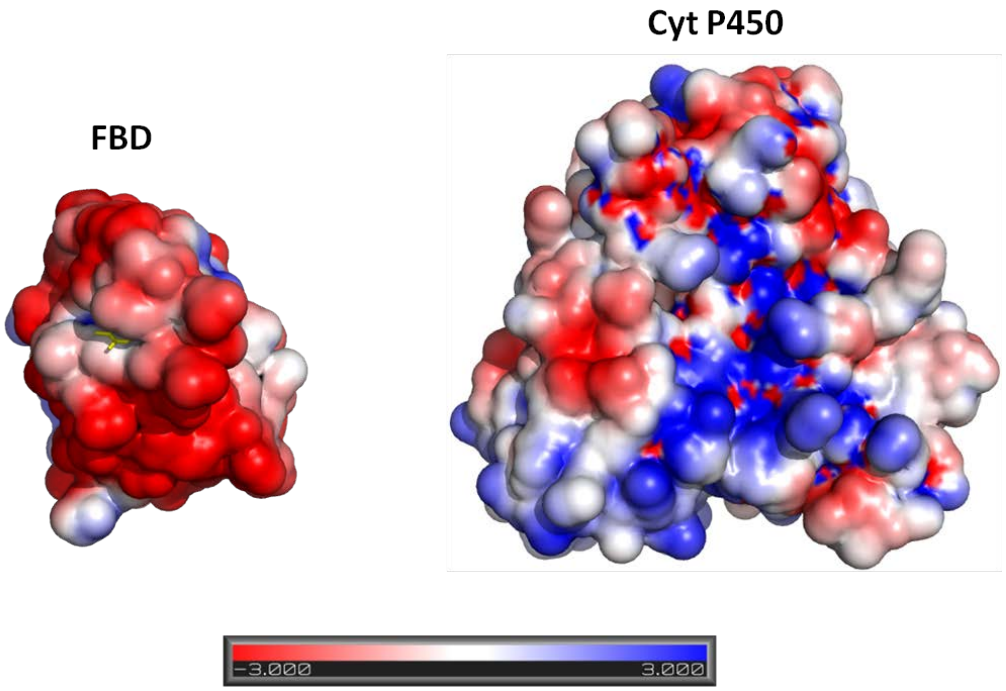

Figure 1.9 Electrostatic potential surface of FBD (PDB code 1AMO) and cyt P450 (PDB code 1SUO) calculated using PyMOL (Version 1.1, Schrödinger, LLC) with APBS plugin (*25*). The left panel shows the solvent exposed edge of the FMN cofactor indicated by yellow sticks. The right panel is the proximal side of cyt P450.

Cyt P450 is present in the endoplasmic reticulum at an approximately 20-fold molar excess over CPR (*96, 97*). Efficient electron transfer between CPR and different isoforms of cyt P450 as well as other redox proteins, *e.g.* cytochrome b_5 (*17*), heme oxygenase (*18*), necessitates rapid association and dissociation between cyt P450 and CPR. Transient complex is formed upon collision while the two proteins diffuse laterally across the membrane surface. What is the role of membrane and how the interaction between membrane and the proteins affects complex

formation is not yet well understood. It is known that in the absence of the transmembrane anchor, CPR is incapable of transferring electrons to cyt P450 (*6*). And composition of phospholipids in the membrane could potentially affect the interaction between CPR and cyt P450 (*98, 99*). The topography of the two proteins was characterized in nanodiscs by AFM, revealing that the height of cyt P450 above the membrane surface is approximately 3.5 nm which is consistent with an insertion of a hydrophobic tip. A model of the spatial arrangement of the complex on the membrane was proposed with both the FMN and NADPH/FAD binding domains of CPR lying close to the membrane surface for productive communication with cyt P450 (*100*). A complete understanding of the complex formation in membrane environment requires a thorough structural and dynamic characterization of the complex in a lipid membrane environment.

1.4 Interaction and electron transfer between CPR and cytochrome c

CPR was first isolated and identified as an NADPH-dependent cytochrome c (cyt c) reductase in the 1950 (*3*). In the later studies the true physiological redox partner of CPR was revealed to be cyt P450 after successful achievement of hydroxylase activity from a reconstitution system composed of cytochrome P450, CPR and phospholipid (*101*), while cyt c – an important component of electron transfer chain in mitochondria – is unlikely to be a physiological redox partner of CPR which was found to be localized at endoplasmic reticulum (4). Nevertheless, redox reaction between CPR and cyt c has continued to been widely used as a standard model to characterize the redox properties and the activities of CPR (*21, 53, 93, 102, 103*). Oxidized cyt c can also accept electrons from reductase domains of P450-BM_3 and NOS which are also in the diflavin reductase family, and it is suggested that electrons flow from the FMN of these flavoproteins to the heme of cyt c during electron transfer (*104*).

Electron transfer between proteins plays an essential role in a number of important biological processes including photosynthesis and respiration. It usually requires formation of transient protein complexes which are characterized with high association and dissociation rates to ensure rapid turnovers. Interaction and complex formation between CPR and cyt c has been investigated by cross-linking (*105, 106*), site-direct mutagenesis studies (*21, 50, 93*), etc. It has been proposed that charge-pairing between the negatively charged CPR and the positively

charged cyt c contributes greatly in the complex formation. Methylamidation of the carboxyl groups on CPR leads to strong inhibition of cyt c reduction (*107*), and a decrease on V_{max} of the reaction (*106*). Increase in ionic strength also causes disruption in complex formation and electron transfer between CPR and cyt c due to masking effect of the charges residues (*93*). In particular, a cluster of acidic residues Glu-213-Glu-214-Asp-215 on the N-terminus of helix α7 on CPR are potentially located in the CPR – cyt c complex interface suggested by site-directed mutagenesis studies (*21*, *50*). It has also been shown that Lys-13 of cyt c can be cross-linked to one of the carboxyl groups from the two acidic clusters Asp-207, -208 and -209 and Glu-213-Glu-214-Asp-215 (*105*). However, antibody binding studies reveal that an antibody designed to bind against Gly-204 to Gly-218 region of CPR fails to show effect on CPR – cyt c interaction (*108*). On the other hand, mutation of another acidic cluster Asp-113 and Glu-115-Glu-116 on the β2-α4 coil of CPR improves the cyt c reductase activity, facilitating a more functional complex formation (*93*). With the controversy in the literature, a high-resolution mapping of the binding interface of CPR and cyt c will be necessary to gain a better insight on the interaction and electron transfer between the two proteins.

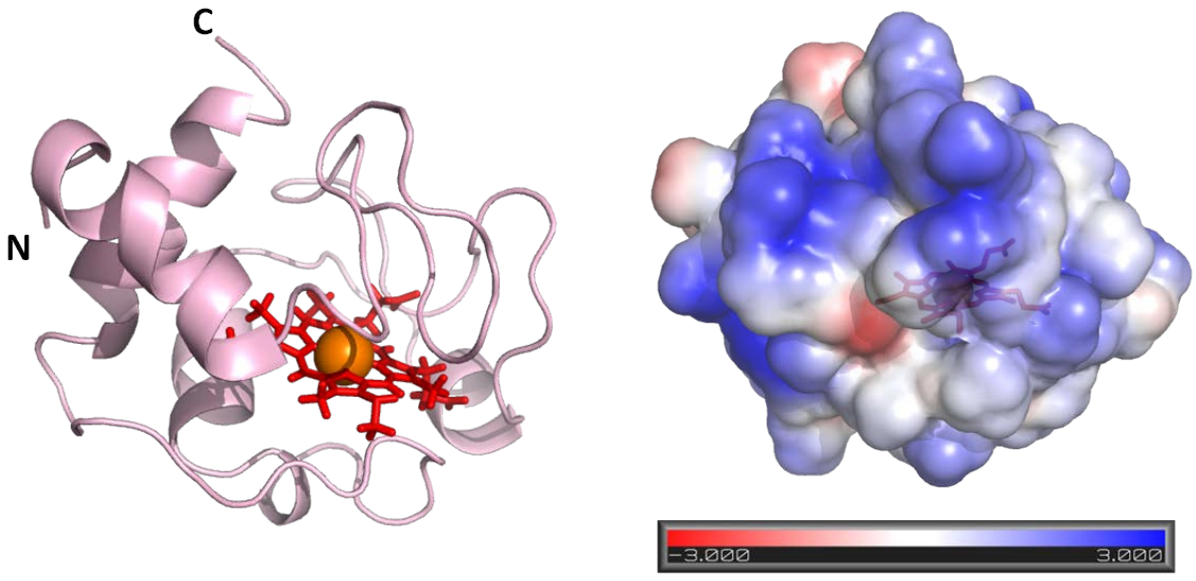

Figure 1.10 Structure of cyt c. The left panel is the cartoon presentation of cyt c (PDB code 1AKK). The right panel shows its electrostatic potential surface calculated using PyMOL (Version 1.1, Schrödinger, LLC) with APBS plugin (*25*).

Table 1.1 Summary of important residues proposed to be at the binding interface of cyt P450-CPR complex.

CPR	Cyt P450	Experiment techniques	Critical Residues	reference
rat	1A1	Site-directed mutagenesis	**Cyt P450:** K94, K99, K105, K440, K453, R455, K463; Less significant: R135, R136, R137	(*90*)
	1A1	Site-directed mutagenesis	**Cyt P450:** K271, K279	(*89*)
rat	2B1	Acetylation of lysine residues on cyt P450; Radiolabeling lysine residues followed by trypsin digestion	**Cyt P450:** K251, K384, K422, K433, K473	(*87*)
rat	2B1	Inhibitory peptides binding	**Cyt P450:** R125, helices C and L	(*95*)
rabbit	2B4	Site-directed mutagenesis	**Cyt P450**: R122, R126, R133, F135, M137, K139, K433, R422, R443	(*91*)
rat	2B4	Site-directed mutagenesis; Fluorescence labeling; Stopped-flow spectroscopy	**Cyt P450:** V267, L270	(*109*)
rabbit	2B4	Site-directed mutagenesis	**Cyt P450:** H226, K225, R232, R253, F223, F227, F244	(*110*)
	2B6	Cross-linking; MS	**Cyt P450 :** C-helix **CPR:** connecting domain[1]	(*94*)
rat	3A4	Chemical modification of tyrosine residues; Site-directed mutagenesis	**Cyt P450:** Y430; one or more residues among Y99, Y347, Y430	(*111*)
porcine	17alpha	Chemical modification; MS	**Cyt P450:** K326, K327	(*88*)
rat	PB-b	Chemical modification of carboxyl residues on CPR	**CPR:** Asp and Glu	(*92*)
Human[2]	2D6	Site-directed mutagenesis	**CPR:** D208	(*21*)
rat		Site-directed mutagenesis	**CPR:** D208	(*50*)
rat	2B1	Site-directed mutagenesis	**CPR:** D113, E115/E116	(*93*)

[1] It may be an artifact caused by cross-linking. [2] Isolated FMN binding domain instead of the intact CPR was investigated.

1.5 Goal of this research

The ultimate goal of this project is to understand the interaction and electron transfer between CPR and its redox partners – cyt P450 and cyt c, from both structural and kinetic perspectives. Isolated FMN binding domain (FBD) of rat CPR, which is the direct electron donor to its redox partners, will be expressed, purified and characterized. The kinetics of electron transfer between FBD and cyt P450/cyt c will be studied and compared with wild-type CPR. A combination of solution and solid-state NMR will be carried out to investigate the interaction between FBD and cyt P450/cyt c. In the solution NMR experiments, we will perform chemical shift perturbation and line broadening analysis to map out the binding interfaces and to generate structural models for the complexes. We will also apply static solid-state NMR approaches to study the interaction between FBD and cyt P450 in a native-like environment. By characterizing the structure and dynamics of the transmembrane domain of CPR, we will obtain a better understanding of its physiological role in the complex formation between CPR and cyt P450.

1.6 Experimental methods for studying interaction and electron transfer between proteins

1.6.1 Solution NMR

Solution nuclear magnetic resonance (NMR) spectroscopy has developed into a powerful tool for high-resolution mapping of protein-protein interactions, especially for studying transient protein complexes which are usually difficult to crystallize. NMR detects the magnetic properties of certain atomic nuclei, among which the most commonly used isotopes include ^{1}H, ^{13}C and ^{15}N. Due to the high nature abundance of ^{1}H (~99.99%) and its common distribution, one-dimensional ^{1}H-NMR is widely used in characterization of small organic compounds. In studies of biomacromolecules, such as proteins, multi-dimensional NMR experiments are necessary to achieve higher resolution of the spectra or to assist spectral assignment. In protein NMR spectroscopy, one of the most frequently used experiments is the two-dimensional (2D) Heteronuclear Single Quantum Coherence (HSQC) experiment. It correlates $^{13}C/^{15}N$ and ^{1}H nuclei and presents in the spectra crosspeaks of ^{13}C-^{1}H or ^{15}N-^{1}H pairs that are directly bonded. For example, in ^{15}N-HSQC spectra of a protein, most of the peaks come from the backbone amides – each residue corresponds to one N-H crosspeak in the spectra, except for tryptophan, asparagine, lysine, arginine and glutamine which have additional peaks from the side-chain N-H pairs. ^{15}N-HSQC experiment provide a unique pattern for each protein depending on its overall structure, thus this spectrum is usually considered a “fingerprint” of a protein. It is extensively used to examine the overall fold of a protein and monitor residue-specific response to variables such as ligand/protein binding and environmental changes.

1.6.1.1 TROSY-HSQC experiments

Application of solution NMR in studying very large biomacromolecules is limited by intrinsic line broadening due to fast transverse relaxation (T_2) of the resonances, which is associated with long correlation time of large molecules. The development of transverse relaxation-optimized spectroscopy (TROSY) experiments increases the size limit of molecules that are amendable for solution NMR studies several fold (*112*). Today, TROSY-based experiments are widely used in studying biomacromolecules which are larger than 50 kDa. A TROSY-HSQC pulse sequence is shown in Figure 1.11. The TROSY scheme effectively increases the resolution of ^{15}N-^{1}H resonances by using the constructive interference between dipole-dipole interaction and chemical shift anisotropy. The TROSY effect is more profound in

large molecules and high external magnetic field. The theoretical foundation lies in how cross-correlation between dipolar coupling and chemical shift perturbation affects the relaxation process (*113*).

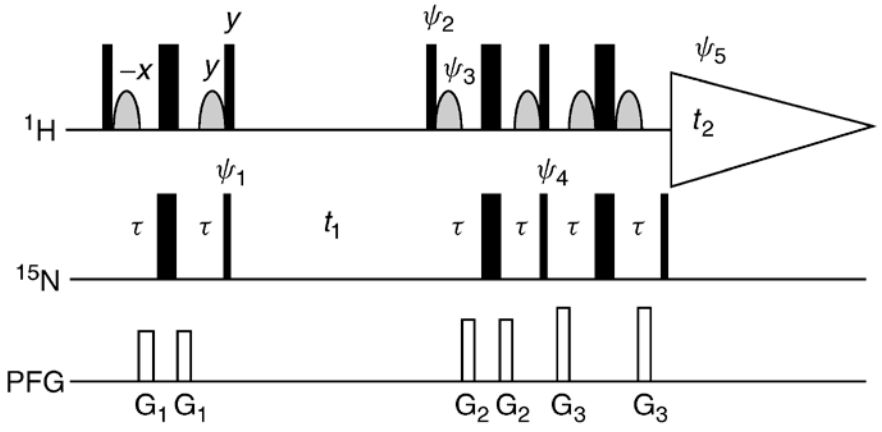

Figure 1.11 [^{15}N, ^{1}H]-TROSY-HSQC pulse sequence.

1.6.1.2 Chemical shift perturbation and line broadening analysis

Chemical shift of a resonance is determined by the shielding effect of the electron cloud surrounding the nucleus, which is strictly dependent on its chemical environment. Line width/peak height indicates the transverse relaxation rate of a resonance, which is affected by the dynamics of the nucleus. These two parameters are predominantly analyzed in this project to monitor the structural and dynamic changes of a protein as a response to interacting with its partner. Chemical shift perturbation analysis is routinely used for mapping the binding interface in studies of protein-protein interactions (*114*). For interactions occurring at different NMR time scales, the phenomenon of chemical shift perturbations varies accordingly (assuming a two-site exchange): 1. Upon fast exchange ($k_{ex} \ll \Delta\nu$), the resonance of the complex will appear at a population-weighted chemical shift of the unbound and bound species; 2. Upon slow exchange ($k_{ex} \gg \Delta\nu$), both bound and unbound species will present as separate resonances at individual chemical shifts; 3. Upon intermediate exchange ($k_{ex} \cong \Delta\nu$), line broadening occurs which leads to low-resolution and poorly defined resonance(s). Chemical shift perturbation is also sensitive to allosteric regulation which is usually hard to distinguish from the effect of surface contact with protein/ligand. Line broadening of resonances upon protein-protein interaction can attribute

to two possible reasons: 1. Increase of overall correlation time upon binding to another protein leads to faster transverse relaxation; 2. Chemical exchange in the intermediate time scale. The former has a general effect on most of the residues in the proteins, while the latter is more specific towards the residues involved in the binding interface or undergoing dynamic changes upon interaction. The phenomenon is more profound when the size of the complex is large (*115*).

1.6.2 High Ambiguity Driven biomolecular DOCKing (HADDOCK)

HADDOCK is a data-driven docking program for predicting biomacromolecular complexes (*116, 117*). Since its debut in 2003 (*117*), it has been applied to generate a number of structural models of protein-protein, protein-DNA, protein-RNA and protein-ligand complexes with renowned accuracy (*118-121*). A noted difference of HADDOCK from other rigid body docking programs, *e.g.* GRAMM-X, Z-DOCK, is that it uses ambiguous restraints defined by the user – based on experimental data or bioinformatic predictions – to drive the docking process. A variety of restraints can be input including NMR experimental data (*e.g.* chemical shift perturbation data, paramagnetic relaxation enhancement, residual dipolar couplings, etc.), site-directed mutagenesis data and bioinformatics (*122*).

In this project, we use chemical shift perturbations/line broadening data as ambiguous restraints to drive the docking. Ambiguous Interaction Restraints (AIR) can be generated on the HADDOCK website (*122*), which include “active” and “passive” residues. In the case of NMR titration data, the active residues should be chosen to be the residues showing significant chemical shift perturbations upon complex formation as well as having high solvent accessibilities in the unbound form (>50% relative accessibility as calculated by NACCESS (*123*)) (*117*). The passive residues correspond to the residues that show a less significant chemical shift perturbation and/or that are in close proximity to the active residues and have high solvent accessibilities (>50%). An AIR is defined as an ambiguous intermolecular distance between any atom of an active residue of protein A and any atom of both active and passive residues of protein B with a maximum of 2 Å. This ambiguous definition of AIR allows the program to search through all possible configurations around the interacting site defined by the user and find the most energy-favorable pairs of interacting residues among the active and passive residues (*117*). The default upper threshold of 2 Å is set as a result of a compromise

between hydrogen-hydrogen and heavy atom-heavy atom minimum van de Waals distances, and can be modified in the AIR restraint table (*122*).

HADDOCK docking algorithm includes three consecutive steps—1. rigid body docking in which the two molecules are rotated and translated randomly in turn in order to minimize intermolecular energy, 2. Semi-rigid simulated annealing of structures, in which annealing in torsion angle space is performed to refine the orientation of the proteins and the side chains and/or backbones of the interface residues defined by AIR table, 3. Solvent refinement, in which the structures are further refined in explicit solvent layers. The final structures with lowest energies are clustered, scored and analyzed as outputs of the docking.

1.6.3 Electron transfer pathway prediction

Obtaining direct information of electron transfer pathway between proteins is a challenging but beneficial task for a better understanding of the mechanism of many electron-transfer enzymes, including the cyt P450 system we are investigating. The commonly used experimental procedure to determine the electron transfer pathway is through site-directed mutagenesis – by mutating the residues which are potentially located on the pathway and evaluating how the mutation affects the interprotein electron transfer. However, performing mutations is not only time and money consuming but also might introduce perturbations on the structure of the proteins or interrupt protein-protein interaction. Alternatively, computational tools can be applied to predict electron transfer pathway, given a fair-resolution structure of the complex (*124-127*).

In this project, we predict electron transfer pathway using HAmiltonian to Research LargE Molecules (HARLEM) (*128*). It employs PATHWAYS analysis of donor/acceptor interactions (*129*) and topological search algorithms to find the shortest pathways between the pre-defined electron donor and acceptor. The input file of the program is the structure of the complex with the redox centers defined. The PATHWAY model searches for the combination of bonded and nonbonded interactions that maximizes the total Donor-Acceptor interaction (T_{DA}) (Equation 1.1) mediated by combination of through-bond and through-space coupling in the proteins (*130*). In Equation 1.1, ε_C, ε_S and ε_H present the decay factors for electron tunneling through covalent bonds, through-space and through hydrogen bonding, respectively, and are

empirically set as shown in Equation 1.2, 1.3, 1.4, in which R represents distances in Å. Since electron tunneling is much more efficient through bonded orbitals than through space due to the effectively lower potential barrier, the pathway obtained contains mainly bounded interactions with limited through-space connections. Electron transfer pathways have been predicted by HARLEM for protein complexes, including putidaredoxin/cyt P450 camphor (*131*), cytochrome c/cupredoxin (*132*), adrenodoxin/cyt P450 11A1 (*133*) and cyt b5/cyt P450 2B4 (*134*) complexes.

$$T_{\mathrm{DA}} \propto \prod_i \varepsilon_{\mathrm{C}}(i) \prod_j \varepsilon_{\mathrm{S}}(j) \prod_k \varepsilon_{\mathrm{H}}(k) \quad (1.1)$$

$$\varepsilon_{\mathrm{C}} = 0.6 \quad (\#) \quad (1.2)$$

$$\varepsilon_{\mathrm{S}} = {\varepsilon_{\mathrm{C}}}^2 \exp[-1.7(\mathrm{R} - 2.8)] \quad (1.3)$$

$$\varepsilon_{\mathrm{H}} = 0.5\, \varepsilon_{\mathrm{C}} \exp[-1.7(R - 1.4)] \quad (1.4)$$

1.6.4 Kinetics studies by stopped-flow spectroscopy

Stopped-flow is a rapid mixing spectroscopic technique used to study chemical kinetics of a fast reaction in solution. Reacting reagents are pushed out of the syringes and mixed in a mixing chamber, and shortly after mixing the reacting mixture is monitored by a spectrometer coupled to the instrument as a function of time (*e.g.* UV-Vis, fluorescence, etc.) (Figure 1.12). The dead time of the technique is between the end of mixing and the start of spectroscopic measurement, which is typically on the order of milliseconds. This allows for fast reactions with half-lives as short as a few milliseconds or tens of seconds to be accurately measured.

The kinetics of electron transfer from the FMN binding domain (FBD) of CPR to its redox partner cyt c is studied using stopped-flow spectroscopy. Due to a relative slow rate of reaction between FBD and cyt P450 upon instant mix (on the order of minutes), the kinetics of electron transfer between these two is monitored directly using real-time UV-Vis single-wavelength detection. In order to fulfill pseudo-first-order conditions, the concentration of cyt P450/cyt c is in large excess over FBD. The apparent rates (K_{obs}, Equation 1.5, 1.6) of electron

transfer from FBD are compared with those from wild-type CPR to assess the effect of structural integrity on complex formation between CPR and its redox partners.

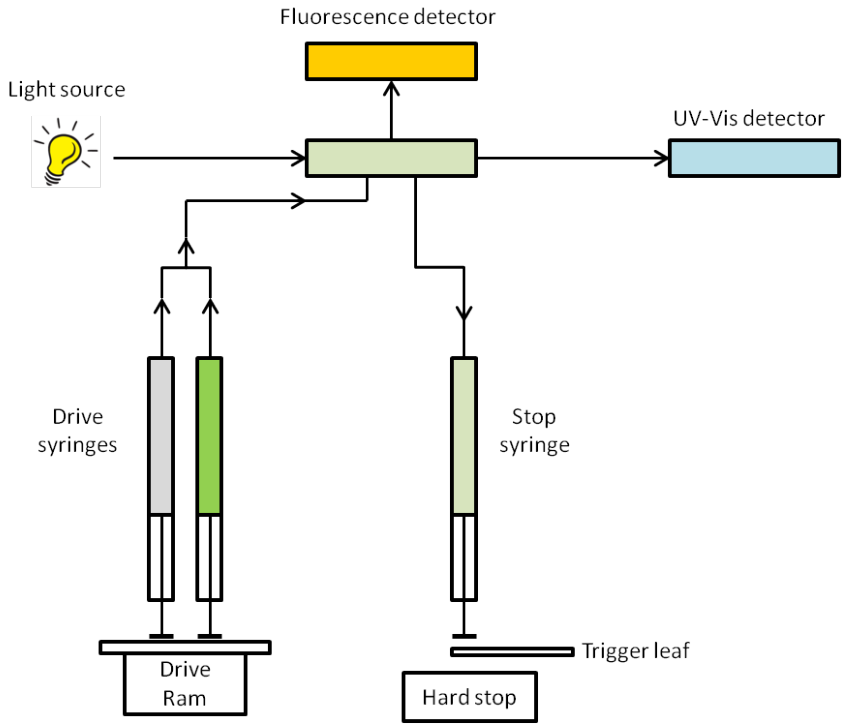

Figure 1.12 Stopped-flow spectroscopy.

$$rate = \frac{\mathrm{d[FBD]}}{\mathrm{dt}} = k_{\mathrm{obs}}[\mathrm{FBD}] \qquad (1.5)$$

$$k_{\mathrm{obs}} = k\,[\mathrm{acceptor}] \qquad (1.6)$$

1.6.5 Solid-state NMR experiments

Solid-state NMR spectroscopy is a powerful approach to probe high-resolution structure and dynamics of insoluble, non-crystalline or amorphous biomolecules like membrane proteins – systems which usually pose great difficulties for crystallization. One early problem of applying solid-state NMR in membrane protein studies comes from severe line broadening of resonances due to anisotropic magnetic interactions such as chemical shift anisotropy and dipolar interaction, caused by reduced mobility of proteins embedded in the lipid bilayer. This difficulty

has been overcome by using aligned samples or magic angle spinning (MAS), which drastically improve the spectral resolution and allow for structural and dynamic studies of membrane proteins in a native-like membrane environment.

1.6.5.1 Aligned sample in solid-state NMR

There are two methods commonly used to make oriented membranes for solid-state NMR studies – glass plates and lipid bicelles. In glass plate samples, the lipid-protein mixture fills in the space between a stack of glass plates, where the lipids spontaneously form bilayers in the orientation parallel to the surface of the plates. Lipid bicelles are assemblies of long-chain lipids and detergents at certain molar proportions, which form disk-like bilayer patches shown in Figure 1.13. Because of their magnetic susceptibility and geometric property, these assemblies spontaneously align in the external magnetic field inside the NMR spectrometer, typically with their bilayer normal perpendicular to B_0 (Figure 1.13). The properties of bicelles can be adjusted by changing the lipid composition. For example, one of the most frequently used bicelles is composed of 1,2-dimyristoyl-sn-glycero-3-phosphocholine (DMPC) and 1,2-dihexanoyl-sn-glycero-3-phosphor-choline (DHPC), which aligns at the temperature range between 25 °C and 45 °C, while substitution of DMPC with DLPC can expand the temperature range required for alignment allowing the bicelles to orient at as low as 5 °C (*76*). The thickness of the bilayer can also be adjusted by composing the bicelles using lipids with increased or reduced acyl chain length, which can be used to study the effect of hydrophobic mismatch (*135*). In addition, interaction between proteins and charged membrane surface can be investigated by incorporation of charged lipids in the bicelles.

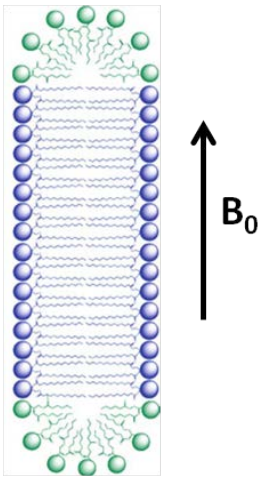

Figure 1.13 Alignment of bicelles in an external magnetic field B_0. Long chain lipids tend to locate at the planar region of the bicelles (blue), while short chain detergents are more concentrated on the rim (green).

1.6.5.2 Dynamics of cross polarization

Cross polarization is generally used to transfer magnetization from protons to low γ (gyromagnetic ratio) nuclei such as ^{13}C, ^{15}N and ^{29}Si for sensitivity enhancement. It's an essential element in the conventional multidimensional heteronuclear solid-state NMR experiments. In order to allow magnetization transfer to occur, the strength of B_1 radio frequency field must fulfill the Hartmann-Hahn conditions described in Equation 1.7, in which I and S represent proton and low γ nuclei respectively. During cross polarization (CP), the system approaches equilibrium under the dynamics governed by dipolar coupling and relaxation in the rotating-frame. For CP between dilute (S) and abundant nuclei (I), the peak intensity of S spin can be approximated to Equation 1.8 (*136*). And a typical buildup curve is shown in Figure #. Earlier solid-state NMR studies on cyt b_5 demonstrated that differences in dynamics between the soluble and transmembrane domain of cyt b_5 were reflected clearly by the respective CP kinetics (*34, 137, 138*).

$$\gamma^I B_1^I = \gamma^S B_1^S \quad (1.7)$$

$$I(t) = \frac{I(0)}{T_{IS}}\left(\frac{1}{T_{IS}} - \frac{1}{T_{1\rho}^I}\right)^{-1}\left(e^{-\frac{t}{T_{1\rho}^I}} - e^{-\frac{t}{T_{IS}}}\right) \quad (1.8)$$

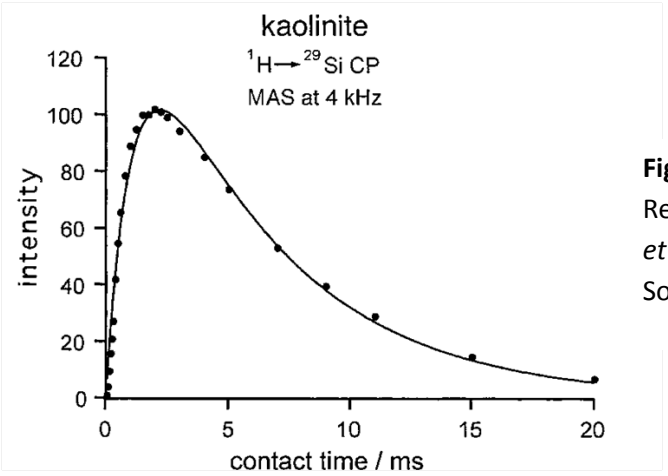

Figure 1.14 Typical classical CP kinetics. Reprinted with permission of Kolodziejski *et al*. Copyright 2002 American Chemical Society.

1.6.5.3 Separated Local Field (SLF) experiment

Separated Local Field (SLF) experiment correlates ^{15}N chemical shift with ^1H-^{15}N dipolar couplings in a two-dimensional NMR spectrum. For static aligned protein samples, SLF spectra typically show very characteristic features. In particular, α-helices result in circular patterns in

the spectra which we call “PISA wheel”. The phenomenon is a result of the fixed geometric relationship between the ^{15}N magnetic interaction tensors and peptide plane (Figure 1.15A). The shape and position of the “PISA wheel” pattern are sensitive to the tilt angle of the helix with respect to the bilayer normal as well as its dynamics in the membrane (Figure 1.15B). By fitting the wheel pattern, structural and dynamic information can be extracted even in the absence of spectral assignment.

Different SLF pulse sequences have been developed. The original sequence PISEMA sequence is sensitive to the chemical shift and frequency resonance offset, which limits its application in high magnetic field where the effect is more pronounced (*34*). Later on, SAMMY (*139*) and SAMPI4 (*140*) sequences were developed to reduce the offset dependence of the experiment by using a less sensitive homonuclear decoupling scheme. In this project, we utilize a HIMSELF sequence (Figure 1.15C) referring to “heteronuclear isotropic mixing by separated local field spectroscopy” developed by Dvinskikh *et al* (*141*), which uses double channel homonuclear decoupling sequences of BLEW or WIM in the indirect dimension. This sequence has shown to be less sensitive to the offset effect (*141*) and thus could be suited to study uniformly labeled samples.

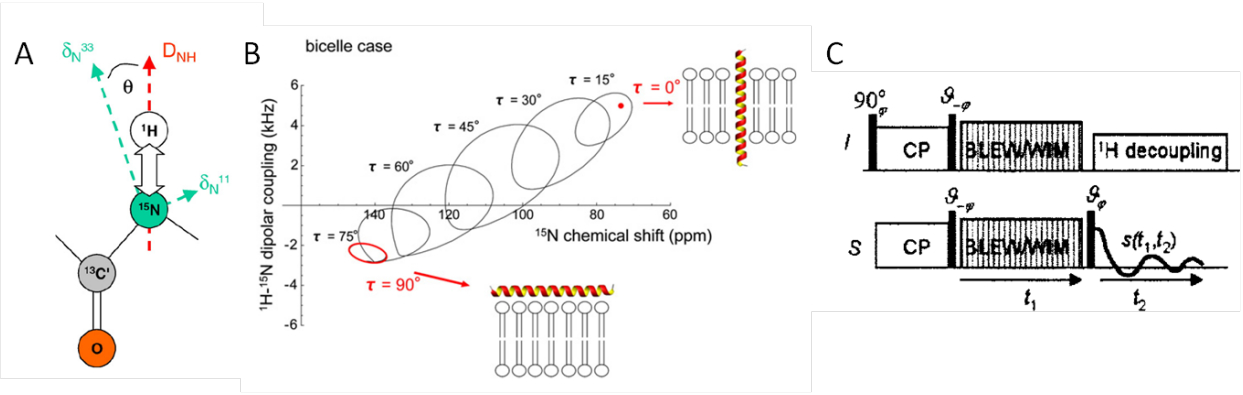

Figure 1.15 Separated local field spectroscopy. A, Peptide plane NMR interactions that allow for angle measurements in static ^{15}N NMR. Dipolar coupling is labeled in red arrow, green arrows indicates two principle axis of ^{15}N chemical shift anisotropy. B, PISA wheel patterns of ^{15}N-labeled helix at different tilt angles with respect to membrane normal. Reprinted with permission from Dürr *et al*. Copyright 2007 Elsevier B.V. C, A two-dimensional HIMSELF sequence. Reprinted with permission from Dvinskikh *et al*. Copyright 2006 American Institute of Physics.

1.7 References

1. Guengerich, F. P. (2008) Cytochrome p450 and chemical toxicology, *Chem Res Toxicol 21*, 70-83.
2. Haas, E., Horecker, B. L., and Hogness, T. R. (1940) The enzymatic reduction of cytochrome c - Cytochrome c reductase, *J. Biol. Chem. 136*, 747-774.
3. Horecker, B. L. (1950) Triphosphopyridine nucleotide-cytochrome-c reductase in liver *J. Biol. Chem. 183*, 593-605.
4. Williams, C. H., Jr., and Kamin, H. (1962) Microsomal triphosphopyridine nucleotide-cytochrome c reductase of liver, *J Biol Chem 237*, 587-595.
5. Phillips, A. H., and Langdon, R. G. (1962) Hepatic triphosphopyridine nucleotide-cytochrome c reductase: isolation, characterization, and kinetic studies, *J Biol Chem 237*, 2652-2660.
6. Wang, M., Roberts, D. L., Paschke, R., Shea, T. M., Masters, B. S., and Kim, J. J. (1997) Three-dimensional structure of NADPH-cytochrome P450 reductase: prototype for FMN- and FAD-containing enzymes, *Proc Natl Acad Sci U S A 94*, 8411-8416.
7. McMillan, K., Bredt, D. S., Hirsch, D. J., Snyder, S. H., Clark, J. E., and Masters, B. S. (1992) Cloned, expressed rat cerebellar nitric oxide synthase contains stoichiometric amounts of heme, which binds carbon monoxide, *Proc Natl Acad Sci U S A 89*, 11141-11145.
8. Paine, M. J., Garner, A. P., Powell, D., Sibbald, J., Sales, M., Pratt, N., Smith, T., Tew, D. G., and Wolf, C. R. (2000) Cloning and characterization of a novel human dual flavin reductase, *J Biol Chem 275*, 1471-1478.
9. Leclerc, D., Wilson, A., Dumas, R., Gafuik, C., Song, D., Watkins, D., Heng, H. H., Rommens, J. M., Scherer, S. W., Rosenblatt, D. S., and Gravel, R. A. (1998) Cloning and mapping of a cDNA for methionine synthase reductase, a flavoprotein defective in patients with homocystinuria, *Proc Natl Acad Sci U S A 95*, 3059-3064.
10. Narhi, L. O., and Fulco, A. J. (1986) Characterization of a catalytically self-sufficient 119,000-dalton cytochrome P-450 monooxygenase induced by barbiturates in Bacillus megaterium, *J Biol Chem 261*, 7160-7169.
11. Ostrowski, J., Barber, M. J., Rueger, D. C., Miller, B. E., Siegel, L. M., and Kredich, N. M. (1989) Characterization of the flavoprotein moieties of NADPH-sulfite reductase from Salmonella typhimurium and Escherichia coli. Physicochemical and catalytic properties, amino acid sequence deduced from DNA sequence of cysJ, and comparison with NADPH-cytochrome P-450 reductase, *J Biol Chem 264*, 15796-15808.
12. Porter, T. D., and Kasper, C. B. (1986) NADPH-cytochrome P-450 oxidoreductase: flavin mononucleotide and flavin adenine dinucleotide domains evolved from different flavoproteins, *Biochemistry 25*, 1682-1687.
13. Smith, G. C., Tew, D. G., and Wolf, C. R. (1994) Dissection of NADPH-cytochrome P450 oxidoreductase into distinct functional domains, *Proc Natl Acad Sci U S A 91*, 8710-8714.
14. Henderson, C. J., Otto, D. M., Carrie, D., Magnuson, M. A., McLaren, A. W., Rosewell, I., and Wolf, C. R. (2003) Inactivation of the hepatic cytochrome P450 system by conditional deletion of hepatic cytochrome P450 reductase, *J Biol Chem 278*, 13480-13486.
15. Shen, A. L., O'Leary, K. A., and Kasper, C. B. (2002) Association of multiple developmental defects and embryonic lethality with loss of microsomal NADPH-cytochrome P450 oxidoreductase, *J Biol Chem 277*, 6536-6541.
16. Le, Y., and Sauer, B. (2001) Conditional gene knockout using Cre recombinase, *Mol Biotechnol 17*, 269-275.
17. Enoch, H. G., and Strittmatter, P. (1979) Cytochrome b5 reduction by NADPH-cytochrome P-450 reductase, *J Biol Chem 254*, 8976-8981.

18. Schacter, B. A., Nelson, E. B., Marver, H. S., and Masters, B. S. (1972) Immunochemical evidence for an association of heme oxygenase with the microsomal electron transport system, *J Biol Chem 247*, 3601-3607.
19. Bachur, N. R., Gordon, S. L., Gee, M. V., and Kon, H. (1979) NADPH cytochrome P-450 reductase activation of quinone anticancer agents to free radicals, *Proc Natl Acad Sci U S A 76*, 954-957.
20. Keyes, S. R., Fracasso, P. M., Heimbrook, D. C., Rockwell, S., Sligar, S. G., and Sartorelli, A. C. (1984) Role of NADPH:cytochrome c reductase and DT-diaphorase in the biotransformation of mitomycin C1, *Cancer Res 44*, 5638-5643.
21. Zhao, Q., Modi, S., Smith, G., Paine, M., McDonagh, P. D., Wolf, C. R., Tew, D., Lian, L. Y., Roberts, G. C., and Driessen, H. P. (1999) Crystal structure of the FMN-binding domain of human cytochrome P450 reductase at 1.93 A resolution, *Protein Sci 8*, 298-306.
22. Barsukov, I., Modi, S., Lian, L. Y., Sze, K. H., Paine, M. J., Wolf, C. R., and Roberts, G. C. (1997) 1H, 15N and 13C NMR resonance assignment, secondary structure and global fold of the FMN-binding domain of human cytochrome P450 reductase, *J Biomol NMR 10*, 63-75.
23. Shen, A. L., Porter, T. D., Wilson, T. E., and Kasper, C. B. (1989) Structural analysis of the FMN binding domain of NADPH-cytochrome P-450 oxidoreductase by site-directed mutagenesis, *J Biol Chem 264*, 7584-7589.
24. Hamdane, D., Xia, C., Im, S. C., Zhang, H., Kim, J. J., and Waskell, L. (2009) Structure and function of an NADPH-cytochrome P450 oxidoreductase in an open conformation capable of reducing cytochrome P450, *J Biol Chem 284*, 11374-11384.
25. Lerner, M. G., and Carlson, H. A. (2006) APBS plugin for PyMOL, University of Michigan, Ann Arbor.
26. Shen, A. L., and Kasper, C. B. (2000) Differential contributions of NADPH-cytochrome P450 oxidoreductase FAD binding site residues to flavin binding and catalysis, *J Biol Chem 275*, 41087-41091.
27. Gutierrez, A., Doehr, O., Paine, M., Wolf, C. R., Scrutton, N. S., and Roberts, G. C. (2000) Trp-676 facilitates nicotinamide coenzyme exchange in the reductive half-reaction of human cytochrome P450 reductase: properties of the soluble W676H and W676A mutant reductases, *Biochemistry 39*, 15990-15999.
28. Elmore, C. L., and Porter, T. D. (2002) Modification of the nucleotide cofactor-binding site of cytochrome P-450 reductase to enhance turnover with NADH in Vivo, *J Biol Chem 277*, 48960-48964.
29. Aigrain, L., Pompon, D., Morera, S., and Truan, G. (2009) Structure of the open conformation of a functional chimeric NADPH cytochrome P450 reductase, *EMBO Rep 10*, 742-747.
30. Aigrain, L., Pompon, D., and Truan, G. (2011) Role of the interface between the FMN and FAD domains in the control of redox potential and electronic transfer of NADPH-cytochrome P450 reductase, *Biochem J 435*, 197-206.
31. Black, S. D., and Coon, M. J. (1982) Structural features of liver microsomal NADPH-cytochrome P-450 reductase. Hydrophobic domain, hydrophilic domain, and connecting region, *J Biol Chem 257*, 5929-5938.
32. Sundermann, A., and Oostenbrink, C. (2013) Molecular dynamics simulations give insight into the conformational change, complex formation, and electron transfer pathway for cytochrome P450 reductase, *Protein Sci 22*, 1183-1195.
33. Im, S. C., and Waskell, L. (2011) The interaction of microsomal cytochrome P450 2B4 with its redox partners, cytochrome P450 reductase and cytochrome b(5), *Arch Biochem Biophys 507*, 144-153.

34. Durr, U. H., Waskell, L., and Ramamoorthy, A. (2007) The cytochromes P450 and b5 and their reductases--promising targets for structural studies by advanced solid-state NMR spectroscopy, *Biochim Biophys Acta 1768*, 3235-3259.
35. Gideon, D. A., Kumari, R., Lynn, A. M., and Manoj, K. M. (2012) What is the Functional Role of N-terminal Transmembrane Helices in the Metabolism Mediated by Liver Microsomal Cytochrome P450 and its Reductase?, *Cell Biochem Biophys 63*, 35-45.
36. Gum, J. R., and Strobel, H. W. (1981) Isolation of the membrane-binding peptide of NADPH-cytochrome P-450 reductase. Characterization of the peptide and its role in the interaction of reductase with cytochrome P-450, *J Biol Chem 256*, 7478-7486.
37. Otvos, J. D., Krum, D. P., and Masters, B. S. (1986) Localization of the free radical on the flavin mononucleotide of the air-stable semiquinone state of NADPH-cytochrome P-450 reductase using 31P NMR spectroscopy, *Biochemistry 25*, 7220-7228.
38. Vermilion, J. L., and Coon, M. J. (1978) Identification of the high and low potential flavins of liver microsomal NADPH-cytochrome P-450 reductase, *J Biol Chem 253*, 8812-8819.
39. Vermilion, J. L., and Coon, M. J. (1978) Purified liver microsomal NADPH-cytochrome P-450 reductase. Spectral characterization of oxidation-reduction states, *J Biol Chem 253*, 2694-2704.
40. Munro, A. W., Noble, M. A., Robledo, L., Daff, S. N., and Chapman, S. K. (2001) Determination of the redox properties of human NADPH-cytochrome P450 reductase, *Biochemistry 40*, 1956-1963.
41. Iyanagi, T., Makino, N., and Mason, H. S. (1974) Redox properties of the reduced nicotinamide adenine dinucleotide phosphate-cytochrome P-450 and reduced nicotinamide adenine dinucleotide-cytochrome b5 reductases, *Biochemistry 13*, 1701-1710.
42. Das, A., and Sligar, S. G. (2009) Modulation of the cytochrome P450 reductase redox potential by the phospholipid bilayer, *Biochemistry 48*, 12104-12112.
43. Iyanagi, T. (2005) Structure and function of NADPH-cytochrome P450 reductase and nitric oxide synthase reductase domain, *Biochem Biophys Res Commun 338*, 520-528.
44. Gutierrez, A., Lian, L. Y., Wolf, C. R., Scrutton, N. S., and Roberts, G. C. (2001) Stopped-flow kinetic studies of flavin reduction in human cytochrome P450 reductase and its component domains, *Biochemistry 40*, 1964-1975.
45. Bhattacharyya, A. K., Lipka, J. J., Waskell, L., and Tollin, G. (1991) Laser flash photolysis studies of the reduction kinetics of NADPH:cytochrome P-450 reductase, *Biochemistry 30*, 759-765.
46. Gutierrez, A., Munro, A. W., Grunau, A., Wolf, C. R., Scrutton, N. S., and Roberts, G. C. (2003) Interflavin electron transfer in human cytochrome P450 reductase is enhanced by coenzyme binding. Relaxation kinetic studies with coenzyme analogues, *Eur J Biochem 270*, 2612-2621.
47. Gutierrez, A., Paine, M., Wolf, C. R., Scrutton, N. S., and Roberts, G. C. (2002) Relaxation kinetics of cytochrome P450 reductase: internal electron transfer is limited by conformational change and regulated by coenzyme binding, *Biochemistry 41*, 4626-4637.
48. Page, C. C., Moser, C. C., Chen, X., and Dutton, P. L. (1999) Natural engineering principles of electron tunnelling in biological oxidation-reduction, *Nature 402*, 47-52.
49. Iyanagi, T., Xia, C., and Kim, J. J. (2012) NADPH-cytochrome P450 oxidoreductase: prototypic member of the diflavin reductase family, *Arch Biochem Biophys 528*, 72-89.
50. Kasper, C. B. (1995) Role of Acidic Residues in the Interaction of NADPH-Cytochrome P450 Oxidoreductase with Cytochrome P450 and Cytochrome c, *J Biol Chem 270*, 27475-27480.
51. Pudney, C. R., Heyes, D. J., Khara, B., Hay, S., Rigby, S. E., and Scrutton, N. S. (2012) Kinetic and spectroscopic probes of motions and catalysis in the cytochrome P450 reductase family of enzymes, *FEBS J 279*, 1534-1544.

52. Gruez, A., Pignol, D., Zeghouf, M., Coves, J., Fontecave, M., Ferrer, J. L., and Fontecilla-Camps, J. C. (2000) Four crystal structures of the 60 kDa flavoprotein monomer of the sulfite reductase indicate a disordered flavodoxin-like module, *J Mol Biol 299*, 199-212.
53. Xia, C., Hamdane, D., Shen, A. L., Choi, V., Kasper, C. B., Pearl, N. M., Zhang, H., Im, S. C., Waskell, L., and Kim, J. J. (2011) Conformational changes of NADPH-cytochrome P450 oxidoreductase are essential for catalysis and cofactor binding, *J Biol Chem 286*, 16246-16260.
54. Ellis, J., Gutierrez, A., Barsukov, I. L., Huang, W. C., Grossmann, J. G., and Roberts, G. C. (2009) Domain motion in cytochrome P450 reductase: conformational equilibria revealed by NMR and small-angle x-ray scattering, *J Biol Chem 284*, 36628-36637.
55. Vincent, B., Morellet, N., Fatemi, F., Aigrain, L., Truan, G., Guittet, E., and Lescop, E. (2012) The closed and compact domain organization of the 70-kDa human cytochrome P450 reductase in its oxidized state as revealed by NMR, *J Mol Biol 420*, 296-309.
56. Hay, S., Brenner, S., Khara, B., Quinn, A. M., Rigby, S. E., and Scrutton, N. S. (2010) Nature of the energy landscape for gated electron transfer in a dynamic redox protein, *J Am Chem Soc 132*, 9738-9745.
57. Pudney, C. R., Khara, B., Johannissen, L. O., and Scrutton, N. S. (2011) Coupled motions direct electrons along human microsomal P450 Chains, *PLoS Biol 9*, e1001222.
58. Nelson, D. R. (2003) Comparison of P450s from human and fugu: 420 million years of vertebrate P450 evolution, *Arch Biochem Biophys 409*, 18-24.
59. Guengerich, F. P., Wu, Z. L., and Bartleson, C. J. (2005) Function of human cytochrome P450s: characterization of the orphans, *Biochem Biophys Res Commun 338*, 465-469.
60. Stier, A. (1976) Lipid structure and drug metabolizing enzymes, *Biochem Pharmacol 25*, 109-113.
61. Lewis, D. F. (1996) *Cytochromes P450: Structure, Function and Mechenism* Taylor & Francis, London.
62. Ortiz de Montellano, P. R. (2005) *Cytochrome P450: Structure, Mechanism, and Biochemistry*, Kluwer Academic/Plenum Publishers, New York.
63. Nebert, D. W., and Russell, D. W. (2002) Clinical importance of the cytochromes P450, *Lancet 360*, 1155-1162.
64. Yun, C. H., Kim, K. H., Calcutt, M. W., and Guengerich, F. P. (2005) Kinetic analysis of oxidation of coumarins by human cytochrome P450 2A6, *J Biol Chem 280*, 12279-12291.
65. Isin, E. M., and Guengerich, F. P. (2006) Kinetics and thermodynamics of ligand binding by cytochrome P450 3A4, *J Biol Chem 281*, 9127-9136.
66. Scott, E. E., White, M. A., He, Y. A., Johnson, E. F., Stout, C. D., and Halpert, J. R. (2004) Structure of mammalian cytochrome P450 2B4 complexed with 4-(4-chlorophenyl)imidazole at 1.9-A resolution: insight into the range of P450 conformations and the coordination of redox partner binding, *J Biol Chem 279*, 27294-27301.
67. Gay, S. C., Sun, L., Maekawa, K., Halpert, J. R., and Stout, C. D. (2009) Crystal structures of cytochrome P450 2B4 in complex with the inhibitor 1-biphenyl-4-methyl-1H-imidazole: ligand-induced structural response through alpha-helical repositioning, *Biochemistry 48*, 4762-4771.
68. Gay, S. C., Zhang, H., Wilderman, P. R., Roberts, A. G., Liu, T., Li, S., Lin, H. L., Zhang, Q., Woods, V. L., Jr., Stout, C. D., Hollenberg, P. F., and Halpert, J. R. (2011) Structural analysis of mammalian cytochrome P450 2B4 covalently bound to the mechanism-based inactivator tert-butylphenylacetylene: insight into partial enzymatic activity, *Biochemistry 50*, 4903-4911.
69. Gay, S. C., Roberts, A. G., Maekawa, K., Talakad, J. C., Hong, W. X., Zhang, Q., Stout, C. D., and Halpert, J. R. (2010) Structures of cytochrome P450 2B4 complexed with the antiplatelet drugs ticlopidine and clopidogrel, *Biochemistry 49*, 8709-8720.

70. Zhao, Y., Sun, L., Muralidhara, B. K., Kumar, S., White, M. A., Stout, C. D., and Halpert, J. R. (2007) Structural and thermodynamic consequences of 1-(4-chlorophenyl)imidazole binding to cytochrome P450 2B4, *Biochemistry 46*, 11559-11567.
71. Wilderman, P. R., Shah, M. B., Liu, T., Li, S., Hsu, S., Roberts, A. G., Goodlett, D. R., Zhang, Q., Woods, V. L., Jr., Stout, C. D., and Halpert, J. R. (2010) Plasticity of cytochrome P450 2B4 as investigated by hydrogen-deuterium exchange mass spectrometry and X-ray crystallography, *J Biol Chem 285*, 38602-38611.
72. Wilderman, P. R., Gay, S. C., Jang, H. H., Zhang, Q., Stout, C. D., and Halpert, J. R. (2012) Investigation by site-directed mutagenesis of the role of cytochrome P450 2B4 non-active-site residues in protein-ligand interactions based on crystal structures of the ligand-bound enzyme, *FEBS J 279*, 1607-1620.
73. Zhao, Y. (2005) Structure of Microsomal Cytochrome P450 2B4 Complexed with the Antifungal Drug Bifonazole: INSIGHT INTO P450 CONFORMATIONAL PLASTICITY AND MEMBRANE INTERACTION, *J Biol Chem 281*, 5973-5981.
74. Scott, E. E., He, Y. A., Wester, M. R., White, M. A., Chin, C. C., Halpert, J. R., Johnson, E. F., and Stout, C. D. (2003) An open conformation of mammalian cytochrome P450 2B4 at 1.6-A resolution, *Proc Natl Acad Sci U S A 100*, 13196-13201.
75. von Wachenfeldt, C., and Johnson, E. F. (1995) *Structures of Eukaryotic Cytochrome P450 Enzymes. In Cytochrome P450: Structure, Mechanism, and Biochemistry*, Plenum Press, New York.
76. Yamamoto, K., Gildenberg, M., Ahuja, S., Im, S. C., Pearcy, P., Waskell, L., and Ramamoorthy, A. (2013) Probing the transmembrane structure and topology of microsomal cytochrome-p450 by solid-state NMR on temperature-resistant bicelles, *Sci Rep 3*, 2556.
77. Yamamoto, K., Pearcy, P., and Ramamoorthy, A. (2014) Bicelles exhibiting magnetic alignment for a broader range of temperatures: a solid-state NMR study, *Langmuir 30*, 1662-1629.
78. Pochapsky, T. C., Kazanis, S., and Dang, M. (2010) Conformational plasticity and structure/function relationships in cytochromes P450, *Antioxid Redox Signal 13*, 1273-1296.
79. Ohta, Y., Sakaki, T., Yabusaki, Y., Ohkawa, H., and Kawato, S. (1994) Rotation and membrane topology of genetically expressed methylcholanthrene-inducible cytochrome P-450IA1 lacking the N-terminal hydrophobic segment in yeast microsomes, *J Biol Chem 269*, 15597-15600.
80. Larson, J. R., Coon, M. J., and Porter, T. D. (1991) Purification and properties of a shortened form of cytochrome P-450 2E1: deletion of the NH2-terminal membrane-insertion signal peptide does not alter the catalytic activities, *Proc Natl Acad Sci U S A 88*, 9141-9145.
81. Sagara, Y., Barnes, H. J., and Waterman, M. R. (1993) Expression in Escherichia coli of functional cytochrome P450c17 lacking its hydrophobic amino-terminal signal anchor, *Arch Biochem Biophys 304*, 272-278.
82. Li, Y. C., and Chiang, J. Y. (1991) The expression of a catalytically active cholesterol 7 alpha-hydroxylase cytochrome P450 in Escherichia coli, *J Biol Chem 266*, 19186-19191.
83. Kempf, A. C., Zanger, U. M., and Meyer, U. A. (1995) Truncated human P450 2D6: expression in Escherichia coli, Ni(2+)-chelate affinity purification, and characterization of solubility and aggregation, *Arch Biochem Biophys 321*, 277-288.
84. Dong, M. S., Bell, L. C., Guo, Z., Phillips, D. R., Blair, I. A., and Guengerich, F. P. (1996) Identification of retained N-formylmethionine in bacterial recombinant mammalian cytochrome P450 proteins with the N-terminal sequence MALLLAVFL...: roles of residues 3-5 in retention and membrane topology, *Biochemistry 35*, 10031-10040.
85. Williams, P. A., Cosme, J., Sridhar, V., Johnson, E. F., and McRee, D. E. (2000) Mammalian microsomal cytochrome P450 monooxygenase: structural adaptations for membrane binding and functional diversity, *Mol Cell 5*, 121-131.

86. Shank-Retzlaff, M. L., Raner, G. M., Coon, M. J., and Sligar, S. G. (1998) Membrane topology of cytochrome P450 2B4 in Langmuir-Blodgett monolayers, *Arch Biochem Biophys 359*, 82-88.
87. Shen, S., and Strobel, H. W. (1993) Role of lysine and arginine residues of cytochrome P450 in the interaction between cytochrome P4502B1 and NADPH-cytochrome P450 reductase, *Arch Biochem Biophys 304*, 257-265.
88. Nikfarjam, L., Izumi, S., Yamazaki, T., and Kominami, S. (2006) The interaction of cytochrome P450 17alpha with NADPH-cytochrome P450 reductase, investigated using chemical modification and MALDI-TOF mass spectrometry, *Biochim Biophys Acta 1764*, 1126-1131.
89. Cvrk, T., and Strobel, H. W. (2001) Role of LYS271 and LYS279 residues in the interaction of cytochrome P4501A1 with NADPH-cytochrome P450 reductase, *Arch Biochem Biophys 385*, 290-300.
90. Shimizu, T., Tateishi, T., Hatano, M., and Fujii-Kuriyama, Y. (1991) Probing the role of lysines and arginines in the catalytic function of cytochrome P450d by site-directed mutagenesis. Interaction with NADPH-cytochrome P450 reductase, *J Biol Chem 266*, 3372-3375.
91. Bridges, A., Gruenke, L., Chang, Y. T., Vakser, I. A., Loew, G., and Waskell, L. (1998) Identification of the binding site on cytochrome P450 2B4 for cytochrome b5 and cytochrome P450 reductase, *J Biol Chem 273*, 17036-17049.
92. Nadler, S. G., and Strobel, H. W. (1991) Identification and characterization of an NADPH-cytochrome P450 reductase derived peptide involved in binding to cytochrome P450, *Arch Biochem Biophys 290*, 277-284.
93. Jang, H. H., Jamakhandi, A. P., Sullivan, S. Z., Yun, C. H., Hollenberg, P. F., and Miller, G. P. (2010) Beta sheet 2-alpha helix C loop of cytochrome P450 reductase serves as a docking site for redox partners, *Biochim Biophys Acta 1804*, 1285-1293.
94. Bumpus, N. N., and Hollenberg, P. F. (2010) Cross-linking of human cytochrome P450 2B6 to NADPH-cytochrome P450 reductase: Identification of a potential site of interaction, *J Inorg Biochem 104*, 485-488.
95. Omata, Y., Dai, R., Smith, S. V., Robinson, R. C., and Friedman, F. K. (2000) Synthetic peptide mimics of a predicted topographical interaction surface: the cytochrome P450 2B1 recognition domain for NADPH-cytochrome P450 reductase, *J Protein Chem 19*, 23-32.
96. Cawley, G. F., Batie, C. J., and Backes, W. L. (1995) Substrate-dependent competition of different P450 isozymes for limiting NADPH-cytochrome P450 reductase, *Biochemistry 34*, 1244-1247.
97. Backes, W. L., and Kelley, R. W. (2003) Organization of multiple cytochrome P450s with NADPH-cytochrome P450 reductase in membranes, *Pharmacol Ther 98*, 221-233.
98. Ingelman-Sundberg, M., Haaparanta, T., and Rydstrom, J. (1981) Membrane charge as effector of cytochrome P-450LM2 catalyzed reactions in reconstituted liposomes, *Biochemistry 20*, 4100-4106.
99. Ingelman-Sundberg, M., Blanck, J., Smettan, G., and Ruckpaul, K. (1983) Reduction of cytochrome P-450 LM2 by NADPH in reconstituted phospholipid vesicles is dependent on membrane charge, *Eur J Biochem 134*, 157-162.
100. Bayburt, T. H., and Sligar, S. G. (2002) Single-molecule height measurements on microsomal cytochrome P450 in nanometer-scale phospholipid bilayer disks, *Proc Natl Acad Sci U S A 99*, 6725-6730.
101. Lu, A. Y., and Coon, M. J. (1968) Role of hemoprotein P-450 in fatty acid omega-hydroxylation in a soluble enzyme system from liver microsomes, *J Biol Chem 243*, 1331-1332.
102. Sem, D. S., and Kasper, C. B. (1994) Kinetic mechanism for the model reaction of NADPH-cytochrome P450 oxidoreductase with cytochrome c, *Biochemistry 33*, 12012-12021.

103. Grunau, A., Paine, M. J., Ladbury, J. E., and Gutierrez, A. (2006) Global effects of the energetics of coenzyme binding: NADPH controls the protein interaction properties of human cytochrome P450 reductase, *Biochemistry 45*, 1421-1434.
104. Murataliev, M. B., Feyereisen, R., and Walker, F. A. (2004) Electron transfer by diflavin reductases, *Biochim Biophys Acta 1698*, 1-26.
105. Nisimoto, Y. (1986) Localization of cytochrome c-binding domain on NADPH-cytochrome P-450 reductase, *J Biol Chem 261*, 14232-14239.
106. Nadler, S. G., and Strobel, H. W. (1988) Role of electrostatic interactions in the reaction of NADPH-cytochrome P-450 reductase with cytochromes P-450, *Arch Biochem Biophys 261*, 418-429.
107. Tamburini, P. P., and Schenkman, J. B. (1986) Differences in the mechanism of functional interaction between NADPH-cytochrome P-450 reductase and its redox partners, *Mol Pharmacol 30*, 178-185.
108. Shen, S., and Strobel, H. W. (1994) Probing the putative cytochrome P450- and cytochrome c-binding sites on NADPH-cytochrome P450 reductase by anti-peptide antibodies, *Biochemistry 33*, 8807-8812.
109. Kenaan, C., Zhang, H., Shea, E. V., and Hollenberg, P. F. (2011) Uncovering the role of hydrophobic residues in cytochrome P450-cytochrome P450 reductase interactions, *Biochemistry 50*, 3957-3967.
110. Lehnerer, M., Schulze, J., Achterhold, K., Lewis, D. F., and Hlavica, P. (2000) Identification of key residues in rabbit liver microsomal cytochrome P450 2B4: importance in interactions with NADPH-cytochrome P450 reductase, *J Biochem 127*, 163-169.
111. Lin, H. L., Kenaan, C., Zhang, H., and Hollenberg, P. F. (2012) Reaction of human cytochrome P450 3A4 with peroxynitrite: nitrotyrosine formation on the proximal side impairs its interaction with NADPH-cytochrome P450 reductase, *Chem Res Toxicol 25*, 2642-2653.
112. Pervushin, K., Riek, R., Wider, G., and Wuthrich, K. (1997) Attenuated T2 relaxation by mutual cancellation of dipole-dipole coupling and chemical shift anisotropy indicates an avenue to NMR structures of very large biological macromolecules in solution, *Proc Natl Acad Sci U S A 94*, 12366-12371.
113. Wuthrich, K., and Wider, G. (2003) Transverse relaxation-optimized NMR spectroscopy with biomacromolecular structures in solution (Reprinted from Encyclopedia Nuclear Magnetic Resonance, vol 9, pg 468-477, 2002), *Magn. Reson. Chem. 41*, S80-S88.
114. Zuiderweg, E. R. (2002) Mapping protein-protein interactions in solution by NMR spectroscopy, *Biochemistry 41*, 1-7.
115. Matsuo, H., Walters, K. J., Teruya, K., Tanaka, T., Gassner, G. T., Lippard, S. J., Kyogoku, Y., and Wagner, G. (1999) Identification by NMR spectroscopy of residues at contact surfaces in large, slowly exchanging macromolecular complexes, *J. Am. Chem. Soc. 121*, 9903-9904.
116. de Vries, S. J., van Dijk, A. D., Krzeminski, M., van Dijk, M., Thureau, A., Hsu, V., Wassenaar, T., and Bonvin, A. M. (2007) HADDOCK versus HADDOCK: new features and performance of HADDOCK2.0 on the CAPRI targets, *Proteins 69*, 726-733.
117. Dominguez, C., Boelens, R., and Bonvin, A. M. (2003) HADDOCK: a protein-protein docking approach based on biochemical or biophysical information, *J Am Chem Soc 125*, 1731-1737.
118. Nicastro, G., Menon, R. P., Masino, L., Knowles, P. P., McDonald, N. Q., and Pastore, A. (2005) The solution structure of the Josephin domain of ataxin-3: structural determinants for molecular recognition, *Proc Natl Acad Sci U S A 102*, 10493-10498.
119. Gamsjaeger, R., Swanton, M. K., Kobus, F. J., Lehtomaki, E., Lowry, J. A., Kwan, A. H., Matthews, J. M., and Mackay, J. P. (2008) Structural and biophysical analysis of the DNA binding properties of myelin transcription factor 1, *J Biol Chem 283*, 5158-5167.

120. Rutten, L., Geurtsen, J., Lambert, W., Smolenaers, J. J., Bonvin, A. M., de Haan, A., van der Ley, P., Egmond, M. R., Gros, P., and Tommassen, J. (2006) Crystal structure and catalytic mechanism of the LPS 3-O-deacylase PagL from Pseudomonas aeruginosa, *Proc Natl Acad Sci U S A 103*, 7071-7076.
121. Kamphuis, M. B., Bonvin, A. M., Monti, M. C., Lemonnier, M., Munoz-Gomez, A., van den Heuvel, R. H., Diaz-Orejas, R., and Boelens, R. (2006) Model for RNA binding and the catalytic site of the RNase Kid of the bacterial parD toxin-antitoxin system, *J Mol Biol 357*, 115-126.
122. Bonvin, A. M. High Ambiguity Driven biomolecular DOCKing based on biochemical and/or biophysical information.
123. Hubbard, S. J., and Thornton, J. M. (1993) NACCESS, Department of Biochemistry and Molecular Biology, University College London
124. Roitberg, A. E., Holden, M. J., Mayhew, M. P., Kurnikov, I. V., Beratan, D. N., and Vilker, V. L. (1998) Binding and electron transfer between putidaredoxin and cytochrome P450cam. Theory and experiments, *J. Am. Chem. Soc. 120*, 8927-8932.
125. Liang, Z. X., Kurnikov, I. V., Nocek, J. M., Mauk, A. G., Beratan, D. N., and Hoffman, B. M. (2004) Dynamic docking and electron-transfer between cytochrome b5 and a suite of myoglobin surface-charge mutants. Introduction of a functional-docking algorithm for protein-protein complexes, *J Am Chem Soc 126*, 2785-2798.
126. Lin, J., Balabin, I. A., and Beratan, D. N. (2005) The nature of aqueous tunneling pathways between electron-transfer proteins, *Science 310*, 1311-1313.
127. Guallar, V., and Wallrapp, F. (2008) Mapping protein electron transfer pathways with QM/MM methods, *J R Soc Interface 5 Suppl 3*, S233-239.
128. Kurnikov, I. V. (2000) HARLEM molecular modeling package, Department of Chemistry, University of Pittsburgh, Pittsburgh, PA.
129. Beratan, D. N., Betts, J. N., and Onuchic, J. N. (1991) Protein electron transfer rates set by the bridging secondary and tertiary structure, *Science 252*, 1285-1288.
130. Onuchic, J. N., Beratan, D. N., Winkler, J. R., and Gray, H. B. (1992) Pathway analysis of protein electron-transfer reactions, *Annu Rev Biophys Biomol Struct 21*, 349-377.
131. Hiruma, Y., Hass, M. A., Kikui, Y., Liu, W. M., Olmez, B., Skinner, S. P., Blok, A., Kloosterman, A., Koteishi, H., Lohr, F., Schwalbe, H., Nojiri, M., and Ubbink, M. (2013) The structure of the cytochrome p450cam-putidaredoxin complex determined by paramagnetic NMR spectroscopy and crystallography, *J Mol Biol 425*, 4353-4365.
132. Lyons, J. A., Aragao, D., Slattery, O., Pisliakov, A. V., Soulimane, T., and Caffrey, M. (2012) Structural insights into electron transfer in caa3-type cytochrome oxidase, *Nature 487*, 514-518.
133. Strushkevich, N., MacKenzie, F., Cherkesova, T., Grabovec, I., Usanov, S., and Park, H. W. (2011) Structural basis for pregnenolone biosynthesis by the mitochondrial monooxygenase system, *Proc Natl Acad Sci U S A 108*, 10139-10143.
134. Ahuja, S., Jahr, N., Im, S. C., Vivekanandan, S., Popovych, N., Le Clair, S. V., Huang, R., Soong, R., Xu, J., Yamamoto, K., Nanga, R. P., Bridges, A., Waskell, L., and Ramamoorthy, A. (2013) A model of the membrane-bound cytochrome b5-cytochrome P450 complex from NMR and mutagenesis data, *J Biol Chem 288*, 22080-22095.
135. Whiles, J. A., Glover, K. J., Vold, R. R., and Komives, E. A. (2002) Methods for studying transmembrane peptides in bicelles: consequences of hydrophobic mismatch and peptide sequence, *J Magn Reson 158*, 149-156.
136. Kolodziejski, W., and Klinowski, J. (2002) Kinetics of cross-polarization in solid-state NMR: a guide for chemists, *Chem Rev 102*, 613-628.

137. Durr, U. H., Yamamoto, K., Im, S. C., Waskell, L., and Ramamoorthy, A. (2007) Solid-state NMR reveals structural and dynamical properties of a membrane-anchored electron-carrier protein, cytochrome b5, *J Am Chem Soc 129*, 6670-6671.
138. Yamamoto, K., Durr, U. H., Xu, J., Im, S. C., Waskell, L., and Ramamoorthy, A. (2013) Dynamic interaction between membrane-bound full-length cytochrome P450 and cytochrome b5 observed by solid-state NMR spectroscopy, *Sci Rep 3*, 2538.
139. Nevzorov, A. A., and Opella, S. J. (2003) A "magic sandwich" pulse sequence with reduced offset dependence for high-resolution separated local field spectroscopy, *J Magn Reson 164*, 182-186.
140. Nevzorov, A. A., and Opella, S. J. (2007) Selective averaging for high-resolution solid-state NMR spectroscopy of aligned samples, *J Magn Reson 185*, 59-70.
141. Dvinskikh, S. V., Yamamoto, K., and Ramamoorthy, A. (2006) Heteronuclear isotropic mixing separated local field NMR spectroscopy, *J Chem Phys 125*, 34507.

CHAPTER 2

Characterization of Interaction and Electron Transfer between the FMN Binding Domain of Cytochrome P450 Reductase and Cytochrome c

2.1 Summery

Cytochrome c reduction has been extensively used as a model reaction to assess the redox activity of cytochrome P450 reductase (CPR). In this chapter, electron transfer and complex formation between the FMN binding domain (FBD) of cytochrome P450 reductase and cytochrome c (cyt c) were investigated. Kinetics of electron transfer between FBD and cyt c show distinct rates depending on the redox states of FBD. When compared with wild-type CPR, FBD reduces cyt c at a much higher rate in both its semiquinone and hydroquinone state, suggesting that conformational gating of CPR plays a key role in the electron transfer process. The results of NMR titration experiments reveal the formation of dynamic complexes between FBD and cyt c on a fast exchange time scale with a dissociation constant K_d of 0.024 mM. Chemical shift mapping identifies the specific residues of FBD involved in the binding interface with cyt c, most of which are located around the solvent exposed edge of the FMN cofactor. The structure model of the FBD-cyt c complex generated using HADDOCK indicates two probable orientations of complex formation. The major structure shows potential salt bridge formation between Glu-213/Glu-214 of FBD and Lys-87 of cyt c which may be essential to the stability of the complex, and electron transfer pathway mediated by Lys-13 of cyt c was predicted. This work provides a structural basis for a better understanding of the interaction between CPR and cyt c and allows comparisons to be drawn with other electron transfer complexes involving CPR or cyt c.

2.2 Introduction

Cytochrome P450 reductase (CPR) is a diflavin protein which donates electrons to a variety of microsomal cytochrome P450s (1), heme oxygenase (2), cytochrome b5 (3),

cytochrome c (4) as well as therapeutic prodrugs (5). It plays an dispensible role in the cytochrome P450 monoxygenase system, which is responsible for the metablism of myriads of endogenous compounds including vitamins, steroids and hormones, as well as exogenous compounds including environmental toxins and drugs. CPR is a ~78 kDa membrane-bound protein composed of four distinct domains: the N-terminal transmembrane segment, the FMN binding domain (FBD), the connecting domain and the FAD/NADPH binding domain (6). It shuttles electrons from its physiological reductant NADPH, via the FAD and FMN cofactors, to its acceptor proteins, *e.g.* cytochrome P450s. The FMN binding domain is the ultimate donor of electrons to the acceptor proteins.

CPR was first isolated and identified as an NADPH-dependent cytochrome c (cyt c) reductase in the 1950s (7). In later studies, the true physiological redox partner of CPR was revealed to be cytochrome P450 after successful achievement of hydroxylase activity from a reconstitution system composed of cytochrome P450, CPR and phospholipids (8), while cyt c – an important component in the electron transfer chain in mitochondria –is unlikely to be a physiological redox partner of CPR which was found to be localized on the endoplasmic reticulum (4). Nevertheless, the redox reaction between CPR and cyt c continued to be widely used as a standard model to characterize the redox properties and the activities of CPR (9-13). Oxidized cyt c can also accept electrons from the reductase domains of both P450-BM_3 and nitric oxide synthase (NOS) which are also in the diflavin reductase family, and it is suggested that electrons flow from the FMN of these flavoproteins to the heme of cyt c during electron transfer (14).

Electron transfer between proteins plays an essential role in a number of important biological processes including photosynthesis and respiration. It usually requires formation of transient protein complexes which are characterized with high association and dissociation rates to ensure quick turnovers. Interaction and complex formation between CPR and cyt c has been investigated by cross-linking (15, 16), site-direct mutagenesis studies (12, 13, 17), etc. It has been proposed that charge-pairing between the negatively-charged CPR and the positively-charged cyt c contributes greatly in the complex formation and stability. Methylamidation of the carboxyl groups on CPR leads to strong inhibition of cyt c reduction (18), and a decrease on V_{max}

of the reaction (16). Increase in ionic strength also causes disruption in complex formation and electron transfer between CPR and cyt c due to masking effect of the charged residues (12). In particular, a cluster of acidic residues Glu-213-Glu-214-Asp-215 on the N-terminus of helix α7 are potentially located on the CPR – cyt c complex interface, as suggested by site-directed mutagenesis studies (13, 17). It has also been shown that Lys-13 of cyt c and be cross-linked to one of the carboxyl groups from the two acidic clusters Asp-207, -208 and -209 and Glu-213-Glu-214-Asp-215 (15). However, antibody binding studies reveal that an antibody designed to bind against Gly-204 to Gly-218 region of CPR fails to show effect on CPR – cyt c interaction (19). On the other hand, mutation of another acidic cluster Asp-113 and Glu-115-Glu-116 on the β2-α4 coil of CPR improves the cyt c reductase activity, facilitating a more functional complex formation (12). With the controversy in the literature, a high-resolution mapping of the binding interface of CPR and cyt c is necessary to gain insight into the interaction and electron transfer between the two proteins. The nature of weak interactions between electron transfer proteins makes the complex difficult to crystallize. Meanwhile, solution NMR techniques have been well developed to investigate such transient complexes including myoglobin – cyt b5 (20), cyt b5 – cyt c (21), cyt c – cyt c peroxidase (22), P450cam – putidaredoxin (23) etc. Therefore in this chapter the interaction between CPR and cyt c will be probed by solution NMR.

CPR-mediated electron transfer from NADPH to cytochrome P450/cyt c is highly orchestrated between intraprotein electron transfer (from NADPH to FAD and from FAD to FMN) and interprotein electron transfer (from FMN to heme). Internal electron transfer from NADPH to FAD is regulated with the side chain movement of Trp-676 of CPR (human) (24), and interflavin electron transfer has been suggested to be gated by interdomain movements between the FMN binding domain and the rest of the reductase (6, 25). On the other hand, interprotein electron transfer between FMN and heme depends on complex formation. In order to focus only on complex formation and simplify the electron transfer process, we choose to investigate electron transfer and complex formation between cyt c and isolated FMN binding domain, which is the direct electron donor to cyt c.

In this study, we characterized the kinetics of electron transfer from the FMN binding domain (FBD) of CPR to cyt c, and compared with that from wild-type CPR to cyt c, demonstrating the effect of conformational changes of CPR on interprotein electron transfer.

Using solution NMR in combination with molecular docking, we mapped the binding interface on the FMN binding domain and proposed a structural model of the FBD – cyt c complex. The NMR results imply formation of a dynamic complex and indicate the primary binding sites on FBD. The structural models generated by HADDOCK based on NMR restraints suggest potential electron pathways that provide strong electronic coupling between the redox centers. The details on the FBD – cyt c binding interface also allow comparisons to be drawn with that of FBD – P450 complex or other electron transfer complexes involving cyt c.

2.3 Materials and Methods

2.3.1 Materials

E. coli C41 cells for protein overexpression were purchased from Lucigen (Middleton, MI). Yeast extract, tryptone for unlabeled growth media were purchased from Sigma-Aldrich. [^{15}N]ammonium chloride for M9 medium and D_2O were purchased from Cambridge Isotope Laboratories (Andover, MA). Horse heart cyt c, resins, buffer components, and all the chemicals were purchased from Sigma-Aldrich. Glycerol used in NMR experiments was purchased from Roche Applied Science.

2.3.2 Expression and purification of a uniformly ^{15}N-labeled FMN binding domain of rat CPR

The FMN binding domain (residue 1-239) (FBD) was expressed and purified from *E. coli* C41 cell. *E. coli* C41 cells were transformed with a pSC-CPR plasmid (26) containing the FBD gene and adapted in 100mL Lysogeny Broth (LB) medium for 5 hours before transferred into M9 minimal medium (40 mM Na_2HPO_4, 20 mM KH_2PO_4, 8.5 mM NaCl, 18 mM $^{15}NH_4Cl$, 1 mM $MgSO_4$, 1 µM $CaCl_2$, 16 nM riboflavin, 0.4 % (w/v) glucose). Expression of FBD was induced by adding 0.4 mM Isopropyl β-D-1-thiogalactopyranoside (IPTG) when the cell growth reaches log phase (OD_{600}=0.7). Afterwards, cells were grown for 14 hours at 30°C and with a shaking speed of 140 rpm, and harvested. The harvested cells were lysed via treatment with lysozyme (30 µg per mL of cell suspension) for 30 min and sonication by alternating 1-min pulses for a total of 8 min. The membrane fraction of the cells was recovered by ultracentrifugation (105,000 × g, 45 min) and the protein were solubilized from the membrane

with 0.3 w/v% TritonX-100 at 4 °C via stirring overnight. Solubilized protein was loaded to DEAE Sepharose column equilibrated with loading buffer (50 mM Tris-acetate, 0.1 mM EDTA, 0.2 mM DTT, 10 % glycerol, 1 µM FMN, pH 6.7). The column was washed with 2 column volumns (CV) of loading buffer and 5 CV of washing buffer (loading buffer with additional 0.17 M NaCl and 0.3 % (w/v) sodium cholate), and gradient-eluted with a total of 4 CV of washing buffer and eluting buffer (loading buffer with additional 0.5 M NaCl and 0.3 % (w/v) sodium cholate). The eluted protein solution was subjected to hydroxyapatite column to remove the detergents. Full-length rat CPR was overexpressed and purified according to published protocol (26). Each purified protein exhibited a single band on the SDS-polyacrylamide gel. The concentration of the oxidized MFBD and CPR was determined using extinction coefficients of 12.2 $mM^{-1}cm^{-1}$ and 21 $mM^{-1}cm^{-1}$ at 454 nm respectively (27) .

2.3.3 Titration of FBD by dithionite under anaerobic conditions

FBD and CPR were titrated with sodium dithionite solution under anaerobic conditions monitored by UV-Vis spectra. The solution of the FMN binding domain was incubated overnight at 4 °C in an anaerobic Belle Technology glove box (Hi-Tech, Salisbury, UK) to remove oxygen. The titrant (sodium dithionite solution) was prepared in the glove box in oxygen-free buffer, and its concentration was calculated using an extinction coefficient of 8 mM^{-1} cm^{-1} at 315 nm. The titrand solution of FBD or CPR contains 11.3 µM of the protein, 3 µM of methylviologen, 100 mM potassium phosphate buffer, 5 % (w/v) of glycerol, pH 7.4. The titration was carried out in a home-made anaerobic titration apparatus to minimize contamination of oxygen, and monitored by UV-Vis spectrum.

2.3.4 Pre-steady-state kinetics of cyt c reduction by FBD/CPR

All experiments were performed at 25 °C under anaerobic conditions using a Hi-Tech SF61DX2 stopped-flow spectrophotometer housed in an anaerobic Belle Technology glove box. The buffer was purged with nitrogen gas for 30 min for deoxygenation prior to being transferred to the glove box. The solution of cyt c was incubated overnight at 4 °C in the glove box to eliminate oxygen. For measuring the kinetics of cyt c reduction by FBD/CPR, FBD (11.3 µM) and wild-type CPR (11.3 µM) were pre-reduced to the intended redox state anaerobically as

described above, and then loaded in syringe 1 of the stopped flow, whereas syringe 2 was loaded with ferric cyt c. The reaction was started by rapid mixing of an equal volume from both syringes and monitored at 550 nm and 630 nm. Traces were fitted using a standard single exponential equation (28). The buffer contains 100 mM potassium phosphate, 5 % (w/v) glycerol, pH 7.4.

2.3.5 Kinetics of auto-oxidation of hydroquinone FBD

Auto-oxidation of hydroquinone FBD was studied using the stopped-flow spectrophotometer apparatus descried above. FBD (11.3 µM) was pre-reduced to two electron-reduced state, and loaded in syringe 1 of the stopped flow, and syringe 2 was loaded with buffer saturated with oxygen. The reaction was started by rapid mixing of an equal volume of both syringes and monitored at 585 nm and 454 nm. The traces were fitted using a standard single exponential equation.

2.3.6 NMR titration experiments

All NMR experiments were performed on a Bruker Avance 900 MHz NMR spectrometer equipped with an x,y,z axis PFG-5mm TCI cryoprobe at 298K. Samples for 2D NMR experiments contain 0.3 mM ^{15}N-labeled FBD in 100 mM potassium phosphate buffer with 5% (w/v) glycerol at pH 7.4. Titration of unlabeled cyt c into ^{15}N-labeled FBD was carried out by addition of concentrated cyt c solution corresponding to 0.3, 0.6, 1 and 5 molar equivalents of FBD. 2D ^{15}N, ^{1}H TROSY-HSQC spectra were collected at each titration point with 32 scans and 144 t_1 increments. The average amide chemical shift perturbation ($\Delta\delta_{avg}$) was calculated using the equation below

$$\Delta\delta_{\mathrm{avg}} = \sqrt{(\Delta\delta\mathrm{N} \times \frac{SW2}{SW1})^2 + \Delta\delta\mathrm{H}^2}$$

where $\Delta\delta$N and $\Delta\delta$H are changes in chemical shift observed between the bound and unbound states and $SW1$ and $SW2$ represent spectrum width of the first and second dimension respectively. Titration of unlabeled FBD to cyt c was performed by adding aliquots of FBD solution to a final concentration of 0.3, 0.6, 0.9, 2 and 3 molar equivalents of cyt c. The dissociation constant K_d was determined by fitting the titration data (21). All NMR spectra were

processed using TopSpin 2.0 (Bruker). Resonance assignments and data analysis were performed using Sparky (29).

2.3.7 Structural modeling of FBD-cyt c complex

HADDOCK 2.1 (30) program was utilized to calculate the structural models of FBD-cyt c complex based on defined ambiguous restraints. HADDOCK docking algorithm includes three consecutive steps—1. rigid body docking in which the two molecules are rotated and translated randomly in turn in order to minimize intermolecular energy, 2. simulated annealing of structures in which annealing in torsion angle space is performed to refine the orientation of the proteins and the side chains and/or backbones of the interface residues, 3. solvent refinement in which the structures are further refined in explicit solvent layers. In this docking, the crystal structure of FBD (PDB code 1AMO) and the solution NMR structure of the house heart cyt c (PDB code 1AKK) were used as the starting structures. Ligand and topology files were generated from the PRODRG server (31). 1000 structures were generated in the rigid body docking step, followed by simulated annealing of the 200 lowest-energy structures from the last step and finally the best 50 structures were selected for solvent refinement in an 8.0 Å shell of TIP3P water molecules. The resulting 50 final structures were analyzed and grouped into clusters based on the backbone r.m.s.d. values. Molecular structures of the complexes were viewed and graphed using PYMOL.

2.4 Results

2.4.1 Characterization of the FMN binding domain

Isolated FMN binding domain (FBD) was expressed, purified and characterized by SDS-PAGE analysis and redox titration (Figure 2.1A-B). The spectral properties of FBD during redox titration are quite similar to those of the FMN binding domain of human CPR reported (32). Reduction of FBD from fully-oxidized state to semiquinone (one electron-reduced) is featured by spectral intensity decrease at 454 nm and an increase of a broad band centered at 585 nm – characteristic of blue semiquinone formation – with isosbestic points at 502 nm and 361 nm. Transition from semiquinone to hydroquinone (two electron-reduced) can be visualized in the spectra with further intensity decrease at 454 nm as well as at 585 nm with isosbestic points at

327 nm, 386 nm and 432 nm (Figure 2.1B). Auto-oxidation of hydroquinone FBD is characterized by rapid mixing of two electron-reduced FBD and oxygen-saturated buffer, and monitoring the oxidation of hydroquinone at 454 nm and formation of the air-stable semiquinone at 585 nm (Figure 2.1C). The observed rate of blue semiquinone formation (0.746 ± 0.006 s^{-1}) (Figure 2.1C-a) is slower than that of hydroquinone oxidation (1.33 ± 0.08 s^{-1}) (Figure 2.1C-b), which might attribute to proton diffusion or potential protein side chain rearrangement necessary for stabilizing the blue semiquinone.

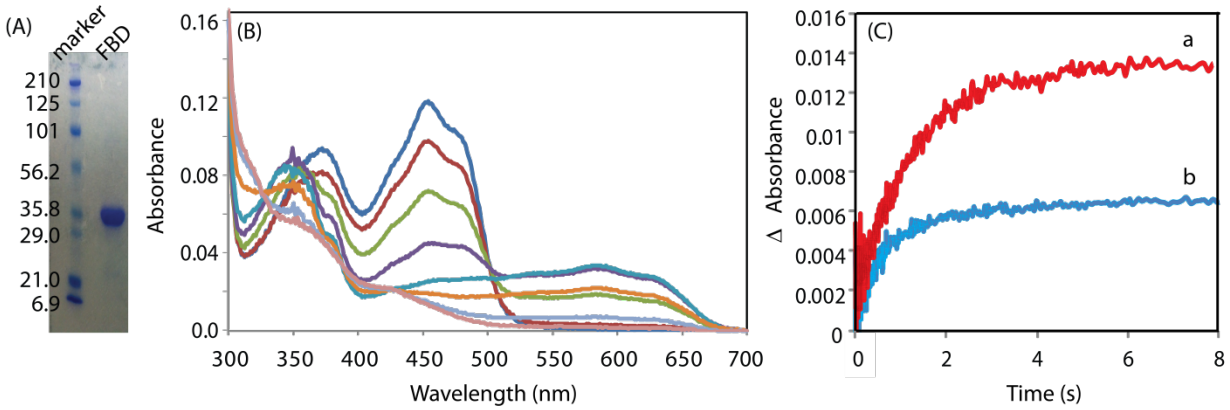

Figure 2.1 Characterization of FBD. A, SDS-PAGE gel of FBD. The single band reveals the purity of the protein. B, spectral changes during a redox titration of FBD with sodium dithionite under anaerobic conditions. The titration was performed as described in "Experimental Procedures". C, Kinetic transients of auto-oxidation of two electron-reduced FBD. FBD was reduced to two-electron level by stoichiometric titration with dithionite. The reaction was initiated by mixing two electron-reduced FBD and oxygen-saturated buffer and monitored at 585 nm (a) and 454 nm (b).

2.4.2 Kinetics studies of electron transfer between the FMN binding domain and cytochrome c in comparison with wild-type CPR

In order to gain insight into interactions between cyt c and FBD, we investigated electron transfer from reduced FBD to oxidized cyt c under pseudo-first order conditions and compared with wild-type CPR. In these experiments, wild-type CPR/FBD were reduced to one and two electron-reduced states respectively prior to mixing with cyt c. Lacking the FAD/NADPH binding domain, the isolated FMN binding domain cannot be reduced by the physiological

reductant of CPR—NADPH (supporting information). Therefore, sodium dithionite was used to titrate FBD and wild-type CPR to the intended redox states. Kinetic transients are measured at 550 nm and 630 nm to monitor cyt c reduction and semiquinone oxidation of the reductases, respectively.

Reduction of cyt c is initiated by rapid mixing of the reduced reductase and a 10-fold excess of ferric cyt c. Under this condition, a total of one molar equivalent of cyt c was reduced by two electron-reduced CPR with a k_{obs} of 16.8 ± 0.2 s^{-1} (Figure 2.2A), which is comparable with that in human CPR (k_{obs} = 12 ± 0.4 s^{-1}) (27), while with one electron-reduced CPR the kinetic transient does not show signs of cyt c reduction (Figure 2.2A) which is consistent with the literature reports (33). In comparison, mixing one electron-reduced FMN binding domain with cyt c leads to reduction of one molar equivalent of cyt c with a k_{obs} of 0.0227 ± 0.0004 s^{-1} (Figure 2.2B). As for two electron-reduced FMN binding domain, a total of two molar equivalents of cyt c was reduced (Figure 2.2B). The kinetic transient shows an initial increase at 550 nm within the dead time of the instrument corresponding to one molar equivalent of reduced cyt c, followed by a slow phase with a k_{obs} of 0.0225 ± 0.0005 s^{-1}. This implies a two-step reaction mechanism as in Scheme 1, in which step 1 occurs at a very high rate (>10^4 s^{-1}) – mostly completed within the dead time, whereas step 2 occurs at a rate of around 0.0225 s^{-1} agree with the rate of cyt c reduction by one electron-reduced FMN binding domain. The hypothesized mechanism is also verified by the transients at 630 nm – where the absorbance of cyt c is negligible – to indicate the oxidation of FMN semiquinone. For two electron-reduced FMN binding domain, mixing with cyt c instantaneously lead to an accumulation of FMN semiquinone indicated by the absorbance at 630 nm. This agrees with a rapid reduction of cyt c by the hydroquinone FMN suggested in step 1 of the mechanism (Scheme 1-1). The following decay of absorbance at 630 nm at a rate of 0.0257 ± 0.0007 s^{-1} implies the oxidation of semiquinone FMN by cyt c in step 2 (Scheme 1-2) coincide with the rate of cyt c reduction. The two step reaction can also be observed by the spectra by photodiode array detection (Figure 2.2E). The rate constants are summarized in Table 2.1.

$$FMN_{hq} + \text{cyt } c_{ox} \underset{k_{-1}}{\overset{k_1}{\rightleftharpoons}} \text{complex} \xrightarrow{k_2} FMN_{sq} + \text{cyt } c_{red} \qquad (1)$$

$$FMN_{sq} + \text{cyt } c_{ox} \underset{k_{-3}}{\overset{k_3}{\rightleftharpoons}} \text{complex} \xrightarrow{k_4} FMN_{ox} + \text{cyt } c_{red} \qquad (2)$$

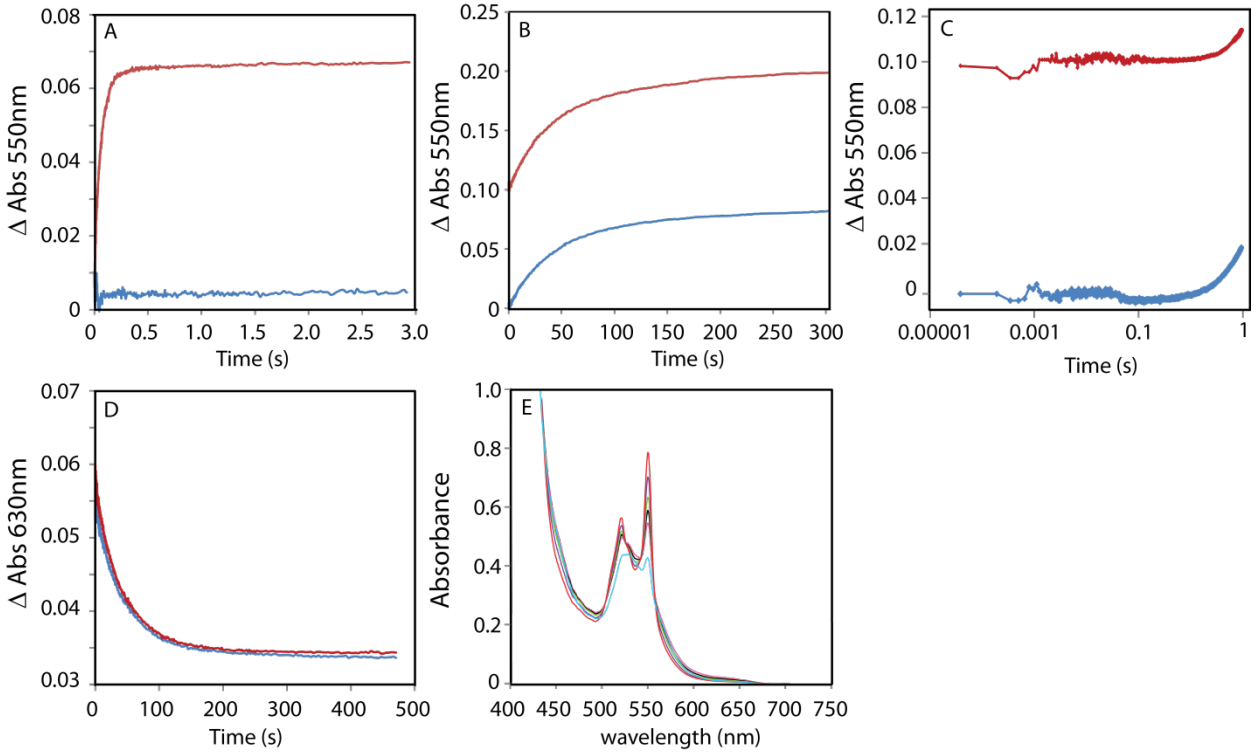

Figure 2.2. Electron transfer between the FMN binding domain/wild-type CPR and cyt c. A, CPR (11.3 µM) was reduced to one electron- and two electron-reduced states by stoichiometric titration with dithionite, and rapidly mixed with cytochrome c (100 µM) in the stopped-flow spectroscopy. Reduction of cyt c by one electron-reduced (blue) and two electron–reduced (red) CPR was monitored at 550 nm respectively. B-E, The FMN binding domain (11.3 µM) was reduced to one electron- and two electron-reduced states by dithionite, and rapidly mixed with cytochrome c (100 µM). Reduction of cyt c by one electron-reduced (blue) and two electron–reduced (red) FMN binding domain was monitored at 550 nm (B, C), 630 nm (D). The diode array-detected spectra (E) of the mixture were recorded 0.00074 s (pink), 28.5 s (black), 56.4 s (green), 125.4 s (purple) and 285 s (red) after rapid mixing. Spectrum of oxidized cyt c mixed with buffer is shown in blue.

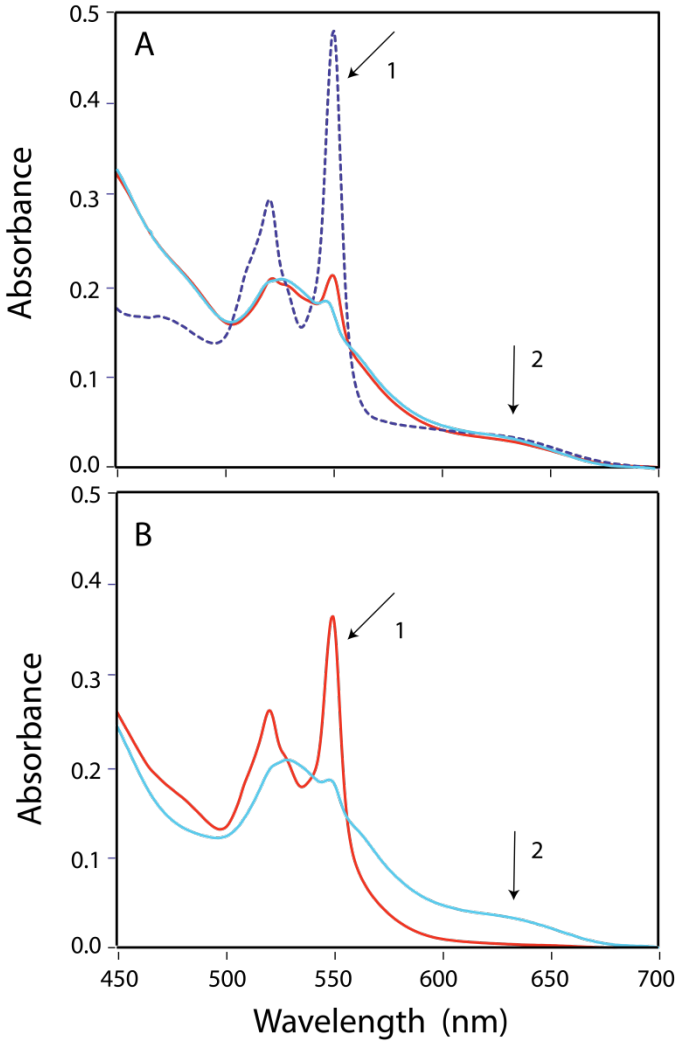

Figure 2.3 Cyt c reduction by pre-reduced wild-type CPR and FMN binding domain. A, CPR (7 µM) was reduced to one electron-reduced state (semiquinone) by dithionite and mixed with oxidized cyt c (14 µM) under anaerobic conditions. Spectrum of the mixture was taken 20 min after mixing (red). NADPH (20 µM) was added into the mixture anaerobically and resulted in total reduction of cyt c (purple) indicated by arrow 1, meanwhile CPR rested in one electron-reduced (semiquinone) state indicated by arrow 2. B, the FMN binding domain (7 µM) was reduced to one electron-reduced state (semiquinone) by dithionite and mixed with oxidized cyt c (14 µM) under anaerobic conditions. Spectrum of the mixture was taken 20 min after mixing (red). The reduction and cyt c and oxidation of FMN semiquinone are indicated by arrow 1 and 2, respectively. The spectra before mixing were calculated by addition of individual spectra of the two components (blue).

Table 2.1 Kinetics of cyt c reduction by the FMN binding domain and CPR

Reductase	Wavelength (nm)	$k_{1\ obs}$ (s^{-1})	$k_{2\ obs}$ (s^{-1})
One electron-reduced CPR	550	--	
Two electron-reduced CPR	550	16.8 ± 0.2[a]	--
	520	16.2 ± 0.2	--
One electron-reduced FBD	550	0.0227 ± 0.004	
	630	0.0239 ± 0.006	
Two electron-reduced FBD	550	> 10^4	0.0225 ± 0.0005
	630	> 10^4	0.0257 ± 0.0007

[a] standard deviations were calculated among three kinetic transients monitored at the same wavelength.

The distinct abilities of semiquinone FMN binding domain and CPR in reducing cyt c are shown in Figure 2.3. Mixing of pre-reduced semiquinone CPR and cyt c did not lead to proportional cyt c reduction until NADPH was added into the reaction mixture indicated by absorbance at 550 nm (Figure 2.3A). The shoulder at 630 nm, indicating blue semiquinone of CPR, remains even after addition of NADPH, showing CPR rests in one electron-reduced state (Figure 2.3A). In contrast, one electron-reduced FBD, after mixed with excess cyt c, leads to reduction of one molar equivalent of cyt c (550 nm) accompanied by oxidation of semiquinone (630 nm) (Figure 2.3B).

2.4.3 Determination of dissociation constant of FBD and cyt c by NMR titrations

The backbone assignments of the FMN binding domain of CPR have been previously reported (34) and utilized in the current study. The two-dimensional ^{15}N, ^{1}H-HSQC spectra were recorded to monitor the titration of unlabeled cyt c to 0.3 mM ^{15}N-FBD. Throughout the titration only one set of backbone resonances of FBD were observed, implying that the interaction between FBD and cyt c occurs in fast-exchange NMR time scale. Figure 2.4 shows

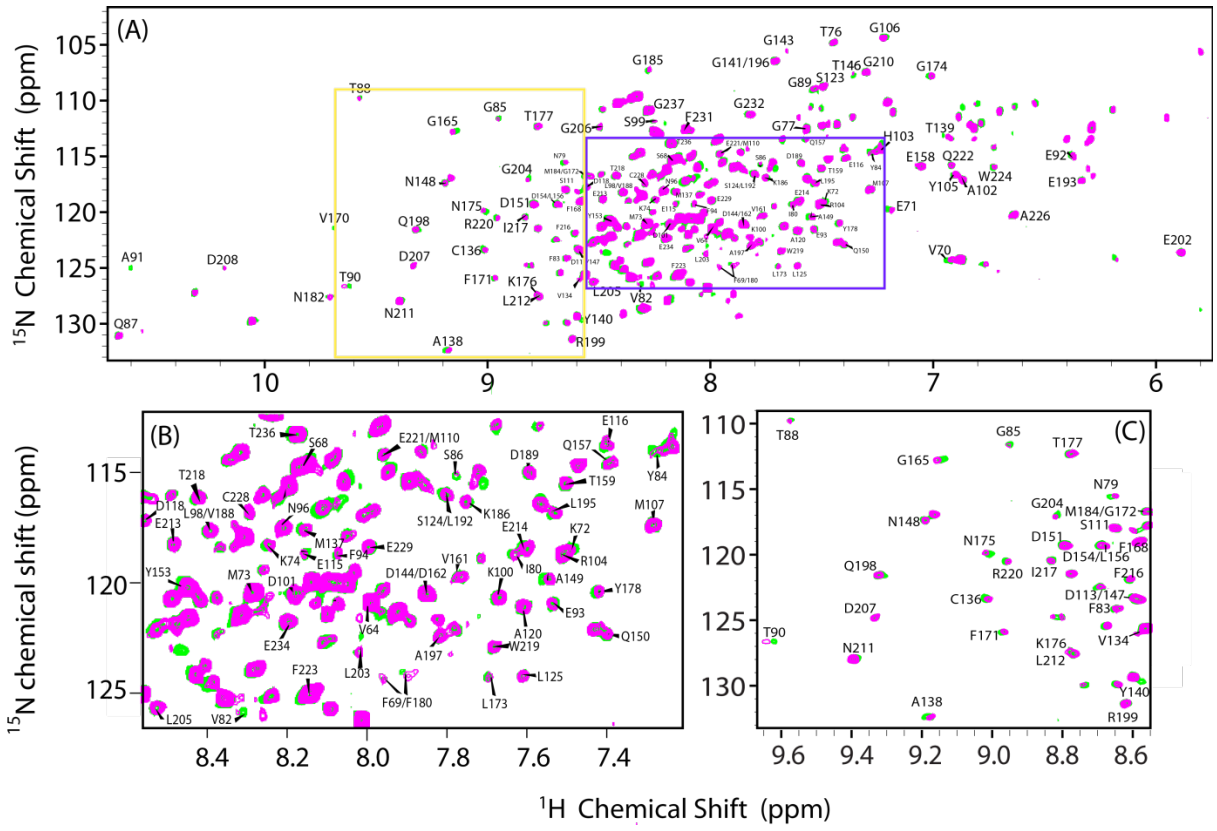

Figure 2.4 A, superposition of the ^{1}H-^{15}N HSQC spectra of the FMN binding domain in the free form (green) and in complex with unlabeled cyt c (magenta). The FBD : cyt c molar ratio was 1:5 in 100 mM potassium phosphate buffer at pH 7.4 containing 5 % (w/v) glycerol. B, expansion of the crowded region of the spectra (purple rectangle). C, expansion to show the chemical shift perturbations of certain residues (yellow rectangle).

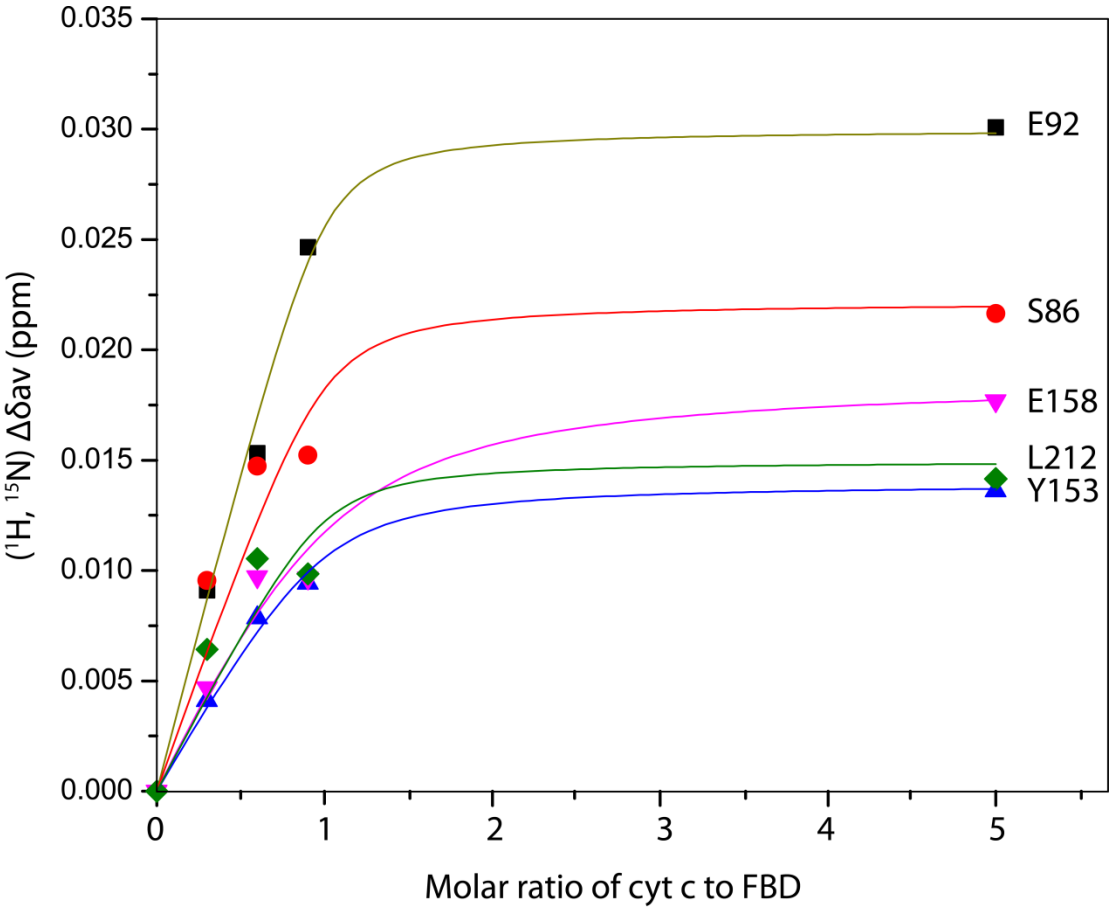

Figure 2.5 Titration of ^{15}N-labeled FMN binding domain with cyt c. Changes in weighted average of chemical shifts ($\Delta\delta_{ave}$) as a function of the molar ratio of cyt c to FBD for backbone amides of S86, E92, Y153, E158 and L212. Curves are fitted using the equation 1 under the assumption of 1:1 complex formation, with an average K_d of 0.024 ± 0.012 mM.

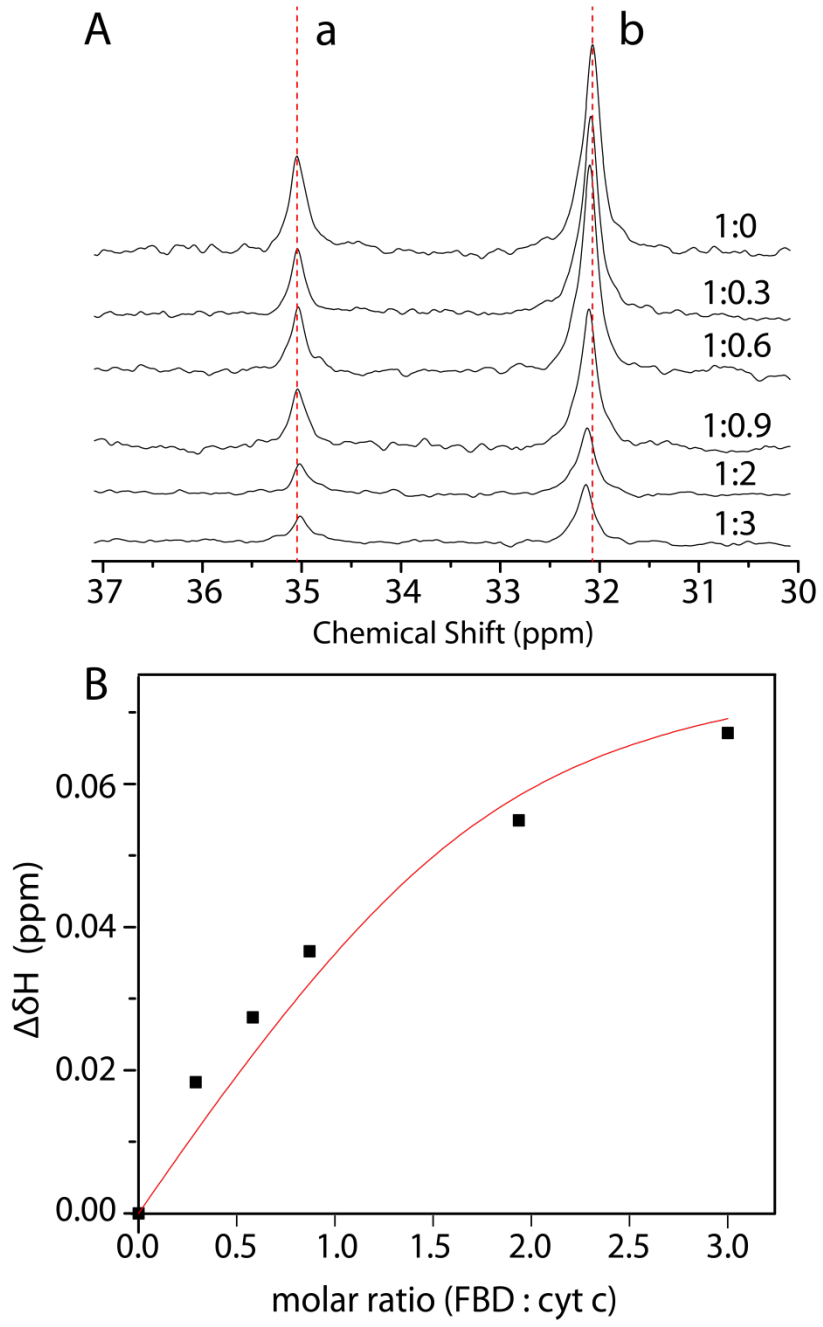

Figure 2.6 Titration of cyt c by the FMN binding domain. A, 1D ^{1}H spectra for the titration of cyt c by the FMN binding domain with an increasing ratio of cyt c and the FMN binding domain. Peaks at 35.1 (a) and 32.1 ppm (b) are assigned to heme methyl protons. Both peaks show intensity decease with increasing amount of FBD, while peak b shows chemical shift perturbation in addition. B, Titration curves for the ^{1}H chemical shift of peak b as a function of the molar ratio of FBD : cyt c. The best fit corresponds to a K_d of 0.046 mM assuming 1:1 complex formation.

superposition of the HSQC spectra of free FBD (green) and FBD in complex with cyt c (red) (the molar ratio of FBD : cyt c is 1:5). Chemical shift changes were observed for specific residues of FBD upon complex formation with cyt c, clearly shown in Figure 2.4C. Most of the chemical shift perturbations occur in a saturable manner throughout the titration. Figure 2.5 shows perturbations of averaged ^{1}H, ^{15}N chemical shift for selected backbone amides as a function of increasing molar ratio of cyt c to FBD. Assuming complex formation of 1:1 stoichiometry, the dissociation constant of FBD and cyt c was calculated from the chemical shift-monitored titration curves, which turned out to be 0.024 ± 0.012 mM, coincide with the apparent K_d (0.021 mM) measured by rapid-mixing stopped-flow spectroscopy (11). The uncertainty represents the standard deviation of K_d values among the examined five residues.

Titration of FBD to cyt c was also performed by monitoring ^{1}H chemical shift of cyt c. The low field resonances at 35.1 and 32.2 ppm are assigned to heme 8-methyl and 3-methyl protons, respectively (35) (Figure 2.6A). Upon titration of FBD, both the heme methyl peaks showed line broadening while the heme 3-methyl resonance shifts to downfield position (Figure 2.6A). The chemical shift perturbation of heme 3-methyl resonance as a function of the molar ratio of FBD and cyt c was also fitted to calculate the K_d value, which turned out to be 0.046 mM (Figure 2.6B). The two sets of measurements confirm that the dissociation constant of the two proteins lies at the range of $10^{-5} \sim 10^{-4}$ M, which verifies fast exchange between the bound and unbound states. The measured K_d value between FBD and cyt c is similar to that of human CPR-cyt c complex (3.7×10^{-5} M) (11) and flavodoxin-cyt c complex (10^{-5} M) (35).

2.4.4 Chemical shift mapping of binding interface on FBD

Chemical shift perturbation observed for the backbone amides of FBD upon complex formation with cyt c is depicted in Figure 2.7. Upon interacting with molar equivalent of cyt c, the residues of FBD (residue 64-239) have an average chemical shift change of 0.007 ppm with a standard deviation of 0.008 ppm. The overall relatively small magnitude of chemical shift perturbation may be attributed to: (1) low binding affinity between FBD and cyt c; (2) formation of “encounter complexes” as have been previously reported for other electron transfer

complexes, which is characterized by an ensemble of various orientations in the complex formation leading to averaging effect of chemical shift perturbations (20, 21, 36, 37).

Distribution of chemical shift perturbations was mapped onto the structure of FBD (Figure 2.8) according to the color scale in Figure 2.7. The structure of FBD (PDB code 1AMO) is composed of five strands of parallel β sheets flanked by six α helices – a typical wound α-β-α folding pattern – as shown in Figure 2.8A. The FMN cofactor locates between the loops at the C-terminus of the β sheets with its isoalloxazine ring sandwiched between Tyr-140 and Tyr-178. Among the solvent accessible residues, those whose chemical shift perturbations are above the average value (Figure 2.8B-C, orange and red) were found to mainly locate surrounding the solvent exposable edge of the FMN cofactor, which is the putative binding interface on FBD for efficient electron transfer. These residues (Gln-87, Thr-88, Thr-90, Glu-92, Tyr-140, Asn-175, and Leu-212) are mostly neutral, and their chemical shift perturbations are likely due to hydrogen bonding and van der Waals interaction with cyt c. There are other solvent exposable residues with modest chemical shift perturbations distributed around the surface of FBD distant from the cofactor, most of which are charged residues including Lys-72, Glu-116, Arg-104, Lys-176, Asp-207 and Glu-221.The dispersed distribution of chemical shift mapping (Figure 2.8) is another sign of the formation of a dynamic complex between the two proteins. This attributes to the fact that FBD is rich in negatively charged residues not only localized in close proximity of the FMN cofactor but widely spread out on the surface of FBD. Long-range electrostatic interaction between these negatively charged regions on FBD and the positively charged cyt c directs collisions on different parts of FBD, leading to small-scale chemical shift changes over a large surface area. Despite the variety of orientations that the two proteins may sample during complex formation, electron transfer still occurs at a decent rate according to the kinetic results. This might attribute to the fact that the two proteins are both small in size and their cofactors are both located close to the protein surface.

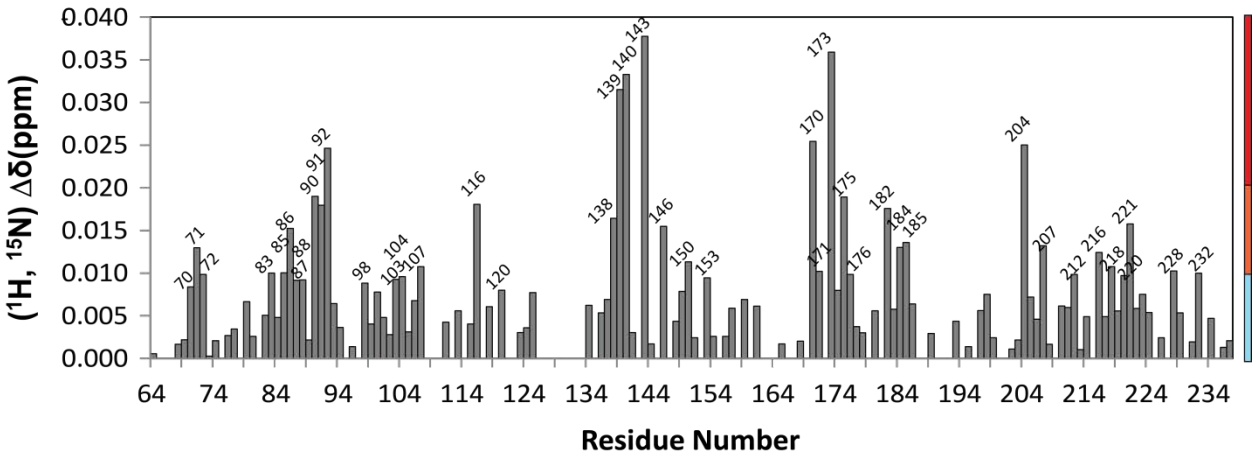

Figure 2.7 Chemical shift perturbation analysis. A histogram presenting the average amide chemical shift of FBD upon complex formation with cyt c. The molar ratio of FBD and cyt c is 1:1. The chemical shift perturbation is categorized as high (red), medium (orange) and not significant (cyan) presented by the vertical color strips and mapped onto the structure of FBD in Figure 8.

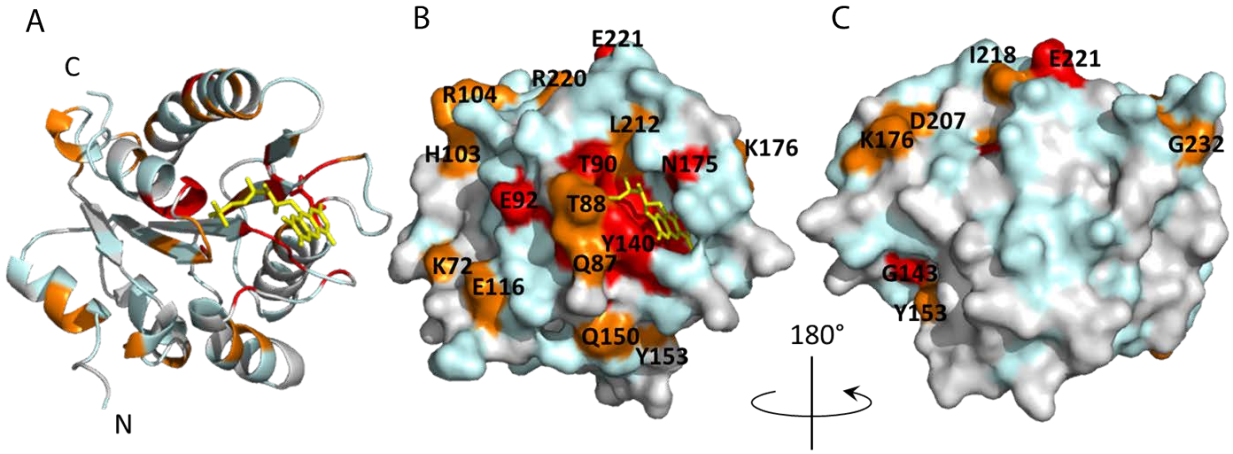

Figure 2.8 Chemical shift mapping of FBD upon complex formation with cyt c. A, cartoon representation of the FBD. Residues are colored according to the amplitudes of amide chemical shift changes on binding cyt c, following the color codes in Figure 7. Red, orange and cyan represent residues with high, medium and not significant chemical shift perturbations, respectively. Overlapped and unassigned residues are colored gray. B, surface representation of the panel A. C, A 180° rotation view of panel B.

2.4.5 Structural model of FBD-cyt c complex

A structural model of FBD-cyt c complex was generated using a data-driven docking program HADDOCK (High Ambiguity Driven biomolecular DOCKing) (30). The FMN binding domain of a crystal structure of CPR (PDB code 1AMO) and a solution NMR structure of the horse heart cyt c (PDB code 1AKK) were used as the starting structures in HADDOCK calculations. The docking was driven under defined intermolecular ambiguous restraints (supplemental Table 1), including active and passive residues with >40% solvent-accessibility from both proteins. As shown in Figure 2.8, solvent-accessible residues on FBD which show significant chemical shift perturbation upon complex formation are selected as the active ambiguous residues from FBD. Passive restraints were defined by the solvent-accessible residues flanking the active ones. Active ambiguous restraints on cyt c were selected to be the common residues in the binding interfaces of several electron-transfer complexes involving cyt c (21, 22, 38). The restraints were filtered once by carefully examining the results of the docking. Active restraints which created violations in more than 45 out of the 50 final structures were removed. The refined restraint table was shown in Table 2.2 and applied in the docking program using the same protocol.

Two clusters of complex structures were identified from the 50 lowest energy structures, titled cluster I (major) and cluster II (minor). The energy statistics of the clusters are summarized in Table 2.3. The average intermolecular energies of the two clusters are -514.7 and -342.4 kcal/mol, of which the major contribution comes from electrostatic energies. This implies the significance of electrostatic interaction in the complex formation between FBD and cyt c. Two lowest energy structures from each cluster were shown in cartoon and surface representations (Figure 2.9), which demonstrates two unique but overlapping interfaces on both FBD and cyt c. Residues involved in the binding interface largely surround the heme of cyt c and the cofactor FMN of FBD, albeit variations in specific residues involved. In cluster I, the interface is mainly composed of β1-α3 coil, N-terminus of of α3, N-terminus of β4-α6 coil, β5-α7 coil and the N-terminus of α7 of FBD and α1 helix, α3-α4 coil, α4-α5 coil of cyt c. In cluster II, β1-α3 coil, β3-α5 coil, β4-α6 coil and N-terminus of β5-α7 coil of FBD and C-terminus of α1 helix, N-terminus of α1-α2 coil and α4-α5 coil of cyt c are predominantly involved in the binding interface. The interfacial residues which are common in the two clusters are Gln-87, Thr-88, Thr-90, Tyr-140,

Asn-175, Thr-177, Tyr-178, Asp-208 of FBD and Ile-9, Gln-12, Lys-13, Ile-81, Ala-83, Gly-84, Ile-85, Lys-86 of cyt c, which are tightly surrounding the redox centers of the two proteins. In the two clusters, the dihedral angles between the heme plane and the isoalloxazine ring of FMN are 60° and 110°. The shortest distances between the edges of heme and FMN are 6.1 and 1.9 Å in cluster I and cluster II respectively, which is well within the 14.0 Å limit predicted for efficient electron transfer (39).

Table 2.2 List of restraints used in HADDOCK

	FBD	cyt c
Ambiguous restraints, active	Q87, T88, T90, E92, Y140, N175, L212, R220	Q12, K13, Q16, C17, I81, A83, I85
Ambiguous restraints, passive	G141, G143, P145, D147, T177, Y178, D208, D209, D215, I217	D2, K5, K8, V11, K79, K86, K87, K88, T89

Table 2.3 Statistic analysis of the two lowest-energy clusters of the FBD-cyt c complex generated from HADDOCK

Parameters	Cluster I	Cluster II
Number of structures	35	7
Backbone r.m.s.d. (Å)[a]	2.93 ± 1.98	1.46 ± 0.77
Total intermolecular energy (kcal/mol)	-514.7 ± 63.8	-342.4 ± 60.1
van der Waals energy (kcal/mol)	-35.8 ± 7.6	-48.8 ± 6.3
Electrostatic energy (kcal/mol)	-478.8 ± 67.0	-293.6 ± 65.1
Buried surface area ($Å^2$)	1299.2 ± 78.2	1312.5 ± 48.7

[a] Average r.m.s.d and standard deviation compared with the lowest energy structure within the cluster.

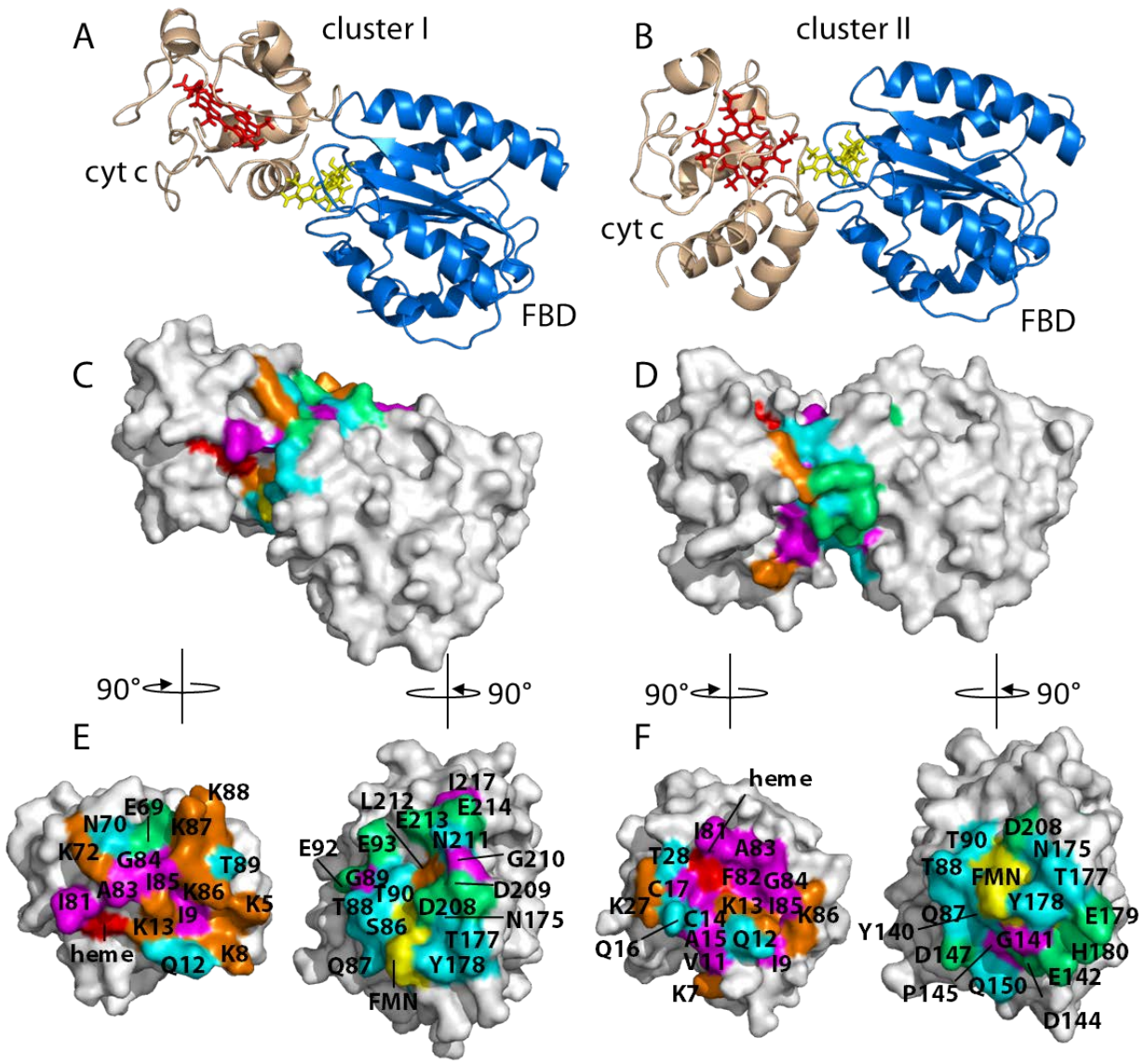

Figure 2.9 Structure models of the FBD-cyt c complex. A-B, two clusters of the lowest-energy structures of the FBD-cyt c complex generated from HADDOCK driven by NMR restraints. PDB 1AMO (cite) and PDB 1AKK (cite) are used as the initial structures of FBD and cyt c in the docking. Heme molecule and cofactor FMN are presented by red and yellow sticks, respectively. C-D, surface representation of the two complexes in panel A-B. Interfacial residues involved in protein-protein contacts in the complex models are highlighted and color-coded based on properties of the amino acids. Polar neutral, nonpolar, positive and negative residues are colored cyan, magenta, orange and green, respectively. Heme and cofactor FMN are colored red and yellow, respectively. E-F, from panel C-D, FBD and cyt c are rotated around their vertical axes by 90° as indicated, in order to display the binding interfaces. Residues are identified with the single-letter amino acid code.

Table 2.4 Summary of hydrogen bonds/salt bridges in the FBD-cyt c binding interface

Cluster I		Cluster II	
FBD	cyt c	FBD	cyt c
Gln-87	Gln-12	Gln-87	Ile-85
Glu-92	Lys-5	Glu-142	Gln-16
Glu-93	Lys-86	Asp-147	Lys-13
Glu-93	Thr-89	Glu-179	Lys-27
Asp-208	Lys-13	His-180	Gln-16
Asp-209	Lys-72		
Glu-213	Lys-87		
Glu-214	Lys-87		

2.5 Discussion

2.5.1 Electron transfer between FBD and cyt c in comparison with CPR

Our study reveals that the isolated FMN binding domain both in its one electron- and two electron-reduced redox states can reduce cyt c but at distinct rates (Table 2.1). The observation that one electron-reduced FMN binding domain is capable of reducing oxidized cyt c has been previously reported (11), even though the approach in the reported study of using NADPH to reduce the isolated FMN binding domain (11) cannot be achieved under our current experimental conditions. And the argument that no electron transfer occurs between two electron-reduced CPR and cyt c when CPR is reduced by dithionite (11) was proved otherwise in the present study. Considering the large redox potential differences between the semiquinone FBD (-68 mV) (40) and oxidized cyt c (250 mV) (41), the slow electron transfer rate between the two proteins (K_{obs} = 0.0227 s^{-1}) implies that the process may be gated. One hypothesis is that hydrogen bonds between the semiquinone FMN cofactor and the FMN binding loop Gly-141-Glu-142-Gly-143 effectively stabilizes the semiquinone form of the FBD, rendering high activation energy for the

electron transfer. Previous studies have shown that mutation of the Gly-61 in *D. vulgaris* flavodoxin, which is homologous to Gly-141 in CPR, destabilizes the semiquinone state and causes shifts of the midpoint potentials (42). Deletion of Gly-141 and/or Gly-143 leads to red semiquinone instead of blue semiquinone formation in one electron-reduced CPR and significantly alters the midpoint potentials of each redox state (data not published).

A comparison of cyt c reduction by wild-type CPR and the isolated FMN binding domain (Table 2.1) reveals that FBD reduces cyt c in a rate significantly faster than the wild-type CPR, both in its one electron- and two electron-reduce states. Since the midpoint redox potentials of the isolated domain has been proved to be near identical to those of the intact CPR (11, 32) and the dissociation constants of CPR-cytc and FBD-cyt c are also largely the same, the contrast in the reaction rates probably attributes to the distinct accessibility of the FMN cofactor to cyt c. In the isolated FMN binding domain the cofactor FMN is partially exposed to the solvent (Figure 2.8), while in the resting state CPR exists in a predominant "closed conformation" in which the FMN cofactor is in close proximity with FAD but buried in the interface between the FMN and FAD binding domains making it unfavorable to access cyt c (6, 43). A movement of the FMN binding domain relative to the rest of the CPR molecule is essential for electron transfer from CPR to its redox partners, the process of which might be regulated by nucleotide binding, redox states of the cofactors, solvent condition, *et cetera* (44-46). Electron transfer between one-electron reduced CPR and cyt c is probably prohibited due to the "lock-up" of the FMN binding domain, while cyt c reduction by two electron-reduced CPR is likely to be gated by domain movement of the protein.

2.5.2 Complex formation between FBD and cyt c

It has been proposed that weak and transient complexes are commonly formed between electron transfer proteins to ensure high turnover rates (47). The relative orientation of two proteins in the complex can range from well-fined to highly dynamic (37).The latter is featured by an ensemble of various orientations interchanging among themselves in a fast exchange timescale. This results in overall averaged intermolecular effects observed in NMR experiments (*e.g.* chemical shift perturbations, Nuclear Overhauser Effects, Paramagnetic Enhancement Effects) in the complex and extensive binding sites. As shown in Figure 2.7 and Figure 2.8, the relative small scale of overall chemical shift perturbations and distribution of the affected

residues distant from the FMN cofactor suggests the existence of an ensemble of dynamic complexes. Such type of complexes were observed in a number of other electron transfer proteins, including adrenodoxin-cyt c complex (37), myoglobin-cyt b5 complex (20), cyt c-cyt b5 complex (21, 36) and plastocyanin-cyt f complex (48). They are usually formed between two proteins rich in complimentary charges and dominantly driven by long-range electrostatic interactions (47). However, most of the orientations involved in dynamic complexes are not optimized to facilitate interprotein electron transfer. Instead, one or more specific complexes need to form, which are usually characterized with a higher affinity of the two proteins and sufficient proximity of the redox centers, for efficient electron transfer. These complexes are represented by the structural models obtained from HADDOCK.

The structure model of FBD-cyt c complex generated by HADDOCK reveals two probable orientations of complex formation between FBD and cyt c. The orientations of cyt c are almost perpendicular between the two structures with respect to FBD, resulting in overlapping but not identical interfaces. It is evident from the comparison that there is a higher proportion of electrostatic interaction involved in the binding interface of cluster I, while in cluster II hydrophobic interaction and/or van der Waals contact are predominant in the interface. A close look at the interfaces suggests several pairs of hydrogen bond and/or salt bridge formation (Table 4), which attribute to the stability of the complex and aid in electron transfer. In the previous studies, it was reported that mutations on the acidic cluster composed of Glu-213, Glu-214, Asp-215 leads to significant decrease in catalytic activity of both wild-type CRP and isolated FMN binding domain on cyt c reduction (13, 17). In the cluster I of our structural models, we observe salt bridge formation between Glu-213 O^{ε} of FBD and Lys-87 N of cyt c as well as Glu-214 O^{ε} of FBD and Lys-87 N^{ζ} of cyt c, which probably plays a vital role in the binding and electron transfer between the two redox partners. Salt bridges can also form between Asp-208 O^{δ} of FBD and Lys-13 N^{ζ} of cyt c as well as Asp-209 O^{δ} of FBD and Lys-72 N^{ζ} of cyt c, consistent with the previous chemical crosslinking study (15) and prediction from putative docking (6). However, as reported, single mutation of Asp-208 or Asp-209 does not affect the cyt c reductase activity significantly (13, 17), implying that these salt bridges might not be as essential for the stability of the complex as those formed on Glu-213 and Glu-214. Single mutation on other negatively charged residues of FBD including Glu-142, Asp-133, Asp-147, Asp-207 and Asp215 also leads

to insignificant effect on cyt c reduction (13), which might be due to the abundant/excess electrostatic interactions between the two proteins. In addition to the distinguished salt bridges and hydrogen bonds, the complex is also stabilized by hydrophobic and van de Waals interactions (supplemental Table 2). In cluster II, only two salt bridges are observed – between Glu-147 O^{δ} of FBD and Lys-13 N^{ζ} of cyt c and between Glu-179 O^{ε} of FBD and Lys-27 N^{ζ} of cyt c, although single mutation of Glu-147 does not seem to affect the catalytic activity for cyt c reduction significantly (13).

Cyt c has been widely used as a model redox partner of CPR. The binding interface of CPR in the CPR-cyt c complex has been shown to be overlapping but somehow different from that between CPR and its physiological redox partner cytochrome P450 (12, 13, 15, 17, 19). Site-directed mutagenesis studies reveal that mutation of Asp-208 of CPR significantly affects substrate turnover by cyt P450 (13, 17), the residue of which also turned out to be in the FBD-cyt c interface in the structural model. Residues 110-119, 118-130 of CPR are suggested to be involved in the interaction with cyt P450 by antipeptide antibody studies (19), while none of the residues are observed in the binding interface between FBD and cyt c. Mutating Asp-113, Glu-115, Glu-116 in CPR was reported to influence the catalytic activity towards both cyt c and P450 and suggested to alter electron transfer pathways between CPR and its redox partners. In our structural model, these residues are not involved in the binding interface between FBD and cyt c. However, Glu-116 shows significant chemical shift perturbations during titration of cyt c (Figure 2.8) implying that it may be involved in the formation of nonspecific dynamic complexes which do not facilitate electron transfer. The proposed model allows us to draw comparison with CPR-P450 complex and other electron transfer complexes involving CPR.

In order to elucidate which residues are crucial for electron transfer, we use the program HARLEM (49) to predict the shortest electron transfer pathways between the two proteins. In cluster I, the predicted coupling pathway initiates at the C8M atom of the FMN cofactor, and continues via the C^{α}, C(O) and O of Lys-13 of cyt c consecutively until the conjugated heme ring (Figure 2.10A). The pathway suggests the importance of Lys-13 in mediating the electron transfer process. Lys-13 of cyt c locates in close proximity of the heme and forms a salt bridge with Asp-208 of FBD in the complex (cluster I). This residue is mostly conserved in cyt c among animals and plants, and has been observed to involve in the binding interfaces between cyt c and

other redox proteins including L-galactono-1,4-lactone dehydrogenase in plant mitochondria (38), cytochrome b_5 (21) and cytochrome c oxidase (50). In cluster II, due to the short edge-to-edge distance between FMN and heme (1.9 Å), electron transfer is predicted to occur directly from C7M atom of FMN to the heme (Figure 2.10B).

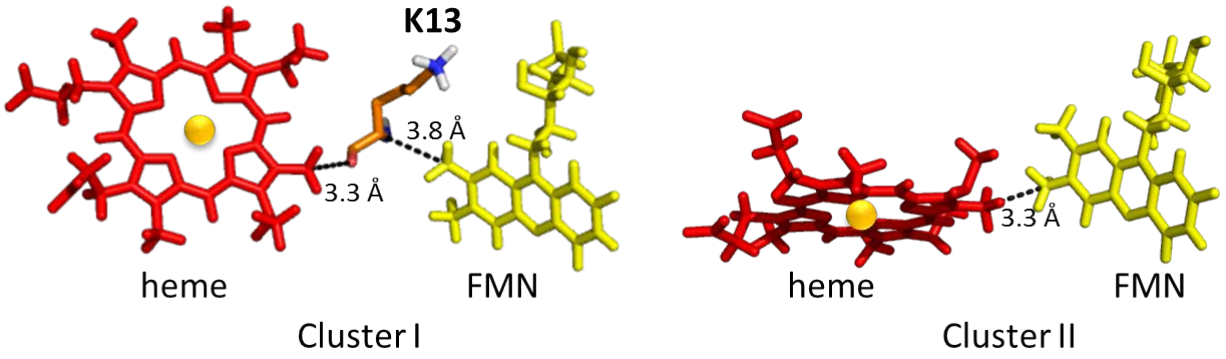

Figure 2.10 Electron transfer pathway predicted using HARLEM. Black dotted lines show the predicted electron transfer pathway for cluster I and II.

2.6 Conclusion

In summary, we characterized the kinetics of electron transfer from FBD to cyt c by stopped-flow spectroscopy and investigated the complex formation using solution NMR spectroscopy in conjunction with HADDOCK program. A comparison of cyt c reduction by FBD and wild-type CPR supports the key role of conformational gating on electron transfer from CPR to its redox partners. Our NMR results not only revealed the formation of dynamic complex between FBD and cyt c on a fast exchange time scale (K_d = 0.024 mM), but also identified the specific residues of FBD involved in the binding interface with cyt c. A structure model of FBD-cyt c complex was generated using HADDOCK, unveiling two probable orientations of complex formation. The proposed model allows us to identify the potential interactions on the interface and to propose electron transfer pathway from FBD to cyt c. Combined kinetic and structural information presented in this study provides insights into the interaction between CPR and cyt c,

and will facilitate our further understanding of the mechanistic details on how electron transfer occurs from CPR to its redox partners.

2.7 References

1. Paine, M. J., Scrutton, N. S., Munro, A. W., Gutierrez, A., Roberts, G. C., and Wolf, C., R. (2005) in *Cytochrome P450* (Ortiz de Montellano, P. R., ed) 3rd Ed., pp. 115-148, Kluwer Academic/Plenum Publishers, New York.

2. Schacter, B. A., Nelson, E. B., Marver, H. S., and Masters, B. S. (1972) Immunochemical evidence for an association of heme oxygenase with the microsomal electron transport system, *J Biol Chem 247*, 3601-3607.

3. Oshino, N., Imai, Y., and Sato, R. (1971) A function of cytochrome b5 in fatty acid desaturation by rat liver microsomes, *J Biochem 69*, 155-167.

4. Williams, C. H., Jr., and Kamin, H. (1962) Microsomal triphosphopyridine nucleotide-cytochrome c reductase of liver, *J Biol Chem 237*, 587-595.

5. Bachur, N. R., Gordon, S. L., Gee, M. V., and Kon, H. (1979) NADPH cytochrome P-450 reductase activation of quinone anticancer agents to free radicals, *Proc Natl Acad Sci U S A 76*, 954-957.

6. Wang, M., Roberts, D. L., Paschke, R., Shea, T. M., Masters, B. S., and Kim, J. J. (1997) Three-dimensional structure of NADPH-cytochrome P450 reductase: prototype for FMN- and FAD-containing enzymes, *Proc Natl Acad Sci U S A 94*, 8411-8416.

7. Horecker, B. L. (1950) TRIPHOSPHOPYRIDINE NUCLEOTIDE-CYTOCHROME-C REDUCTASE IN LIVER, *J. Biol. Chem. 183*, 593-605.

8. Lu, A. Y., and Coon, M. J. (1968) Role of hemoprotein P-450 in fatty acid omega-hydroxylation in a soluble enzyme system from liver microsomes, *J Biol Chem 243*, 1331-1332.

9. Sem, D. S., and Kasper, C. B. (1994) Kinetic mechanism for the model reaction of NADPH-cytochrome P450 oxidoreductase with cytochrome c, *Biochemistry 33*, 12012-12021.

10. Xia, C., Hamdane, D., Shen, A. L., Choi, V., Kasper, C. B., Pearl, N. M., Zhang, H., Im, S. C., Waskell, L., and Kim, J. J. (2011) Conformational changes of NADPH-cytochrome P450 oxidoreductase are essential for catalysis and cofactor binding, *J Biol Chem 286*, 16246-16260.

11. Grunau, A., Paine, M. J., Ladbury, J. E., and Gutierrez, A. (2006) Global effects of the energetics of coenzyme binding: NADPH controls the protein interaction properties of human cytochrome P450 reductase, *Biochemistry 45*, 1421-1434.

12. Jang, H. H., Jamakhandi, A. P., Sullivan, S. Z., Yun, C. H., Hollenberg, P. F., and Miller, G. P. (2010) Beta sheet 2-alpha helix C loop of cytochrome P450 reductase serves as a docking site for redox partners, *Biochim Biophys Acta 1804*, 1285-1293.

13. Zhao, Q., Modi, S., Smith, G., Paine, M., McDonagh, P. D., Wolf, C. R., Tew, D., Lian, L. Y., Roberts, G. C., and Driessen, H. P. (1999) Crystal structure of the FMN-binding domain of human cytochrome P450 reductase at 1.93 A resolution, *Protein Sci 8*, 298-306.

14. Murataliev, M. B., Feyereisen, R., and Walker, F. A. (2004) Electron transfer by diflavin reductases, *Biochim Biophys Acta 1698*, 1-26.

15. Nisimoto, Y. (1986) Localization of cytochrome c-binding domain on NADPH-cytochrome P-450 reductase, *J Biol Chem 261*, 14232-14239.

16. Nadler, S. G., and Strobel, H. W. (1988) Role of electrostatic interactions in the reaction of NADPH-cytochrome P-450 reductase with cytochromes P-450, *Arch Biochem Biophys 261*, 418-429.

17. Kasper, C. B. (1995) Role of Acidic Residues in the Interaction of NADPH-Cytochrome P450 Oxidoreductase with Cytochrome P450 and Cytochrome c, *J Biol Chem 270*, 27475-27480.

18. Tamburini, P. P., and Schenkman, J. B. (1986) Differences in the mechanism of functional interaction between NADPH-cytochrome P-450 reductase and its redox partners, *Mol Pharmacol 30*, 178-185.

19. Shen, S., and Strobel, H. W. (1994) Probing the putative cytochrome P450- and cytochrome c-binding sites on NADPH-cytochrome P450 reductase by anti-peptide antibodies, *Biochemistry 33*, 8807-8812.

20. Worrall, J. A., Liu, Y., Crowley, P. B., Nocek, J. M., Hoffman, B. M., and Ubbink, M. (2002) Myoglobin and cytochrome b5: a nuclear magnetic resonance study of a highly dynamic protein complex, *Biochemistry 41*, 11721-11730.

21. Deep, S., Im, S. C., Zuiderweg, E. R., and Waskell, L. (2005) Characterization and calculation of a cytochrome c-cytochrome b5 complex using NMR data, *Biochemistry 44*, 10654-10668.

22. Volkov, A. N., Worrall, J. A., Holtzmann, E., and Ubbink, M. (2006) Solution structure and dynamics of the complex between cytochrome c and cytochrome c peroxidase determined by paramagnetic NMR, *Proc Natl Acad Sci U S A 103*, 18945-18950.

23. Hiruma, Y., Hass, M. A., Kikui, Y., Liu, W. M., Olmez, B., Skinner, S. P., Blok, A., Kloosterman, A., Koteishi, H., Lohr, F., Schwalbe, H., Nojiri, M., and Ubbink, M. (2013) The structure of the cytochrome p450cam-putidaredoxin complex determined by paramagnetic NMR spectroscopy and crystallography, *J Mol Biol 425*, 4353-4365.

24. Gutierrez, A., Doehr, O., Paine, M., Wolf, C. R., Scrutton, N. S., and Roberts, G. C. (2000) Trp-676 facilitates nicotinamide coenzyme exchange in the reductive half-reaction of human cytochrome

P450 reductase: properties of the soluble W676H and W676A mutant reductases, *Biochemistry 39*, 15990-15999.

25. Gutierrez, A., Munro, A. W., Grunau, A., Wolf, C. R., Scrutton, N. S., and Roberts, G. C. (2003) Interflavin electron transfer in human cytochrome P450 reductase is enhanced by coenzyme binding. Relaxation kinetic studies with coenzyme analogues, *Eur J Biochem 270*, 2612-2621.

26. Bridges, A., Gruenke, L., Chang, Y. T., Vakser, I. A., Loew, G., and Waskell, L. (1998) Identification of the binding site on cytochrome P450 2B4 for cytochrome b5 and cytochrome P450 reductase, *J Biol Chem 273*, 17036-17049.

27. Gutierrez, A., Lian, L. Y., Wolf, C. R., Scrutton, N. S., and Roberts, G. C. (2001) Stopped-flow kinetic studies of flavin reduction in human cytochrome P450 reductase and its component domains, *Biochemistry 40*, 1964-1975.

28. Gutierrez, A., Paine, M., Wolf, C. R., Scrutton, N. S., and Roberts, G. C. (2002) Relaxation kinetics of cytochrome P450 reductase: internal electron transfer is limited by conformational change and regulated by coenzyme binding, *Biochemistry 41*, 4626-4637.

29. Kneller, D. G., and Kuntz, I. D. (1993) UCSF SPARKY - AN NMR DISPLAY, ANNOTATION AND ASSIGNMENT TOOL, *J. Cell. Biochem.*, 254-254.

30. de Vries, S. J., van Dijk, A. D., Krzeminski, M., van Dijk, M., Thureau, A., Hsu, V., Wassenaar, T., and Bonvin, A. M. (2007) HADDOCK versus HADDOCK: new features and performance of HADDOCK2.0 on the CAPRI targets, *Proteins 69*, 726-733.

31. Schuttelkopf, A. W., and van Aalten, D. M. F. (2004) PRODRG: a tool for high-throughput crystallography of protein-ligand complexes, *Acta Crystallogr. Sect. D-Biol. Crystallogr. 60*, 1355-1363.

32. Munro, A. W., Noble, M. A., Robledo, L., Daff, S. N., and Chapman, S. K. (2001) Determination of the redox properties of human NADPH-cytochrome P450 reductase, *Biochemistry 40*, 1956-1963.

33. Masters, B. S., Kamin, H., Gibson, Q. H., and Williams, C. H., Jr. (1965) Studies on the Mechanism of Microsomal Triphosphopyridine Nucleotide-Cytochrome C Reductase, *J Biol Chem 240*, 921-931.

34. Barsukov, I., Modi, S., Lian, L. Y., Sze, K. H., Paine, M. J., Wolf, C. R., and Roberts, G. C. (1997) 1H, 15N and 13C NMR resonance assignment, secondary structure and global fold of the FMN-binding domain of human cytochrome P450 reductase, *J Biomol NMR 10*, 63-75.

35. Hazzard, J. T., and Tollin, G. (1985) Proton NMR study of the cytochrome c:flavodoxin electron transfer complex, *Biochem Biophys Res Commun 130*, 1281-1286.

36. Shao, W., Im, S. C., Zuiderweg, E. R., and Waskell, L. (2003) Mapping the binding interface of the cytochrome b5-cytochrome c complex by nuclear magnetic resonance, *Biochemistry 42*, 14774-14784.

37. Worrall, J. A., Reinle, W., Bernhardt, R., and Ubbink, M. (2003) Transient protein interactions studied by NMR spectroscopy: the case of cytochrome C and adrenodoxin, *Biochemistry 42*, 7068-7076.

38. Hervas, M., Bashir, Q., Leferink, N. G., Ferreira, P., Moreno-Beltran, B., Westphal, A. H., Diaz-Moreno, I., Medina, M., de la Rosa, M. A., Ubbink, M., Navarro, J. A., and van Berkel, W. J. (2013) Communication between (L)-galactono-1,4-lactone dehydrogenase and cytochrome c, *FEBS J 280*, 1830-1840.

39. Page, C. C., Moser, C. C., and Dutton, P. L. (2003) Mechanism for electron transfer within and between proteins, *Curr Opin Chem Biol 7*, 551-556.

40. Das, A., and Sligar, S. G. (2009) Modulation of the cytochrome P450 reductase redox potential by the phospholipid bilayer, *Biochemistry 48*, 12104-12112.

41. Rodkey, F. L., and Ball, E. G. (1947) Oxidation-reduction potentials of cytochrome c, *Fed Proc 6*, 286.

42. O'Farrell, P. A., Walsh, M. A., McCarthy, A. A., Higgins, T. M., Voordouw, G., and Mayhew, S. G. (1998) Modulation of the redox potentials of FMN in Desulfovibrio vulgaris flavodoxin: thermodynamic properties and crystal structures of glycine-61 mutants, *Biochemistry 37*, 8405-8416.

43. Vincent, B., Morellet, N., Fatemi, F., Aigrain, L., Truan, G., Guittet, E., and Lescop, E. (2012) The closed and compact domain organization of the 70-kDa human cytochrome P450 reductase in its oxidized state as revealed by NMR, *J Mol Biol 420*, 296-309.

44. Wadsater, M., Laursen, T., Singha, A., Hatzakis, N. S., Stamou, D., Barker, R., Mortensen, K., Feidenhans'l, R., Moller, B. L., and Cardenas, M. (2012) Monitoring shifts in the conformation equilibrium of the membrane protein cytochrome P450 reductase (POR) in nanodiscs, *J Biol Chem 287*, 34596-34603.

45. Hay, S., Brenner, S., Khara, B., Quinn, A. M., Rigby, S. E., and Scrutton, N. S. (2010) Nature of the energy landscape for gated electron transfer in a dynamic redox protein, *J Am Chem Soc 132*, 9738-9745.

46. Pudney, C. R., Khara, B., Johannissen, L. O., and Scrutton, N. S. (2011) Coupled motions direct electrons along human microsomal P450 Chains, *PLoS Biol 9*, e1001222.

47. Ubbink, M. (2012) Dynamics in transient complexes of redox proteins, *Biochem Soc Trans 40*, 415-418.

48. Scanu, S., Forster, J., Finiguerra, M. G., Shabestari, M. H., Huber, M., and Ubbink, M. (2012) The complex of cytochrome f and plastocyanin from Nostoc sp. PCC 7119 is highly dynamic, *Chembiochem 13*, 1312-1318.

49. Kurnikov, I. V. (2000) *HARLEM Molecular Modeling Package*, Version 1.0, Department of Chemistry, University of Pittsburgh, Pittsbburgh.

50. Sakamoto, K., Kamiya, M., Imai, M., Shinzawa-Itoh, K., Uchida, T., Kawano, K., Yoshikawa, S., and Ishimori, K. (2011) NMR basis for interprotein electron transfer gating between cytochrome c and cytochrome c oxidase, *Proc Natl Acad Sci U S A 108*, 12271-12276.

CHAPTER 3

Characterization of Electron Transfer and Interaction between the FMN binding domain of Cytochrome P450 Reductase and Cytochrome P450

3.1 Summary

Complex formation and electron transfer from cytochrome P450 reductase to cytochrome P450 is an essential step in cytochrome P450 catalysis, which is responsible for the metabolism of a dazzling array of endogenous and endogenous substrates. Here we report a study of the interaction between cytochrome P450 and the FMN binding domain of cytochrome P450 reductase by solution NMR. NMR titration experiments reveal that binding of the two proteins occurs on a slow-to-intermediate time scale. Chemical shift perturbation and line broadening analysis identifies the epitope on the FMN binding domain recognized by cyt P450. Subsequently, a structural model was generated by HADDOCK (high ambiguity driven biomolecular docking) program based on NMR restraints and previous site-directed mutagenesis studies. The model reveals detail information on the binding interface, including the residues involved in direct binding and intermolecular interactions. Based on the structural model, a potential pathway was predicted involving Met-132 and Arg-133 of cyt P450.

3.2 Introduction

Cytochromes P450 (cyt P450) are a ubiquitous superfamily of oxygenases that are responsible for the metabolism of myriads of endogenous and exogenous compounds, including vitamins, steroids, hormones, environmental toxins and ~70% of marketed drugs. Microsomal P450s catalyze the oxidation of substrates using two electrons from the redox partners: cytochrome P450 reductase and cytochrome b_5 (cyt b_5). While the second electron can be donated by either cytochrome P450 reductase (CPR) or cyt b_5, the first electron has to be delivered to cyt P450 by CPR due to the high redox potential of cyt b_5 ($\cong$ +25 mV) (*1*).

As an indispensable component in the cyt P450 catalysis, CPR is a ~78 kDa microsomal diflavin protein composed of multiple domains: an N-terminal transmembrane segment, the FMN binding domain (FBD), the connecting domain and the FAD/NADPH binding domain (*2*). It shuttles electrons from its physiological reductant NADPH, via the FAD and FMN cofactors, eventually to cyt P450. The FMN binding domain is the ultimate donor of electrons to the acceptor proteins. It is indicated that in its resting state CPR exists predominantly in a "closed and compact" form (*3*) resembling the crystalline structure (*2*), in which the two flavins are in van de Waals contact satisfactory for interflavin electron transfer but the solvent inaccessibility of FMN prevents inter-protein electron transfer to cyt p450. A large-scale domain movement is hypothesized to allow the access of cyt P450 to the reduced FMN cofactor (*3*), the process of which might be regulated by nucleotide binding, redox states of the cofactors, solvent condition, *et cetera* (*4-6*). Although most of the studies have been devoted to understand the role of CPR in cyt P450 catalysis, CPR also donates electrons to heme oxygenase (*7*), cytochrome b5 (*8*), cytochrome c (*9*) as well as therapeutic prodrugs (*10*).

To get an insight into how CPR interacts with and transfer electrons to cyt P450, studies have been carried out using a number of methods including site-direct mutagenesis (*11-14*), enzyme kinetic assays (*15-19*), fluorescence (*20-22*), cross-linking (*23, 24*), FTIR (*25*), AFM (*26*), optical biosensor (*27*), chemical modification (*28-32*), etc. It has been postulated that the electrostatic interactions between the basic proximal surface of cyt P450 and the acidic surface of the FMN binding domain of CPR plays an crucial role in the formation of the cyt P450-CPR complex (*11, 12, 17, 22*). In particular, positively-charged lysine and arginine residues on cyt P450 and negatively-charged aspartic acid and glutamic acid residues on CPR were identified to be potentially located on the cyt P450-CPR binding interface by site-directed mutagenesis studies (*11-13, 33-35*). On the other hand, it is suggested that certain hydrophobic residues on the binding interface, *e.g.* Val-267 and Leu-270 of cyt P450 2B4, also contributes in mediating complex formation (*13*). A structural model of cyt P450-CPR has been proposed based on rigid docking between cyt P450 2B4 with an extended conformation of CPR with shortened linker region (*36*), which gives insight into some intermolecular interactions on the interface. However, to gain a better understanding of the interaction and electron transfer between the two proteins, a high-resolution mapping of the binding interface is essential.

A high-resolution structure of the cyt P450-CPR complex is lacking due to the difficulty in co-crystallizing the two proteins as a complex. This could attribute to either the nature of the transient complex or the conformational rearrangement in CPR required for interacting with cyt P450. Solution NMR has developed into a powerful tool for high-resolution mapping of protein-protein interactions. In this study, we investigate the interaction between cyt P450 2B4 and the FMN binding domain of CPR, using solution NMR techniques. NMR titration experiments reveal that binding of the two proteins occurs on a slow-to-intermediate time scale. The results of chemical shift perturbation and line broadening analysis indicate the primary binding site of cyt P450 on FBD surrounding the solvent-exposed edge of the FMN cofactor. A structural model was generated by HADDOCK using the NMR data and previously published site-directed mutagenesis studies. It provides detailed information of the cyt P450-FBD binding interface and intermolecular interactions. Based on the structural model, a potential electron pathway was predicted involving Met-132 and Arg-133 of cyt P450.

3.3 Materials and Methods

3.3.1 Materials

E. coli C41 cells for protein overexpression were purchased from Lucigen (Middleton, MI). Yeast extract, tryptone for unlabeled growth media were purchased from Sigma-Aldrich. [^{15}N]ammonium chloride for M9 medium and D_2O was purchased from Cambridge Isotope Laboratories (Andover, MA). Resins, buffer components, and all the chemicals were purchased from Sigma-Aldrich. Glycerol used in NMR experiments was purchased from Roche Applied Science.

3.3.2 Expression and purification of proteins

Uniformly ^{15}N-labeled FMN binding domain of CPR (residue 1-239) (FBD), unlabeled cyt P450 2B4 (cyt P450) and wild-type cytochrome P450 reductase (CPR) were expressed from *E. coli* C41 cells and purified as described previously (cite FBD-cyt c)(*11, 37*). Each purified protein exhibited a single band on the SDS-polyacrylamide gel. The concentration of the oxidized FBD and CPR was determined using extinction coefficients of 12.2 $mM^{-1}cm^{-1}$ and 21 $mM^{-1}cm^{-1}$ at 454 nm respectively (*38*). Cyt p450 concentration was quantified as described previously (*39*).

3.3.3 Pre-steady-state kinetics of cyt P450 reduction by FBD/CPR

FBD and CPR were titrated with sodium dithionite solution under anaerobic conditions monitored by UV-Vis spectra. The stock solutions of FBD and CPR were incubated overnight at 4 °C in an anaerobic Belle Technology glove box (Hi-Tech, Salisbury, UK) to remove oxygen. The titrant (sodium dithionite solution) was prepared in the glove box in oxygen-free buffer, and its concentration was calculated using an extinction coefficient of 8 mM^{-1} cm^{-1} at 315 nm. The titrand solution of FBD or CPR contains 10 μM of the protein, 100 mM potassium phosphate buffer, 5 % (w/v) of glycerol, pH 7.4. The titration was carried out in a home-made anaerobic titration apparatus to minimize contamination of oxygen, and monitored by UV-Vis spectrum. FBD/CPR was first titrated to two electron-reduced state. Oxidized cyt P450 (2 μM) was then introduced into the enclosed titration apparatus (isolated from the reductase) anaerobically. The apparatus was filled with carbon monoxide. Reaction was started by rapid mixing of FBD/CPR and cyt P450 solutions and monitored at 450 nm by UV-Vis absorbance. Traces were fitted using a standard single exponential equation (*40*). The buffer contains 100 mM potassium phosphate, 5 % (w/v) glycerol, pH 7.4.

3.3.4 NMR titration experiments

All NMR experiments were performed on a Bruker Avance 900 MHz NMR spectrometer equipped with an x,y,z axis PFG-5mm TCI cryoprobe at 298K. Samples for NMR experiments contain 0.3 mM ^{15}N-labeled FBD in 100 mM potassium phosphate buffer with 5% (w/v) glycerol at pH 7.4. Titration of unlabeled cyt P450 into ^{15}N-labeled FBD was carried out by stepwise addition of cyt P450 solution corresponding to 0.3, 0.5, 0.7 and 0.9 molar equivalents of FBD. 2D ^{15}N TROSY-HSQC spectra were collected at each titration point with 32 scans and 144 t_1 increments. The average amide chemical shift perturbation ($\Delta\delta_{avg}$) was calculated using the equation below

$$\Delta\delta_{\mathrm{avg}} = \sqrt{(\Delta\delta\mathrm{N} \times \frac{SW2}{SW1})^2 + \Delta\delta\mathrm{H}^2}$$

where $\Delta\delta$N and $\Delta\delta$H are changes in chemical shift observed between the bound and unbound states and $SW1$ and $SW2$ represent spectrum width of the first and second dimension respectively. All NMR spectra were processed using TopSpin 2.0 (Bruker). Resonance assignments and data analysis were performed using Sparky (*41*).

3.3.5 Structural modeling of FBD-P450 complex

HADDOCK 2.1 (*42*) program was utilized to calculate the structural models of FBD-P450 complex based on defined ambiguous restraints. Crystal structure of FBD (PDB code 1AMO) and cyt P450 2B4 (PDB code 1SUO/2Q6N) were used as the starting structures. Ligand and topology files were generated from the PRODRG server (*43*). 1000 structures were generated in the rigid body docking step, followed by simulated annealing of the 200 lowest-energy structures from the last step and finally the best 50 structures were selected for solvent refinement in an 8.0 Å shell of TIP3P water molecules. The resulting 50 final structures were analyzed and grouped into clusters based on the backbone r.m.s.d. values. Molecular structures of the complexes were viewed and graphed using PYMOL.

3.4 Results

3.4.1 Kinetics of cyt P450 reduction by FBD

In order to assess catalytic activity of FBD, we investigated the ability of FBD to reduce cyt P450 under single turnover conditions and compared with the wild-type CPR. In this experiment, wild-type CPR and FBD were reduced to two electron-reduced states respectively prior to mixing with cyt P450. Lacking the FAD/NADPH binding domain, the isolated FMN binding domain cannot be reduced by the physiological reductant of CPR—NADPH. Alternatively, sodium dithionite was used to titrate FBD and wild-type CPR to the intended redox states. The reaction is initiated by rapid mixing of the pre-reduced reductase and and cyt P450. Since the binding between the ferrous cyt P450 and carbon monoxide is known to occur very fast (*44-46*), electron transfer from flavin to heme was monitored by the formation of Fe(II)-CO specie at 450 nm. As shown in Figure 3.1, mixing of the pre-reduced wild-type CPR and cyt P450 leads to the reduction of one molar equivalent of cyt P450 with a k_{obs} of 0.06227 ± 0.0002 min^{-1}. This slow reaction rate coincides with the previous observation under similar conditions (*44*), and is significantly lower than what was observed in the reconstituted cyt P450

systems (*44*, *47*). This is due to the fact the rate-limiting step of this reaction is random collision and complex formation between the two proteins driven by diffusion. Electron transfer from FBD to cyt P450 occurs three times faster than wild-type CPR, with a k_{obs} of 0.195 ± 0.002 min^{-1}, implying either a faster diffusion rate due to the relatively smaller size of FBD or more productive complex formation between FBD and cyt P450.

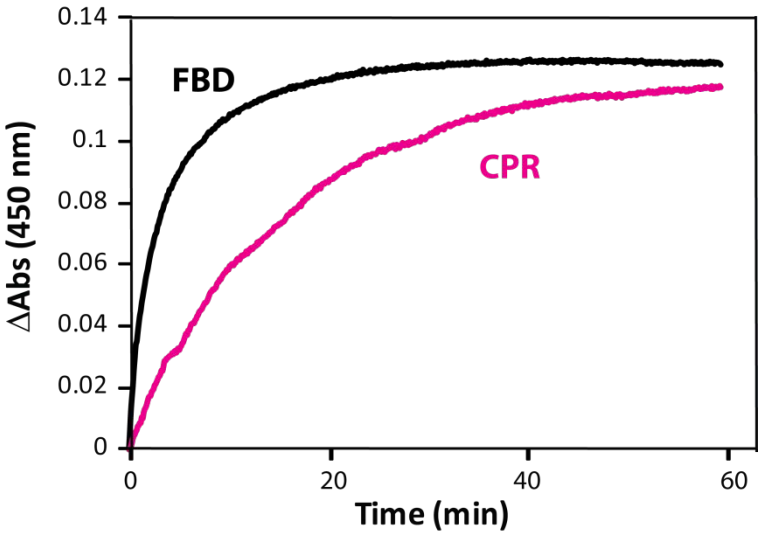

Figure 3.1 Cyt P450 reduction by the FMN binding domain/wild-type CPR. FBD/CPR (10 μM) was reduced to two electron-reduced states by stoichiometric titration with dithionite, and rapidly mixed with cytochrome P450 in the environment of carbon monoxide. The formation of Fe(II)-CO specie in cyt P450 was monitored at 450 nm.

3.4.2 2D NMR titrations of cyt P450 to FBD

The 2D ^{15}N-^{1}H HSQC spectrum and the backbone assignments of the FMN binding domain have been previously reported (*48*) and utilized in the current study. In order to gain insight of the protein-protein interaction between FBD and cyt P450, a series of two-dimensional ^{15}N, ^{1}H-TROSY-HSQC spectra were recorded to monitor the titration of unlabeled cyt P450 to ^{15}N-FBD. The stepwise addition of cyt P450 leads to significant line broadening of most of the residues in the spectrum of FBD (Figure 3.2). After titrating 0.3, 0.5, 0.7, 0.9 molar equivalent of cyt P450, the intensities of the resonances decreased averagely to 48%, 31%, 21%, 18% of those in free FBD, respectively. This suggests an intermediate-to-slow exchange on the NMR time scale between the free FBD and a fast-relaxing FBD-P450 complex (>80 kDa). For each residue, the extent of intensity decease highly depends on its mobility in free FBD and in the FBD-P450 complex. As an example, residues at the N- and C- terminus of soluble domain of FBD (*e.g.* Val-

64, Thr-236, Gly-237) exhibit much smaller decrease in peak intensity than those in the well-structured region (*e.g.* Phe-83, Met-137 located in the middle of beta sheets), as shown in Figure 3.3. Modest chemical shift perturbations were also observed for specific residues and analyzed for the first titration point.

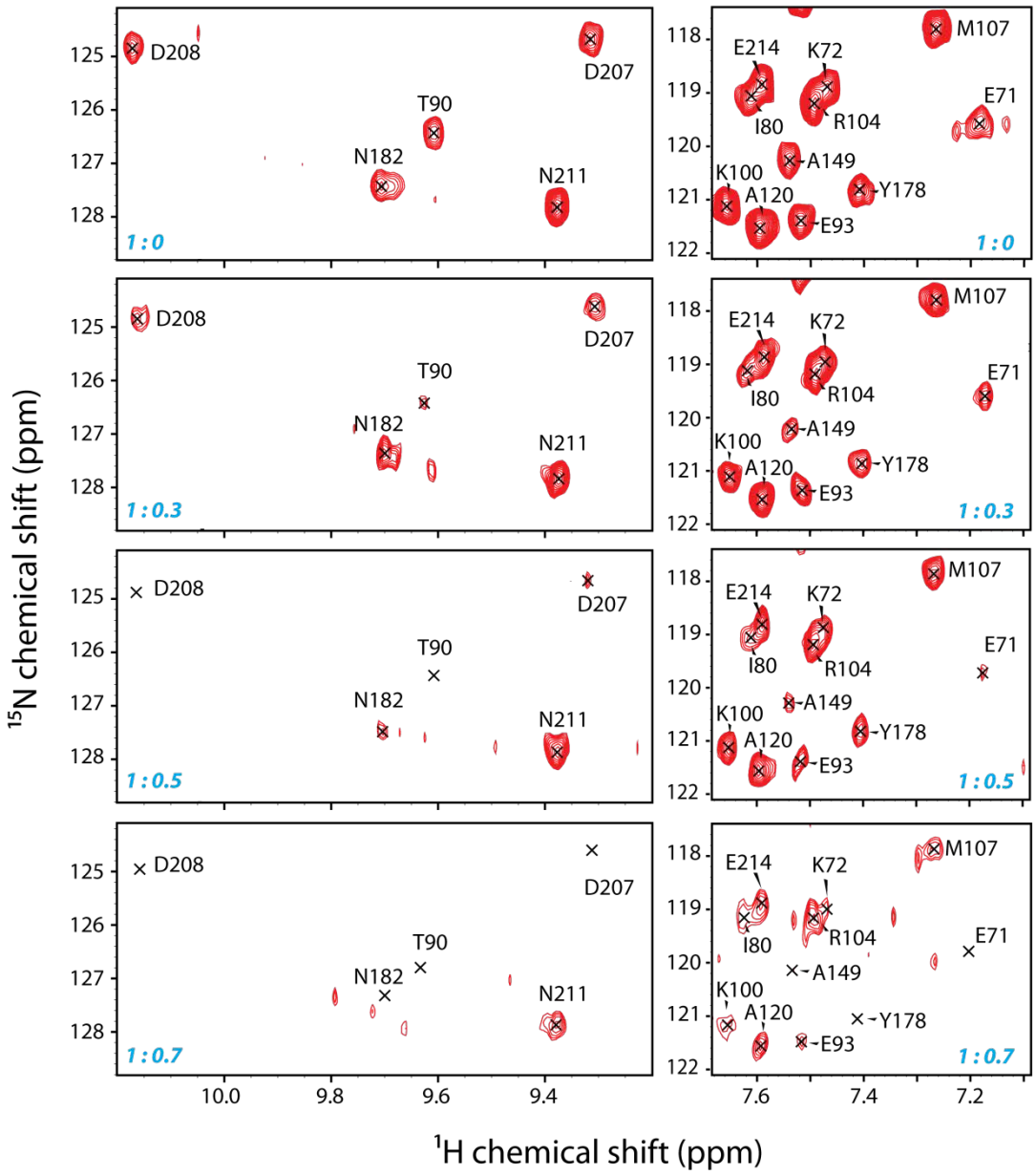

Figure 3.2 ^{15}N,^{1}H-TROSY-HSQC spectra of FBD upon titration of cyt P450. The representative regions of the spectra are shown for free FBD and in the presence of 0.3, 0.5 and 0.7 molar equivalent of cyt P450.

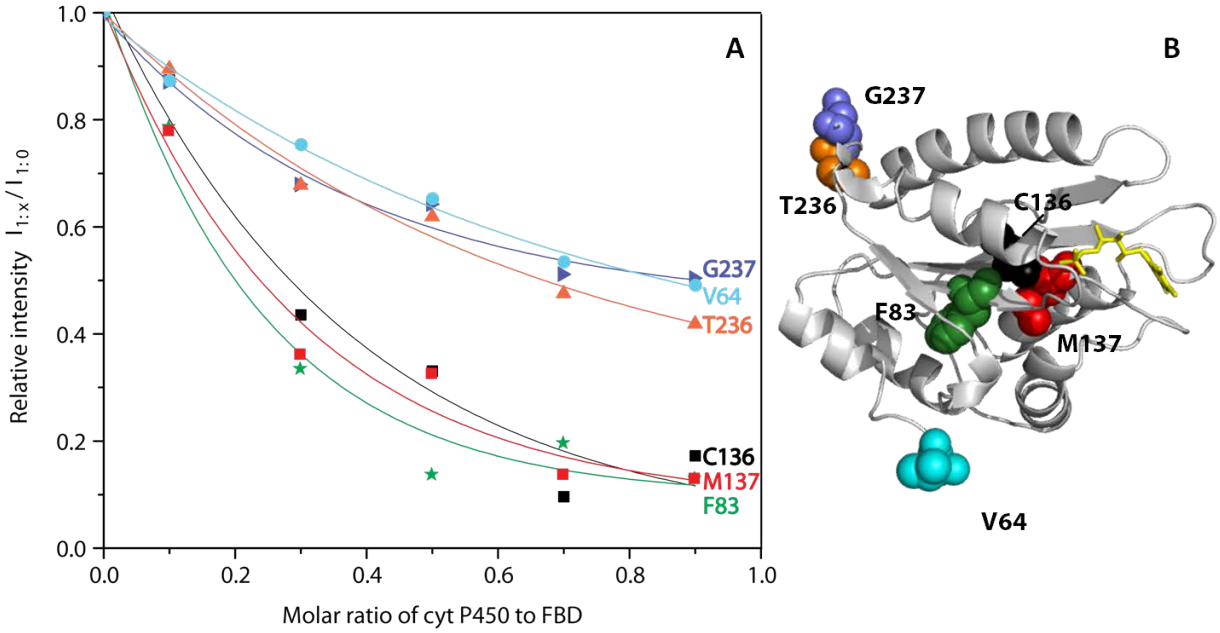

Figure 3.3 Intensity decrease of FBD resonances upon titration of cyt P450. A, distinct rates of intensity decrease are shown for selected residues. The curves were fitted with a simple exponential decay function. B, location of the selected residues in the structure of FBD. Val-64, Thr-236 and Gly-237 are at the N- and C-terminus of the soluble FBD, and Phe-83, Cys-136 and Met-137 are in the middle of beta sheet structures.

3.4.3 Mapping the cyt P450-binding epitope on FBD by NMR

Chemical shift perturbation and line broadening in the backbone amides of FBD upon complex formation with cyt P450 were analyzed to help identify the epitope on FBD for binding cyt P450. A histogram (Figure 3.4A) depict the weighted amide chemical shift perturbations of FBD resonances in the presence of 0.3 molar equivalent of cyt P450, as compared to the free FBD. An average chemical shift change of 0.013 ppm was observed with a standard deviation of 0.007 ppm (Figure 3.4A). The most significant chemical shift perturbations (Figure 3.4A, above the dash line) were observed on the residues mostly located on the loops following the C-terminus of the beta sheet structures, including Thr-90, Thr-139, Tyr-140, Gly-141, Gly-143, Thr-146, Lys-176. These residues are located in close proximity of the FMN cofactor, which could be involved

in direct interaction with cyt P450 or affected by a change in FMN positioning upon binding to cyt P450. Distribution of chemical shift perturbation was mapped onto the surface representation of FBD (Figure 3.5A) according to the color code in Figure 3.4A. Among the solvent accessible residues, those which show modest chemical shift perturbations (Figure 3.4A, red, orange and pink) were found to mainly locate surrounding the solvent exposable edge of the FMN cofactor, which is the putative binding site on FBD for efficient electron transfer. Exceptionally, residues Lys-74 and Thr-76 which are distant from the FMN cofactor also show significant chemical shift changes, implying a potential non-productive secondary binding site for cyt P450.

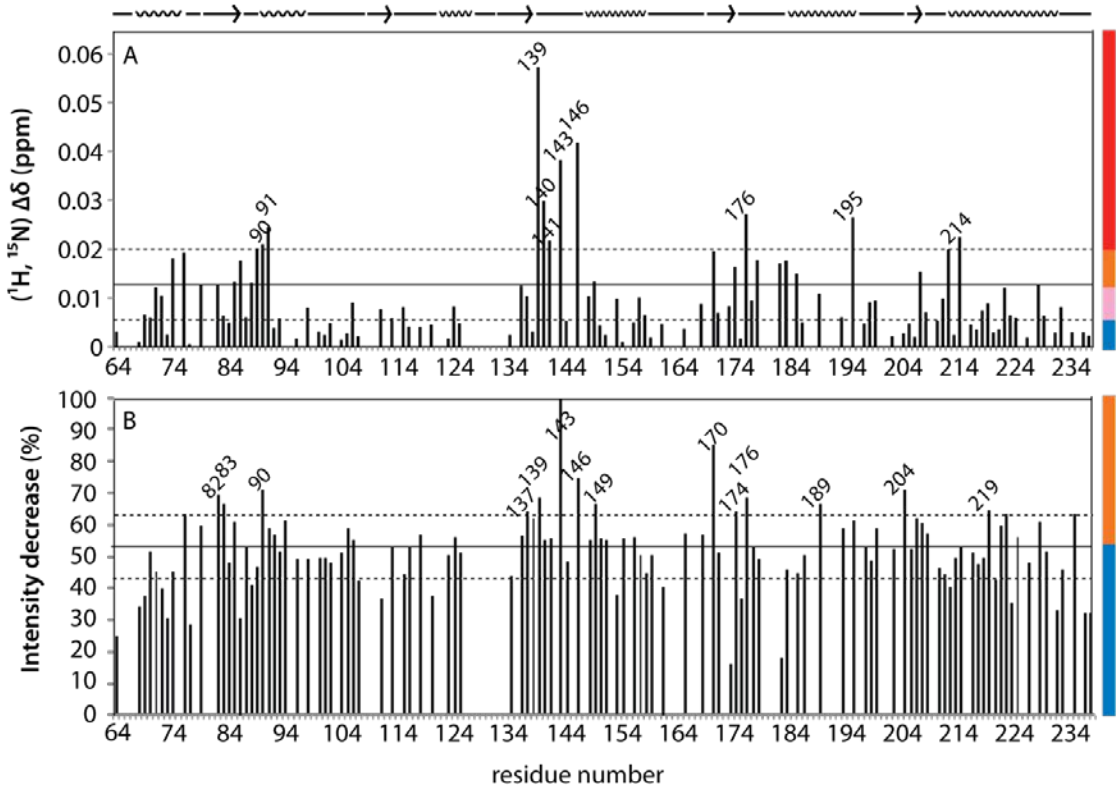

Figure 3.4 Chemical shift perturbation and line broadening analysis. Changes of weighted backbone amide chemical shifts (A) and percentages of intensity decrease (B) upon interacting with cyt P450 are presented. The molar ratio between FBD and cyt c is 1 : 0.3. The solid line represents the mean value of all measured residues, and the dash line represents one standard deviation beyond the mean value. The color codes are used to categorize the changes and map onto the structure of FBD in Figure 3.5.

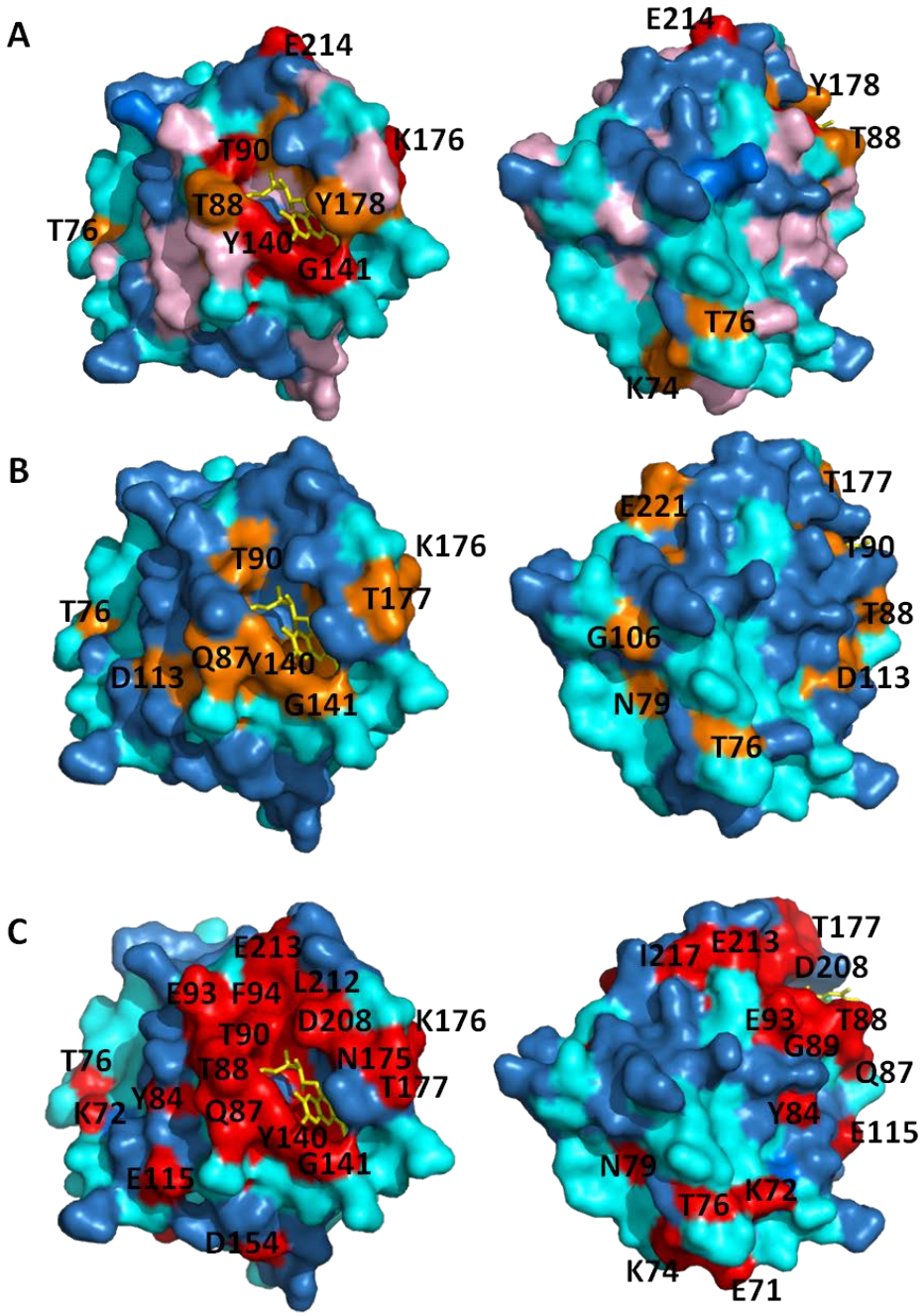

Figure 3.5 Mapping the effect of cyt P450 interacting with FBD. A, residues of FBD that exhibit chemical shift perturbations upon interacting with cyt P450 are color coded according to the categories in Figure 3.4: red for ≥ 0.02 ppm, orange for ≥ 0.013 ppm, pink for ≥ 0.006 ppm, and blue for < 0.006 ppm. B, residues of FBD whose intensity decrease upon complex formation are color-coded according to Figure 3.4: orange for residues whose intensities decreased more than the average percentage, and blue for those less than average. For A and B, the molar ratio between FBD and cyt P450 is 1 to 0.3. C, residues of FBD whose resonances are broadened beyond detection upon complex formation with one molar equivalent of cyt P450 are colored red. The right panels are 90° rotation views of the left panels.

Intensity decrease is plotted as a function of FBD residue number in the presence of 0.3 molar equivalent of cyt P450 (Figure 3.4B). All the residues with the most significant decrease in intensity (Figure 3.4B, above the dash line) are solvent inaccessible, except for Thr-90. This suggests that the main cause for the observed line broadening comes from an increase in correlation time upon complex formation. In order to assess the distribution of line broadening, residues with different extents of intensity decrease was mapped onto the structure of FBD (Figure 3.5) according to the color code in Figure 3.4B. Most of the residues on the surface of FBD do not show significant line broadening (Figure 3.4, blue) except several residues close to the solvent exposed edge of the FMN cofactor (Gln-87, Thr-90, Asp-113, Tyr-140, Gly-141, Lys-176, Thr-177) as well as a few residues distant from the FMN cofactor (Thr-76, Asn-79, Gly-106, Glu-221). These residues coincide with the ones showing significant chemical shift perturbations in Figure 3.4, and are likely involved in the interaction with cyt P450. As the titration of cyt P450 proceeds, line broadening for some residues becomes so severe that they start to disappear from the spectrum. When the molar ratio between FBD and cyt P450 reaches 1: 0.9, the intensities of a number of residues decreased to the noise level (Figure 3.5, red). These residues cover a fairly large surface area surrounding the solvent exposed edge of FMN with the exception of a few residues located at the back side of the protein. An overall examination of Figure 3.5 shows that the effect of complex formation on the chemical shifts and line broadening of FBD resonances is most pronounced for residues fringing the solvent exposed edge of FMN on the surface, implying the primary binding site of cyt P450 on FBD.

3.4.4 Structural model of FBD-cyt p450 complex

A structural model of FBD-cyt p450 was generated by a data-driven docking program HADDOCK (High Ambiguity Driven biomolecular DOCKing) (*42*). The FMN binding domain of a crystal structure of CPR (PDB code 1AMO) and a crystal structure of cyt P450 (PDB code 1SUO) were used as the starting structures in HADDOCK calculations. The docking was driven under defined intermolecular ambiguous restraints including active and passive residues with >40% solvent-accessibility from both proteins. Solvent-accessible residues on FBD which show significant chemical shift perturbation upon complex formation are selected as the active ambiguous residues from FBD (Figure 3.5A, red and orange). Passive restraints for FBD are chosen from the surface residues which show above-average intensity decrease upon binding to

cyt P450 (Figure 3.5B, orange) but are not included in the active restraints. Active ambiguous restraints on cyt P450 were selected according to a site-directed mutagenesis study in which nine residues on cyt P450 are suggested to be involved in the binding interface with cytochrome P450 reductase (*11*). No passive restraints were input for cyt P450. Active restraints which created violations in more than 45 out of the 50 final structures were removed. The refined restraint table was shown in Table 3.1 and applied in the docking program using the same protocol. The restraints were filtered once by carefully examining the results of a training run. Active restraints which created violations in more than 45 out of the 50 final structures were removed. The refined restraint table was shown in Table 3.1 and applied in the docking program.

Table 3.1 List of restraints used in HADDOCK

	FBD	cyt P450
Ambiguous restraints, active	Thr-88, Thr-90, Tyr-140, Gly-141, Lys-176, Tyr-178, Glu-214	Arg-122, Arg-126, Arg-133, Phe-135, Met-137, Lys-139, Arg-422, Lys-433, Arg-443
Ambiguous restraints, passive	Gln-87, Asp-113, Thr-177, Glu-221	

Among 50 lowest-energy structures resulted from the docking, an ensemble of 41 structures forms a major cluster with an average backbone r.m.s.d. of 2.54 Å compared to the mean. The energy statistics of the cluster are summarized in Table3.2. The average intermolecular energies of the clusters is -568.4 kcal/mol, of which the major contribution comes from electrostatic energies (-534.8 kcal/mol), implying the importance of electrostatic interaction in the complex formation between FBD and cyt p450. A representative structure of the cluster is shown in Figure 3.6A. The isoalloxazine ring of the FMN cofactor and the porphyrin ring of heme are nearly perpendicular to one another, and the shortest edge-to-edge distance between heme and FMN is 12.4 Å, which is within the 14.0 Å limit predicted for efficient electron transfer (*49*). In order to elucidate which residues are essential for electron transfer between the two proteins, we use the program HARLEM (*50*) to predict the shortest electron transfer pathway in the presented structure. The result of HARLEM calculation suggests a coupling pathway (Figure 3.6B) involving the FMN cofactor, Met-132, Arg-133 and heme of the cyt P450. This pathway reveals the crucial role that Met-132 and Arg-133 of cyt P450 play in mediating electron transfer.

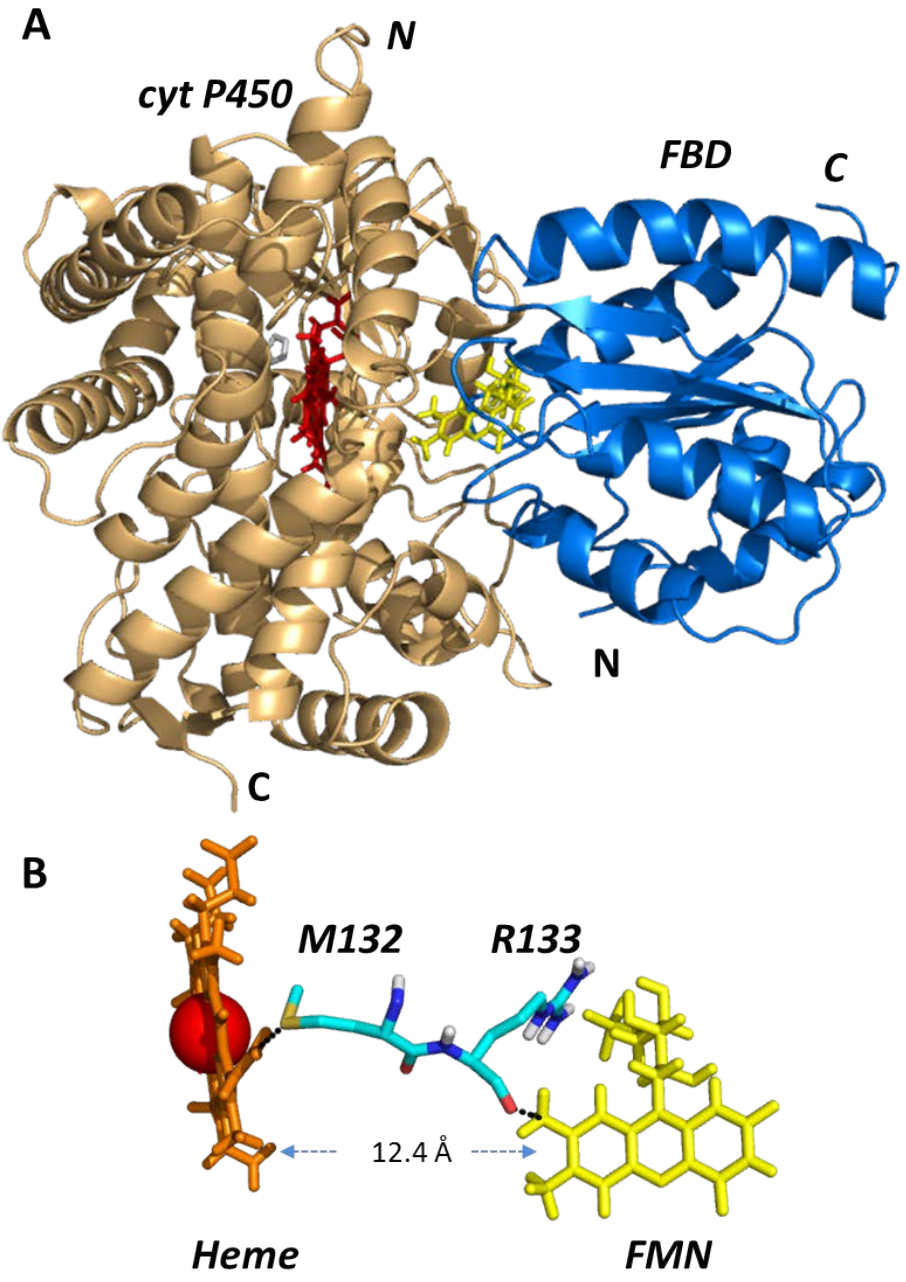

Figure 3.6 Structure model of the FBD-cyt P450 complex. A, a representative structure of the major cluster among the 50 lowest-energy structures generated from HADDOCK. PDB 1AMO and PDB 1SUO are used as the initial structures of FBD and cyt P450 in the docking. Heme and the FMN cofactor are presented by red and yellow sticks, respectively. B, electron transfer pathway predicted using HARLEM (*50*). Electron transfer initiates at C8 methyl group of the FMN cofactor, via the O, C, C^{α}, N atom of Arg-133 and the C, C^{α}, C^{β}, C^{γ} and S^{δ} atom of Met-132 on cyt P450 consecutively, and ends at the vinyl group of the heme. Black dash lines show through-space tunneling of electrons.

Table 3.2 Statistic analysis of the 50 lowest-energy structures of the FBD-cyt P450 complex generated from HADDOCK

Parameters	
Backbone r.m.s.d. (Å)[a]	2.54 ± 0.91
Total intermolecular energy (kcal/mol)	-568.4 ± 55.7
van der Waals energy (kcal/mol)	-33.6 ± 8.0
Electrostatic energy (kcal/mol)	-534.8 ± 58.5
Buried surface area ($Å^2$)	1818.5 ± 152.2

[a] Average r.m.s.d compared to the lowest energy structure and standard deviation within the cluster.

Table 3.3 Summary of hydrogen bonds/salt bridges in the FBD-cyt P450 binding interface

FBD	cyt P450
Gln-87 (O^{ε})	Arg-343 (N^{η})
Gln-87 (N^{ε})	Glu-439 (O^{ε})
Asp-113 (O^{δ})	Arg-422 (N^{η})
Glu-115 (O^{ε})	Arg-422 (N^{ε})
Glu-115 (O^{ε})	Arg-422 (N^{η})
Glu-116 (O^{ε})	Arg-422 (N^{η})
Asp-147 (O^{δ})	Arg-343 (N^{ε})
Asp-147 (O^{δ})	Arg-343 (N^{η})
Thr-177 (O^{γ})	Asp-134 (O^{δ})
Thr-177 (O)	Met-137 (N)
Tyr-178 (O^{η})	Lys-139 (O)
Asp-208 (O^{δ})	Arg-133 (N^{η})
Glu-213 (O^{ε})	Arg-126 (N^{η})
Glu-214 (O^{ε})	Arg-126 (N^{η})
FMN (O4')	Arg-133 (N^{η})

The binding interface in the FBD-cyt P450 complex model is shown in Figure 3.7. Residues on FBD which are involved in binding cyt P450 are mostly polar residues with negative/no charges. They are mainly located on the loops connecting the C-terminus of the beta sheets and N-terminus of the helices, including Gln-87, Thr-88 and Thr-90 on β1-α3 coil, Asp-113, Glu-115 and Glu-116 on β2-α4 coil, Tyr-140, Gly-141 and Asp-147 on β3-α5 coil, Asn-175, Thr-177, Tyr-178 and Glu-179 on β4-α6 coil and Asp-208 and Asn-211 on β5-α7 coil. Other residues of FBD located on the helices, including Glu-93 on helix α3, Asn-148 and Gln-150 on helix α5, Glu-213 and Glu-214 on helix α7 are also involved in the binding interface according to the structural model. On the other hand, interface on cyt P450 is largely composed of positively charged and hydrophobic residues, including Arg-126, Leu-129, Ala-130 and Arg-133

on helix αC, Phe-135-Lys-139 on αC-αD loop, Leu-340, Arg-343 and Ala-344 on αJ-αK loop, Ala-416, Ala-419, Leu-420, Arg-422, Lys-433 and Leu-437 on αK-αL loop and Gly-440 and Arg-443 on helix αL. Polar residues with negative/no charges are also involved in the binding interface, including Asp-134 on helix αC, Ser-141 on αC-αD loop, Glu-143 and Glu-144 on helix αD, Asp-415 and Asn-417 on αK-αL loop and Glu-439 on helix αL. Salt bridge/hydrogen bond formation was observed in the complex model (Table 3.3).

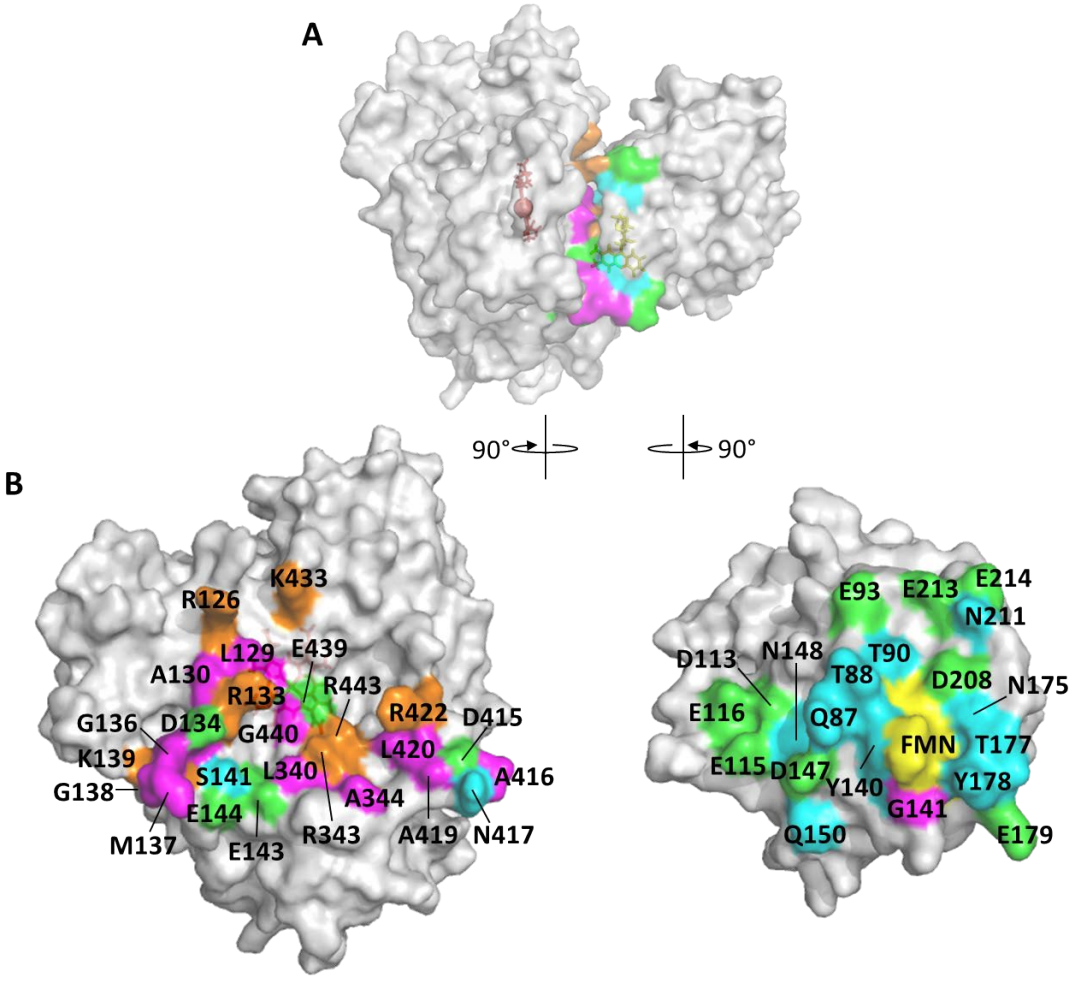

Figure 3.7 Binding interface of the FBD-cyt P50 complex. A, a surface representation of the FBD-cyt P450 complex. B, two proteins are rotated by 90° in opposite directions to reveal the interface. Interfacial residues involved in protein-protein contacts in the complex model are highlighted and color-coded based on properties of the amino acids. Polar neutral, nonpolar, positive and negative residues are colored cyan, magenta, orange and green, respectively. Heme and cofactor FMN are colored red and yellow, respectively.

3.5 Discussion

Our study reveals that the isolated FMN binding domain (FBD) in its two electron-reduced state is able to transfer electron to cyt P450 at a rate three times higher than the wild-type CPR. Under the described experimental conditions, productive complex formation by random collision is the rate limiting step of the inter-protein electron transfer. A higher rate of electron transfer between FBD and cyt P450 can attribute to two possible reasons: 1. FBD diffuses faster in solution due to its smaller hydrodynamic radius compared to CPR; 2. lacking the FAD/NADPH binding domain makes the FMN cofactor more solvent exposed in FBD, improving the chance of FMN to be in close proximity with heme for efficient electron transfer. Electron transfer between cyt c and FBD also occurs at a much higher rate than that between cyt c and wild-type CPR (see chapter II).

We investigated complex formation between FBD and cyt P450 using solution NMR techniques. In the NMR titration experiments, chemical shift perturbation and line broadening were observed and analyzed to probe the potential binding interface (*51, 52*). Significant line broadening observed on FBD resonances upon complex formation with cyt P450 attributes to a combination of increased correlation time due to the large size of cyt P450 and an interaction in slow-to-intermediate exchange time scale. Similar phenomenon was also observed in cyt b_5-cyt P450 complex (*51*). As illustrated in Figure 3.7, the majority of the residues on FBD which are affected by complex formation with cyt P450 are located on the fringe of the solvent-exposed edge of FMN, suggesting the primary binding site for cyt P450. Among these residues, single-site mutations of Thr-88, Asp-113 and Try-178 on FBD into Ala lead to decreased activities of the reconstituted cyt P450 system towards benzphetamine metabolism (data not published). There are a few other affected residues located in the opposite side of FMN, which may result from a potential secondary binding site or conformational perturbation.

Previous studies have suggested the importance of electrostatic interaction in the complex formation between CPR and cyt P450 by chemical modification of charged residues on the two proteins and site-directed mutagenesis (*11, 28, 33, 53*). Increasing ionic strength has been shown to disrupt the interaction between CPR and various P450s by masking the charged residues (*14*). The result of our structure model generated by HADDOCK confirmed that the formation of a number of salt bridges between the acidic residues on FBD and the basic residues on cyt P450 (Table 3.3), among which the majority of the intermolecular energy attributes to the charge-

charge interaction between Asp-113, Glu-115, Asp-147, Asp-208 and Glu-214 from FBD and Arg-126, Arg-133, Arg-343, Arg-422 from cyt P450. Asp-113 and Glu-115 are located on the β2-α4 coil in FBD, which was proposed to be a potential binding site for cyt P450 by chemical modification (*53*) and antipeptide antibody inhibition studies (*29*). These two residues are conserved through all mammalian and yeast CPRs. Mutations of Asp-113 and Glu-115/116 affected the stability of the CPR-cyt P450 2B1 complex (*14*), implying they are important contact sites in complex formation. Asp-208 of CPR plays a crucial role in interaction and electron transfer between CPR and cyt P450, mutation of which renders significant decrease in P450 activity (*35, 54*). The importance of Asp-147 and Glu-214 of CPR was also investigated by previous site-directed mutagenesis study. Mutating Asp-147 in FBD of human CPR into serine leads to 20-30% decrease in cyt P450 2D6 activity, while removing the charge of Glu-214 only seems to affect cytochrome c reduction but not cyt P450 2D6 activity (*35*). On the other hand, Arg-126, Arg-133 and Arg-422 have shown to be involved in interacting with cyt P450 2B4 by mutagenesis studies (*11*), while mutation of Arg-122 was also found to decrease the ability of cyt P450 to bind CPR we do not observe Arg-122 to be on the binding interface in our structural model. In addition, hydrogen bonds between Thr-177, Tyr-178 and FMN from FBD and Glu-134, Met-137, Lys-139 and Arg-133 from cyt P450 along with hydrophobic and van de Waals interactions also contribute to the stability of the FBD-cyt P450 complex. The best electron transfer pathway predicted by HARLEM involves Met-132 and Arg-133 of cyt P450. It has been reported that mutation of Asp-133, out of nine positively charged residues on the surface of cyt P450, leads to the greatest reduction in the affinity with CPR (*11*).

A previous structural model of the CPR-cyt P450 complex has been reported by Hamdane *et al* (*36*), generated by rigid body docking between an open conformation of CPR and cyt P450 2B4. The binding interfaces on FBD and cyt P450 proposed in this model are largely overlapping with what we observed in our NMR results as well as in our structural model. The most notable difference between our structural model and the previous proposed one is the relative orientation of the two proteins. The orientation of FBD in our structural model is rotated by approximately 90° around the axis perpendicular to the heme pophyrin ring of cyt P450 with respect to the previously proposed model. Therefore, the interactions between specific residues on the binding interface in our model, including hydrogen bonds, salt bridges and van de Waals contacts, differ

from the reported model, except the salt bridge formed between Asp-208 of FBD and Arg-133 of cyt P450. The difference in protein orientation could be a consequence of different starting structures utilized in the docking. Hamdane *et al* generated the model using a partially open conformation of CPR in which the FMN cofactor is solvent exposed while the relative orientation of the FMN binding domain is restrained with respect to the rest of CPR. Unlike the isolated FMN binding domain, the steric hindrance imposed by the FAD/NADPH domain or the interaction between the FAD/NADPH domain and cyt P450 (as suggested by the model) might alter the orientation of FBD with respect to cyt P450 during the docking process.

On the other hand, there is a possibility that isolated FMN binding domain interacts with cyt P450 in a different orientation compared to the wild-type CPR *in vitro*, due to its lack of restraints from the FAD/NADPH domain. It has been reported that CPR exists in a predominant "closed conformation" in the resting state, in which the domains are arranged in a way that the FMN cofactor is buried in the interface between the FMN and FAD/NADPH binding domains (*2*, *3*). A movement of the FMN binding domain relative to the rest of the CPR molecule is essential for electron transfer from CPR to its redox partners (*4*-*6*). However, in an extended conformation of CPR, it remains unknown whether the FBD tumbles nearly isotropically in solution and samples a number of orientations on the surface of cyt P450 searching for an optimal contact for electron transfer or the FMN binding domain and FAD/NADPH domain collectively interact with cyt P450 restraining the orientations the FBD can adopt for binding cyt P450. In the latter case, it may occur that the wild-type CPR interacts with cyt P450 differently from the isolated FBD, which also leads to an alternative electron transfer pathway.

3.6 Conclusion

In this study, we investigated the interaction between the FMN binding domain of CPR and cyt P450 by solution NMR. Specific residues of FBD involved in the binding interface with cyt P450 were identified by chemical shift perturbation and line broadening analysis. A structural model of FBD-cyt P450 complex was generated using HADDOCK based on the NMR data and previous site-directed mutagenesis studies. The proposed model allows to identify the potential interactions including salt bridges, hydrogen bonds and van de Waals contacts on the interface and residues that are important for complex formation. An electron transfer pathway was predicted using HARLEM, which involves mediation via Met-132 and Arg-133 of cyt P450.

3.7 References

1. Vergeres, G., and Waskell, L. (1995) Cytochrome b5, its functions, structure and membrane topology, *Biochimie 77*, 604-620.

2. Wang, M., Roberts, D. L., Paschke, R., Shea, T. M., Masters, B. S., and Kim, J. J. (1997) Three-dimensional structure of NADPH-cytochrome P450 reductase: prototype for FMN- and FAD-containing enzymes, *Proc Natl Acad Sci U S A 94*, 8411-8416.

3. Vincent, B., Morellet, N., Fatemi, F., Aigrain, L., Truan, G., Guittet, E., and Lescop, E. (2012) The closed and compact domain organization of the 70-kDa human cytochrome P450 reductase in its oxidized state as revealed by NMR, *J Mol Biol 420*, 296-309.

4. Wadsater, M., Laursen, T., Singha, A., Hatzakis, N. S., Stamou, D., Barker, R., Mortensen, K., Feidenhans'l, R., Moller, B. L., and Cardenas, M. (2012) Monitoring shifts in the conformation equilibrium of the membrane protein cytochrome P450 reductase (POR) in nanodiscs, *J Biol Chem 287*, 34596-34603.

5. Hay, S., Brenner, S., Khara, B., Quinn, A. M., Rigby, S. E., and Scrutton, N. S. (2010) Nature of the energy landscape for gated electron transfer in a dynamic redox protein, *J Am Chem Soc 132*, 9738-9745.

6. Pudney, C. R., Khara, B., Johannissen, L. O., and Scrutton, N. S. (2011) Coupled motions direct electrons along human microsomal P450 Chains, *PLoS Biol 9*, e1001222.

7. Schacter, B. A., Nelson, E. B., Marver, H. S., and Masters, B. S. (1972) Immunochemical evidence for an association of heme oxygenase with the microsomal electron transport system, *J Biol Chem 247*, 3601-3607.

8. Oshino, N., Imai, Y., and Sato, R. (1971) A function of cytochrome b5 in fatty acid desaturation by rat liver microsomes, *J Biochem 69*, 155-167.

9. Williams, C. H., Jr., and Kamin, H. (1962) Microsomal triphosphopyridine nucleotide-cytochrome c reductase of liver, *J Biol Chem 237*, 587-595.

10. Bachur, N. R., Gordon, S. L., Gee, M. V., and Kon, H. (1979) NADPH cytochrome P-450 reductase activation of quinone anticancer agents to free radicals, *Proc Natl Acad Sci U S A 76*, 954-957.

11. Bridges, A., Gruenke, L., Chang, Y. T., Vakser, I. A., Loew, G., and Waskell, L. (1998) Identification of the binding site on cytochrome P450 2B4 for cytochrome b5 and cytochrome P450 reductase, *J Biol Chem 273*, 17036-17049.

12. Lehnerer, M., Schulze, J., Achterhold, K., Lewis, D. F., and Hlavica, P. (2000) Identification of key residues in rabbit liver microsomal cytochrome P450 2B4: importance in interactions with NADPH-cytochrome P450 reductase, *J Biochem 127*, 163-169.

13. Kenaan, C., Zhang, H., Shea, E. V., and Hollenberg, P. F. (2011) Uncovering the role of hydrophobic residues in cytochrome P450-cytochrome P450 reductase interactions, *Biochemistry 50*, 3957-3967.

14. Jang, H. H., Jamakhandi, A. P., Sullivan, S. Z., Yun, C. H., Hollenberg, P. F., and Miller, G. P. (2010) Beta sheet 2-alpha helix C loop of cytochrome P450 reductase serves as a docking site for redox partners, *Biochim Biophys Acta 1804*, 1285-1293.

15. Eyer, C. S., and Backes, W. L. (1992) Relationship between the rate of reductase-cytochrome P450 complex formation and the rate of first electron transfer, *Arch Biochem Biophys 293*, 231-240.

16. Zhang, H., Im, S. C., and Waskell, L. (2007) Cytochrome b5 Increases the Rate of Product Formation by Cytochrome P450 2B4 and Competes with Cytochrome P450 Reductase for a Binding Site on Cytochrome P450 2B4, *J Biol Chem 282*, 29766-29776.

17. Voznesensky, A. I., and Schenkman, J. B. (1994) Quantitative analyses of electrostatic interactions between NADPH-cytochrome P450 reductase and cytochrome P450 enzymes, *J Biol Chem 269*, 15724-15731.

18. Shimada, T., Mernaugh, R. L., and Guengerich, F. P. (2005) Interactions of mammalian cytochrome P450, NADPH-cytochrome P450 reductase, and cytochrome b5 enzymes, *Archives of Biochemistry and Biophysics 435*, 207-216.

19. Murataliev, M., Guzov, V., Walker, F., and Feyereisen, R. (2008) P450 reductase and cytochrome b5 interactions with cytochrome P450: Effects on house fly CYP6A1 catalysis, *Insect Biochemistry and Molecular Biology 38*, 1008-1015.

20. Davydov, D. R., Knyushko, T. V., Kanaeva, I. P., Koen, Y. M., Samenkova, N. F., Archakov, A. I., and Hui Bon Hoa, G. (1996) Interactions of cytochrome P450 2B4 with NADPH-cytochrome P450 reductase studied by fluorescent probe, *Biochimie 78*, 734-743.

21. Centeno, F., and Gutierrez-Merino, C. (1992) Location of functional centers in the microsomal cytochrome P450 system, *Biochemistry 31*, 8473-8481.

22. Davydov, D. R., Kariakin, A. A., Petushkova, N. A., and Peterson, J. A. (2000) Association of cytochromes P450 with their reductases: opposite sign of the electrostatic interactions in P450BM-3 as compared with the microsomal 2B4 system, *Biochemistry 39*, 6489-6497.

23. Voznesensky, A. I., and Schenkman, J. B. (1992) The cytochrome P450 2B4-NADPH cytochrome P450 reductase electron transfer complex is not formed by charge-pairing, *J Biol Chem 267*, 14669-14676.

24. Bumpus, N. N., and Hollenberg, P. F. (2010) Cross-linking of human cytochrome P450 2B6 to NADPH-cytochrome P450 reductase: Identification of a potential site of interaction, *Journal of Inorganic Biochemistry 104*, 485-488.

25. Kariakin, A., Davydov, D., Peterson, J. A., and Jung, C. (2002) A new approach to the study of protein-protein interaction by FTIR: complex formation between cytochrome P450BM-3 heme domain and FMN reductase domain, *Biochemistry 41*, 13514-13525.

26. Kiselyova, O. I., Yaminsky, I. V., Ivanov, Y. D., Kanaeva, I. P., Kuznetsov, V. Y., and Archakov, A. I. (1999) AFM study of membrane proteins, cytochrome P450 2B4, and NADPH-cytochrome P450 reductase and their complex formation, *Arch Biochem Biophys 371*, 1-7.

27. Ivanov, Y. D., Kanaeva, I. P., Kuznetsov, V. Y., Lehnerer, M., Schulze, J., Hlavica, P., and Archakov, A. I. (1999) The optical biosensor studies on the role of hydrophobic tails of NADPH-cytochrome P450 reductase and cytochromes P450 2B4 and b5 upon productive complex formation within a monomeric reconstituted system, *Arch Biochem Biophys 362*, 87-93.

28. Shen, S., and Strobel, H. W. (1993) Role of lysine and arginine residues of cytochrome P450 in the interaction between cytochrome P4502B1 and NADPH-cytochrome P450 reductase, *Arch Biochem Biophys 304*, 257-265.

29. Nadler, S. G., and Strobel, H. W. (1991) Identification and characterization of an NADPH-cytochrome P450 reductase derived peptide involved in binding to cytochrome P450, *Arch Biochem Biophys 290*, 277-284.

30. Lin, H.-l., Kenaan, C., Zhang, H., and Hollenberg, P. F. (2012) Reaction of Human Cytochrome P450 3A4 with Peroxynitrite: Nitrotyrosine Formation on the Proximal Side Impairs Its Interaction with NADPH-Cytochrome P450 Reductase, *Chemical Research in Toxicology 25*, 2642-2653.

31. Nikfarjam, L., Izumi, S., Yamazaki, T., and Kominami, S. (2006) The interaction of cytochrome P450 17alpha with NADPH-cytochrome P450 reductase, investigated using chemical modification and MALDI-TOF mass spectrometry, *Biochim Biophys Acta 1764*, 1126-1131.

32. Shen, S., and Strobel, H. W. (1992) The role of cytochrome P450 lysine residues in the interaction between cytochrome P450IA1 and NADPH-cytochrome P450 reductase, *Arch Biochem Biophys 294*, 83-90.

33. Shimizu, T., Tateishi, T., Hatano, M., and Fujii-Kuriyama, Y. (1991) Probing the role of lysines and arginines in the catalytic function of cytochrome P450d by site-directed mutagenesis. Interaction with NADPH-cytochrome P450 reductase, *J Biol Chem 266*, 3372-3375.

34. Cvrk, T., and Strobel, H. W. (2001) Role of LYS271 and LYS279 residues in the interaction of cytochrome P4501A1 with NADPH-cytochrome P450 reductase, *Arch Biochem Biophys 385*, 290-300.

35. Zhao, Q., Modi, S., Smith, G., Paine, M., McDonagh, P. D., Wolf, C. R., Tew, D., Lian, L. Y., Roberts, G. C., and Driessen, H. P. (1999) Crystal structure of the FMN-binding domain of human cytochrome P450 reductase at 1.93 A resolution, *Protein Sci 8*, 298-306.

36. Hamdane, D., Xia, C., Im, S. C., Zhang, H., Kim, J. J., and Waskell, L. (2009) Structure and function of an NADPH-cytochrome P450 oxidoreductase in an open conformation capable of reducing cytochrome P450, *J Biol Chem 284*, 11374-11384.

37. Saribas, A. S., Gruenke, L., and Waskell, L. (2001) Overexpression and purification of the membrane-bound cytochrome P450 2B4, *Protein Expr Purif 21*, 303-309.

38. Gutierrez, A., Lian, L. Y., Wolf, C. R., Scrutton, N. S., and Roberts, G. C. (2001) Stopped-flow kinetic studies of flavin reduction in human cytochrome P450 reductase and its component domains, *Biochemistry 40*, 1964-1975.

39. Sato, Y., Nomura, S., Kamio, Y., Omura, S., and Hata, T. (1967) Studies on cerulenin, 3. Isolation and physico-chemical properties of cerulenin, *J Antibiot (Tokyo) 20*, 344-348.

40. Gutierrez, A., Paine, M., Wolf, C. R., Scrutton, N. S., and Roberts, G. C. (2002) Relaxation kinetics of cytochrome P450 reductase: internal electron transfer is limited by conformational change and regulated by coenzyme binding, *Biochemistry 41*, 4626-4637.

41. Kneller, D. G., and Kuntz, I. D. (1993) UCSF SPARKY - AN NMR DISPLAY, ANNOTATION AND ASSIGNMENT TOOL, *J. Cell. Biochem.*, 254-254.

42. de Vries, S. J., van Dijk, A. D., Krzeminski, M., van Dijk, M., Thureau, A., Hsu, V., Wassenaar, T., and Bonvin, A. M. (2007) HADDOCK versus HADDOCK: new features and performance of HADDOCK2.0 on the CAPRI targets, *Proteins 69*, 726-733.

43. Schuttelkopf, A. W., and van Aalten, D. M. F. (2004) PRODRG: a tool for high-throughput crystallography of protein-ligand complexes, *Acta Crystallogr. Sect. D-Biol. Crystallogr. 60*, 1355-1363.

44. Oprian, D. D., Vatsis, K. P., and Coon, M. J. (1979) Kinetics of reduction of cytochrome P-450LM4 in a reconstituted liver microsomal enzyme system, *J Biol Chem 254*, 8895-8902.

45. Rosen, P., and Stier, A. (1973) Kinetics of CO and O 2 complexes of rabbit liver microsomal cytochrome P 450, *Biochem Biophys Res Commun 51*, 603-611.

46. Gray, R. D. (1978) Kinetics of CO binding to and dissociation from microsomal cytochrome P-450 induced by phenobarbital in rat liver, *J Biol Chem 253*, 4364-4369.

47. Taniguchi, H., Imai, Y., Iyanagi, T., and Sato, R. (1979) Interaction between NADPH-cytochrome P-450 reductase and cytochrome P-450 in the membrane of phosphatidylcholine vesicles, *Biochim Biophys Acta 550*, 341-356.

48. Barsukov, I., Modi, S., Lian, L. Y., Sze, K. H., Paine, M. J., Wolf, C. R., and Roberts, G. C. (1997) 1H, 15N and 13C NMR resonance assignment, secondary structure and global fold of the FMN-binding domain of human cytochrome P450 reductase, *J Biomol NMR 10*, 63-75.

49. Page, C. C., Moser, C. C., and Dutton, P. L. (2003) Mechanism for electron transfer within and between proteins, *Curr Opin Chem Biol 7*, 551-556.

50. Kurnikov, I. V. (2000) HARLEM molecular modeling package, Department of Chemistry, University of Pittsburgh, Pittsburgh, PA.

51. Ahuja, S., Jahr, N., Im, S. C., Vivekanandan, S., Popovych, N., Le Clair, S. V., Huang, R., Soong, R., Xu, J., Yamamoto, K., Nanga, R. P., Bridges, A., Waskell, L., and Ramamoorthy, A. (2013) A model of the membrane-bound cytochrome b5-cytochrome P450 complex from NMR and mutagenesis data, *J Biol Chem 288*, 22080-22095.

52. Estrada, D. F., Laurence, J. S., and Scott, E. E. (2013) Substrate-modulated cytochrome P450 17A1 and cytochrome b5 interactions revealed by NMR, *J Biol Chem 288*, 17008-17018.

53. Nadler, S. G., and Strobel, H. W. (1988) Role of electrostatic interactions in the reaction of NADPH-cytochrome P-450 reductase with cytochromes P-450, *Arch Biochem Biophys 261*, 418-429.

54. Kasper, C. B. (1995) Role of Acidic Residues in the Interaction of NADPH-Cytochrome P450 Oxidoreductase with Cytochrome P450 and Cytochrome c, *J Biol Chem 270*, 27475-27480.

CHAPTER 4

Interaction between the Transmembrane Domains of Cytochrome P450 and Cytochrome P450 Reductase by solid-state NMR

4.1 Summery

Structure and dynamics studies of membrane proteins are essential to better understand their physiological function. Solid-state NMR spectroscopy is a powerful tool for high-resolution structural studies of membrane proteins. In this chapter, we characterized the structure and dynamics of the transmembrane domain of cytochrome P450 reductase (CPR) in native membrane-like environment by solid-state NMR techniques in conjunction with spectra simulation. Our results reveal that the N-terminal transmembrane domain of CPR adopts an α-helical conformation in the lipid environment. Most notably, we show that the transmembrane helix is tilted approximately 13° from the lipid bilayer normal, and exhibits motions on submillisecond time scale including rotational diffusion of the whole helix and fluctuation of the helical director axis. Using the same approach, we also investigated the interaction between the FMN binding domain of CPR and cytochrome P450 (cyt P450) in the lipid environment. Our results show clear evidence of the interaction between the soluble domains of the two proteins in the lipid bicelles, and suggest transient interplay between their transmembrane helices.

4.2 Introduction

Approximately 75% of the pharmaceuticals in use today are metabolized by a group of heme-containing monooxygenases known as the cytochrome P450 superfamily. These enzymes are responsible for the metabolism of myriads of endogenous compounds including vitamins, steroids and hormones, as well as exogenous compounds including environmental toxins and drugs. Cyt P450s catalyze a variety of chemical transformations by activating stable carbon-hydrogen bonds of alkanes using oxygen and electrons from their redox partners. Due to the

strong and versatile oxidizing capability of cyt P450, they are referred to as “mother nature’s blowtorch”.

Cytochrome P450 reductase (CPR) is an essential redox partner of microsomal cyt P450s, which shuttles electrons from NADPH to cyt P450s. Additionally, CPR plays an indispensable role in the development of high-level organisms; it is also able to reduce cytochrome c, cytochrome b_5 and heme oxygenase as well as a variety of therapeutic prodrugs (1-5). CPR is a multi-domain membrane protein composed of a soluble 70 kDa carboxyl terminal catalytic domain, a 5 kDa amino terminal transmembrane segment, and a 2 kDa linker connecting these two domains. The soluble domain of CPR, the structure of which has been characterized by X-ray crystallography (6, 7), can be further divided into the FAD/NADPH binding domain and the FMN binding domain. However, the structures of the transmembrane and the linker region between the soluble and transmembrane domains remain unidentified. Electron transfer pathway originates from NADPH, which transfers a hydride ion to the cofactor FAD, which proceeds to donate the electrons to the cofactor FMN. The FMN binding domain is the ultimate donor of electrons to cyt P450s and other protein acceptors.

It has long been postulated that the transmembrane domain of CPR plays a vital role in aiding electron transfer between CPR and cyt P450 (8-10). Lacking the transmembrane anchor, CPR is still able to reduce cytochrome c and other artificial acceptors, but is impaired to transfer electrons to cyt P450 (6). Truncation of the N-terminal segment leads to a severe decrease/prohibition of substrate turnover in a reconstituted cyt P450 system (8). However, the mechanism on how the transmembrane domain affects the cyt P450/CPR interaction and catalysis remains under debate. It is generally believed that the transmembrane domain of CPR anchors the enzyme on the surface of the membrane constraining the diffusion of the catalytic soluble domain and mediating the CPR/cyt P450 interaction in proper orientation (9). Other hypothesis has been raised that the N-terminal transmembrane domain of CPR in its free form can alter diffusive reduced oxygen species dynamics, thus affect the substrate catalysis (8). A complete understanding of the physiological function of the transmembrane domain requires a thorough characterization of its structure and dynamics in a lipid membrane environment. Despite postulations of its secondary structure (10-13), the atomic-level structure of the transmembrane domain has not been revealed experimentally since the first structure of the soluble domain of rat CPR was reported in 1997 by X-ray crystallography (6). The major

difficulty lies in the hydrophobicity and mobility of the transmembrane domain preventing it from co-crystalizing with the soluble domain.

Interaction between CPR and cyt P450 has been studied with a number of methods including site-direct mutagenesis (14-17), enzyme kinetic assays (17-23), fluorescence (24, 25), cross-linking (26, 27), FTIR (28), AFM (29), optical biosensor (30), chemical modification (31-35), etc.; however, detailed structural information on this protein complex, especially in the membrane-bound form, is still deficient. In particular, evidence of the interaction between the two transmembrane domains and their roles in the formation of the complex is elusive (8, 36, 37). This is partially due to the fact that studying protein-protein interactions in lipid membrane environment remains a challenge, in spite of previous efforts (38-40).

Solid-state NMR spectroscopy is a powerful approach to probe the structure and dynamics of insoluble, non-crystalline or amorphous biomolecules like membrane proteins. It has been applied as a unique tool to probe conformation and dynamics of large biomolecular complexes in native-like lipid bilayers (41, 42) either under magic angle sample spinning (MAS) conditions or in uniformly aligned samples. In this chapter, we first probed the structural and dynamic features of the N-terminal FMN binding domain of CPR – including the transmembrane domain and linker region – in a native-like membrane environment, using a combination of one-dimensional cross polarization (CP) and two-dimensional separated local field (SLF) solid-state NMR techniques in conjunction with spectral simulations. And later, we investigate the interaction of the membrane-bound FMN binding domain (FBD) with cytochrome P450 2B4 (cyt P450) in the lipid environment using the same approaches. The results reveal the characteristics of the interaction between the soluble domains as well as the transmembrane domains of FBD and cyt P450.

4.3 Materials and Methods

4.3.1 Materials

E. coli C41 cells for protein overexpression were purchased from Lucigen (Middleton, MI). Yeast extract, tryptone for unlabeled growth media were purchased from Sigma-Aldrich. [^{15}N]ammonium chloride for M9 medium and D_2O was purchased from Cambridge Isotope Laboratories (Andover, MA). 1,2-dilauroyl-sn-glycero-3-phosphatidylcholine (DLPC) and 1,2-

dihexanoyl-sn-glycero-3-phosphatidylcholine (DHPC) were purchased from Avanti Polar Lipids, Inc. (Alabaster, AL).

4.3.2 Expression and purification of proteins

Expression and purification of a uniformly ^{15}N labeled membrane-bound FMN binding domain of rat CPR and unlabeled cytochrome P450 2B4 was carried out as described in Chapter 3 and Chapter 4.

4.3 3 Preparation of bicelles

35.95 mg DLPC, 6.55 mg DHPC and 2.23 mg cholesterol corresponding to a molar ratio of [DLPC]:[DHPC]:[cholesterol]=4:1:0.4 were co-solubilized in chlorofosrm. Solvent was removed under a stream of N_2 gas to produce a lipid film on the walls of a glass vessel, which was kept in vacuum overnight to remove any residual solvent. 21.3 µl of 40 mM phosphate buffer, pH 7.4, with 5% (w/v) glycerol was added to lipids. The resulting mixture of extreme viscosity was homogenized by vortexing, and freeze/heat cycles between 0 °C and room temperature for 5-8 times until the bicelles look transparent and homogenous. Protein was added in the final step of the preparation. Addition of 2.5 mg or 92.6 nmol protein in 65 µL 40 mM phosphate buffer, pH 7.4, with 5% (w/v) glycerol into the bicelle mixture resulted in a protein: DLPC molar ratio of 1:625. The homogeneously mixed sample was packed in a flat-bottom glass tube and used for subsequent NMR experiments. Prior to NMR measurements, the sample inside the probe was treated with a minimum of 3 cooling/heating cycles between 7 and 25 °C to ensure homogenous alignment of bicelles (43). Hydrogen-deuterium exchange experiment was carried out on a sample with membrane-bound FMN binding domain incorporated in DLPC/DHPC/cholesterol bicelles prepared following the protocol descried above. The sample was placed under a stream of N_2 gas to remove H_2O until three fourth of the total sample volume remained. Equivalent amount of the D_2O (one fourth of the total sample volume) was added into the sample and mixed until homogeneous by vortexing. After 10 cycles of H_2O evaporation/D_2O addition, the sample tube was sealed and the sample was transferred to the magnet for subsequent NMR experiments.

4.3.4 NMR experiments

All one-dimensional ^{31}P and ^{15}N spectra were obtained from a 600 MHz Bruker NMR spectrometer using a home-built 5 mm electric-field-free flat-coil probe. ^{31}P spectra were obtained using a one pulse sequence with a recycle delay of 3 s and 25 kHz proton decoupling during ^{31}P signal acquisition. ^{15}N spectra were obtained using RINEPT and CP pulse sequences with a recycle delay of 3.5 s and 55 kHz proton decoupling during ^{15}N signal acquisition. In RINEPT experiments, refocusing delays of 1.3 and 0.65 ms were used before and after a pair of 90° pulses, respectively. In the cross polarization experiments, CP contact time was varied from 0.05 ms to 2 ms. The two-dimensional Separated Local Field (SLF) spectrum was obtained on a 720 MHz Varian NMR spectrometer under static conditions using a SAMPI4 sequence with 0.5 ms cross polarization contact time and 25 kHz SPINAL (Small Phase Incremental Alternation) decoupling of protons. The spectrum was acquired with 28 t1 increments, 25 ms acquisition time, 2000 scans and a 2.5 s recycle delay, resulting in a total experimental time of 39 hours. A 5 mm electric-field-free double-resonance static probe (home-built) (44) was used to prevent sample heating. All experiments were recorded at 20 °C.

4.3.5 Helical wheel fitting

A list of resolved peaks from the SLF spectrum was extracted as pairs of ^{15}N chemical shift and ^{15}N-^{1}H dipolar coupling values and arranged to fit into the helical wheels by using a home-written program in which the helical wheel patterns are predicted by geometrical calculations (45).

4.4 Results

4.4.1 Reconstitution of FBD into bicelles and regional assignment of one-dimensional ^{15}N solid-state spectra

In this study, experiments were performed on a uniformly ^{15}N-labeled membrane-bound FMN binding domain (FBD) in bicelles composed of DLPC/DHPC/cholesterol, the schematic of which is shown in Figure 4.1A. The single band on the SDS-PAGE gel reveals the purity of the protein (Figure 4.1B). The bicelles magnetically align with the lipid bilayer normal perpendicular to the external magnetic field B_0, as confirmed by the static ^{31}P NMR spectrum (Figure 4.1C).

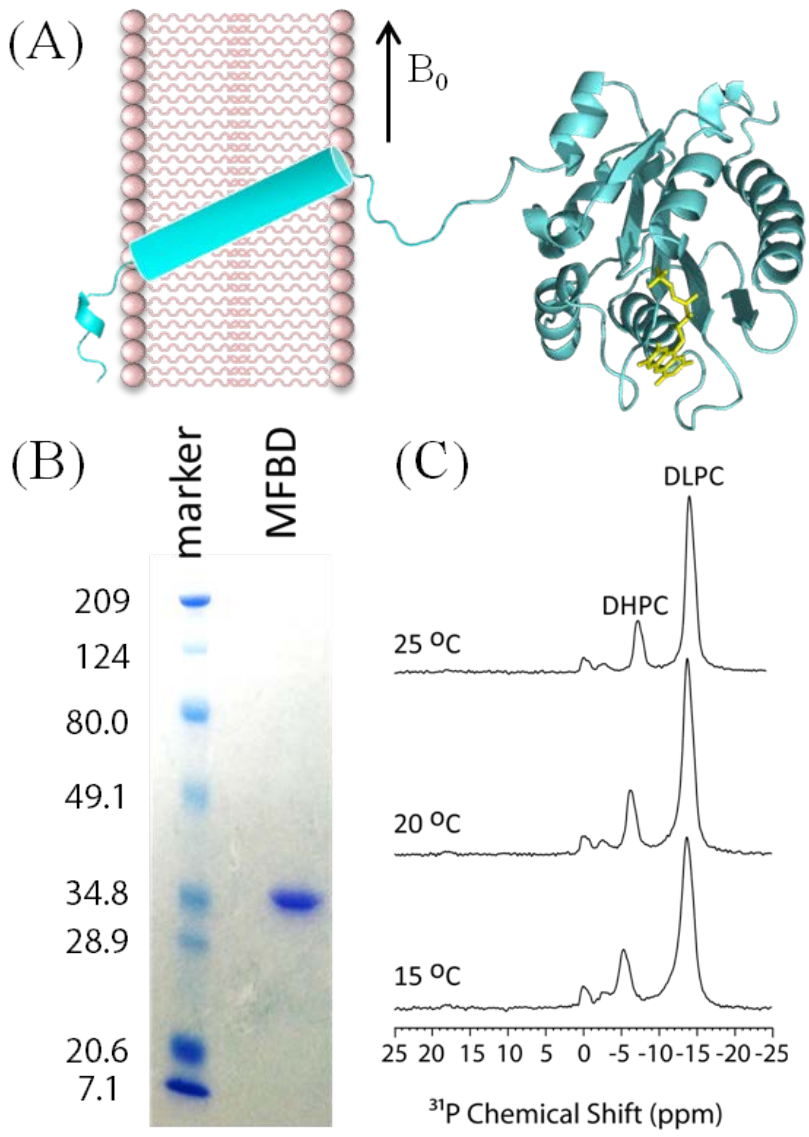

Figure 4.1 (A) A schematic of FBD with its N-terminal TM domain incorporated in lipid bilayers. (B) SDS-PAGE gel of FBD. (C) Proton-decoupled ^{31}P chemical shift spectra of DLPC/DHPC/cholesterol bicelles containing FBD. The narrow peaks for DLPC and DHPC demonstrate a high degree of alignment of bicelles. The peaks at 0 ppm and -2.5 ppm are from phosphorous atoms on FMN.

One-dimensional ^{1}H-^{15}N cross polarization (CP) experiment gives rise to distinct profiles in the ^{15}N spectra of FBD. The resonances distribute in two different chemical shift regions — 70-100 ppm and 100-140 ppm (Figure 4.2A-C, Figure 4.3B-E). In order to distinguish resonances from the soluble and transmembrane domains, we utilize the approach of hydrogen-deuterium (H/D) exchange to suppress the ^{15}N signals from the solvent-accessible residues. After 5 hours of H/D exchange, ^{15}N spectra of FBD shows only resonances from 70-100 ppm chemical shift region, suggesting resonances from this region correspond to the solvent-inaccessible residues which are probably located in the transmembrane domain embedded in the lipid bicelles. In comparison, resonances in 100-140 ppm chemical shift region show drastic reduction of intensities upon H/D exchange, implying that they might correspond to residues from the soluble domain. Similar phenomenon of segmented chemical shift regions for the soluble and transmembrane domains of a membrane protein is also observed in cytochrome b_5 (42, 46). A longer time exposure of the FBD to D_2O leads to further reduction of ^{15}N signals (Figure 4.2C) in both 100-140 ppm and 70-100 ppm regions possibly due to dynamics of the bicelles.

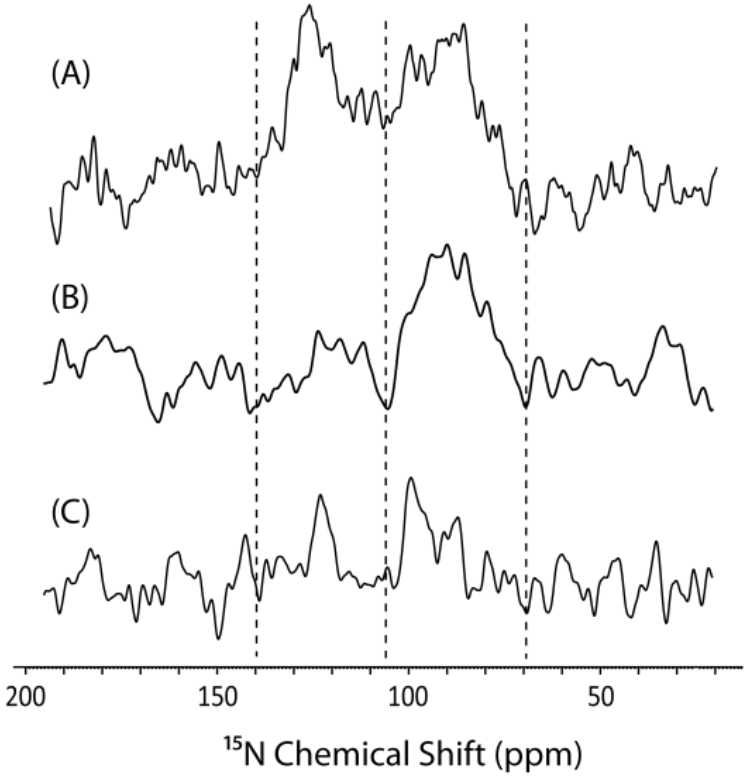

Figure 4.2 Hydrogen/Deuterium exchange spectra of FBD. ^{15}N NMR spectra were obtained using ramped cross-polarization (CP) with a contact time of 0.5 ms before (A) H/D exchange, 5 hours (B) and 17 hours (C) after H/D exchange.

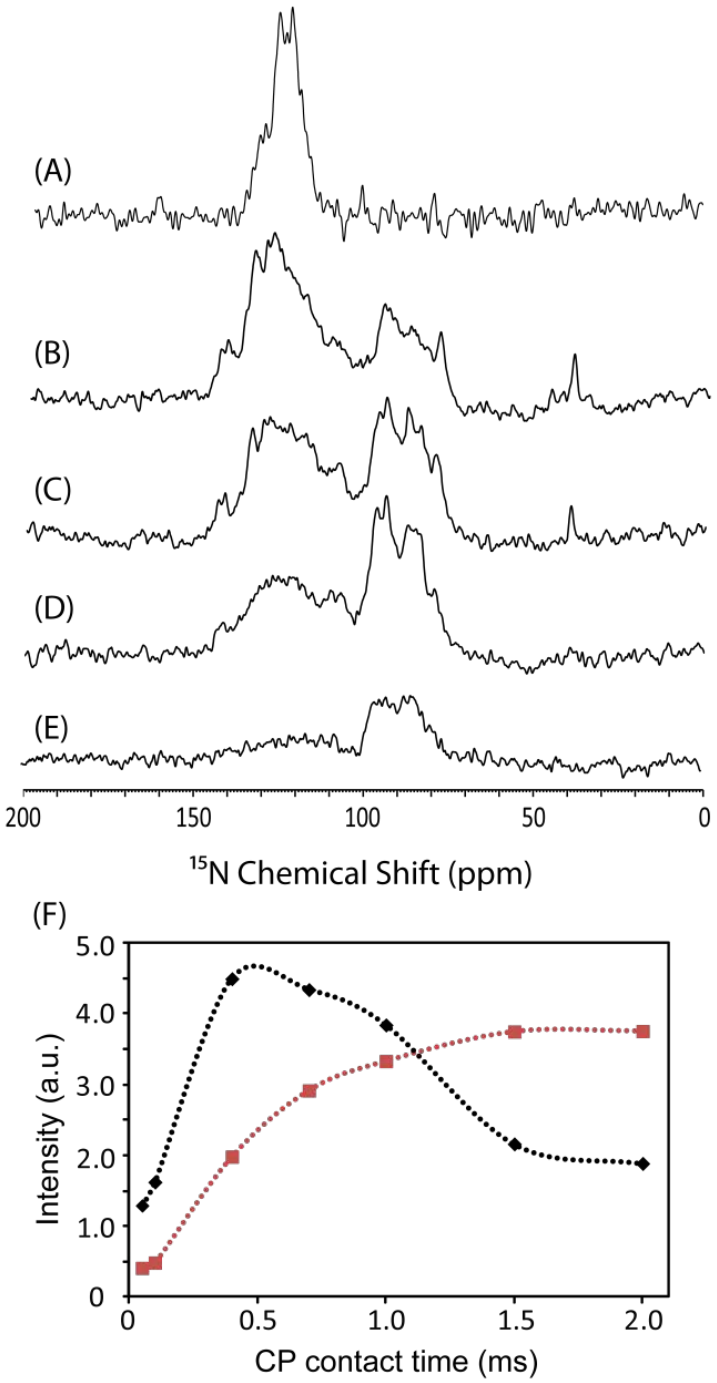

Figure 4.3 **^{15}N NMR spectra of FBD** were obtained using RINEPT (A) and ramped cross-polarization (CP) with a contact time of 2.0 ms (B), 1.0 ms (C), 0.4 ms (D), 0.1 ms (E). The RINEPT spectrum (A) shows spectral intensity only in the 100-140 ppm region, indicating the high mobility of the soluble domain. Resonances in the 70-100 ppm region in the CP spectra (B-E) are assigned to the immobile TM domain. Buildup curves (F) were measured for resonances at 93.5 ppm (black) and 128.4 ppm (red) representing the two chemical shift regions corresponding to two different domains.

4.4.2 CP dynamics revealing distinct characteristics of the soluble and transmembrane domains of FBD

In order to achieve optimal intensities of ^{15}N resonances, one-dimensional ^{15}N spectra were recorded with different ^{1}H-^{15}N polarization transfer schemes and varied cross polarization (CP) contact times. In the series of ^{15}N CP spectra (Figure 4.3B-E), the overall relative intensities in the two chemical shift regions —70-100 ppm and 100-140 ppm— change when CP contact time is varied to control the extent of magnetization transfer from ^{1}H to ^{15}N nuclei. The appearance of peaks in the 70-100 ppm region even for a short CP contact time (Figure 4.3E) indicates that these signals arise from immobile residues of the protein, most likely from the transmembrane domain. Use of longer CP contact times (Figure 4.3B-D) allows the magnetization to transfer not only to the rigid transmembrane region (70-100 ppm) but also to some relatively mobile residues in the soluble domain of the protein, which gives rise to signals in the 100-140 ppm region. These observations support our assignment from the results of the H/D exchange experiment. ^{15}N refocused-INEPT (RINEPT) experiment was employed to detect the mobile region of the protein (42, 46, 47). In the RINEPT spectrum (Figure 4.3A), peaks in the 70-100 ppm region arising from the transmembrane domain are significantly suppressed while most peaks from the soluble domain region (100-140 ppm) are present. This difference is due to the fast dephasing of the transverse magnetization from the transmembrane domain residues during the evolution and refocusing delays in RINEPT, caused by strong ^{1}H-^{15}N and ^{1}H-^{1}H dipolar couplings. An increase of the CP contact time (Figure 4.3B-C) increases the signal intensity for the soluble domain (100-140 ppm) but decreases that for the transmembrane domain (70-100 ppm) due to $T_{I\rho}$ relaxation. This observation also indicates that motions in the transmembrane domain are more restricted than in the soluble domain.

Dynamics are crucial for the physiological function of a protein and for protein-protein interactions. Parameters characterizing protein dynamics can be extracted from CP build-up curves. The buildup rates of peak intensities at 93.5 and 128.4 ppm are different indicating the significant difference in the dynamics between the transmembrane and soluble domains (Figure 4.3F). Typical behavior of CP buildup was observed at 93.5 ppm—intensity build-up during short CP contact time dominated by ^{1}H-^{15}N polarization transfer due to dipolar interaction and a loss of magnetization after saturation due to $T_{I\rho}$. Conversely, the peak at 128.4 ppm builds up slowly and does not decay with the increasing CP contact time, indicating the effect of a smaller

dipolar coupling due to faster dynamics in the soluble domain. Fitting the CP build-up curves using Eq. 1 provided a crude measurement of proton spin-lattice relaxation time in the rotating frame ($T_{1\rho}^{H}$) and the polarization transfer time-constant (T_{NH}) (48) for the transmembrane domain (at 93.5 ppm), which are 1.61 ±0.36 ms and 0.26 ± 0.05 ms, respectively. These two relaxation parameters reflect submillisecond timescale motions of the corresponding residues, which may include rotational diffusion of the whole helix and fluctuation of the helical director axis, and thus can be used to indicate changes in the dynamics of the transmembrane domain upon changes in the lipid membrane composition or interaction with other proteins. This is demonstrated here by using a lipid composition of DLPC/DHPC. The removal of cholesterol from bicelles increases the dynamics of the transmembrane domain as reflected by a longer $T_{1\rho}^{H}$ value of 2.08 ± 0.57 ms at 93.5 ppm (data not shown). This probably attribute to the effect of cholesterol on the rigidity of the lipid membrane, which in turn might affect the rotational

$$I(t) = \frac{I(0)}{T_{\mathrm{NH}}}\left(e^{-\frac{t}{T_{1\rho}}} - e^{-\frac{t}{T_{\mathrm{NH}}}}\right)\left(\frac{1}{T_{\mathrm{NH}}} - \frac{1}{T_{1\rho}^{\mathrm{H}}}\right)^{-1} \quad (1)$$

diffusion of the transmembrane helix.

4.4.3 SLF experiment and simulation of helical wheels reveal the conformation and tilt angle of the FBD transmembrane domain

Two-dimensional (2D) separated local field (SLF) spectra, which correlate ^{15}N chemical shift with ^{1}H-^{15}N dipolar coupling, were obtained to characterize the structure and further investigate the dynamics of the transmembrane domain (Figure 4.4). In the frequency region assigned to the transmembrane domain (70-100 ppm) in 1D ^{15}N spectra, a discernible circular wheel-like pattern of resonances was observed, which is unique for proteins with an α-helical conformation. This is the first experimental evidence of an α-helical secondary structure for the transmembrane domain of CPR, agreeing with some of the postulations in the literature (11-13). In the region assigned to the soluble domain (100-140 ppm), we also observed resonances with small dipolar coupling values, suggesting a weak alignment of the soluble domain in the bicelle environment.

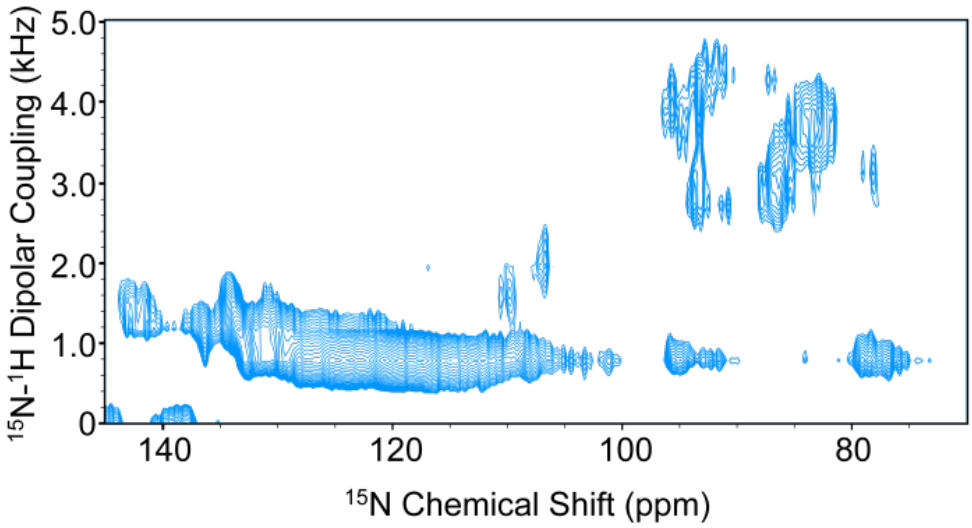

Figure 4.4 2D ^{15}N separated-local-field solid-state spectrum of uniformly ^{15}N labeled MFBD incorporated in DLPC/DHPC/ cholesterol bicelles. This spectrum was collected with a 0.5 ms CP contact time and 25 kHz SPINAL16 decoupling.

In order to further characterize the orientation and dynamics of the transmembrane helix, we performed a spectral simulation to fit the observed resonances into a helical wheel pattern. Simulations demonstrate the sensitivity of the wheel patterns to the helix tilt angle (with respect to membrane normal) and the order parameter (Figure 4.5A-C). The best-fit helical wheel (Figure 4.5D-E) indicates an average tilt angle of 13°±2° (49) and the overall order parameter S of 0.80. The order parameter reflects a collection of motions that the α-helix exhibits in the lipid bilayer, ranging from rotational diffusion to fluctuation of the helical director axis, the schematic of which is shown in Figure 4.5F. Similar tilt angle and order parameter have also been observed for the transmembrane domain of cytochrome b_5 (42, 45). As shown in Figure 4.5D-E, no single wheel can fit all the resonances in the circular pattern, implying nonideality of the transmembrane helix. Additional experiments using selectively labeled FBD will be carried out to assign the spectra and to study FBD-P450 interaction.

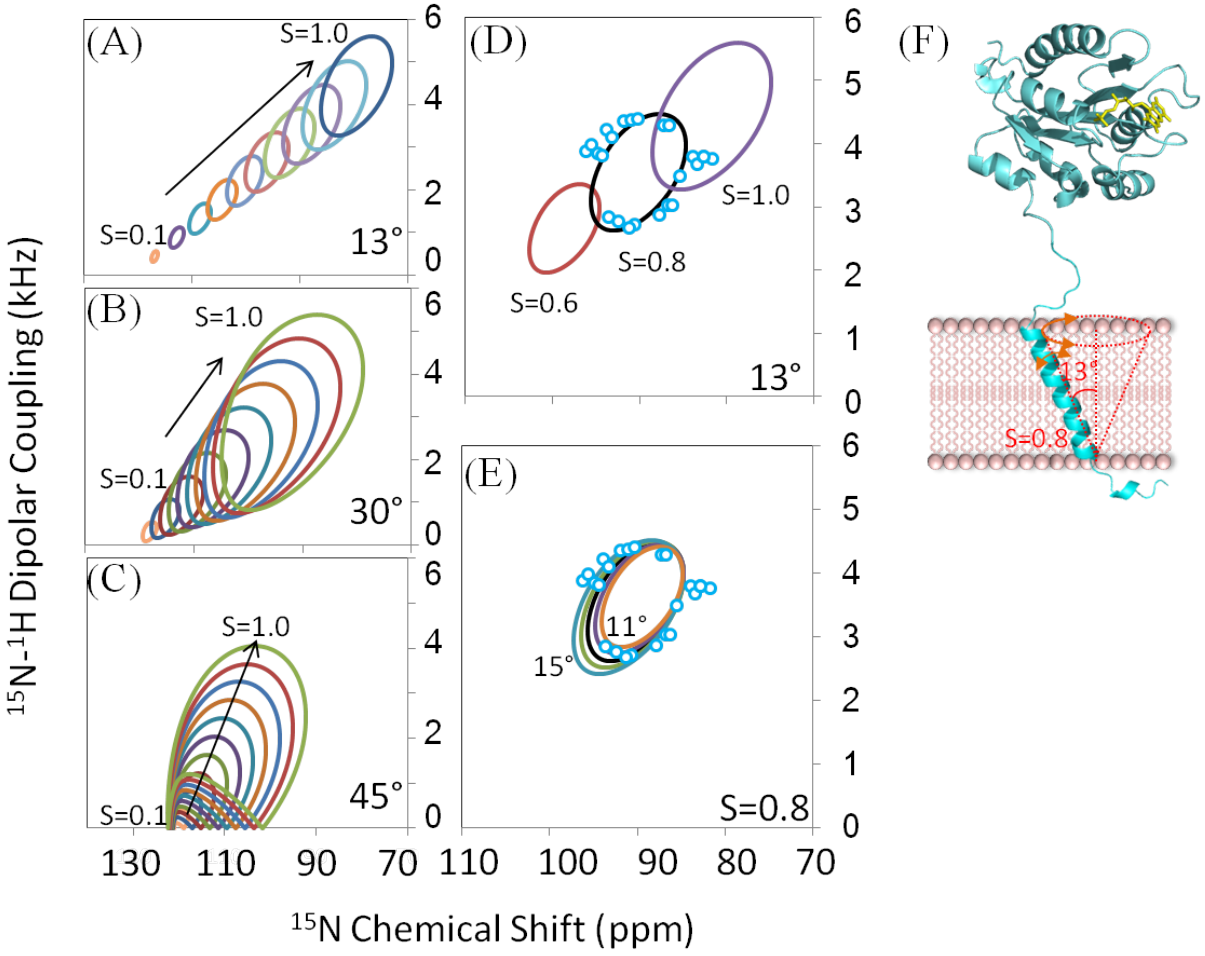

Figure 4.5 Simulated helical wheels showing the sensitivity of the wheel pattern to the indicated tilt angle. (*D & E*) Fitting of the observed resonances in the SLF spectra of FBD (blue circles) with different tilt angles and order parameters. The tilt angle used in (*D*) is 13° with order parameters S of 0.6 (*red*), 0.8 (*black*), 1.0 (*purple*). The order parameter used in (*E*) is 0.8 with varied tilt angles: 11° (*orange*), 12° (*purple*), 13° (*black*), 14° (*green*) and 15° (*blue*). The best-fitting wheel indicates an average helical tilt angle of 13° and an order parameter S of 0.8 (*F*).

4.4.4 One-dimensional ^{15}N solid-state spectra and CP dynamics of FBD-P450 complex

In order to investigate the interaction between FBD and cyt P450, experiments were performed on a uniformly ^{15}N-labeled FBD incorporated in magnetically aligned DLPC/DHPC/cholesterol bicelles in the presence of equal molar unlabeled cyt P450. Alignment of the bicelles is confirmed by the static ^{31}P spectra shown in Figure 4.6. One-dimensional ^{15}N spectra of the complex were recorded with varied cross polarization (CP) contact times (Figure 4.7, red) and compared with those of free FBD (Figure 4.7, black). In the series of ^{15}N CP spectra, the resonances of FBD distribute into two chemical shift regions — 70-100 ppm region corresponding to residues from the transmembrane domain and 100-140 ppm region corresponding to those from the soluble domain as described above. We observe differences in the line shape and intensities of the FBD resonances (Figure 4.7, red and black), implying changes in dynamics and/or orientation of FBD due to interaction with cyt P450. In the soluble domain region (100-140 ppm), it is evident that the signal intensities of FBD in the presence of cyt P450 have a faster buildup and decay rate with respect to CP contact time compared with those of free FBD. This observation indicates that motions in the FBD soluble domain are more restricted as a consequence of interaction with cyt P450, which leads to stronger dipolar coupling and thus more efficient polarization transfer and faster relaxation. In the transmembrane domain region (100-140 ppm), differences between the ^{15}N spectra of cyt P450-bound and unbound FBD are less pronounced; therefore, CP build-up curves were analyzed and compared between these two cases.

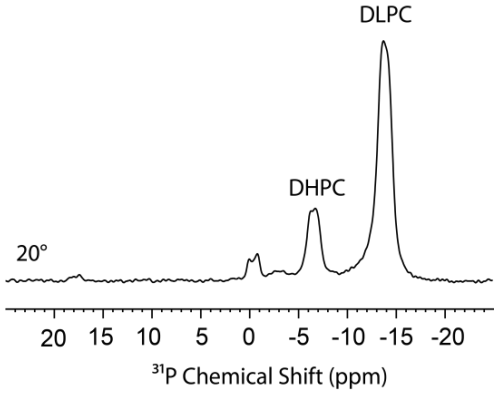

Figure 4.6 Proton-decoupled ^{31}P chemical shift spectra of DLPC/DHPC/cholesterol (molar ratio=4:1:0.4) bicelles containing 1:1 molar ratio of FBD and cyt P450. The narrow peaks for DLPC and DHPC demonstrate a high degree of alignment of bicelles. The peak at around 0 ppm is due to phosphate buffer.

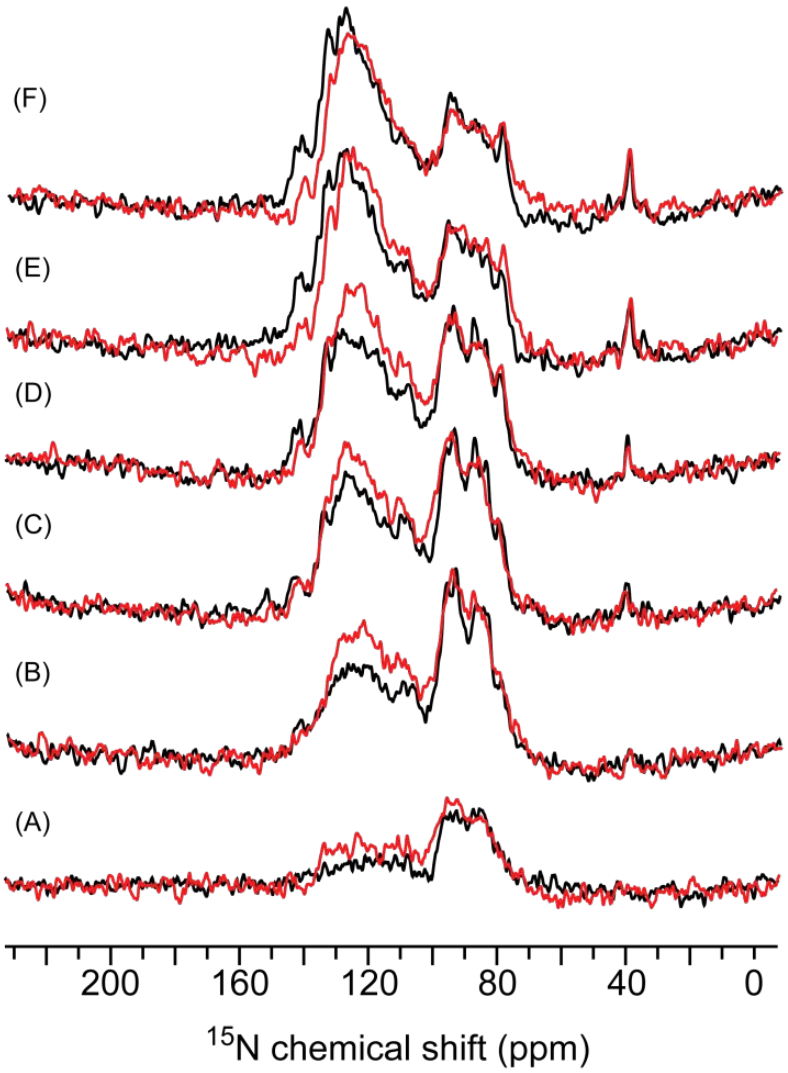

Figure 4.7 1D ^{15}N NMR spectra of uniformly ^{15}N-labeled FBD of CPR in the presence (red) and absence (black) of cyt P450 at molar ratio of 1:1. Spectra were recorded using ramped CP with a contact time of 0.1 ms (A), 0.4 ms (B), 0.7 ms (C), 1.0 ms (D), 1.5 ms (E), 2.0 ms (F). The differences between the spectra of cyt P450-bound FBD (red) and of free FBD (black) reflect changes in structure and dynamics of FBD due to cyt P450-FBD interaction. An evidently faster buildup rate of intensities in the 100-140 ppm region implies significant increased rigidity in the soluble domain of MFBD when bound to cyt P450.

Distinct buildup profiles of the transmembrane domain (Figure 4.8 A-C) and the soluble domain (Figure 4.8 D-F) demonstrate marked differences in the dynamics between the two domains. The transmembrane domain resonances have apparently faster buildup and decay rates than the soluble domain, suggesting higher rigidity of the transmembrane domain. Fitting the CP buildup curves using equation (1) provides the proton spin-lattice relaxation time in the rotating frame ($T_{1\rho}{}^{H}$) and polarization transfer time-constant (T_{NH}) (*48*) where *I(0)* denotes the initial peak intensity. For the soluble domain resonances (Figure 4.8 D-F), accurate $T_{1\rho}{}^{H}$ and T_{NH} values cannot be drawn from the fitting due to insufficient $T_{1\rho}{}^{H}$ relaxation during the experimental CP contact times. However, it is clear that intensities build up and decay faster in the presence of cyt P450 (Figure 4.8D-E, red) than in its absence (Figure 4.8D-E, black), implying an interaction between the soluble domains of MFBD and cyt P450. $T_{1\rho}{}^{H}$ and T_{NH} values for the transmembrane domain resonances are summarized in Table 1. In comparison, FBD interaction with cyt P450 leads to slight increase in the $T_{1\rho}{}^{H}$ values, suggesting enhanced dynamics in the transmembrane domain of FBD on the submillisecond time scale (48).

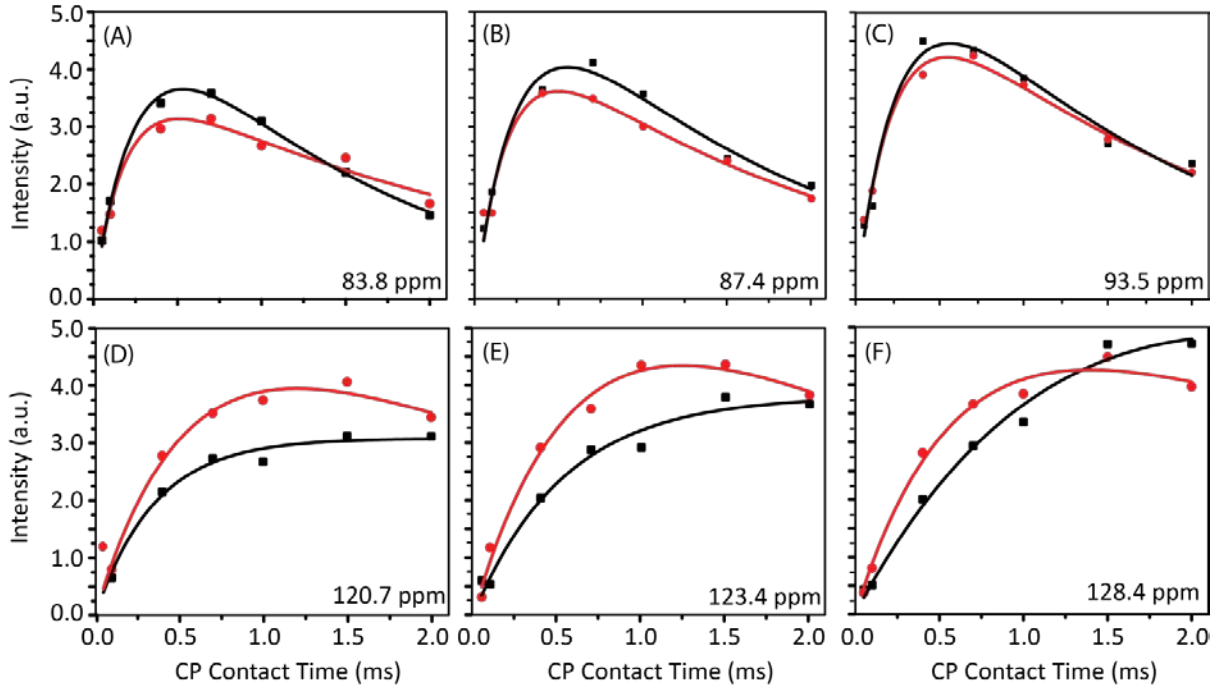

Figure 4.8 Build-up curves of resonances in the transmembrane domain region (83.8 ppm (A), 87.4 ppm (B), 93.5 ppm (C)) and the soluble domain region (120.7 ppm (D), 123.4 ppm (E), 128.4 ppm (F)) for the free MFBD (black) and cyt P450-bound MFBD (red). The intensity scales were set arbitrary but identical for all curves. Curves were fit into equation (1) to obtain dynamic parameters $T_{1\rho}{}^{H}$ and T_{NH}.

Table 4.1 T_{NH} and $T_{1\rho}^{H}$ values for the transmembrane domain resonances of MFBD calculated from 1D ^{15}N CP buildup curves of free MFBD and cyt P450-bound MFBD

peaks (ppm)	T_{NH} (ms)		$T_{1\rho}^{H}$ (ms)	
	Free MFBD	P450-bound MFBD	Free MFBD	P450-bound MFBD
83.8	0.26±0.02	0.18±0.04	1.33±0.12	2.39±0.59
87.4	0.25±0.05	0.20±0.05	1.58± 0.30	1.84±0.47
93.5	0.26±0.06	0.23±0.03	1.61±0.36	1.86±0.29

4.4.5 SLF experiment on the FBD-P450 complex and simulation of helical wheels

In order to further investigate the effect of FBD-cyt P450 complex formation on the structure and dynamics of the transmembrane domain of FBD, two-dimensional separated local field (SLF) spectra were obtained (Figure 4.9). The characteristic α-helical transmembrane domain of free FBD gives rise to a discernible circular PISA (Polarity Index Slant Angle)-wheel pattern in the transmembrane domain region (70-100 ppm) (Figure 4.9A, red). In the presence of cyt P450, the distribution of the FBD resonances is disturbed, resulting in a more dispersed wheel pattern and overall reduced dipolar couplings (Figure 4.9A, blue). This observation suggests a change in the tilt angle of the FBD transmembrane helix and enhanced dynamics by interacting with cyt P450. A spectral simulation was performed to further characterize the orientation and dynamics of the transmembrane helix of cyt P450-bound FBD. When compared with the 13° tilt angle and an order parameter of 0.4 for the transmembrane helix of free FBD (Figure 4.9B), resonances of cyt P450-bound FBD are distributed in a more scattered fashion (Figure 4.9C) and cannot be fitted with a single tilt angle. Two PISA wheels simulated with tilt angles of 13° and 18° respectively with an order parameter of S=0.35 largely cover the majority of the resonances (Figure 4.9C). This simulation implies inhomogeneous tilt angles adopted by the FBD transmembrane helix, which are potentially caused by interaction with the transmembrane domain of cyt P450. A decreased order parameter for the cyt P450-bound FBD (S=0.35) compared with that for the free FBD (S=0.4) suggests higher mobility of the FBD transmembrane domain due to complex formation, in agreement with our hypothesis from $T_{1\rho}$ analysis.

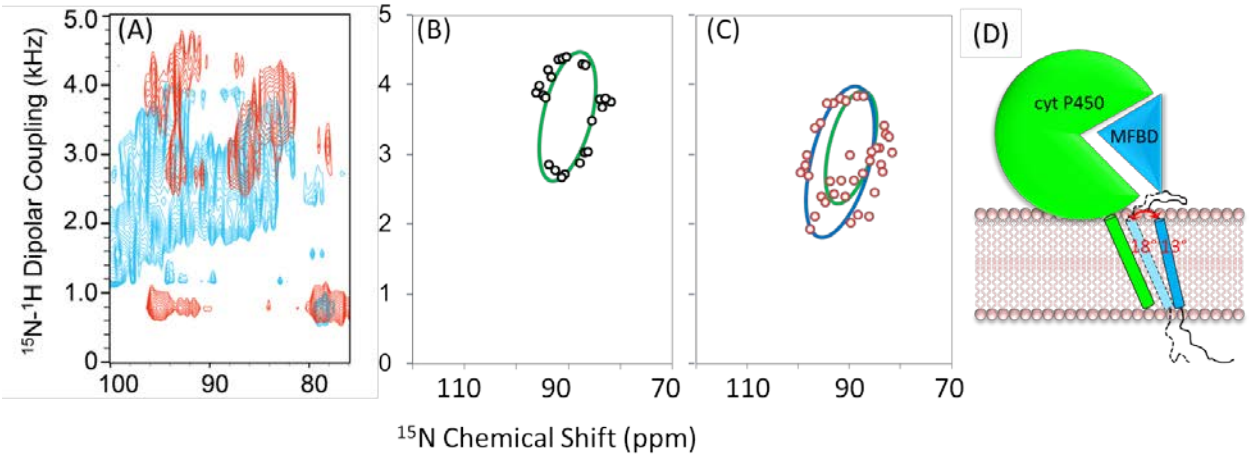

Figure 4.9 2D ^{15}N separated-local-field spectra of uniformly ^{15}N-labeled MFBD in the presence (A, blue) and absence (A, red) of equal equivalence of cyt P450 in DLPC/DHPC/cholesterol bicelles. The spectra were collected at 720 MHz with a 0.5 ms CP contact time and 25 kHz SPINAL16 decoupling. Best fit of the observed resonances (open circles) with simulated helical wheel patterns. Resonances of the free MFBD can be fit with a tilt angle of 13° and an order parameter of 0.8 (B, green), and resonances of cyt P450-bound MFBD can be fit into two wheels with tilt angles of 13° (C, green) and 18° (C, blue) with the same order parameter of 0.7. A cartoon (D) demonstrates complex formation between the soluble domains of MFBD and cyt P450 and a transient interaction between the transmembrane helices.

4.5 Discussion

4.5.1 Secondary structure of the transmembrane domain of CPR in lipid environment

The criticality of the transmembrane domain of CPR in the complex formation with cyt P450 and substrate metabolism mediated by cyt P450 has been predicated through the decades (8-10, 50-52). It is general believed that the N-terminal hydrophobic segment of CPR serves as an anchor to the endoplasm reticulum and nuclear envelope and aid in interaction and electron transfer between CPR and cyt P450 (6). However, the mechanism on how the transmembrane domain affects cyt P450/CPR interaction and substrate catalysis remains under debate (8), and the experimental evidences to unveil the mist are highly deficient. In order to better understand the physiological function of the transmembrane domain of CPR, we decided to carefully characterize its structure and dynamics in a lipid membrane environment.

The transmembrane domain of CPR was predicted to contain a β-sheet structure and possibly adopt a “U” shape in the membrane in the early literature (10), while in recent years it has been mostly presumed that the transmembrane anchor spans the lipid bilayer in an α-helical

conformation (11-13). Our studies present the first experimental evidence of an α-helical secondary structure for the transmembrane domain, in line with the previous hypotheses (11-13). The overall order parameter of the transmembrane domain coincides with those observed in the membrane-spanning transmembrane helices in the literature, further supporting that the transmembrane helix of CPR spans the bilayer in the bicelles (53-55). The helix tilt can be determined precisely from the range and average of the dipolar couplings, and it can be affected by the hydrophobic mismatch between the length of the transmembrane helix and the hydrophobic region of the phospholipids (54). The tilt angle of 13° for the transmembrane helix of CPR is comparable with those measured in cytochrome b_5 (13°) and cytochrome P450 (17°) in bicelles, revealing geometrical similarity in the transmembrane domains of these electron transfer partners. The interplay between the transmembrane domains of these proteins and their role in affecting electron transfer and complex formation are currently under investigation in our laboratory.

4.5.2 Distinct dynamics of the soluble and transmembrane domain of CPR

Motions and structural dynamics are essential to the physiological function of membrane proteins. In order to gain insight into the role of the transmembrane domain of CPR in protein-protein interaction, we first seek to elucidate the dynamic behavior of FBD. In a series of CP experiments (Figure 4.3), we observe distinct buildup dynamics between the soluble and transmembrane domain. In our immobilized system, the CP dynamics are dominated by dipolar interactions, which are sensitive to submillisecond motions. Evidently faster CP buildup and decay rates of the transmembrane domain signals (Figure 4.3F) indicate restrained motions of this domain compared with the soluble domain. Analysis of CP dynamics also leads to an estimation of $T_{1\rho}{}^{H}$ and T_{NH} values, which qualitatively reflect the mobility of the corresponding resonances. In the 2D SLF spectrum, difference between the mobility of the two domains is clearly presented by the values of the dipolar couplings (Figure 4.4). Heteronuclear dipolar coupling reports on the amplitude of local motions occurring on a time scale faster than the inverse of interaction. The average dipolar couplings for the transmembrane domain are approximately three times larger than those observed for the soluble domain, implying the soluble domain undergoes motions of larger amplitude in the submillisecond timescale, in line with the result of CP dynamics.

The distinct dynamic characteristics of the two domains are highly correlated with their functions. The soluble FMN binding domain is suggested to be able to diffuse rapidly in the cytosol in order for fast association and dissociation with cyt P450 to maximize the turnover rate of electron transfer. On the other hand, we observe small dipolar couplings of approximately 1 kHz in the soluble domain (Figure 4.4), implying weak alignment of this domain or transient interaction with the lipid bilayer instead of isotropic tumbling/diffusion like a globular protein. This may attribute to the anchoring effect of the transmembrane domain, which may constrain the diffusion of the soluble domain to the proximity of the membrane surface and meanwhile orient the protein properly for interacting with cyt P450. Besides serving as an anchor, the transmembrane domain of CPR might also be involved in hetero-recognition with the transmembrane domain of cyt P450. These interactions can be reflected by characterizing the dynamics of the transmembrane domain in the presence of cyt P450. In lipid bilayer, the motions of a single α-helix can be visualized as rotational diffusion around the membrane normal and fluctuation of the helix tilt (45). The amplitude of these motions collectively influences the magnitude of NMR parameters, in particular chemical shift anisotropies and dipolar couplings (56, 57). By measuring the dipolar coupling values and determining the order parameter, we can monitor the dynamic changes of the transmembrane domain upon changes of the lipid environment or protein-protein interaction.

In the presence of cyt P450, we observed enhanced dipolar coupling in the soluble domain of FBD, indicating complex formation between the two proteins in the DLPC/DHPC bicelles. This coincides with the physiological role of FBD in transferring electrons to cyt P450 in the lipid membrane. On the other hand, the transmembrane helix of MFBD shows inhomogeneous tilt angles from 13° to 18° with increased mobility upon interaction with cyt P450. This observation might attribute to the transient interaction between the two transmembrane domains, which deviates the transmembrane helix of MFBD from its thermal equilibrium tilt angle in the free form (13°) towards the tilt angle of cyt P450 transmembrane helix (17°) (43). Furthermore, slightly decreased dipolar coupling and order parameter of the FBD transmembrane domain suggests a fairly weak interaction between the two transmembrane domains where the helix of FBD fluctuates between the bound and unbound states besides its axial rotational motion (45), inducing averaging of the dipolar coupling (Figure 4.2D). This transient interaction between the transmembrane domains could aid in orienting the soluble

domains of the two proteins for proper complex formation without hampering the fast dissociation that is required for efficient turnover of the cyt P450 substrates.

4.6 Conclusion

In this chapter, we have shown the first structural and dynamic study on the FMN binding domain of CPR including the transmembrane helix and the linker region in the protein's native-like membrane environment using solid-state NMR. We have provided the first experimental evidence of an α-helical conformation for the rigid transmembrane anchor of CPR. The focal point is the orientation and dynamic information of the transmembrane domain obtained in absence of spectral assignment, the knowledge of which is useful to better understand the role of the CPR transmembrane domain. We have also investigated the interaction between the FMN binding domain and cyt P450 in DLPC/DHPC bicelles. The results not only reveal the interaction between the soluble domains of FBD and cyt P450 in the membrane environment, but also provide some of the first direct evidences for the transient interplay between the transmembrane helices. This information sheds light on the physiological role of the transmembrane domains in CPR-cyt P450 interaction and/or catalysis.

The successful implementation of a combination of 1D CP and 2D SLF spectra provides a simple method for further investigating the structural and dynamic properties of full-length CPR and its interaction with other membrane proteins in a membrane environment. Compared with alternative approaches that determine secondary structures (*e.g.* circular dichroism spectroscopy), our approach allows us not only to obtain conformational information of the transmembrane helix but also to investigate the dynamics behavior of the soluble domain and the transmembrane domain simultaneously, rendering great convenience in direct comparison of the two domains. Along with the resonance assignments, the approaches demonstrated in this work can be extended to structural studies of other membrane proteins.

4.7 References

1. Shen, A. L., O'Leary, K. A., and Kasper, C. B. (2002) Association of multiple developmental defects and embryonic lethality with loss of microsomal NADPH-cytochrome P450 oxidoreductase, *J Biol Chem 277*, 6536-6541.

2. Williams, C. H., Jr., and Kamin, H. (1962) Microsomal triphosphopyridine nucleotide-cytochrome c reductase of liver, *J Biol Chem 237*, 587-595.

3. Enoch, H. G., and Strittmatter, P. (1979) Cytochrome b5 reduction by NADPH-cytochrome P-450 reductase, *J Biol Chem 254*, 8976-8981.

4. Schacter, B. A., Nelson, E. B., Marver, H. S., and Masters, B. S. (1972) Immunochemical evidence for an association of heme oxygenase with the microsomal electron transport system, *J Biol Chem 247*, 3601-3607.

5. Bachur, N. R., Gordon, S. L., Gee, M. V., and Kon, H. (1979) NADPH cytochrome P-450 reductase activation of quinone anticancer agents to free radicals, *Proc Natl Acad Sci U S A 76*, 954-957.

6. Wang, M., Roberts, D. L., Paschke, R., Shea, T. M., Masters, B. S., and Kim, J. J. (1997) Three-dimensional structure of NADPH-cytochrome P450 reductase: prototype for FMN- and FAD-containing enzymes, *Proc Natl Acad Sci U S A 94*, 8411-8416.

7. Xia, C., Panda, S. P., Marohnic, C. C., Martasek, P., Masters, B. S., and Kim, J. J. (2011) Structural basis for human NADPH-cytochrome P450 oxidoreductase deficiency, *Proc Natl Acad Sci U S A 108*, 13486-13491.

8. Gideon, D. A., Kumari, R., Lynn, A. M., and Manoj, K. M. (2012) What is the Functional Role of N-terminal Transmembrane Helices in the Metabolism Mediated by Liver Microsomal Cytochrome P450 and its Reductase?, *Cell Biochem Biophys 63*, 35-45.

9. Gum, J. R., and Strobel, H. W. (1981) Isolation of the membrane-binding peptide of NADPH-cytochrome P-450 reductase. Characterization of the peptide and its role in the interaction of reductase with cytochrome P-450, *J Biol Chem 256*, 7478-7486.

10. Black, S. D., and Coon, M. J. (1982) Structural features of liver microsomal NADPH-cytochrome P-450 reductase. Hydrophobic domain, hydrophilic domain, and connecting region, *J Biol Chem 257*, 5929-5938.

11. Sundermann, A., and Oostenbrink, C. (2013) Molecular dynamics simulations give insight into the conformational change, complex formation, and electron transfer pathway for cytochrome P450 reductase, *Protein Sci 22*, 1183-1195.

12. Im, S. C., and Waskell, L. (2011) The interaction of microsomal cytochrome P450 2B4 with its redox partners, cytochrome P450 reductase and cytochrome b(5), *Arch Biochem Biophys 507*, 144-153.

13. Durr, U. H., Waskell, L., and Ramamoorthy, A. (2007) The cytochromes P450 and b5 and their reductases--promising targets for structural studies by advanced solid-state NMR spectroscopy, *Biochim Biophys Acta 1768*, 3235-3259.

14. Bridges, A., Gruenke, L., Chang, Y. T., Vakser, I. A., Loew, G., and Waskell, L. (1998) Identification of the binding site on cytochrome P450 2B4 for cytochrome b5 and cytochrome P450 reductase, *J Biol Chem 273*, 17036-17049.

15. Centeno, F., and Gutierrez-Merino, C. (1992) Location of functional centers in the microsomal cytochrome P450 system, *Biochemistry 31*, 8473-8481.

16. Lehnerer, M., Schulze, J., Achterhold, K., Lewis, D. F., and Hlavica, P. (2000) Identification of key residues in rabbit liver microsomal cytochrome P450 2B4: importance in interactions with NADPH-cytochrome P450 reductase, *J Biochem 127*, 163-169.

17. Davydov, D. R., Kariakin, A. A., Petushkova, N. A., and Peterson, J. A. (2000) Association of cytochromes P450 with their reductases: opposite sign of the electrostatic interactions in P450BM-3 as compared with the microsomal 2B4 system, *Biochemistry 39*, 6489-6497.

18. Eyer, C. S., and Backes, W. L. (1992) Relationship between the rate of reductase-cytochrome P450 complex formation and the rate of first electron transfer, *Arch Biochem Biophys 293*, 231-240.

19. Zhang, H., Im, S. C., and Waskell, L. (2007) Cytochrome b5 Increases the Rate of Product Formation by Cytochrome P450 2B4 and Competes with Cytochrome P450 Reductase for a Binding Site on Cytochrome P450 2B4, *J Biol Chem 282*, 29766-29776.

20. Voznesensky, A. I., and Schenkman, J. B. (1994) Quantitative analyses of electrostatic interactions between NADPH-cytochrome P450 reductase and cytochrome P450 enzymes, *J Biol Chem 269*, 15724-15731.

21. Shimada, T., Mernaugh, R. L., and Guengerich, F. P. (2005) Interactions of mammalian cytochrome P450, NADPH-cytochrome P450 reductase, and cytochrome b5 enzymes, *Archives of Biochemistry and Biophysics 435*, 207-216.

22. Murataliev, M., Guzov, V., Walker, F., and Feyereisen, R. (2008) P450 reductase and cytochrome b5 interactions with cytochrome P450: Effects on house fly CYP6A1 catalysis, *Insect Biochemistry and Molecular Biology 38*, 1008-1015.

23. Im, S.-C., and Waskell, L. (2011) The interaction of microsomal cytochrome P450 2B4 with its redox partners, cytochrome P450 reductase and cytochrome b5, *Archives of Biochemistry and Biophysics 507*, 144-153.

24. Kenaan, C., Zhang, H., Shea, E. V., and Hollenberg, P. F. (2011) Uncovering the Role of Hydrophobic Residues in Cytochrome P450−Cytochrome P450 Reductase Interactions, *Biochemistry 50*, 3957-3967.

25. Davydov, D. R., Knyushko, T. V., Kanaeva, I. P., Koen, Y. M., Samenkova, N. F., Archakov, A. I., and Hui Bon Hoa, G. (1996) Interactions of cytochrome P450 2B4 with NADPH-cytochrome P450 reductase studied by fluorescent probe, *Biochimie 78*, 734-743.

26. Voznesensky, A. I., and Schenkman, J. B. (1992) The cytochrome P450 2B4-NADPH cytochrome P450 reductase electron transfer complex is not formed by charge-pairing, *J Biol Chem 267*, 14669-14676.

27. Bumpus, N. N., and Hollenberg, P. F. (2010) Cross-linking of human cytochrome P450 2B6 to NADPH-cytochrome P450 reductase: Identification of a potential site of interaction, *Journal of Inorganic Biochemistry 104*, 485-488.

28. Kariakin, A., Davydov, D., Peterson, J. A., and Jung, C. (2002) A new approach to the study of protein-protein interaction by FTIR: complex formation between cytochrome P450BM-3 heme domain and FMN reductase domain, *Biochemistry 41*, 13514-13525.

29. Kiselyova, O. I., Yaminsky, I. V., Ivanov, Y. D., Kanaeva, I. P., Kuznetsov, V. Y., and Archakov, A. I. (1999) AFM study of membrane proteins, cytochrome P450 2B4, and NADPH-cytochrome P450 reductase and their complex formation, *Arch Biochem Biophys 371*, 1-7.

30. Ivanov, Y. D., Kanaeva, I. P., Kuznetsov, V. Y., Lehnerer, M., Schulze, J., Hlavica, P., and Archakov, A. I. (1999) The optical biosensor studies on the role of hydrophobic tails of NADPH-cytochrome P450 reductase and cytochromes P450 2B4 and b5 upon productive complex formation within a monomeric reconstituted system, *Arch Biochem Biophys 362*, 87-93.

31. Shen, S., and Strobel, H. W. (1993) Role of lysine and arginine residues of cytochrome P450 in the interaction between cytochrome P4502B1 and NADPH-cytochrome P450 reductase, *Arch Biochem Biophys 304*, 257-265.

32. Nadler, S. G., and Strobel, H. W. (1991) Identification and characterization of an NADPH-cytochrome P450 reductase derived peptide involved in binding to cytochrome P450, *Arch Biochem Biophys 290*, 277-284.

33. Lin, H.-l., Kenaan, C., Zhang, H., and Hollenberg, P. F. (2012) Reaction of Human Cytochrome P450 3A4 with Peroxynitrite: Nitrotyrosine Formation on the Proximal Side Impairs Its Interaction with NADPH-Cytochrome P450 Reductase, *Chemical Research in Toxicology 25*, 2642-2653.

34. Nikfarjam, L., Izumi, S., Yamazaki, T., and Kominami, S. (2006) The interaction of cytochrome P450 17alpha with NADPH-cytochrome P450 reductase, investigated using chemical modification and MALDI-TOF mass spectrometry, *Biochim Biophys Acta 1764*, 1126-1131.

35. Shen, S., and Strobel, H. W. (1992) The role of cytochrome P450 lysine residues in the interaction between cytochrome P450IA1 and NADPH-cytochrome P450 reductase, *Arch Biochem Biophys 294*, 83-90.

36. Voznesensky, A. I., Schenkman, J. B., Pernecky, S. J., and Coon, M. J. (1994) The NH2-terminal region of rabbit CYP2E1 is not essential for interaction with NADPH-cytochrome P450 reductase, *Biochem Biophys Res Commun 203*, 156-161.

37. Dong, M. S., Yamazaki, H., Guo, Z., and Guengerich, F. P. (1996) Recombinant human cytochrome P450 1A2 and an N-terminal-truncated form: construction, purification, aggregation properties, and interactions with flavodoxin, ferredoxin, and NADPH-cytochrome P450 reductase, *Arch Biochem Biophys 327*, 11-19.

38. Miller, J. P., Lo, R. S., Ben-Hur, A., Desmarais, C., Stagljar, I., Noble, W. S., and Fields, S. (2005) Large-scale identification of yeast integral membrane protein interactions, *Proc Natl Acad Sci U S A 102*, 12123-12128.

39. Tarassov, K., Messier, V., Landry, C. R., Radinovic, S., Serna Molina, M. M., Shames, I., Malitskaya, Y., Vogel, J., Bussey, H., and Michnick, S. W. (2008) An in vivo map of the yeast protein interactome, *Science 320*, 1465-1470.

40. Costanzo, M., Baryshnikova, A., Bellay, J., Kim, Y., Spear, E. D., Sevier, C. S., Ding, H., Koh, J. L., Toufighi, K., Mostafavi, S., Prinz, J., St Onge, R. P., VanderSluis, B., Makhnevych, T., Vizeacoumar, F. J., Alizadeh, S., Bahr, S., Brost, R. L., Chen, Y., Cokol, M., Deshpande, R., Li, Z., Lin, Z. Y., Liang, W., Marback, M., Paw, J., San Luis, B. J., Shuteriqi, E., Tong, A. H., van Dyk, N., Wallace, I. M., Whitney, J. A., Weirauch, M. T., Zhong, G., Zhu, H., Houry, W. A., Brudno, M., Ragibizadeh, S., Papp, B., Pal, C., Roth, F. P., Giaever, G., Nislow, C., Troyanskaya, O. G., Bussey, H., Bader, G. D., Gingras, A. C., Morris, Q. D., Kim, P. M., Kaiser, C. A., Myers, C. L., Andrews, B. J., and Boone, C. (2010) The genetic landscape of a cell, *Science 327*, 425-431.

41. Miao, Y., and Cross, T. A. (2013) Solid state NMR and protein-protein interactions in membranes, *Curr Opin Struct Biol 23*, 919-928.

42. Yamamoto, K., Durr, U. H., Xu, J., Im, S. C., Waskell, L., and Ramamoorthy, A. (2013) Dynamic interaction between membrane-bound full-length cytochrome P450 and cytochrome b5 observed by solid-state NMR spectroscopy, *Sci Rep 3*, 2538.

43. Yamamoto, K., Gildenberg, M., Ahuja, S., Im, S. C., Pearcy, P., Waskell, L., and Ramamoorthy, A. (2013) Probing the transmembrane structure and topology of microsomal cytochrome-p450 by solid-state NMR on temperature-resistant bicelles, *Sci Rep 3*, 2556.

44. Gor'kov, P. L., Chekmenev, E. Y., Li, C. G., Cotten, M., Buffy, J. J., Traaseth, N. J., Veglia, G., and Brey, W. W. (2007) Using low-E resonators to reduce RF heating in biological samples for static solid-state NMR up to 900 MHz, *J. Magn. Reson. 185*, 77-93.

45. Soong, R., Smith, P. E., Xu, J., Yamamoto, K., Im, S. C., Waskell, L., and Ramamoorthy, A. (2010) Proton-evolved local-field solid-state NMR studies of cytochrome b5 embedded in bicelles, revealing both structural and dynamical information, *J Am Chem Soc 132*, 5779-5788.

46. Durr, U. H., Yamamoto, K., Im, S. C., Waskell, L., and Ramamoorthy, A. (2007) Solid-state NMR reveals structural and dynamical properties of a membrane-anchored electron-carrier protein, cytochrome b5, *J Am Chem Soc 129*, 6670-6671.

47. Xu, J., Soong, R., Im, S. C., Waskell, L., and Ramamoorthy, A. (2010) INEPT-based separated-local-field NMR spectroscopy: a unique approach to elucidate side-chain dynamics of membrane-associated proteins, *J Am Chem Soc 132*, 9944-9947.

48. Kawamura, I., Ohmine, M., Tanabe, J., Tuzi, S., Saito, H., and Naito, A. (2007) Dynamic aspects of extracellular loop region as a proton release pathway of bacteriorhodopsin studied by relaxation time measurements by solid state NMR, *Biochim Biophys Acta 1768*, 3090-3097.

49. Salnikov, E., Bertani, P., Raap, J., and Bechinger, B. (2009) Analysis of the amide (15)N chemical shift tensor of the C(alpha) tetrasubstituted constituent of membrane-active peptaibols, the alpha-aminoisobutyric acid residue, compared to those of di- and tri-substituted proteinogenic amino acid residues, *J Biomol NMR 45*, 373-387.

50. Muller-Enoch, D., and Gruler, H. (2000) Complexation of membrane-bound enzyme systems, *Z Naturforsch C 55*, 747-752.

51. Estabrook, R. W., Franklin, M. R., Cohen, B., Shigamatzu, A., and Hildebrandt, A. G. (1971) Biochemical and genetic factors influencing drug metabolism. Influence of hepatic microsomal mixed function oxidation reactions on cellular metabolic control, *Metabolism 20*, 187-199.

52. Black, S. D., French, J. S., Williams, C. H., Jr., and Coon, M. J. (1979) Role of a hydrophobic polypeptide in the N-terminal region of NADPH-cytochrome P-450 reductase in complex formation with P-450LM, *Biochem Biophys Res Commun 91*, 1528-1535.

53. De Angelis, A. A., Howell, S. C., Nevzorov, A. A., and Opella, S. J. (2006) Structure determination of a membrane protein with two trans-membrane helices in aligned phospholipid bicelles by solid-state NMR spectroscopy, *J Am Chem Soc 128*, 12256-12267.

54. Park, S. H., De Angelis, A. A., Nevzorov, A. A., Wu, C. H., and Opella, S. J. (2006) Three-dimensional structure of the transmembrane domain of Vpu from HIV-1 in aligned phospholipid bicelles, *Biophys J 91*, 3032-3042.

55. Muller, S. D., De Angelis, A. A., Walther, T. H., Grage, S. L., Lange, C., Opella, S. J., and Ulrich, A. S. (2007) Structural characterization of the pore forming protein TatAd of the twin-arginine translocase in membranes by solid-state 15N-NMR, *Biochim Biophys Acta 1768*, 3071-3079.

56. Esteban-Martin, S., Strandberg, E., Fuertes, G., Ulrich, A. S., and Salgado, J. (2009) Influence of whole-body dynamics on 15N PISEMA NMR spectra of membrane proteins: a theoretical analysis, *Biophys J 96*, 3233-3241.

57. Park, S. H., Mrse, A. A., Nevzorov, A. A., De Angelis, A. A., and Opella, S. J. (2006) Rotational diffusion of membrane proteins in aligned phospholipid bilayers by solid-state NMR spectroscopy, *J Magn Reson 178*, 162-165.

CHAPTER 5

NMR Characterization of Monomeric and Oligomeric Conformations of Human Calcitonin and Its Interaction with EGCG

5.1 Summary

Calcitonin is a 32-residue peptide hormone known for its hypocalcemic effect and its inhibition of bone resorption. While calcitonin has been used in therapy for osteoporosis and Paget's disease for decades, human calcitonin (hCT) forms fibrils in aqueous solution that limit its therapeutic application. The molecular mechanism of fiber formation by calcitonin is not well understood. Here, high-resolution structures of hCT at concentrations of 0.3 mM and 1 mM have been investigated using NMR spectroscopy. Comparing the structures of hCT at different concentrations, we discovered that the peptide undergoes a conformational transition from an extended to a β-hairpin structure in the process of molecular association. This conformational transition locates the aromatic side chains of Tyr-12 and Phe-16 in a favorable way for intermolecular π–π stacking, which is proposed to be a crucial interaction for peptide association and fibrillation. One-dimensional ^{1}H NMR experiments confirm that oligomerization of hCT accompanies the conformational transition at 1 mM concentration. The effect of the polyphenol epigallocatechin 3-gallate (EGCG) on hCT fibrillation was also investigated by NMR and electron microscopy, which show that EGCG efficiently inhibits fibril formation of hCT by preventing the initial association of hCT before fiber formation. The NMR experiments also indicate that the interaction between aromatic rings of EGCG and the aromatic side chains of the peptide may play an important role in inhibiting fibril formation of hCT.

5.2 Introduction

Calcitonin is a 32-amino-acid peptide hormone with an N-terminal disulfide bridge between Cys-1 and Cys-7 and a C-terminal proline amidated residue (Figure 5.1). Secreted by the thyroid in response to elevated serum calcium levels (*1, 2*), calcitonin acts to reduce blood

Ca^{2+} levels and to reduce bone resorption by inhibiting the activity of osteoclast cells (*3–6*). Because of its ability to limit bone resorption, calcitonin has been used as a treatment of osteoporosis for more than two decades (*7*). However, the therapeutic application of human calcitonin (hCT) has been limited by its tendency to assemble into inactive, fibril-like aggregates inaqueous solution (*8–10*). Since amyloid fibril formation is also observed in many other peptides associated with degenerative disorders, including Alzheimer's disease, Parkinson's disease and type II diabetes, a comprehensive understanding of the fibrillation process of amyloid peptides and the development of fibril inhibitors are desirable not only for the further improvement of medicinal efficiency of calcitonin but also in general for the development of treatment for amyloid-related diseases. The structure of calcitonin fibers and other oligomeric species have not been determined at high resolution at the molecular level. On a mesoscopic scale, electron microscopy studies have shown that hCT fibers are approximately 80 Å in diameter with the cross-β-sheet architecture common to amyloid fibers.11 At the molecular level, the assembly process of hCT monomers into amyloid fibers has been examined in some detail using NMR and other methodologies. Fibrillogenesis of hCT is a pH-dependent process with rapid association into antiparallel β-sheets at pH 7.5 and slower association into antiparallel and parallel β-sheets at pH 3.3 (*12–14*), a switch that appears to be controlled by the ionization states of Asp-15, Lys-18 and His-20 (*13,14*). The residues in the central region of hCT are sufficient for fiber formation, as a truncated pentapeptide fragment of hCT from Asp-15 to Phe-20 (DFNKF) forms fibrils similar to those formed by the intact peptide (*15,16*). Kinetic studies have suggested that hCT amyloidogenesis is a multistep process, with non-fibrillar intermediates playing a key role in the early stages of amyloidogenesis (*12,17,18*). A time-dependent solution NMR study showed that peaks from residues in the central region (residues 8 to 23) of the peptide broaden and disappear much faster than those in the C-terminus during fibril formation, suggesting that these residues are involved in the formation of an intermediate before assembly of the final amyloid fiber (*19*). The existence of an intermediate state of hCT during fiber formation is supported by transmission and attenuated total reflection FTIR (Fourier transform infrared spectroscopy) experiments that showed the simultaneous increase of α-helix and β-sheet components during fibril formation (*18*). Solid-state NMR studies suggest a localized α-helix structure around Gly-10 at pH 3.3, which is slowly converted into a β-sheet structure as the fibrils are formed (*12,14*). However, a high resolution structure of an intermediate conformation

has not been reported.

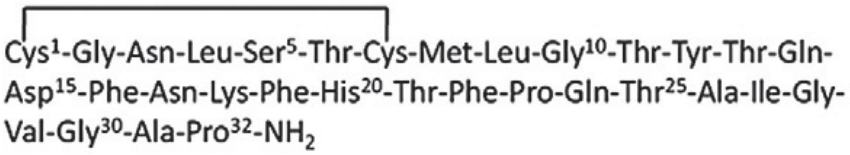

Figure 5.1 Amino acid sequence of hCT.

Knowledge on the oligomerization process may be utilized in the design of drugs to stop it. Fibrillation of amyloid peptides sometimes can be inhibited by small molecules through different pathways: small molecules including dopamide (*20*), calmidazolium chloride (*21*), hydroxyindole derivatives (*22*) and sulfated triphenyl methane derivative acid fuchsin (*23*). (−)-Epigallocatechin 3-gallate (EGCG), a polyphenol compound obtained from green tea, in particular, has raised much interest due to its strongly inhibitory effect on fibrillogenesis and its low toxicity. So far, it has been reported that EGCG efficiently inhibits fiber formation of α-synuclein (*24–26*), Aβ (*26,27*), huntingtin (*28*), IAPP (*29*), and MSP2 (*30*). However, the mechanism of the inhibition has not been well established due to the complexity of the interaction between EGCG and amyloid peptides, which may involve an initial non-covalent interaction, a covalent modification of the peptide (*26,30*) and auto-oxidation and quinone formation of EGCG (*31*). As EGCG provides a promising lead for further development of amyloid fibril inhibitors, a comprehensive understanding of the inhibitory mechanism at the atomic level is desirable.

In this chapter, we have investigated the oligomerization of hCT by examining the influence of peptide concentration and amyloid inhibitors on the conformation of hCT by NMR spectroscopy. Toward this end, we have solved high-resolution structures of hCT at two different concentrations using NMR spectroscopy. Our results indicate a site-specific conformational transition of hCT from an extended structure to a β-hairpin in the central region (Phe-12–Phe-19) of the peptide upon an increase in hCT concentration from 300 μM to 1 mM, consistent with a change in peptide oligomerization state detected by diffusion-ordered NMR. To determine the effect of amyloid inhibitors on the oligomericconformation of hCT, we investigated the inhibitory effect of EGCG on hCT fibril formation. Our results indicate that EGCG efficiently

inhibits fibril formation of hCT by preventing the initial oligomerization step. The interaction between EGCG aromatic rings and peptide aromatic side chains may play an important role in preventing hCT amyloid fibril formation.

5.3 Material and Methods

5.3.1 Materials

EGCG (95% purity) was purchased from Sigma and used without further purification. Concentrated (25 mM) stock solutions of EGCG were prepared by dissolving EGCG in N_2 flushed water. hCT was synthesized by Fmoc chemistry using an Applied Biosystems 431A peptide synthesizer and Fmoc amino acids purchased from Watanabe Chemical Industries (Hiroshima, Japan). An amide resin (Applied Biosystems, Inc., Foster City, CA) was used for the formation of the C-terminal amine. After deprotection and cleavage from the resin, the peptides were purified by reversed-phase HPLC using a mobile phase of water and acetonitrile containing 0.05% trifluoroacetic acid. The disulfide bridge between Cys-1 and Cys-7 was formed overnight by air oxidation of dilute (0.5 mM) hCT solution in 0.1 M sodium acetate (pH 8.0–8.5) in the presence of 6 M urea to prevent fibrillization (*61*). After an Ellman test confirmed the presence of the disulfide bond (*62*) the oxidation reaction was stopped by adding an acetic acid solution. The oxidized product was then repurified by HPLC. After purification, the peptide was lyophilized from aqueous solution in 40% acetonitrile (used to maintain the monomeric conformation) and stored at −4 °C.

5.3.2 H/D exchange

Samples for H/D exchange experiments were prepared by first dissolving lyophilized hCT in phosphate buffer [1 mM hCT, 7% D_2O and 50 mM NaCl (pH 2.9)] to a concentration of 1 mM in the absence and presence of 4 molar equivalents of EGCG. Amide proton/deuteron exchange was initiated by exchanging the original phosphate buffer into equivalent deuterated buffer using a Zeba Spin Desalting Column from Thermo Scientific. We recorded 32 transients for each 1H spectrum before H/D exchange and for the indicated time durations after the H/D exchange.

5.3.3 Electron microscopy measurements

Samples for electron microscopy were prepared by first dissolving lyophilized hCT in phosphate buffer (pH 7.3, 20 mM and 100 mM NaCl) at a peptide concentration of 100 μM and incubating at 25 °C for 36 h in the absence and presence of 3 molar equivalents of EGCG. Aliquots of 10 μL samples were deposited on a 400-mesh copper grid and incubated for 2 min, washed with distilled water twice and negatively stained with 10 μL of 2% (w/v) uranyl acetate for 1.5 min and dried. Observations were performed on a Philips CM-100 electron microscope.

5.3.4. Sample preparation for NMR experiments

A few minutes before starting the NMR experiments, samples were prepared by dissolving the lyophilized hCT peptide in 20 mM phosphate buffer (pH 7.4 or pH 2.9) containing 50 mM NaCl to a final concentration of 0.3 or 1 mM. The stability of the sample over the time course of the experiment was tested by obtaining a series of ^{1}H chemical shift spectra over a period of several days. The high degree of similarity of the spectra confirmed the stability of the sample at an acidic pH of 2.9 over the time course of the experiment. However, the sample at pH 7.4 rapidly aggregated at the concentrations with the solution becoming visibly turbid and with the intensity of the signal rapidly diminishing as time progressed, in agreement with previous reports (*19*). Accordingly, all NMR experiments were performed at pH 2.9.

5.3.5 NMR spectroscopy

All NMR experiments were performed on a Bruker AVANCE 900-MHz spectrometer at 25 °C. Samples were prepared by dissolving lyophilized hCT in phosphate buffer (pH 2.9, 7% D2O and 50 mM NaCl) at peptide concentrations of 0.3 mM and 1 mM. 2D TOCSY and NOESY spectra were obtained for structure determination. TOCSY spectra were recorded using 256 t1 experiments, 80 ms of mixing time and 4 scans, while NOESY spectra were obtained using 512 t1 experiments, 300 ms of mixing time and 16 scans. The proton frequency for each experiment was set on water resonance (4.7 ppm). The spectra were referenced relative to 4,4-dimethyl-4-silapentane-1-sulfonic acid (DSS). Spectra were processed using TOPSPIN and analyzed using Sparky. The NOE cross peak assignments were obtained by an iterative procedure using a combination of manual and automatic approaches. Proton diffusion NMR measurements were carried out using the STE (stimulated echo) PFG pulse sequence with squared gradient pulses of constant duration (5 ms) and a variable gradient amplitude along the longitudinal axis (*63*).

Typical acquisition parameters used in NMR experiments were as follows: a 90° pulse width of 23 μs, a spin echo delay of 10 ms, an STE delay of 150 ms, a recycle delay of 5 s, a spectral width of 10 kHz and 4048 data points. A saturation pulse centered at the water frequency was used for solvent suppression. Radio frequency pulses were phase cycled to remove unwanted echoes. All spectra were processed with an exponential multiplication factor equivalent to a 5-Hz line broadening prior to Fourier transformation and were referenced relative to DSS. The gradient strength was calibrated (G=3.28 T/m) from the known diffusion coefficient of HDO in D_2O at 25 °C (D_0 = 1.9×10− 9 m^2/s) (*64*). The diffusion coefficients were determined from the slope of a log plot of the intensity as a function of gradient strength using the Stejskal–Tanner equation (*65*). The hydrodynamic radius was then calculated from the diffusion coefficient using the Einstein–Stokes relation and the viscosity of water at 25 °C. To investigate the interaction of hCT with EGCG, we added aliquots of the EGCG stock solution to prepare samples with different hCT : EGCG molar ratios. For these samples, 1D ^{1}H NMR, 2D NOESY, 2D TOCSY and ^{1}H/^{15}N band-selective optimized flip-angle short transient (SOFAST) HMQC spectra were recorded in the absence and presence of EGCG. For experiments involving EGCG, NOESY spectra were obtained using 512 t1 experiments, 300 ms of mixing time and 8 scans, while TOCSY spectra were obtained using 256 t1 experiments, 80 ms of mixing time and 4 scans. The SOFAST HMQC spectra were obtained using 128 t1 experiments and 256 scans.

5.3.6 Structure calculations

Structures were calculated from manually and automatically assigned NOEs in 2D NOESY spectra with a 200-ms mixing time using CYANA version 2.0 (*66,67*). The normalized cross peak intensities were qualitatively assigned as strong, medium or weak to assign upper inter-proton distance restraints of 2.7 Å, 3.3 Å and 5.0 Å, respectively, for both 0.3- mM and 1- mM hCT samples (*68*). An additional 0.5 Å was added to the upper bound for proton pairs involving methyl groups. For the 1.0- mM hCT sample, a total of 297 inter-proton distance restraints were derived from the NOESY data, including 175 sequential restraints (i−j=1), 19 medium-range restraints (2≤i−j≤5) and 2 long-range restraints [(i−j>5) residues]. The combination of chemical shift restraints from TALOS and the NOE patterns were used to calculate 23 dihedral angle restraints for the 1- mM sample (*69*). For the 0.3- mM hCT sample, long-range or medium-range NOEs were not observed except for 65 intraresidue and 66 sequential NOEs. A total of 100

conformers for each sample were initially generated by CYANA based on the dihedral angle and NOE restraints obtained, and the bundles of 20 conformers with the lowest target function were used to represent the three-dimensional NMR structures. Hydrogen bond constraints were not included during the entire structure calculation. The disulfide bridges between C1 and C7 were fixed in all structure calculations by constraining the S–S distance to an upper limit of 2.1 Å.

5.4 Results

5.4.1 Oligomerization of hCT

To examine the oligomerization state of hCT in solution, we initially acquired one-dimensional (1D) ^{1}H NMR spectra at two concentrations—0.3mM and 1 mM. A broad peak observed at − 0.1 ppm in the 1-mM hCT sample was absent in the 0.3-mM hCT sample (Figure 5.2a, inset). This peak is commonly found in the spectra of amyloidogenic proteins, and its appearance is consistent with a species in which at least some of the aliphatic protons are significantly protected from solvent and thus shifted to the highfield region of the spectrum (Figure 5.2a) (*32–35*). However, the relatively narrow dispersion of resonances in other regions of the ^{1}H spectra suggests that the peptide is at least partially unfolded at both concentrations (Figure 5.2). This difference is consistent with a heterogeneous sample containing at least two species, one significantly folded and the other largely unfolded. To confirm this hypothesis, we performed pulsed-field gradient (PFG) NMR diffusion experiments to estimate the hydrodynamic radius of peaks that likely represent folded and unfolded species (see Figure 5.3). A hydrodynamic radius of 1.57 nm was obtained for both samples for peaks between 8.6 and 7.4 ppm, suggesting that these peaks correspond to a monomeric, significantly unfolded peptide at both concentrations. For the peak at −0.1 ppm, the radius of gyration could not be measured precisely. However, the insensitivity of the peak intensity to the gradient strength suggests a very slowly diffusing oligomeric species at least 50 nm in diameter, in agreement with previous studies on other amyloidogenic proteins (*34*,*35*). Overall, the ^{1}H spectrum in the 0.3-mM sample is consistent with hCT being exclusively in the monomeric state and the monomer coexisting with large oligomeric species at 1 mM hCT concentration. However, the only contribution of the large oligomeric state to the ^{1}H spectra of the 1-mM sample is the small peak near −0.1 ppm, as other resonances originating from the large oligomeric state are apparently broadened beyond detection.

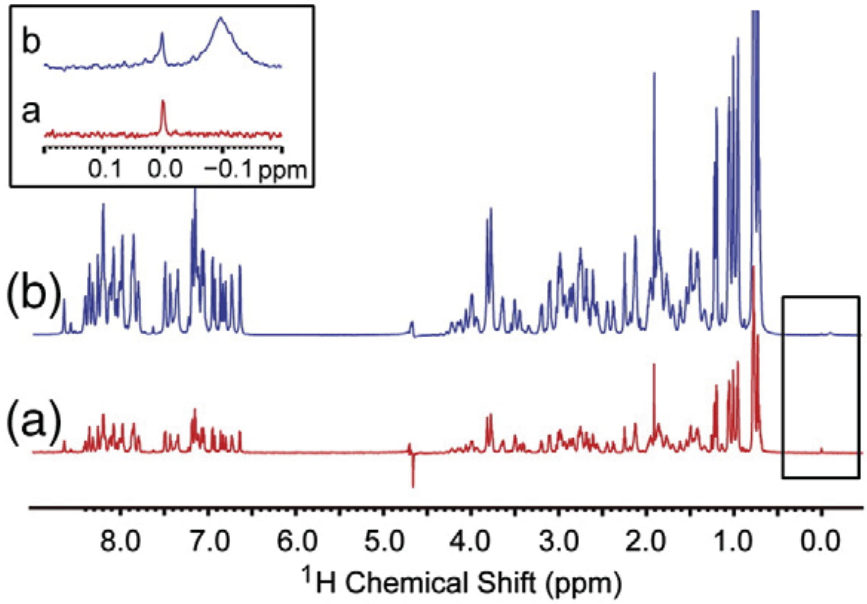

Figure 5.2 hCT forms oligomers at 1 mM concentration but not at 0.3 mM. (a) 1D 1H NMR spectra of hCT at (a) 0.3 mM and (b) 1 mM concentrations showing the characteristic amyloid oligomer peak at −0.1 ppm in the 1- mM sample and its absence in the 0.3- mM sample. The peak at 0 ppm is from the internal chemical shift reference used (DSS).

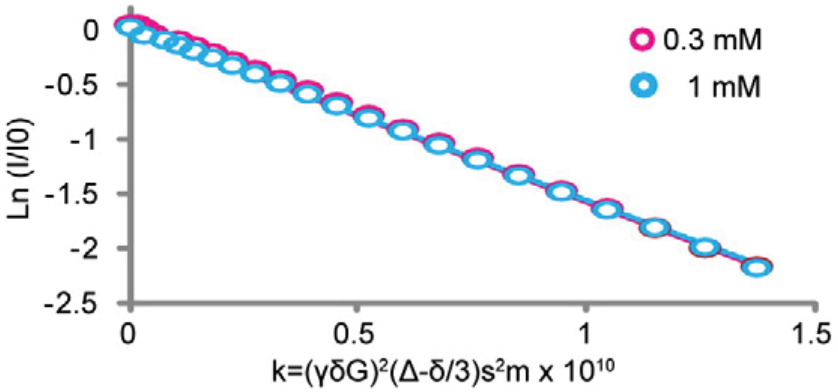

Figure 5.3 hCT is primarily monomeric at both 0.3 and 1 mM concentrations. The decay of normalized STE intensity obtained from STE PFG 1H NMR spectra of 0.3 mM (red circles) and 1 mM (blue squares) hCT samples; the intensity was calculated from the integrated volume of the peaks between 8.6 and 7.4 pm. The similarity of the decays indicates that the peaks within this region correspond to largely unfolded monomeric species of hCT with a hydrodynamic radius of 1.57 nm.

5.4.2 Concentration-dependent NOE patterns of hCT

The partial protection of the amide hydrogen suggests that hCT is at least partially structured at pH 2.9. We confirmed this result by recording two-dimensional (2D) $^1H/^1H$ total correlated spectroscopy (TOCSY) and nuclear Overhauser enhancement spectroscopy (NOESY) spectra of samples of hCT at 0.3 mM and 1 mM concentrations. The spectra showed relatively good resolution at both concentrations; all intraresidue nuclear Overhauser enhancements (NOEs) between backbone amide protons and α protons could be identified except for those originating from C1. Figure 5.4 shows the Hα–HN region of the 2D NOESY spectrum at 1 mM hCT concentration. Figure 5.5 shows the NOE connectivities obtained for both concentrations.

Table 1 summarizes the NOE constraints obtained for both concentrations. A far larger number of NOEs were observed for the 1-mM concentration compared to the 0.3-mM sample. For the 1-mM sample, a total of 291 NOE constraints could be detected, while only 131 could be determined for the 0.3-mM sample. This difference persisted even after the signal was normalized for the difference in concentration between the two samples. The relative increase in the number of NOEs in the 1-mM spectra was not uniform but was largely concentrated in the H^N–$H^{aliphatic}$ region of the 2D NOESY spectrum. The uneven distribution can be seen in Figure 5.6, which shows the superposition of the H^N–$H^{aliphatic}$ regions of the NOESY spectra at both concentrations normalizing for the concentration difference. Normalization is done by reducing the contour level of the 0.3-mM spectra by 3.3 times compared with the 1-mM spectra in Sparky. Several additional NOEs are particularly prominent, mostly those between side-chain protons of residue i and amide protons of residue i or i+1 in the central region of the peptide, for example, those between M8Hγ2-H^N, L9Hδ-H^N, C7HHβ3-M8H^N, T11Qγ2-Y12H^N, T13Qγ2-Q14H^N, D15Hβ3-F16H^N, F19Hβ3-H20H^N, P23Hβ2-Q24H^N and Q24Hβ2-T25H^N (see Figure 5.6). In addition, $^1H/^1H$ NOEs $d_{\alpha N}(i,i+2)$ between Ser-5 and Cys-7, between Gly-10 and Tyr-12 and continuously from Asp-15 to His-20 were observed in the 1-mM hCT sample. These NOEs are absent in the 0.3-mM hCT sample, which suggests a more constrained structure in the central region of the peptide at the higher concentration. A $d_{\alpha N}(i,i+2)$ $^1H/^1H$ NOE connectivity between Asp-15 and Asn-17 is characteristic of a turn structure around these residues (*36*). The presence of a type II β-turn in the 1-mM sample is also well supported by the intense $d_{NN}(i,i+1)$ NOEs between Phe-16 and Phe-17 and medium and long-range interresidue NOEs from either side of

the turn between residues Thr-13/Asn17, Gln-14/Asn-17 and Thr-13/Phe-19. These medium- and long-range NOEs are listed in Table 2.

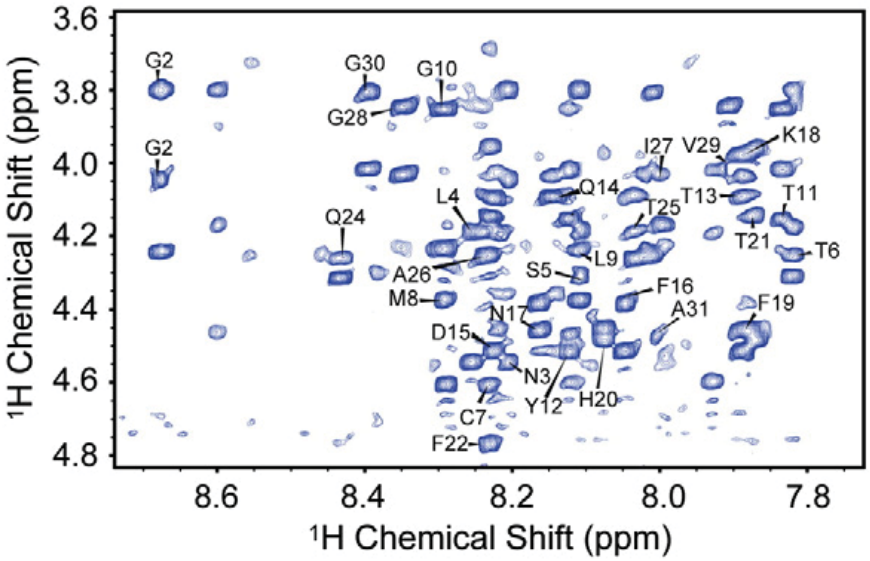

Figure 5.4 H^{α}–H^{N} region of the 2D NOESY spectrum of 1 mM hCT. The spectrum was recorded from 1 mM hCT sample in 2 mM sodium phosphate buffer, 7% D2O and 50 mM NaCl (pH 2.9). Only the NOEs corresponding to cross peaks of amide protons and α protons are labeled.

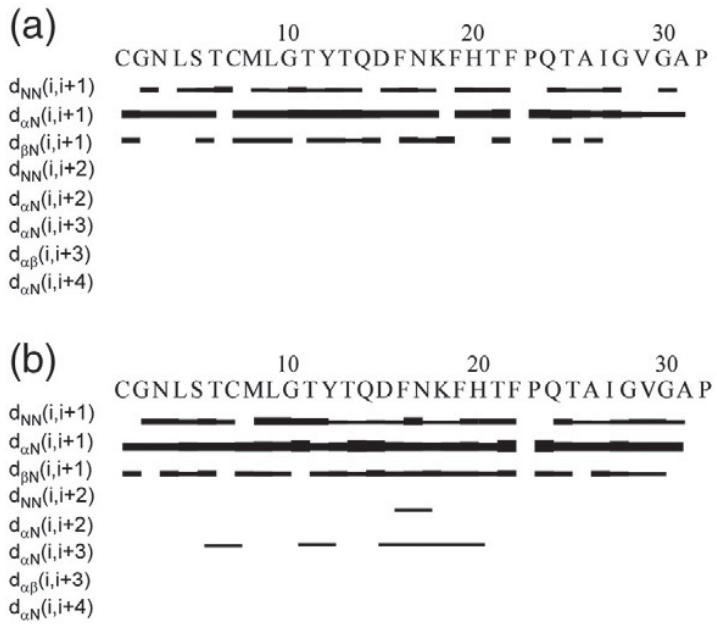

Figure 5.5 NOE connectivity plots for the 0.3- mM (a) and 1- mM (b) hCT samples. The strengths of sequential NOEs are indicated by the height of the bars.

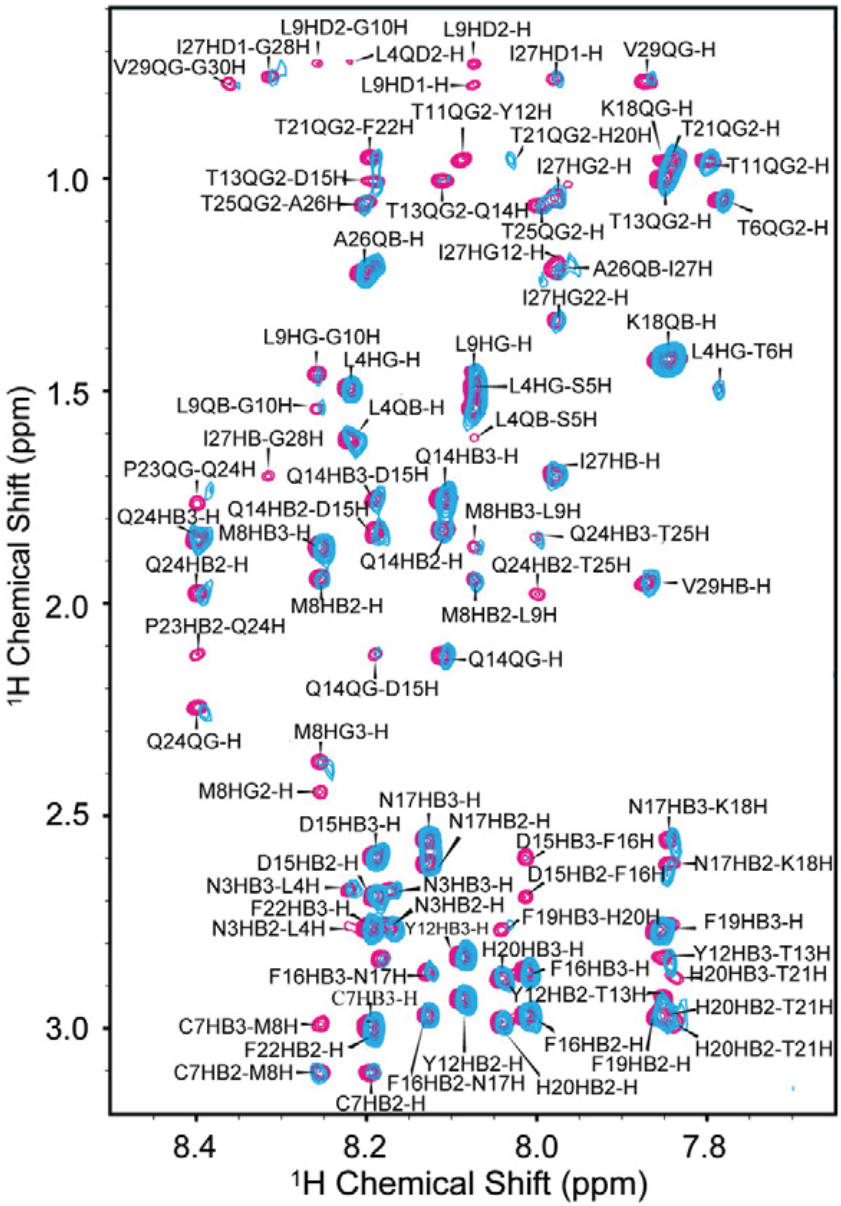

Figure 5.6 Superimposed normalized NOESY spectra of hCT at 0.3 and 1 mM concentrations. The Hside chain–HN regions of NOESY spectra at peptide concentration of 0.3 mM (blue) and 1 mM (magenta) are superimposed. The 1- mM spectrum was normalized by scaling the contour level down to that of the 0.3- mM sample, using the diagonal peak intensity as a reference. Additional NOEs were observed in the 1- mM sample, including intraresidue Hside chain–HN NOEs and interresidue (i–i+1) Hside chain–HN NOEs. Samples were prepared in 2 mM sodium phosphate buffer, 7% D2O and 50 mM NaCl (pH 2.9).

Table 5.1 Structure statistics for the 20 best structures of hCT after energy minimization and structural annealing

	1 mM	0.3 mM
Restraints for structure calculation		
Total restraints	314	158
Total NOE restraints	291	131
Intraresidue	95	65
Sequential	175	66
Medium range	19	0
Long range	2	0
Dihedral angle restraints	23	27
NOE violations (number > 0.2 Å)	0	0
Dihedral violations (number > 3)	0	0
RMS deviation (Å) (residues 9–21)		
Backbone	0.97 ± 0.40	2.72 ± 0.52
Heavy atoms	1.69 ± 0.28	4.07 ± 0.43
Ramachandran data (%)		
Residues in the most favored regions	75.4	50.4
Residues in the additionally allowed regions	24.6	49.6
Residues in disallowed regions	0.0	0

Table 5.2 Selective medium- and long-range NOEs observed from the 2D NOESY spectrum of 1 mM hCT in sodium phosphate and 50 mM NaCl (pH 2.9) at 298 K

From residue	To residue
T13–QG2	F19–QD
T13–HA	F19–QD
T13–HA	N17–QB
T13–QG2	N17–QB
T13–QG2	N17–QD
Q14–HN	N17–HD21
Q14–HN	N17–HD22
Q14–HN	N17–QB
Q14–HN	N17–QD2

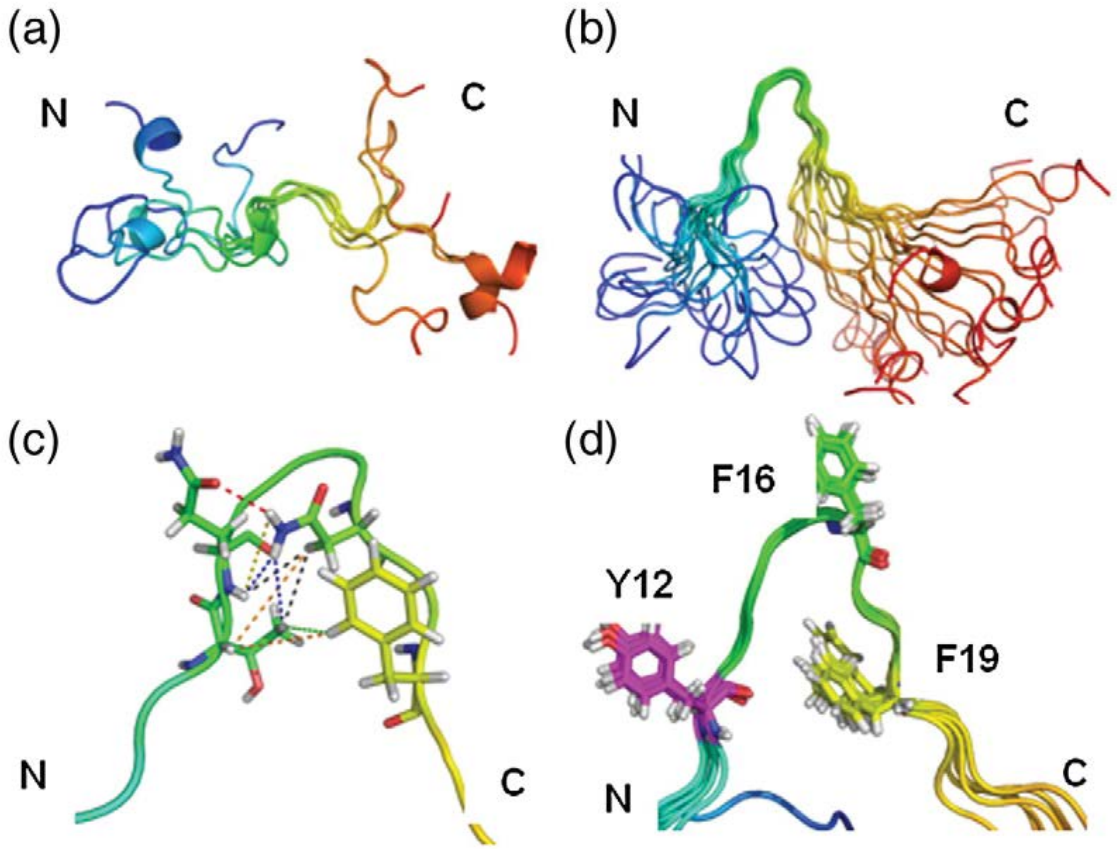

Figure 5.7 Partially folded structures of hCT. (a) A superimposition of five energy-minimized structures of hCT at the concentration of 0.3 mM. (b) A superimposition of 20 energyminimized structures of hCT at the concentration of 1 mM. The peptide chains are labeled with gradient colors from blue to red throughout the sequence from N-terminus to C-terminus. (c) A cartoon plot showing the medium- and longrange NOEs (broken lines) that stabilize the formation of the hairpin structure at 1 mM concentration. Red broken lines indicate a hydrogen bond. (d) Positions and orientations of three aromatic side chains from five randomly chosen energy-minimized structures of the 1- mM sample of hCT.

From these NOEs, structural models of hCT could be constructed for both samples (see Figure 5.7). For the 0.3-mM sample, hCT is largely unstructured, in agreement with the paucity of NOEs detected at this concentration. In the 1-mM sample, on the other hand, a well-defined β-hairpin structure is present in the central region of the peptide from Tyr-12 to Phe-19. The hairpin structure is mainly constrained by 19 medium-range and 2 long-range NOEs observed between the two strands (see Figure 5.7c for a cartoon depiction), especially from residues Thr-13 and Gln-14 on the N-terminal side of the hairpin to residues Asn-17 and Phe-19 on the C-

terminal side. A β-turn from Gln-14 to Asn-17 separates the strands of the hairpin. The β- turn is further stabilized by additional hydrogen bonds originating from side chains within the turn (red broken lines in Figure 5.7c). In all the energy minimized structures, the aromatic residues Tyr-12 and Phe-16 within the turn region are consistently oriented so that the planes of the aromatic rings are parallel with the face of the hairpin, presumably favoring peptide stacking through intermolecular π–π interaction. While the 20 energy-minimized backbone structures superimpose well at the central region of the peptide from Tyr-12 to Phe-19 in the 1-mM sample, the N- and C-terminal residues are largely disordered in both samples.

5.4.3 EGCG inhibits the formation of oligomeric species of hCT

Having characterized a possible oligomeric species of hCT, we next examined the effect of EGCG on hCT oligomerization. We first confirmed that EGCG inhibits amyloid fiber formation by hCT, similar to what has been observed for other amyloidogenic proteins (*26,29,30,37–40*). To observe the effect of EGCG on hCT fibrillization, we incubated samples of 100 μM hCT with and without 500 μM EGCG at pH 7.4 for 36 h. In the absence of EGCG, hCT aggregates to form a dense network of amyloid fibers (Figure 5.8a). On the other hand, when hCT was incubated with a 5-fold excess of EGCG under the same condition, fibers or fiber-like aggregates were not observed (Figure 5.8b). The black dots observed in the hCT/ EGCG sample match those observed in the control sample containing EGCG only, suggesting that they correspond to EGCG aggregates. The absence of amyloid fibers in the hCT/EGCG sample therefore implies that the fibrillation of hCT was efficiently inhibited by interaction with EGCG.

Hydrogen/deuterium (H/D) exchange experiments were carried out to further study the effect of EGCG on the oligomerization process of hCT. The time course of H/D exchange of hCT amide protons with and without EGCG is shown in Figure 5.9. A comparison of the two sets of 1D spectra shows that the H/D exchange rates of amide protons of hCT are much faster in the presence of EGCG. In the absence of EGCG, most of the amide peaks could still be observed after 48 h of deuterium exchange, although the intensity and resolution of the peaks decreased significantly (Figrue 5.9a). In contrast, the peaks from the amide protons were almost disappeared within 15 min in the EGCG-treated hCT sample, indicating near complete exchange in this sample. Since monomeric hCT is almost completely unstructured (see Figure 5.7a), the faster exchange rate is likely to arise from the elimination of oligomeric species of hCT, which

have a substantial degree of intermolecular hydrogen bonding (see Figure 5.2b). This conclusion is further supported by the absence of the oligomer peak at around −0.1 ppm in the EGCG-treated hCT sample (Figure 5.9c), which also suggests the inhibition of the growth of large oligomer species by EGCG.

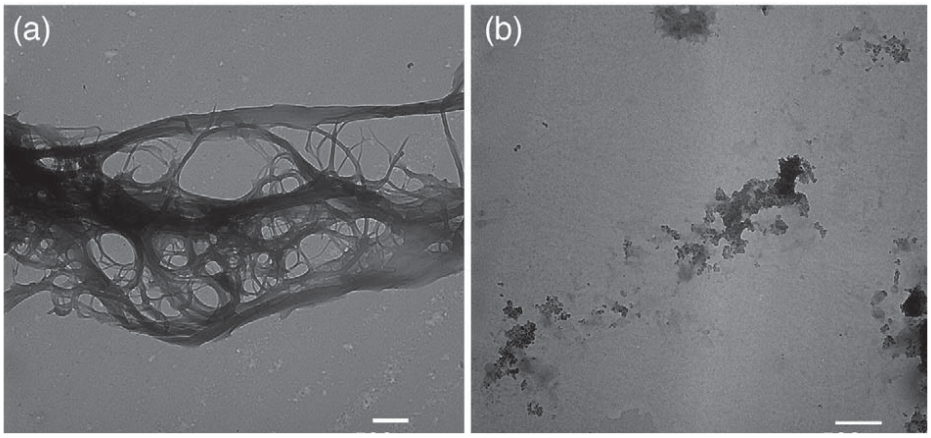

Figure 5.8 Electron microscopy image shows the inhibition of hCT fibrillation by EGCG. Electron microscopy image shows the inhibition of hCT fibrillation by EGCG. We incubated 0.3 mM samples of hCT for 36 h in the absence (a) and presence (b) of 3 molar equivalents of EGCG at pH 7.4, 298 K.

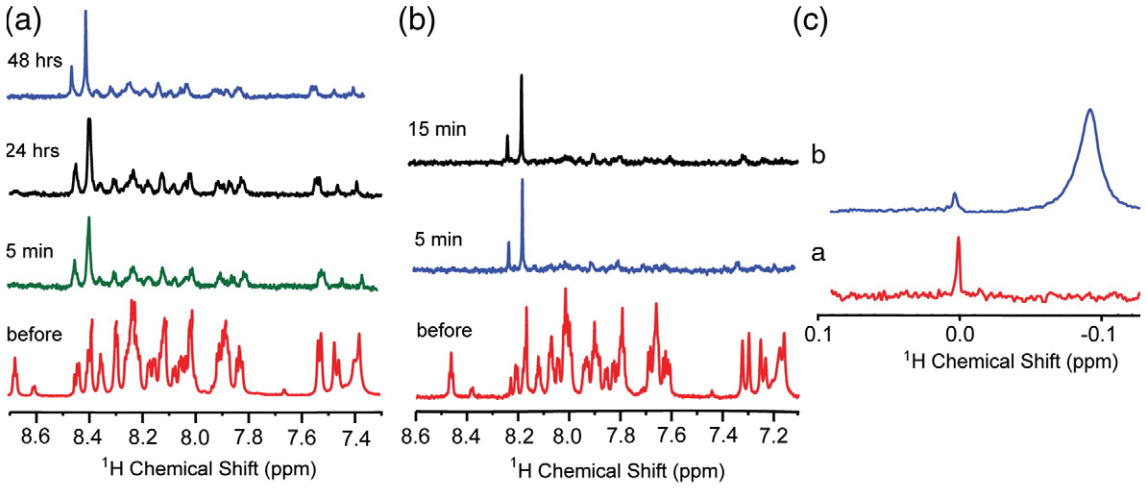

Figure 5.9 EGCG inhibits oligomer formation of hCT by NMR. Time course of the amide region of 1D 1H NMR spectra of hCT in H/D exchange experiments in the absence (a) and presence (b) of 2 molar equivalents of EGCG. (c) 1D 1H NMR spectra of hCT in the presence (a) and absence (b) of 2 molar equivalents of EGCG before deuterium exchange. Samples were prepared in 2 mM sodium phosphate buffer, 7% D2O and 50 mM NaCl (pH 2.9).

5.4.4. Mechanism of EGCG binding to hCT by NMR experiments

To elucidate the binding mechanism of EGCG to hCT, we recorded NMR spectra of hCT in the absence and presence of a 5-fold molar excess of EGCG. A shifting of the resonances of both hCT and EGCG indicated direct binding between EGCG and non-fibrillar forms of the peptide (amyloid fibers are not detected in these experiments as the long rotational correlation time of the fiber broadens the signal beyond detection). The shifting of the resonances of hCT upon the addition of EGCG was investigated in more detail by 2D NMR (see Figure 5.10). A superimposition of the $^{1}H/^{15}N$ heteronuclear multiple quantum coherence (HMQC) spectra of hCT with and without 2 molar equivalents of EGCG shows an almost universal shift of the resonances upon EGCG binding (Figure 10a), indicating that EGCG binding to the monomer is not localized on specific sites within the peptide but is rather largely delocalized, in agreement with previous experiments on α-synuclein (*26*). The chemical shift changes of the amide and α protons of hCT occurring upon EGCG binding are summarized in Figure 10b, calculated from the $^{1}H/^{15}N$ HMQC and NOESY spectra, respectively. The amide protons of residues from Leu-9 to the C-terminus are shifted to high field except for Thr-11 and Asp-15, while the N-terminal residues, where there is a disulfide loop from Cys-1 to Cys-7, are shifted to low field only slightly. The magnitude of the changes suggests that EGCG largely binds in the central and C-terminal regions of the peptide. The general high-field shift observed is most likely due to the shielding effect of the aromatic rings of EGCG. Interestingly, amide protons of Thr-11, Asp-15 and Thr-21 show either “abnormal” low-field shifts or a negligible shifts differing from the adjacent residues. Although changes are apparent throughout the spectrum when EGCG binds to hCT, aromatic side chains appear to play a particular role. The residues with the most significant Hα chemical shift differences ($\delta > 20.1$ Hz, compared to the mean value of 9.2 Hz) are almost all aromatic residues (Tyr-12, Phe-16, Phe-22 and Ala-31), suggesting a close spatial proximity between these residues and EGCG. The resonances from protons on aromatic side chains also show significant chemical shift perturbations induced by EGCG (Figure 10c), which might be due to a π–π stacking interaction between aromatic rings of EGCG and the side chains of these residues. Notably, the amide protons showing atypical shifts upon EGCG interaction (Thr-11, Asp-15 and Thr-21) directly precede the aromatic residues Tyr-12, Phe-16 and Phe-22. This pattern is consistent with parallel stacking of aromatic rings, which should cause a deshielding effect on the α protons in the adjacent residues as they lie perpendicular to the aromatic rings.

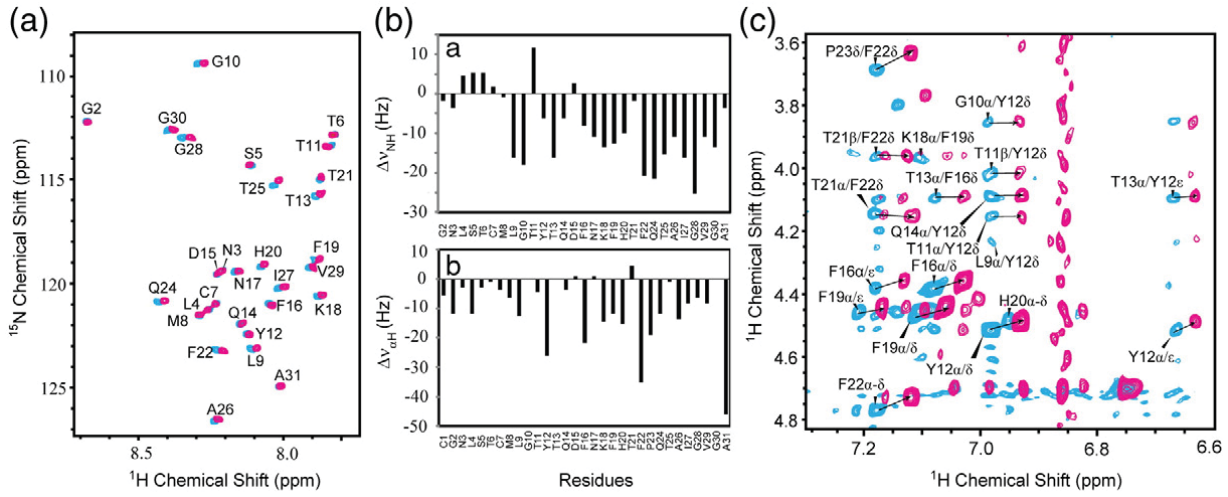

Figure 5.10 NMR analysis of EGCG binding to hCT. NMR spectra of hCT were recorded with and without 2 molar equivalents of EGCG. (a) 2D 1H/15N SOFAST HMQC spectra of hCT in the absence (blue) and presence (red) of EGCG. (b) Chemical shift difference of amide protons and α protons of hCT induced by the addition of EGCG. Δδ is calculated by subtracting the chemical shift values of protons of hCT in the presence of EGCG from those in the absence of EGCG. Δδ(NH) was calculated from 2D 1H/15N SOFAST HMQC spectra. Δδ(αH) was calculated from 2D 1H/1H NOESY spectra. (c) Aromatic region of NOESY spectra of hCT in the absence (blue) and presence (red) of EGCG. Samples were prepared in 2 mM sodium phosphate buffer, 7% D2O and 50 mM NaCl (pH 2.9).

5.5 Discussion

Our study reveals that a conformational change in hCT accompanies peptide association and oligomerization. At a concentration of 0.3 mM, hCT adopts a flexible and extended structure. A small degree of structure is present in the form of a loose turn from Asp-15 to Phe-19 in the central region of the peptide. However, the peptide is almost entirely unstructured at this concentration, a fact supported by the PFG results showing a hydrodynamic radius of 1.57 nm, which is similar to that of completely denatured peptides but is larger than most amyloidogenic peptides of this length that are typically partially folded (*34,35,41*). Both IAPP and Aβ1–40, for example, have low-lying helical states that are believed to nucleate amyloid formation (*42*). However, NOEs consistent with a helical structure were not detected for hCT at pH 2.9, as has been proposed for hCT oligomers in acidic solution and as a low-lying excited state of the monomer at neutral pH (*12,14*). The absence of a helical structure in the monomer is consistent with the finding that metastable secondary structure correlates with amyloidogenicity

of the peptide (*43–45*) as fiber formation is strongly delayed in hCT at an acidic pH compared to neutral pH (*19*). At this concentration, the peptide does not form large oligomers during the experimental time period according to the ^{1}H NMR spectra.

At a higher hCT concentration of 1 mM, many more NOEs could be detected in the sample after normalization, particularly in the central region of the peptide from Gly-10 to His-20. From these additional NOEs, a new structure that is significantly more ordered than the monomeric structure obtained for the 0.3-mM sample could be constructed. The loose turn found in the 0.3-mM structure is transformed into a well-defined type II β-turn between Gln-14 and Asn-17, and the central region of the peptide adopts a well-defined extended conformation from Tyr-12 to His-20, which superimposes perfectly among the 20 energy-minimized structures. The C- and N-termini, including the disulfide ring, are unstructured at both concentrations. The hairpin conformation is similar to that previously obtained for hCT in 85% dimethyl sulfoxide and 15% H_2O; however, the turn was located in a different position in this study (Asn-17 – His-20), possibly because of a different ionization state of the peptide (*46*). The change in the conformation of hCT as the concentration is increased implies that the structure obtained at the 1-mM concentration is of an oligomeric species while the 0.3-mM structure is solely that of a monomer. On the other hand, the hydrodynamic radius of hCT in the 1-mM sample calculated from most of the peaks in the 1D ^{1}H spectrum nearly exactly matches that of the 0.3-mM sample, suggesting that the 1-mM sample still consists largely of monomeric peptide. However, the 1D ^{1}H and diffusion experiments (Figure 2) also indicate large oligomer species in coexistence with the monomer in the samples at 1 mM but not 0.3 mM concentration. Amyloidogenic peptides frequently form micellar-type aggregates at intermediate peptide concentrations (*47–51*) which can undergo exchange with the monomeric peptide (*34, 52*). Such micelles have been proposed as intermediates for calcitonin fibrillization (*12*). Therefore, the most likely explanation is that the additional NOEs observed in the 1-mM sample represent transfer NOEs from a large, mostly NMR-invisible species in rapid exchange with the monomeric peptide. Under particular conditions (koff being fast relative to the T_1 relaxation time of the monomer/oligomer complex and NOE mixing time), the “memory” of the conformation of the hCT in the oligomer can be effectively carried over into the NOESY spectra in the form of additional NOE cross peaks, even though the oligomer itself is not visible to NMR (*53*). Note that transfer NOEs are typically

observed when the binding partner (in this case, the oligomer) is in large excess, in agreement with the similarity of 1D ^{1}H spectra (*53*).

The association of aromatic side chains has been proposed to be a driving force for fibrillization of hCT (*15,17*). For instance, molecular dynamic studies have shown that a five-residue segment of hCT starting from Asp-15 (DFNKF) forms high-ordered fibrils similar to the intact peptide (*54*). In contrast, the phenylalanine-to-alanine analogue (DANKA) does not form amyloid fibrils at all, implying an important role of aromatic interactions in peptide association (*15*). In the hairpin structure of the 1-mM sample, the planes of aromatic rings on the side chains of Tyr-12 and Phe-16 are primarily parallel with the hairpin plane (Figure 5.7c and d), which potentially favors the association of the peptide along the normal of the hairpin plane by the π–π interaction between the phenyl rings from adjacent peptides.

The apparent importance of aromatic interactions in stabilizing oligomeric conformations of hCT is shown by the interaction of hCT with EGCG. EGCG acts as fibril inhibitors of several amyloid peptides by stabilizing their oligomers in an off-pathway conformation that prevents their conversion to a toxic on-pathway oligomer intermediate (*24,26,30*) although apparent exceptions exist (*29,38,55*). Our NMR results indicate that EGCG inhibits fibrillation of hCT by stabilizing the monomeric form of hCT in a largely unstructured conformation and by preventing the oligomerization of hCT. In the ^{1}H NMR spectrum, we did not observe the slowly diffusing oligomer peak of EGCG-treated hCT around −0.1 ppm, which suggests the absence of large oligomer species in the EGCG-treated sample. In addition, the amide peaks of EGCG-treated hCT were quenched before those of the untreated sample in H/D exchange experiments. This suggests that EGCG-treated hCT is in a more solvent exposed environment, most likely due to stabilization of the unstructured monomeric form of the peptide. While the NMR spectra indicate that EGCG affects the chemical shift values of most of the residues (Figrue 5.10), the α protons of the aromatic side chains Tyr-12, Phe-16 and Phe-22 show more significant chemical shift perturbations by EGCG (Figure 5.10b). In addition, the amide protons of the residues preceding the aromatic residues (Thr-11, Asp-15 and Thr-21) show atypical low-field chemical shift changes upon interaction with EGCG, suggesting a ring current effect on these residues. From these results, it is reasonable to conclude that π–π interactions between EGCG and Tyr-11, Phe-16 and Phe-22 are involved in the association of EGCG with hCT. If intermolecular π–π interactions play an important role in amyloid formation of hCT, it can be expected that the

competing interaction of the aromatic rings of EGCG for these side chains blocks potential sites for peptide association and prevents oligomer formation.

It should be noted that, despite apparent superficial similarities with models of β-sheet amyloid oligomers, the oligomer structure reported here would require a conformational change before it can be incorporated into the hCT amyloid fiber. X-ray crystallography and solid-state NMR measurements have suggested that individual protein molecules in amyloid fibers typically adopt a common hairpin-type structure with the side chain of residues forming a tight interface known as a "steric zipper" between the two β-strands (*56–58*). Intermolecular association of the proteins along the fiber axis is responsible for fiber formation.

The tight packing of side chains in the steric zipper interface necessarily gives rise to a high number of NOEs between the β-strands (*59*). NOEs of this type were not observed in the 1-mM oligomer sample except in the immediate vicinity of the type II turn. In addition, the loop separating the β-strands in the hairpin is typically ∼10 residues in length (*57*,*58*). A smaller loop, such as the type II turn observed in the 1-mM oligomer sample, requires either the side chains to be pointed away from the plane of the hairpin or the strands to be separated in space. Either conformation is not likely to be conducive to the formation of the steric zipper interface essential for amyloid formation. For this reason, the oligomer conformation reported here is unlikely to be a direct nucleus for amyloid fiber formation. Measurements of the 1D ^{1}H spectra in real-time and solid-state NMR spectroscopy suggest that α-helical oligomers instead may be involved as a direct intermediate of fiber formation at both low and neutral pH (*12*,*19*). Conformational changes are often observed in amyloidogenic peptides following peptide association in which non-fibrillar oligomers such as those observed here are rapidly formed and then slowly converted into amyloid fibers (the nucleated conversion model) (*60*). Further investigation is needed to determine if the oligomer structure determined here is on- or off-pathway for amyloid formation.

5.6 References

1. Copp, D. H., Davidson, A. G., Henze, K. G., Cheney, B. A., and Cameron, E. C. (1962). Evidence for calcitonin—a new hormone from parathyroid that lowers blood calcium. *Endocrinology*, 70, 638–649.

2. Austin, L.A., and Heath, H. (1981). Calcitonin: physiology and pathophysiology. *N. Engl. J. Med*. 304, 269–278.

3. Chambers, T. J. (1982). Osteoblasts release osteoclasts from calcitonin-induced quiescence. *J. Cell Sci.* 57, 247–260.

4. Chambers, T. J., and Magnus, C. J. (1982). Calcitonin alters behavior of isolated osteoclasts. *J. Pathol.* 136, 27–39.

5. Zaidi, M., Inzerillo, A. M., Moonga, B. S., Bevis, P. J. R., and Huang, C. L. H. (2002). Forty years of calcitonin—where are we now? A tribute to the work of Iain Macintyre, FRS. *Bone*, 30, 655–663.

6. Breimer, L. H., Macintyre, I., and Zaidi, M. (1988). Peptides from the calcitonin genes: molecular genetics, structure and function. *Biochem. J.* 255, 377–390.

7. Henriksen, K., Bay-Jensen, A. C., Christiansen, C., and Karsdal, M. A. (2010). Oral salmon calcitonin—pharmacology in osteoporosis. *Expert Opin. Biol. Ther.* 10, 1617–1629.

8. Zurdo, J., Fowler, S. B., Poon, S., Muff, R., Chiti, F., and Dobson, C. M. (2005). Rational design of aggregationresistant bioactive peptides: reengineering human calcitonin. *Proc. Natl Acad. Sci. USA,* 102, 10105–10110.

9. Malchiodi-Albedi, F., Vanacore, N., and Diociaiuti, M. (2008). Calcitonin therapy and oligomer neurotoxicity: an underestimated risk? *Neurotoxicology,* 29, 1150–1151.

10. Cromwell, M. E. M., Hilario, E., and Jacobson, F. (2006). Protein aggregation and bioprocessing. *AAPS J.* 8, E572–E579.

11. Sieber, P., Riniker, B., Brugger, M., Kamber, B., and Rittel, W. (1970). Human calcitonin. VI. Synthesis of calcitonin. *Helv. Chim. Acta,* 53, 2135–2150.

12. Kamihira, M., Naito, A., Tuzi, S., Nosaka, A. Y., and Saito, H. (2000). Conformational transitions and fibrillation mechanism of human calcitonin as studiedby high-resolution solid-state 13C NMR. *Protein Sci.* 9,867–877.

13. Kamihira, M., Oshiro, Y., Tuzi, S., Nosaka, A. Y., Saito, H., and Naito, A. (2003). Effect of electrostatic interaction on fibril formation of human calcitonin as studied by high resolution solid state 13C NMR. *J. Biol. Chem.* 278, 2859–2865.

14. Naito, A., Kamihira, M., Inoue, R., and Saito, H. (2004). Structural diversity of amyloid fibril formed in human calcitonin as revealed by site-directed 13C solid-state NMR spectroscopy. *Magn. Reson. Chem.* 42, 247–257.

15. Gazit, E., Reches, M., and Porat, Y. (2002). Amyloid fibril formation by pentapeptide and tetrapeptide fragments of human calcitonin. *J. Biol. Chem.* 277, 35475–35480.

16. Jelinek, R., Shtainfeld, A., and Sheynis, T. (2010). Specific mutations alter fibrillation kinetics, fiber morphologies, and membrane interactions of pentapeptides derived from human calcitonin. *Biochemistry*, 49, 5299–5307.

17. Andreotti, G., and Motta, A. (2004). Modulating calcitonin fibrillogenesis. An antiparallel α-helical dimer inhibits fibrillation of salmon calcitonin. *J. Biol. Chem.* 279, 6364–6370.

18. Arvinte, T., Cudd, A., and Drake, A. F. (1993). The structure and mechanism of formation of human calcitonin fibrils. *J. Biol. Chem.* 268, 6415–6422.

19. Kanaori, K., and Nosaka, A. Y. (1995). Study of human calcitonin fibrillation by proton nuclear magnetic resonance spectroscopy. *Biochemistry,* 34, 12138–12143.

20. Conway, K. A., Rochet, J. C., Bieganski, R. M., and Lansbury, P. T. (2001). Kinetic stabilization of the α-synuclein protofibril by a dopamine–α-synuclein adduct. *Science*, 294, 1346–1349.

21. Williams, A. D., Sega, M., Chen, M. L., Kheterpal, I., Geva, M., and Berthelier, V. (2005). Structural properties of Aβ protofibrils stabilized by a small molecule. *Proc. Natl Acad. Sci. USA,* 102, 7115–7120.

22. Cohen, T., Frydman-Marom, A., Rechter,M., and Gazit, E. (2006). Inhibition of amyloid fibril formation and cytotoxicity by hydroxyindole derivatives. *Biochemistry*, 45, 4727–4735.

23. Meng, F. L., Abedini, A., Plesner, A., Middleton, C. T., Potter, K. J., and Zanni, M. T. (2010). The sulfated triphenyl methane derivative acid fuchsin is a potent inhibitor of amyloid formation by human islet amyloid polypeptide and protects against the toxic effects of amyloid formation. *J. Mol. Biol.* 400, 555–566.

24. Bieschke, J., Russ, J., Friedrich, R. P., Ehrnhoefer, D. E., Wobst, H., Neugebauer, K., and Wanker, E. E. (2010). EGCG remodels mature α-synuclein and amyloid-β fibrils and reduces cellular toxicity. *Proc. Natl Acad. Sci. USA,* 107, 7710–7715.

25. Masuda, M., Suzuki, N., Taniguchi, S., Oikawa, T., Nonaka, T., and Iwatsubo, T. (2006). Small molecule inhibitors of α-synuclein filament assembly. *Biochemistry*, 45, 6085–6094.

26. Ehrnhoefer, D. E., Bieschke, J., Boeddrich, A., Herbst, M., Masino, L., Lurz, R. et al. (2008). EGCG redirects amyloidogenic polypeptides into unstructured, offpathway oligomers. *Nat. Struct. Mol. Biol.* 15, 558–566.

27. Mandel, S. A., Amit, T., Weinreb, O., Reznichenko, L., and Youdim, M. B. H. (2008). Simultaneous manipulation of multiple brain targets by green tea catechins: a potential neuroprotective strategy for Alzheimer and Parkinson diseases. *CNS Neurosci. Ther.* 14, 352–365.

28. Ehrnhoefer, D. E., Duennwald, M., Markovic, P., Wacker, J. L., Engemann, S., and Roark, M. (2006). Green tea (−)-epigallocatechin-gallate modulates early events in huntingtin misfolding and reduces toxicity in Huntington's disease models. *Hum. Mol. Genet.* 15,2743–2751.

29. Meng, F. L., Abedini, A., Plesner, A., Verchere, C. B., and Raleigh, D. P. (2010). The flavanol (−)-epigallocatechin 3-gallate inhibits amyloid formation by islet amyloid polypeptide, disaggregates amyloid fibrils, and protects cultured cells against IAPP-induced toxicity. *Biochemistry*, 49, 8127–8133.

30. Chandrashekaran, I. R., Adda, C. G., MacRaild, C. A., Anders, R. F., and Norton, R. S. (2010). Inhibition by flavonoids of amyloid-like fibril formation by plasmodium falciparum merozoite surface protein 2. *Biochemistry*, 49, 5899–5908.

31. Meng, X. Y., Munishkina, L. A., Fink, A. L., and Uversky, V. N. (2009). Molecular mechanisms underlying the flavonoid-induced inhibition of α-synuclein fibrillation. *Biochemistry*, 48, 8206–8224.

32. Robbins, K. J., Liu, G., Lin, G. X., and Lazo, N. D. (2011). Detection of strongly bound thioflavin T species in amyloid fibrils by ligand-detected 1H NMR. *J. Phys. Chem. Lett.* 2, 735–740.

33. Rezaei-Ghaleh, N., Andreetto, E., Yan, L.M., Kapurniotu, A., and Zweckstetter, M. (2011). Interaction between amyloid beta peptide and an aggregation blocker peptide mimicking islet amyloid polypeptide. *PLoS One,* 6, e20289.

34. Narayanan, S., and Reif, B. (2005). Characterization of chemical exchange between soluble and aggregated states of β-amyloid by solution-state NMR upon variation of salt conditions. *Biochemistry*, 44, 1444–1452.

35. Soong, R., Brender, J. R., Macdonald, P. M., and Ramamoorthy, A. (2009). Association of highly compact type II diabetes related islet amyloid polypeptide intermediate species at physiological temperature revealed by diffusion NMR spectroscopy. *J. Am. Chem. Soc.* 131, 7079–7085.

36. Wagner, G., Neuhaus, D., Worgotter, E., Vasak, M., Kagi, J. H. R., and Wuthrich, K. (1986). Nuclear magnetic resonance identification of “half-turn” and 3_{10}-helix secondary structure in rabbit liver metallothionein-2. *J. Mol. Biol.* 187, 131–135.

37. Hauber, I., Hohenberg, H., Holstermann, B., Hunstein, W., and Hauber, J. (2009). The main green tea polyphenol epigallocatechin-3-gallate counteracts semen-mediated enhancement of HIV infection. *Proc. Natl Acad. Sci. USA,* 106, 9033–9038.

38. Hudson, S. A., Ecroyd, H., Dehle, F. C., Musgrave, I. F., and Carver, J. A. (2009). (−)-Epigallocatechin-3-gallate (EGCG) maintains κ-casein in its pre-fibrillar state without redirecting its aggregation pathway. *J. Mol. Biol.* 392, 689–700.

39. Ferreira, N., Cardoso, I., Domingues, M. R., Vitorino, R., Bastos, M., and Bai, G. Y. (2009). Binding of epigallocatechin-3-gallate to transthyretin modulates its amyloidogenicity. *FEBS Lett.* 583, 3569–3576.

40. Roberts, B. E., Duennwald, M. L., Wang, H., Chung, C., Lopreiato, N. P., and Sweeny, E. A. (2009). A synergistic small-molecule combination directly eradicates diverse prion strain structures. *Nat. Chem. Biol.* 5, 936–946.

41. Wilkins, D. K., Grimshaw, S. B., Receveur, V., Dobson, C. M., Jones, J. A., and Smith, L. J. (1999). Hydrodynamic radii of native and denatured proteins measured by pulse field gradient NMR techniques. *Biochemistry*, 38, 16424–16431.

42. Vivekanandan, S., Brender, J. R., Lee, S. Y., and Ramamoorthy, A. (2011). A partially folded structure of amyloid-beta(1–40) in an aqueous environment. *Biochem. Biophys. Res. Commun.* 411, 312–316.

43. Brender, J. R., Nanga, R. P. R., Popovych, N., Soong, R., Macdonald, P. M., and Ramamoorthy, A. (2011). The amyloidogenic SEVI precursor, PAP248-286, is highly unfolded in solution despite an underlying helical tendency. *Biochim. Biophys. Acta,* 1808, 1161–1169.

44. Uversky, V. N., and Fink, A. L. (2004). Conformational constraints for amyloid fibrillation: the importance of being unfolded. *Biochim. Biophys. Acta,* 1698, 131–153.

45. Abedini, A., and Raleigh, D. P. (2009). A critical assessment of the role of helical intermediates in amyloid formation by natively unfolded proteins and polypeptides. *Protein Eng. Des. Sel.* 22, 453–459.

46. Motta, A., Temussi, P. A., Wunsch, E., and Bovermann, G. (1991). A 1H NMR study of human calcitonin in solution. *Biochemistry*, 30, 2364–2371.

47. Benedek, G. B., Yong, W., Lomakin, A., Kirkitadze, M. D., Teplow, D. B., and Chen, S. H. (2002). Structure determination of micelle-like intermediates in amyloid β-protein fibril assembly by using small angle neutron scattering. *Proc. Natl Acad. Sci. USA*, 99, 150–154.

48. Rhoades, E., and Gafni, A. (2003). Micelle formation by a fragment of human islet amyloid polypeptide. *Biophys. J.* 84, 3480–3487.

49. Padrick, S. B., and Miranker, A. D. (2002). Islet amyloid: phase partitioning and secondary nucleation are central to the mechanism of fibrillogenesis. *Biochemistry*, 41, 4694–4703.

50. Estelrich, J., and Sabate, R. (2005). Evidence of the existence of micelles in the fibrillogenesis of β-amyloid peptide. *J. Phys. Chem. B,* 109, 11027–11032.

51. Jean, L., Lee, C. F., Lee, C., Shaw, M., and Vaux, D. J. (2010). Competing discrete interfacial effects are critical for amyloidogenesis. *FASEB J*. 24, 309–317.

52. Fawzi, N. L., Ying, J., Torchia, D. A., and Clore, G. M. (2010). Kinetics of amyloid β monomer-to-oligomer exchange by NMR relaxation. *J. Am. Chem. Soc.* 132, 9948–9951.

53. Campbell, A. P., and Sykes, B. D. (1993). The twodimensional transferred nuclear Overhauser effect: theory and practice. *Annu. Rev. Biophys. Biomol. Struct.* 22, 99–122.

54. Tsai, H. H., Zanuy, D., Haspel, N., Gunasekaran, K., Ma, B. Y., Tsai, C. J., and Nussinov, R. (2004). The stability and dynamics of the human calcitonin amyloid peptide DFNKF. *Biophys. J*. 87, 146–158.

55. Miyata,M., Sato, T., Kugimiya,M., Sho,M.,Nakamura, T., and Ikemizu, S.(2010). The crystal structure of the green tea polyphenol (−)-epigallocatechin gallate–transthyretin complex reveals a novel binding site distinct from the thyroxine binding site. *Biochemistry*, 49, 6104–6114.

56. Sawaya, M. R., Sambashivan, S., Nelson, R., Ivanova, M. I., Sievers, S. A., and Apostol, M. I. (2007). Atomic structures of amyloid cross-β spines reveal varied steric zippers. *Nature*, 447, 453–457.

57. Luca, S., Yau, W. M., Leapman, R., and Tycko, R. (2007). Peptide conformation and supramolecular organization in amylin fibrils: constraints from solid-state NMR. *Biochemistry*, 46, 13505–13522.

58. Luhrs, T., Ritter, C., Adrian, M., Riek-Loher, D., Bohrmann, B., Doeli, H. et al. (2005). 3D structure of Alzheimer's amyloid-β(1–42) fibrils. *Proc. Natl Acad. Sci. USA*, 102, 17342–17347.

59. Yu, L. P., Edalji, R., Harlan, J. E., Holzman, T. F., Lopez, A. P., Labkovsky, B. et al. (2009). Structural characterization of a soluble amyloid β-peptide oligomer. *Biochemistry*, 48, 1870–1877.

60. Lindquist, S. L., Serio, T. R., Cashikar, A. G., Kowal, A. S., Sawicki, G. J., Moslehi, J. J. et al. (2000). Nucleated conformational conversion and the replication of conformational information by a prion determinant. *Science*, 289, 1317–1321.

61. Kanaori, K., and Nosaka, A. Y. (1996). Characterization of human calcitonin fibrillation in aqueous urea solution by ^{1}HNMRspectroscopy. *Biochemistry*, 35, 12671–12676.

62. Ellman, G. L. (1958). A colorimetric method for determining low concentrations of mercaptans. *Arch. Biochem. Biophys.* 74, 443–450.

63. Tanner, J. E. (1970). Use of stimulated echo in NMR diffusion studies. *J. Chem. Phys.* 52, 2523–2526.

64. Mills, R. (1973). Self-diffusion in normal and heavy water in the range 1–45°. *J. Phys. Chem*. 77, 685–688.

65. Stejskal, E. O., and Tanner, J. E. (1965). Spin diffusion measurements: spin echoes in the presence of a timedependent field gradient. *J. Chem. Phys.* 42, 288–292.

66. Guntert, P., Mumenthaler, C., and Wuthrich, K. (1997). Torsion angle dynamics for NMR structure calculation with the new program DYANA. *J. Mol. Biol.* 273, 283–298.

67. Guntert, P. (2004). Automated NMR structure calculation with CYANA. *Methods Mol. Biol.* 278, 353–378.

68. Garrett, D. S., Powers, R., Gronenborn, A. M., and Clore, G. M. (1991). A common sense approach to peak picking in two-, three-, and four-dimensional spectra using automatic computer analysis of contour diagrams. *J. Magn. Reson.* 95, 214–220.

69. Cornilescu, G., Delaglio, F., and Bax, A. (1999). Protein backbone angle restraints from searching a database for chemical shift and sequence homology. *J. Biomol. NMR,* 13, 289–302.

CHAPTER 6

Conclusions and Future Directions

6.1 Conclusions

The overall goal of the presented dissertation is to understand the interaction and electron transfer between cytochrome P450 reductase and its redox partners from a structural point of view. In the preceding chapters, I presented the kinetic and structural characterization of the FBD – cyt c and FBD – cyt P450 complexes, proposed structural models of these two complexes based on our NMR studies, and predicted potential electron transfer pathways from FBD to cyt c/cyt P450. In addition, I showed our approaches to understand the role of the transmembrane domains in the complex formation between CPR and its redox partners by probing the structure and dynamics of the transmembrane domain of CPR using solid-state NMR techinques. On the other hand, I also investigated the structural characteristics of human calcitonin to uncover its aggregation pathway and its interaction with an amyloid fibril inhibitor EGCG.

In chapter 2, we characterized the electron transfer and complex formation between FBD and cyt c. From the kinetic studies, we observed distinct rates of electron transfer between FBD and cyt c depending on the redox states of FBD. Compared to wild-type CPR, FBD reduces cyt c at a much higher rate in both its semiquinone and hydroquinone state, suggesting that conformational gating of CPR plays a key role in the electron transfer process. We utilized NMR titration experiments to investigate the complex formation and identify the residues on the binding interface. The results revealed that the formation of dynamic complexes between FBD and cyt c occurs on a fast exchange time scale with a dissociation constant K_d of 0.024 mM. Specific residues of FBD involved in the binding interface with cyt c were identified by chemical shift perturbation mapping, most of which are located around the solvent exposed edge of the FMN cofactor. Finally, we generated the structure model of the FBD-cyt c complex using HADDOCK, which includes complexes with two probable orientations. Salt bridge formation between Glu-213/Glu-214 of FBD and Lys-87 of cyt c was identified in the major structural

model, which could be essential to the stability of the complex. Based on the complex structure, we predict electron transfer pathway mediated by Lys-13 of cyt c. This work provides a structural basis for a better understanding of the interaction between CPR and cyt c and allows comparisons to be drawn with other electron transfer complexes involving CPR or cyt c.

In chapter 3, we focused on probing the binding interface between FBD and cyt P450 by solution NMR techniques. Our NMR titration experiments indicate the residues of FBD experienced a slow-to-intermediate exchange upon complex formation with cyt P450. By chemical shift perturbation and line broadening analysis, we identified the epitope on FBD recognized by cyt P450 which is similar to the binding site of cyt c. Subsequently, a structural model was generated using NMR restraints and previous site-directed mutagenesis studies. The model revealed detail information on the specific residues involved in interprotein recognition. Based on the structural model, a potential pathway was predicted involving Met-132 and Arg-133 of cyt P450.

Chapter 4 presents our efforts to understand the role of transmembrane domains in complex formation between FBD and its redox partners. We characterized the structure and dynamics of the transmembrane domain of CPR in native membrane-like environment by solid-state NMR techniques in conjunction with spectra simulation. Our results reveal that the N-terminal transmembrane domain of CPR adopts an α-helical conformation in the lipid environment, and is tilted approximately 13° from the lipid bilayer normal. We also investigated the interaction between FBD and cyt P450 in the lipid environment. Our results show binding between the soluble domains of the two proteins in the lipid bicelles, and suggest transient interplay between their transmembrane helices.

In summary, the work presented in these chapters provides rich structural information on the electron transfer complexes between the FMN binding domain of CPR and its redox partners. The formation of the two complexes investigated – the FBD-cyt c and FBD-cyt P450 complexes – occurs at different time scales based on the observations in the NMR experiments. The proposed structural models allow us to zoom in to the binding interfaces and identify the intermolecular interactions that contribute to the complex formation. It provides a structural basis for further investigations on these electron transfer complexes and helps to elucidate the general mechanism of electron transfer from CPR to its redox partners.

Chapter 5 is an investigation on understanding the amyloid aggregation pathway of human calcitonin and its interaction with an amyloid fibril inhibitor EGCG. We found out that at the concentration of 1 mM hCT adopts a β-hairpin conformation, while it is predominantly unstructured at 0.3 mM. This implies a conformation transition from an extended to a β-hairpin structure in the process of hCT association. In the β-hairpin conformation observed in the 1- mM hCT, the aromatic side chains of Tyr-12 and Phe-16 are oriented in a favorable way for intermolecular π–π stacking, which is proposed to be a crucial interaction for peptide association and fibrillation. We also investigated the effect of the polyphenol epigallocatechin 3-gallate (EGCG) on hCT fibrillation by NMR and electron microscopy. The results show that EGCG efficiently inhibits fibril formation of hCT by preventing the initial association of hCT before fiber formation. The NMR experiments was applied to identify the binding site of EGCG on hCT, which revealed that the interaction between aromatic rings of EGCG and the aromatic side chains of the peptide may play an important role in inhibiting fibril formation of hCT.

6.2 Future directions

6.2.1 Refinement of the structure models by paramagnetic labeling approaches

In this thesis, we use chemical shift perturbation and line broadening analysis as ambiguous restraints to generate structural models for the FBD – cyt P450 and FBD – cyt c complexes. These models can be improved by using unambiguous distance restraints, which can be obtained by paramagnetic labeling approaches. Paramagnetic species affect nuclear magnetic resonances in a distance- and geometry-dependent manner, thus can provide powerful restraints for the determination of the three-dimensional structure of proteins and analysis of protein-protein/ligand interactions (*1*). The unpaired electron in the paramagnetic label induces extra magnetic field at the nuclei of the protein, causing enhanced relaxation for the resonances or chemical shift perturbation. Paramagnetic relaxation enhancement (PRE) is proportional to $1/r^6$ in which r is the distance between the paramagnetic center to the measured nucleus, therefore it can be converted to distance restraints for structural determination. Compared to nuclear overhauser effect (NOE) which can indicate spatial proximity up to 5 Å, PRE allows for determination of much longer distance restraints (12-30 Å) which makes it particularly useful for structural studies for protein complexes. The anisotropic dipolar interaction between the paramagnetic center and the measured nucleus also cause chemical shift changes called

pseudocontact shift (PCS) which is dependent on the magnetic susceptibility tensor of the paramagnetic center and its orientations with respect to the nuclear spins. Strong magnetic centers can cause weak molecular alignment with the magnetic field, which provides information about the orientation between scalar coupled spin pairs and the molecular alignment tensor. (*2*). Due to high sensitivity of the paramagnetic effects, paramagnetic NMR approaches exhibit great advantages in investigating transient intermediates of protein-protein complexes which is a common case for electron-transfer protein complexes.

A variety of paramagnetic labels have been developed to attach to proteins. Based on the means of attachment, they can be categorized into terminal metal binding peptide and disulfide-bond tags. One of the most commonly used labels is MTSL spin label (*3*) which contains one unpaired electron and is attached via a disulfide bond to a cysteine residue. Nevertheless, the rotational motion of the MSTL on the protein surface can lead to up to 6 Å of unambiguity in the measured distances. Therefore, novel paramagnetic tags are being developed to immobilize the paramagnetic center. A double-armed caged lanthanide NMR probe (CLaNP) which attachs to two cysteines on the protein surface simultaneously has been developed by Ubbink et al and utilized for structure determination of protein-protein complexes and small molecule-protein complex (*2, 4*). The rigidity of the tag enhances pseudocontact shifts of the resonances and RDC alignments of the proteins, which aids in generating long-range distance information (*2*).

In order to attach the CLaNP tag, we will first introduce double mutations of cycsteines on two proximal residues at various sites on the surface of cyt P450/cyt c. Attachment of the CLaNP with paramagnetic and diamagnetic metal ions will be performed as described in the literature (*5*). A series of tests will be performed on the CLaNP tagged mutants of cyt P450/cyt c to check for their functional viability using metabolism assays as well as measuring the binding affinity between the mutants and FBD. Only mutations with similar functional activity and binding properties as the wild-type will be utilized for further investigation by NMR studies. The second step involves measuring the paramagnetic effect of the tag on the residue of FBD by NMR experiments. ^{15}N-labeled FBD and CLaNP-attached cyt P450/cyt c mutants would be incorporated together at 1:1 ratio into optimized membrane mimetics (e.g. isotropic bicelles, nanodiscs, etc.). 2D ^{1}H- ^{15}N TROSY-HSQC will be recorded to measure the paramagnetic effects of the CLaNP on the resonances of FBD. Pseudocontact shifts (PCS) can be calculated by taking the differences of the chemical shift values with paramagnetic and diamagnetic probes,

and paramagnetic relaxation enhancement (PRE) values can be calculated according to equation 7.1 (*6*). I_p, I_d represent the intensities of resonances with paramagnetic and diamagnetic probes respectively and R_{2d} represents the transverse relaxation rate with diamagnetic probe. PCS and PRE values give information on the distances and angles between a detected nucleus and the paramagnetic center in the probe with the relationship depicted in equation 7.2 and 7.3 (*1*). Finally, the structural models of the complexes can be generated by molecular docking. PCS values and unambiguous distance restraints derived from PRE values could be implemented into docking programs as constraints to drive the formation of complex structures. Available docking programs include XPLOR-NIH program with PARArestraints module (*7*), HADDOCK (*8*), and so on. The lowest energy structures would be analyzed and evaluated by back-calculating the PCS and PRE values and comparing with the experimental values. Good agreements between the back-calculated and experimental values would be implication of valid complex structures.

$$\frac{I_p}{I_d} = \frac{R_{2d}\mathrm{e}^{-\Gamma_2 t}}{R_{2d}+\Gamma_2} \qquad (7.1)$$

$$\Delta\delta^{PCS} = \frac{1}{12\pi r^3}[\Delta\chi_{ax}(3cos^2\theta - 1) + \frac{3}{2}\Delta\chi_{rh}sin^2\theta\, cos\, 2\varphi] \qquad (7.2)$$

$$r = \sqrt[6]{\frac{\gamma^2 g^2 \beta^2}{20\Gamma_2}(4\tau_c + \frac{3\tau_c}{1+\omega_h^2\tau_c^2})} \qquad (7.3)$$

6.2.2 Verification of the electron transfer pathways by site-directed mutagenesis and utilization of other docking/predicting programs

Electron transfer pathways were proposed utilizing our structural models of the complexes by HARLEM (*9*). It employs PATHWAY analysis which is based upon single-tunneling-pathway assumption, while in reality it is possible that the redox centers in the protein complex are coupled via a number of pathways with similar coupling values such that modifying a single pathway in the network will have hardly any effect on the electron transfer rates. Furthermore, the accuracy of the empirical decaying factors input into the program also affects the results of pathway prediction. Therefore, in order to verify the predicted electron transfer pathway, we can perform site-directed mutagenesis studies on the residues identified by the

program in mediating electron transfers. Special caution needs to be taken in conducting these studies due to the possible secondary structural changes of the proteins or disruption of the binding interface caused by mutations. Activity assays will have to be carried out on the mutants to assess the structural integrity of the proteins, and binding affinities between the mutants and FBD will be measured to distinguish the effect of the mutation on the interaction of the two proteins.

Utilization of other programs for molecular docking or electron transfer pathway prediction also helps to validate our proposed complex models. A dynamic docking tailored to the intermolecular ET problem was developed by Liang *et al* (*10*). Instead of generating the structural models and analyzing electron transfer at two independent and consecutive steps as in a conventional way, the novel docking program mathematically combines the electronic coupling calculations with estimation of the docking energies in a Monte Carlo (MC) sampling framework. By the integrated algorithm, it can apply a direct "electronic coupling" filter for functional active complexes in the docking process, and thus is more efficient in sorting out the relevant complex orientations than the conventional methods. This enables us to employ more computationally expensive and accurate methods to describe the relevant intermolecular interaction energies and donor-acceptor coupling upon variations of protein surface and environment (*10*). This approach has been demonstrated on the myoglobin – cyt c complex. Mixed quantum mechanics /molecular mechanics (QM/MM) algorithms have also been developed to track the electron delocalization. Guallar *et al* demonstrate this method on the cytochrome c – cytochrome c peroxidase complex (*11*). In this algorithm, the system is divided into a quantum region in which the Schrödinger equation is solved to extract electronic properties in this region; meanwhile the rest of the protein is treated as charged spheres. By shifting the quantum region on to different residues, the electron transfer pathway coupling the donor and the accepter can be obtained. By utilizing the aforementioned methosds, we can validate the complex models and electron transfer pathway we proposed, and compare the outcome and efficiency of different algorithms.

6.3 References

1. Otting, G. (2010) Protein NMR using paramagnetic ions, *Annu Rev Biophys 39*, 387-405.

2. Keizers, P. H., Desreux, J. F., Overhand, M., and Ubbink, M. (2007) Increased paramagnetic effect of a lanthanide protein probe by two-point attachment, *J Am Chem Soc 129*, 9292-9293.

3. Berliner, L. J., Grunwald, J., Hankovszky, H. O., and Hideg, K. (1982) A novel reversible thiol-specific spin label: papain active site labeling and inhibition, *Anal Biochem 119*, 450-455.

4. Keizers, P. H., Saragliadis, A., Hiruma, Y., Overhand, M., and Ubbink, M. (2008) Design, synthesis, and evaluation of a lanthanide chelating protein probe: CLaNP-5 yields predictable paramagnetic effects independent of environment, *J Am Chem Soc 130*, 14802-14812.

5. Guan, J. Y., Keizers, P. H., Liu, W. M., Lohr, F., Skinner, S. P., Heeneman, E. A., Schwalbe, H., Ubbink, M., and Siegal, G. (2013) Small-molecule binding sites on proteins established by paramagnetic NMR spectroscopy, *J Am Chem Soc 135*, 5859-5868.

6. Scanu, S., Foerster, J. M., Ullmann, G. M., and Ubbink, M. (2013) Role of hydrophobic interactions in the encounter complex formation of the plastocyanin and cytochrome f complex revealed by paramagnetic NMR spectroscopy, *J Am Chem Soc 135*, 7681-7692.

7. Schwieters, C. D., Kuszewski, J. J., Tjandra, N., and Clore, G. M. (2003) The Xplor-NIH NMR molecular structure determination package, *J Magn Reson 160*, 65-73.

8. Dominguez, C., Boelens, R., and Bonvin, A. M. (2003) HADDOCK: a protein-protein docking approach based on biochemical or biophysical information, *J Am Chem Soc 125*, 1731-1737.

9. Kurnikov, I. V. (2000) HARLEM molecular modeling package, Department of Chemistry, University of Pittsburgh, Pittsburgh, PA.

10. Liang, Z. X., Kurnikov, I. V., Nocek, J. M., Mauk, A. G., Beratan, D. N., and Hoffman, B. M. (2004) Dynamic docking and electron-transfer between cytochrome b5 and a suite of myoglobin surface-charge mutants. Introduction of a functional-docking algorithm for protein-protein complexes, *J Am Chem Soc 126*, 2785-2798.

11. Guallar, V., and Wallrapp, F. (2008) Mapping protein electron transfer pathways with QM/MM methods, *J R Soc Interface 5 Suppl 3*, S233-239.

Appendix A

Chemical shift assignments of the ^{15}N-^{1}H TROSY-HSQC spectra

MGDSHEDTSA	TMPEAVAEEV	SLFSTTDMVL	FSLIVGVLTY	WFIFRKKKEE	IPEFSKIQTT
APPVKESSFV	EKMKKTGRNI	IVFYGSQTGT	AEEFANRLSK	DAHRYGMRGM	SADPEEYDLA
DLSSLPEIDK	SLVVFCMATY	GEGDPTDNAQ	DFYDWLQETD	VDLTGVKFAV	FGLGNKTYEH
FNAMGKYVDQ	RLEQLGAQRI	FELGLGDDDG	NLEEDFITWR	EQFWPAVCEF	FGVEATGEE

Figure A.1 Sequence of FBD.

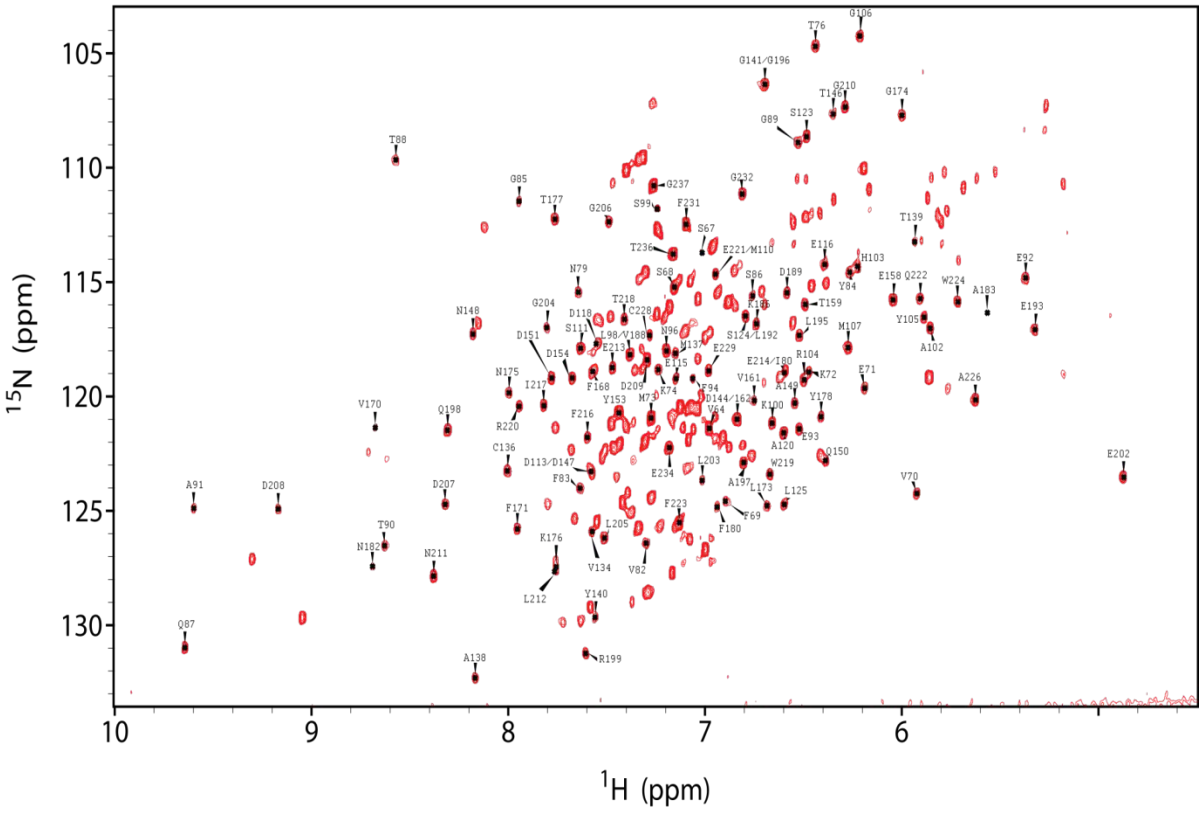

Figure A.2 ^{15}N-^{1}H TROSY-HSQC spectrum of ^{15}N-labeled FBD.

Table A.1 Chemical shift of the resonances in ^{15}N-^{1}H TROSY-HSQC spectrum of ^{15}N-labeled FBD.

Residue	^{15}N chemical shift	^{1}H chemical shift
V64	121.515	8.016
S67	114.996	8.102
S68	114.575	8.169
F69/F181	124.803	7.967
F69/F181	124.912	7.927
V70	124.453	7.005
E71	119.786	7.262
K72	118.92	7.505
K74	118.9	8.295
K75	117.384	8.161
T76	104.789	7.484
N79	115.516	8.688
I80/E214	119.289	7.661
V82	126.469	8.33
F83	124.121	8.68
Y84	114.648	7.306
G85	111.578	8.988
S86	115.712	7.805
T88	109.844	9.639
G89	108.98	7.57
T90	126.758	9.724
A91	125.07	10.676
E92	114.936	6.422
E93	121.566	7.565
F94	119.369	8.11
N96	118.109	8.242
L98/V188	118.241	8.424
S99	111.931	8.292
K100	121.193	7.692
D101	121.065	8.227
A102	117.009	6.893
H103	114.571	7.231
R104	119.262	7.511
Y105	116.66	6.934
G106	104.244	7.262
M107	117.938	7.325
R108	117.168	8.019
S111	117.985	8.664
D113/147	123.377	8.622
E115	119.51	8.22
E116	114.132	7.431
Y117	116.633	7.597
D118	117.771	8.591

A120	121.677	7.649
S123	108.716	7.528
S124/L192	116.562	7.837
L125	124.791	7.64
L132	121.081	8.445
V134	125.938	8.612
C136	123.3	9.045
M137	118.184	8.191
A138	132.401	9.208
T139	113.3	6.973
Y140	129.671	8.589
G141/G196	106.435	7.74
G143	105.5	7.629
D144/D162	121.07	7.879
T146	107.734	7.396
N148	117.373	9.226
A149	120.417	7.59
Q150/D160	122.783	7.441
D151	119.254	8.834
D154	119.31	8.729
E158	115.864	7.082
T159	116.057	7.533
V161	120.299	7.794
L163	125.414	8.71
G165	112.405	9.031
F168	118.998	8.616
A169/R78	118.852	8.383
V170	121.44	9.718
F171	125.834	8.998
L173	124.91	7.733
G174	107.799	7.036
N175	119.896	9.044
K176	127.179	8.799
T177	112.433	8.811
Y178	120.988	7.449
N182	127.562	9.742
A183	116.446	6.624
M184/G172	116.739	8.594
G185	107.276	8.298
K186	116.899	7.789
Y187	120.185	8.068
D189	115.56	7.628
E193	117.157	6.368
L195	117.401	7.562
A197	122.982	7.85
Q198	121.557	9.351

R199	131.318	8.652
I200	124.745	8.838
E202	123.633	5.921
L203	123.754	8.058
G204	117.07	8.844
L205	126.269	8.557
G206	112.434	8.532
D207	124.809	9.37
D208	125.006	10.215
D209	118.128	8.35
G210	107.417	7.333
N211	127.944	9.428
L212	127.678	8.803
E213	118.838	8.516
E214/I80	119.016	7.643
F216	121.889	8.65
I217	120.49	8.87
T218	116.744	8.459
W219	123.456	7.718
R220	120.473	8.987
E221/M110	114.754	7.993
Q222	115.786	6.951
F223	126.335	8.122
W224	115.928	6.767
A226	120.253	6.671
V227	122.226	7.852
C228	117.428	8.331
E229	118.928	8.019
G232	111.275	7.859
V233	116	7.925
E234/F152	122.285	8.218
A235	124.645	8.468
T236	113.928	8.196
G237	110.878	8.304

Appendix B

Solvent accessibility of the FBD residues

The solvent accessibility of FBD residues was assessed using NACCESS (*1*). The results of the solvent accessibility prediction were used to filter the residues input as HADDOCK restraints in chapter 2 and 3.

Table B.1 Residues of FBD that are solvent accessible (>35.0% for all-atoms) based on NACCESS.

Amino acid type	Amino acid number	All-atoms, Relative %SA	Total-side, Relative %SA	Main-chain, Relative %SA	Non-polar, Relative %SA	All-polar, Relative %SA
VAL	64	129.1	116.4	168.4	115.6	172.5
LYS	65	47.9	42.7	70.7	55.9	36.8
GLU	66	57.9	63	39.4	36.1	69.6
SER	67	70.3	99.8	10.2	81	62.7
GLU	71	59.6	74.9	4.8	65	56.7
LYS	72	38.6	47.1	1.4	40	36.6
LYS	74	51.4	48.5	63.8	50.9	52.1
LYS	75	78.5	80.1	71.4	88.7	64.4
GLY	77	69.9	103.4	47.3	96.1	46.9
GLN	87	42.2	34.7	70.3	16.3	52.9
THR	88	80	84.4	67.9	107.3	47.4
GLY	89	44.8	62.2	33.1	59.1	32.3
GLU	92	40.5	51.8	0	16	53.8
GLU	93	59.2	75	2.6	51.4	63.5
ASN	96	51.1	67.5	4.9	44.4	54.2
LYS	100	78.9	90	30.5	87.3	67.2
ARG	104	85.2	89.1	64.1	126.4	65.2
GLY	106	56.4	30.4	74	30.4	79.3
ARG	108	45.2	53.6	0.3	36.1	49.6
GLU	115	49.9	58.3	19.7	38.7	55.9
GLU	116	43.5	55.6	0	27	52.3
ASP	118	55.8	74.8	4.1	52.1	57.9
SER	123	37.8	36.1	41.1	29.1	43.9
PRO	126	37.9	24.2	139.1	25.2	138.9
GLU	127	66.8	64.9	73.5	77	61.3
ASP	129	82.1	99.9	33.7	93.2	76.1
LYS	130	44.1	49.8	19.1	45	42.9
GLY	141	60.1	101.7	31.8	90.6	33.1
GLU	142	82.5	95.7	35.3	79.7	84.1
ASP	144	50.7	69.3	0	49.3	51.4

ASP	147	76.1	98.1	15.9	72	78.3
GLN	150	39	49.4	0	69.7	26.3
ASP	151	62.7	77.4	22.7	54.6	67
ASP	154	51.9	61.3	26.4	69.3	42.6
GLN	157	42.5	46.1	28.7	22.8	50.6
GLU	158	90.2	92.1	83.4	92.3	89.1
ASP	160	95.3	113	47	94.8	95.6
ASP	162	70.5	79.5	45.8	86	62.1
THR	164	63.9	74.3	35.8	82.2	42.1
GLY	165	41.2	75.3	18.1	65.3	19.9
LYS	176	61.2	63.9	49.2	66.6	53.7
THR	177	69.1	64.1	82.6	82.8	52.7
GLU	179	95.9	99.7	82.4	99	94.3
HIS	180	46.9	57.7	2.5	55.2	37.4
LYS	186	40.8	49.8	1.6	39.4	42.8
GLN	190	57	71.6	2.2	69.8	51.8
GLU	193	48.9	55.5	25.5	38.6	54.5
GLN	194	76	75.8	76.8	55.2	84.7
GLY	196	39.6	56.3	28.2	51.3	29.2
GLN	198	47.9	60.6	0.5	77.3	35.8
GLU	202	61.9	75.5	13.1	70.3	57.4
LEU	205	41.9	38.1	56	38.6	54.5
ASP	208	45.7	48.3	38.8	10.5	64.8
ASP	209	58.3	57.3	61.1	11	83.9
GLY	210	71.5	107.8	47	99.7	46.7
ASN	211	54.6	69.1	13.5	51.5	56
GLU	213	37.3	45.9	6.2	70.1	19.6
GLU	214	56.2	70.3	5.3	72.6	47.4
ASP	215	35.7	44.8	10.9	35.8	35.7
THR	218	50.1	68.5	0.3	64.8	32.5
GLU	221	69.4	83.4	19.2	69.9	69.1
GLN	222	52.6	64.1	9.3	66	47
PRO	225	46	49.5	20.1	50.3	11.7
GLU	229	88.4	99	50.1	92.1	86.4
PHE	230	54.8	52.1	67.4	51.8	69.6
GLY	232	50.7	85.9	26.9	86.8	18.9
VAL	233	37.4	32	54	31.7	55.5
GLU	234	83.8	93.4	49.4	86.4	82.5
ALA	235	91.3	36.4	190.2	79.9	113.5

Table B.2 Residues of FBD that are solvent inaccessible (<35.0% for all-atoms) based on NACCESS.

Amino acid type	Amino acid number	All-atoms, Relative %SA	Total-side, Relative %SA	Main-chain, Relative %SA	Non-polar, Relative %SA	All-polar, Relative %SA
		REL	REL	REL	REL	REL
SER	68	23.6	24.4	21.9	34.4	15.8
PHE	69	0	0	0	0	0
VAL	70	1.9	2.5	0	2.5	0
MET	73	0	0	0	0	0
THR	76	24.1	23.6	25.4	37.4	8.2
ARG	78	20.3	22.5	8.8	6	27.3
ASN	79	12.2	16.6	0	24.5	6.4
ILE	80	0.1	0.1	0	0.1	0
ILE	81	0	0	0	0	0
VAL	82	0.2	0.2	0	0.2	0
PHE	83	0	0	0	0	0
TYR	84	16.2	19.4	0	7.7	31.4
GLY	85	0.2	0.4	0	0.3	0
SER	86	13.9	5.8	30.3	9.7	16.8
THR	90	29	39.7	0	25	33.8
ALA	91	0	0	0	0	0
PHE	94	3.3	4	0	4	0
ALA	95	0	0	0	0	0
ARG	97	32	37.9	0.7	44.5	26
LEU	98	0.1	0.1	0	0.1	0
SER	99	7.4	7.8	6.5	1.7	11.4
ASP	101	18	23	4.4	15.4	19.4
ALA	102	0	0	0	0	0
HIS	103	27	26.8	27.7	22.7	31.7
TYR	105	32.5	38.5	2.6	36.6	25.1
MET	107	8.3	8	9.4	8.7	6.4
GLY	109	5.7	0	9.6	0	10.7
MET	110	16.9	21	0	20.8	0
SER	111	25.8	9.1	59.7	0	44.2
ALA	112	3.5	5.5	0	5.3	0
ASP	113	19.7	24.9	5.6	6.9	26.7
PRO	114	2.3	0	19.1	0.3	18.4
TYR	117	6.4	5.4	11.4	0.7	16.8
LEU	119	3.5	1.7	10	1.7	10.4
ALA	120	31.3	43.9	8.6	44.6	5.4
ASP	121	24.4	33.3	0	2.7	36.1
LEU	122	0	0	0	0	0
SER	124	29.5	44.1	0	21.7	35.1
LEU	125	0	0	0	0	0
ILE	128	11.4	13.1	5.1	13	5

SER	131	2.8	2.7	3.1	0	4.8
LEU	132	0	0	0	0	0
VAL	133	0.1	0.1	0	0.1	0
VAL	134	0.2	0.2	0	0.2	0
PHE	135	0	0	0	0	0
CYS	136	0	0	0	0	0
MET	137	0.1	0.1	0	0.1	0
ALA	138	0.4	0	1	0	1.1
THR	139	0	0	0	0.1	0
TYR	140	15.9	18.3	4.1	22.6	3.9
GLY	143	18.2	2.1	29	2.3	32.2
PRO	145	7	0.9	52.7	0.8	56.3
THR	146	0.7	0.8	0.3	0.9	0.4
ASN	148	10.8	12.4	6.2	29	2.2
ALA	149	0.2	0.3	0	0.3	0
PHE	152	2.7	2.4	4.1	2.4	4.2
TYR	153	20.8	25	0	10.3	39.7
TRP	155	22.5	26	3	25.7	12.2
LEU	156	0	0	0	0	0
THR	159	16.7	14.1	23.6	12.9	21.2
VAL	161	25.7	34	0.4	33.6	0.4
LEU	163	0.3	0.3	0	0.3	0
VAL	166	0.1	0.1	0	0.1	0
LYS	167	20.7	25.4	0.2	20.6	20.7
PHE	168	0	0	0	0	0
ALA	169	0	0	0	0	0
VAL	170	0	0	0	0	0
PHE	171	0.5	0.6	0	0.6	0
GLY	172	0	0	0	0	0
LEU	173	0	0	0	0	0
GLY	174	0	0	0	0	0
ASN	175	15.3	20.8	0	0	22.6
TYR	178	36.5	41	13.7	33.9	41.1
PHE	181	16.2	17.5	10.5	17.4	10.9
ASN	182	0	0	0	0	0
ALA	183	27.1	32.9	16.6	33.3	14.9
MET	184	0.6	0.8	0	0.8	0
GLY	185	0	0	0	0	0
TYR	187	27.8	33.2	0.4	39.9	6
VAL	188	0	0	0	0	0
ASP	189	2.2	3	0	0.3	3.3
ARG	191	17.1	20.2	0.7	10.5	20.4
LEU	192	0.1	0.1	0	0.1	0
LEU	195	7.9	8.1	7.1	9.9	0
ALA	197	3.9	0	10.9	0.2	11.2
ARG	199	27	23.8	43.9	26.4	27.2

ILE	200	15.4	2.6	62.9	4	59.5
PHE	201	13	14.8	4.4	15.7	0
LEU	203	19.5	13.2	43.3	13.1	44.8
GLY	204	9.2	22.9	0	19.7	0
GLY	206	0.1	0	0.1	0	0.1
ASP	207	10.3	14	0	15.2	7.6
LEU	212	6	6.1	5.4	6.1	5.6
PHE	216	0	0	0	0	0
ILE	217	32.6	41.3	0.3	40.9	0.3
TRP	219	3.9	4.5	0.8	5	0.5
ARG	220	31.8	37	3.9	6.9	43.8
PHE	223	0	0	0	0	0
TRP	224	1.4	1.6	0	1.8	0
ALA	226	27.5	36.5	11.4	35.5	12
VAL	227	0	0	0	0	0
CYS	228	12.8	15.7	5.3	16.4	3.2
PHE	231	11.5	7	32.7	9.7	20.3

References

1. Hubbard, S. J., and Thornton, J. M. (1993) NACCESS, Department of Biochemistry and Molecular Biology, University College London